

# Experimental Investigation of Magnetohydrodynamic Flow For An Intense Proton Target

A Dissertation Presented

by

Hee Jin Park

to

The Graduate School

in Partial Fulfillment of the

## Requirements

for the Degree of

Doctor of Philosophy

in

# Mechanical Engineering

**Stony Brook University**

December 2009

16

**Stony Brook University**

17

The Graduate School

18

**Hee Jin Park**

19

We, the dissertation committee for the above candidate for the

20

Doctor of Philosophy degree,

21

hereby recommend acceptance of this dissertation.

22

---

Harold G. Kirk, Dissertation Co-Advisor,  
Physicist, Department of Physics, Brookhaven National Laboratory

23

---

Foluso Ladeinde, Dissertation Co-Advisor,  
Professor, Department of Mechanical Engineering

24

---

Thomas Cubaud, Chairperson of Defense,  
Professor, Department of Mechanical Engineering

25

---

Kirk T. McDonald , Outside Member,  
Professor, Physics Department, Princeton University

26

---

James Glimm, Outside Member,  
Professor, Department of Applied Math. & Stat., Stonybrook University

27

This dissertation is accepted by the Graduate School.

28

---

Lawrence Martin  
Dean of the Graduate School

29 Abstract of the Dissertation  
30 **Experimental Investigation of Magnetohydrodynamic**  
31 **Flow For An Intense Proton Target**  
32 by  
33 **Hee Jin Park**  
34 **Doctor of Philosophy**  
35 in  
36 **Mechanical Engineering**  
37 **Stony Brook University**  
38 **2009**

39 Efficient production of pions can be achieved by colliding an intense proton  
40 beam with a high-Z target. It is required to investigate the effect of Hg jet  
41 disruption by the interaction of an intense proton beam for high power target  
42 design. The experiment of mercury (Hg) jet on the interaction of an intense  
43 proton beam in magnetic fields has been carried out. The primary diagnostics  
44 in the experiment employed the technique of back-illuminated laser shadow  
45 photography to freeze the transient events. The images are recorded by several  
46 high speed cameras. The performance of the optical diagnostic system is  
47 presented. Flowing mercury in magnetic fields causes induced currents, which  
48 produce distortions of the mercury jet. The various effects of Lorentz force  
49 induced by magnetic field to liquid flow is investigated in a stability analysis

50 of the conducting flow in the presence of magnetic fields. Also, the role of  
51 joule damping as a loss on a time scale of magnetic damping term in global  
52 kinetic energy is discussed. Quantitative and qualitative data analysis using  
53 image processing based on statistic approach is described. The experimental  
54 measurements of jet distortion as well as flowing velocity of Hg jet in magnetic  
55 fields through image processing are presented. In experiment, it is observed  
56 that the imposition of magnetic field tends to suppress the fluctuating motion  
57 in Hg jet and correspondingly the jet surface is more stabilized, where  $Re$  is  
58 turbulent and  $Re_m$  is 0.26. Numerical Monte Carlo simulation for calculation  
59 of energy deposition by proton beam to Hg jet in magnetic fields is performed  
60 based on the jet shape, trajectory, and proton beam spot size from experiment.  
61 The jet disruption, the filament velocity on the jet surface by the impact of  
62 high energy of protons up to 30 Tp, and magnetic field effect to its suppression  
63 up to 15 T as well as energy deposition to Hg jet are presented. Finally, the  
64 experimental results investigate the performance and feasibility of utilizing  
65 liquid jet as a high power target for future particle accelerator.



# 66 Table of Contents

67	List of Figures	xxiii
68	List of Tables	xxv
69	Acknowledgements	xxvi
70	Nomenclature	xxx
71	1 Introduction	1
72	1.1 Neutrino Factory For High Power Neutrino Beam . . . . .	1
73	1.1.1 The concept of neutrino factory . . . . .	1
74	1.1.2 Neutrino physics . . . . .	3
75	1.2 A High Power Target For Neutrino Factory . . . . .	4
76	1.2.1 Material consideration for a high power target . . . . .	4
77	1.2.2 Moving metallic target for pion production . . . . .	4
78	1.2.3 Free mercury jet flow in magnetic field for a high power	
79	target . . . . .	5
80	1.2.4 Impact of the MHD mercury jet experiment for an intense	
81	proton target . . . . .	8
82	1.3 Mercury Target Issues . . . . .	9

83	1.3.1	Mercury jet disruption by energy deposition from an	
84		intense proton beam . . . . .	9
85	1.3.2	Magnetohydrodynamic issues in mercury jet target . .	10
86	1.3.3	Overview of experimental investigation of MHD flow and	
87		discussion . . . . .	12
88	<b>2</b>	<b>Magnetohydrodynamics of Conducting Flow in Magnetic Field</b>	<b>24</b>
89	2.1	Governing Equations for MHD Flow . . . . .	26
90	2.1.1	Electromagnetic equations . . . . .	26
91	2.1.1.1	<i>electromagnetic relation in a linear material</i> .	27
92	2.1.1.2	<i>Maxwell's equations</i> . . . . .	28
93	2.1.2	The Navier Stokes and magnetic induction equations in	
94		a conducting liquid flow . . . . .	30
95	2.1.2.1	<i>magnetic Reynolds number</i> . . . . .	32
96	2.1.2.2	<i>frozen-in theorem in magnetic induction equation</i>	34
97	2.1.2.3	<i>the diffusion limit in induction equation</i> . . .	34
98	2.2	The Energy Equation in MHD . . . . .	35
99	2.2.1	Energetics and effects of Lorentz force . . . . .	36
100	2.2.2	Proton beam induced energy deposition and equation of	
101		state . . . . .	37
102	2.2.3	Magnetic damping with joule dissipation . . . . .	39
103	2.3	Vorticity Equations in MHD flow . . . . .	42
104	2.3.1	Governing equations for vorticity . . . . .	42
105	2.3.2	Vorticity suppression . . . . .	44
106	2.3.2.1	<i>spanwise magnetic field effect to vorticity suppression</i>	44

107	2.3.2.2	<i>longitudinal and transverse magnetic field effect</i>	
108		<i>to vorticity suppression . . . . .</i>	45
109	2.4	One Dimensional Pipe Flow in Transverse Magnetic Field . . .	47
110	2.4.1	Non-dimensional form of the governing equations using	
111		cylindrical coordinates . . . . .	48
112	2.4.1.1	<i>uncoupled governing equations . . . . .</i>	48
113	2.4.1.2	<i>boundary conditions in pipe flow . . . . .</i>	49
114	2.4.2	Exact solutions of pipe flow in magnetic field . . . . .	49
115	2.5	Stability of Conducting Flow in a Magnetic Field . . . . .	51
116	2.5.1	Propagation of waves at an interface separating two flows	
117		in magnetic field . . . . .	52
118	2.5.2	Magnetic pressure and tension . . . . .	53
119	<b>3</b>	<b>Experimental Method for Investigation of Magnetohydrodynamic</b>	
120		<b>Mercury Jet Flow</b>	<b>59</b>
121	3.1	Optical Diagnostics as a Principal Diagnostics of High Power	
122		Target Experiment . . . . .	60
123	3.1.1	Working principle of shadowgraph for optical diagnostics	60
124	3.1.2	Development of optical diagnostic system . . . . .	62
125	3.1.2.1	<i>the optical imaging system and Viewports design</i>	63
126	3.1.2.2	<i>the consideration for focusing and tilting alignment</i>	
127		<i>of optics . . . . .</i>	67
128	3.1.2.3	<i>high speed cameras and light sources . . . . .</i>	68
129	3.1.2.4	<i>radiation-hardness . . . . .</i>	71
130	3.1.2.5	<i>scintillating fiber channel . . . . .</i>	72

131	3.1.3	Schematic of electronic trigger and high speed camera	
132		control . . . . .	73
133	3.2	Windows Consideration as Viewports for Observation . . . . .	75
134	3.2.1	Fiducial mark on windows . . . . .	75
135	3.2.2	Impact resistance test . . . . .	76
136	3.2.3	Pressure leaking test of sapphire windows . . . . .	76
137	3.3	Integrated Experimental Setup for High Power Target . . . . .	77
138	3.3.1	Mercury loop system in solenoid magnet . . . . .	77
139	3.3.1.1	<i>the considerations in nozzle design</i> . . . . .	78
140	3.3.2	Water jet observation for nozzle performance test . . . .	79
141	<b>4</b>	<b>Experimental Investigation of Mercury Jet Flow in Magnetic</b>	
142		<b>Fields</b>	<b>90</b>
143	4.1	Image Analysis for Data Reduction . . . . .	91
144	4.1.1	Image acquisition . . . . .	91
145	4.1.2	Image processing . . . . .	92
146	4.1.3	Study on the scaling length and the location of center of	
147		window . . . . .	94
148	4.2	Motion of Mercury Jet and Stability in Magnetic Field . . . .	96
149	4.2.1	Jet deflection and surface flattening . . . . .	96
150	4.2.2	Trajectory of mercury jet projectile in magnetic field .	102
151	4.3	Dynamics of Liquid Jet Flow From Nozzle . . . . .	105
152	4.3.1	Jet flow in surrounding medium . . . . .	105
153	4.3.2	Pressure loss and magnetic effect to the Hg delivery pipe	107
154	4.3.2.1	<i>pressure loss in pipe flow</i> . . . . .	109
155	4.3.2.2	<i>the measurement of wall tap pressure</i> . . . . .	113

156	<b>5 Interaction of an Intense Proton Beam with Hg Jet in Magnetic</b>	
157	<b>Field</b>	<b>133</b>
158	5.1 High Energy Proton Beam Structure . . . . .	133
159	5.1.1 Proton synchrotron machine . . . . .	133
160	5.1.2 Proton beam pulse length . . . . .	135
161	5.1.3 Proton beam envelope by optics and camera screen . .	136
162	5.2 MARS Simulation for Energy Deposition to Mercury Jet by	
163	Proton Beam . . . . .	137
164	5.2.1 Physics model . . . . .	137
165	5.2.2 Mercury jet modeling in MARS code . . . . .	138
166	5.2.3 Energy deposition to mercury jet . . . . .	139
167	5.2.3.1 <i>energy deposition in magnetic field</i> . . . . .	139
168	5.2.3.2 <i>geometric distribution of energy deposition in</i>	
169	<i>elliptic Hg jet cross section</i> . . . . .	140
170	5.2.3.3 <i>proton beam spot size to the energy deposition</i>	141
171	5.3 Observation of Interaction and Hg Jet Response to The Energy	
172	Deposition by Proton Beam . . . . .	144
173	5.3.1 Hg jet pressurization by energy deposition of proton beam	144
174	5.3.2 Observation of proton beam interaction and jet breakup	145
175	5.3.2.1 <i>energy deposition calculation with low intensity</i>	
176	<i>of proton beam and its observation</i> . . . . .	146
177	5.3.2.2 <i>energy deposition calculation with high intensity</i>	
178	<i>of proton beam and its observation</i> . . . . .	147
179	5.3.3 Hg jet disruption and magnetic suppression of the disruption	148

180	5.3.3.1	<i>characteristics of beam structure in disruption</i>	
181		<i>length, harmonic 8 and 16 . . . . .</i>	149
182	5.3.3.2	<i>disruption length with 14 GeV proton beam .</i>	150
183	5.3.3.3	<i>disruption length with 24 GeV proton beam .</i>	150
184	5.3.3.4	<i>validation of measurements of Viewport 3 through</i>	
185		<i>comparison with Viewport 4 . . . . .</i>	152
186	5.3.3.5	<i>disruption measurement in pump-probe condition</i>	
187		<i>as a check of experiment . . . . .</i>	153
188	5.4	<i>Disruption of Hg Jet By Energy Deposition . . . . .</i>	153
189	<b>6</b>	<b>Mercury Jet Surface Development in Magnetic Field</b>	<b>186</b>
190	6.1	<i>Filament Model on Jet Surface . . . . .</i>	186
191	6.1.1	<i>Geometry of viewing mercury filaments . . . . .</i>	186
192	6.1.2	<i>Distribution of filaments on jet surface . . . . .</i>	188
193	6.1.3	<i>Estimation of filaments velocity . . . . .</i>	189
194	6.2	<i>Observation of Filaments Development on Mercury Jet Surface</i>	190
195	6.2.1	<i>Image calibration . . . . .</i>	190
196	6.2.1.1	<i>image calibration with proton beam arrival signal</i>	190
197	6.2.1.2	<i>time delay structure of proton beam to light</i>	
198		<i>source triggering . . . . .</i>	191
199	6.2.2	<i>Parameter optimization with uncertainty . . . . .</i>	192
200	6.2.2.1	<i>nonlinear curve fit for estimation of model . .</i>	192
201	6.2.2.2	<i>Levenberg-Marquardt minimization . . . . .</i>	195
202	6.2.2.3	<i>chi-square probability . . . . .</i>	197
203	6.2.3	<i>Filaments distribution and uncertainty of measurement</i>	198
204	6.2.3.1	<i>onset of filamentation on jet surface . . . . .</i>	198

205	6.2.3.2	<i>measurement of traveled distance of filament .</i>	199
206	6.2.4	Linear regression with the first order polynomial . . . .	200
207	6.2.4.1	<i>curve fit function . . . . .</i>	200
208	6.2.4.2	<i>parameter estimation using multiple position of</i>	
209		<i>filaments . . . . .</i>	201
210	6.2.4.3	<i>filaments velocity distribution on jet surface .</i>	202
211	6.3	Velocity of Filaments on Mercury Jet Surface . . . . .	203
212	6.3.1	Magnetic dissipation of energy . . . . .	203
213	6.3.2	Time response of filaments in magnetic field . . . . .	204
214	6.3.3	Beam induced filaments velocity in magnetic field . . .	205
215	6.3.3.1	<i>filaments velocity with 14 GeV beam in magnetic</i>	
216		<i>field . . . . .</i>	205
217	6.3.3.2	<i>filaments velocity with 24 GeV beam in magnetic</i>	
218		<i>field . . . . .</i>	206
219	6.3.3.3	<i>filament velocity measurement in pump-probe</i>	
220		<i>condition as a check of experiment . . . . .</i>	207
221	6.4	Filament Velocity on Jet Surface By Energy Deposition . . . .	207
222	<b>7</b>	<b>Conclusions</b>	<b>224</b>
223		<b>Bibliography</b>	<b>232</b>
224	<b>A</b>	<b>Tabular Data for Chapter 3, Chapter 4, Chapter 5, and Chapter 6</b>	<b>240</b>
225	A.1	Specifications of Optics . . . . .	240
226	A.2	Mercury Properties . . . . .	242
227	A.3	Specifications of Hg Pressure Sensor . . . . .	243
228	A.4	Measurement of Events with Pump-Probe Conditions . . . . .	244

<b>229</b>	A.5 Beam Program List and Disruption Length Measurements . . .	<b>245</b>
<b>230</b>	<b>B Image Data for Chapter 6</b>	<b>256</b>
<b>231</b>	B.1 Images for Filament Velocity Measurement at Viewport 2 . . .	<b>256</b>
<b>232</b>	<b>C Mathematical Derivation for Chapter 2</b>	<b>273</b>
<b>233</b>	C.1 The Governing Equations of MHD Flow in Cylindrical Coordinates	<b>273</b>
<b>234</b>	C.2 Derivation of Rayleigh's Instability at An Interface Separating	
<b>235</b>	Two Flows in Magnetic Field . . . . .	<b>275</b>
<b>236</b>	C.2.1 Kinematic boundary condition at interface . . . . .	<b>275</b>
<b>237</b>	C.2.2 Hydrodynamic stability in magnetic field . . . . .	<b>276</b>
<b>238</b>	C.2.3 Dynamic boundary condition at interface . . . . .	<b>277</b>



## 239 List of Figures

240	1.1	Pion yield versus atomic mass number of the target at three	
241		proton beam energies (Osaki, 2001 and Mokhov, 2000). . . . .	16
242	1.2	Pion yield from Hg targets versus tilt angle between the target/beam	
243		axis and the solenoid axis and versus the radius of the target	
244		(Osaki, 2001 and Mokhov, 2000). a.) Pion yield versus tilt	
245		angle. b.) Pion yield versus target radius. . . . .	17
246	1.3	Geometry of key elements of target system and Viewports, showing	
247		the overlap between the mercury jet, magnetic axis, and the	
248		proton beam. a.) Top view. b.) Side view. . . . .	18
249	1.4	Schematics of the relative overlap between proton beam axis,	
250		Hg jet axis , and solenoid magnet axis. . . . .	19
251	1.5	Photographs of the entire MERIT experiment. a.) Sectional	
252		side view of mercury loop system integrated with 15 T solenoid	
253		magnet. b.) Fabricated mercury loop system assembled with	
254		15 T solenoid magnet (Top view). . . . .	20
255	1.6	Calculated behavior of the 15 T magnet during a pulse. . . . .	21

256	1.7	Cryogenic process of cooling 15 T solenoid magnet (Haug, 2009).	
257		a.) Cooling of proximity cryogenics. b.) Magnet cooldown. c.)	
258		Magnet at 80 K. d.) Emptying of the magnet cryostat. e.)	
259		Magnet pulse. f.) Re-cooling of magnet. . . . .	22
260	1.8	Schematics of mercury loop system for MERIT experiment (Graves,	
261		2007). . . . .	23
262	2.1	Wave-shaped interface separating two different fluids traveling	
263		at different average speeds. . . . .	56
264	2.2	Axes and electrodes of circular duct. . . . .	57
265	2.3	Energy decay in magnetic field. a.)Normalized energy decay.	
266		b.)Dissipation of normalized energy. . . . .	58
267	3.1	Displacement of light beam for shadowgraph. . . . .	80
268	3.2	Design of optical layout and installation of 4 Viewports of primary	
269		containment vessel. a.) Conceptual integration of optics to	
270		primary containment vessel. b.) Photograph of installation of	
271		optics to primary containment vessel. c.) Schematic layout of	
272		optical components. . . . .	81
273	3.3	Photograph of optical head assembly and its illumination of	
274		laser. a.) Front view of optical head assembly. b.) Side view	
275		of optical head assembly. c.) Illumination of fiber-optics head	
276		assembly. . . . .	82
277	3.4	Polished fiber end, 50 X and 800 X magnifications, respectively	83
278	3.5	Schematic of synchronized signal of high speed camera and laser	
279		pulse. . . . .	84
280	3.6	The triggering time for high speed camera upon beam arrival.	85

281	3.7	Schematic of electrical triggering and high speed camera control	
282		in tunnel for experiment. . . . .	86
283	3.8	Top fiducial on the front window and bottom fiducial on the	
284		rear window. a.) Photo of fiducial on the sapphire window	
285		assembled in Viewport. b.) Image of fiducial captured by camera.	87
286	4.1	Image data conversion for image analysis. a.) Collected image	
287		data. b.) 2 bit scaled image data. . . . .	117
288	4.2	Jet height determination from image analysis. a.) Sensitivity	
289		of threshold in a 2 bit scaled image conversion. b.) Histogram	
290		of number of events in the jet height measurement. . . . .	118
291	4.3	Mercury jet flows as observed from the 3 Viewports. The jet	
292		flows from left to right on each image. The first, second, and	
293		third columns represent Viewport 1, 2, and 3, respectively. The	
294		individual caption shows the applied magnetic induction field.	
295		The jet velocity is 15 m/s. Images on Viewport 2 has a 14°	
296		clockwise rotation due to the SMD software. a.) B=0 T. b.)	
297		B=0 T. c.) B=0 T. d.) B=5 T. e.) B=5 T. f.) B=5 T. g.)	
298		B=10 T. h.) B=10 T. i.) B=10 T. j.) B=15 T. k.) B=15 T. l.)	
299		B=15 T. . . . .	119
300	4.4	Same as Fig. 4.3 but with a jet velocity of 20 m/s. a.) B=0 T.	
301		b.) B=0 T. c.) B=0 T. d.) B=5 T. e.) B=5 T. f.) B=5 T. g.)	
302		B=10 T. h.) B=10 T. i.) B=10 T. j.) B=15 T. k.) B=15 T. l.)	
303		B=15 T. . . . .	120

304	4.5	Calculated solenoid magnetic induction field map. a.) Radial	
305		field map. b.) Axial field map. c.) Transverse component	
306		of magnetic induction field along jet axis. d.) Longitudinal	
307		component of magnetic induction field along jet axis. . . . .	121
308	4.6	Hg jet height measurement from direct average of vertical height	
309		in magnetic fields on each image. . . . .	122
310	4.7	Comparison of Hg jet deflection ratio at 15 T to that at 10 T.	
311		a.) Numerical calculation of deflection ratio. b.) Comparison	
312		of ratio of jet deflection. . . . .	123
313	4.8	Intermittency of Hg jet at Viewport 2. The jet velocity is	
314		15 m/s. a.) B=0 T. b.) B=5 T. c.) B=10 T. d.) B=15 T	
315		(continued). . . . .	124
316	4.8	Intermittency of Hg jet at Viewport 2. The jet velocity is	
317		20 m/s. e.) B=0 T. f.) B=5 T. g.) B=10 T. h.) B=15 T. . . .	125
318	4.9	Surface fluctuations in a magnetic field. . . . .	126
319	4.10	Trajectory of beam axis and Hg jet axis projectile with respect	
320		to magnetic axis in magnetic field. Solid line represents the	
321		simulated value using trajectory of projectile with different velocity.	127
322	4.11	Hg jet angle at the center of magnetic axis (Viewport 2) as a	
323		function of magnetic field. . . . .	128
324	4.12	Boundary layer induced by a jet emerging from a nozzle. . . .	129
325	4.13	Stream velocity and boundary layer thickness for various values	
326		of density ratio. . . . .	130
327	4.14	Pipe inlet pressure for driving Hg jet. a.) Static pressure. b.)	
328		Dynamic pressure. c.) Jet velocity in nozzle (Graves, 2007). .	131

329	4.15	Longitudinal Hg jet flow velocity in magnetic field. a.) Velocity	
330		at each Viewport dependent of magnetic field. b.) Averaged	
331		velocity at each Viewport independent of magnetic field. . . .	132
332	5.1	Infrastructures for experiment at CERN. a.) CERN accelerator	
333		complex and TT2 tunnel for experiment. b.) 16 harmonics of	
334		beam extraction in proton synchrotron. . . . .	158
335	5.2	Installation of integrated experimental components in tunnel	
336		TT2/TT2A for high power target experiment. Extracted proton	
337		beam comes from left to right in tunnel TT2A. . . . .	159
338	5.3	Schematics of beam to jet interaction in magnetic field and the	
339		location of each Viewport. . . . .	160
340	5.4	$1\sigma$ proton beam size at the center of magnet by optics (Efthymiopoulos,	
341		2008). . . . .	161
342	5.5	$1\sigma$ proton beam size by camera screen (Skoro, 2008). a.)	
343		14 GeV beam. b.) 24 GeV beam. . . . .	162
344	5.6	Beam size measured by phosphor screen monitor as a function	
345		of time interval between beam shots. a.) Histogram of beam	
346		size in horizontal plane. b.) Histogram of beam size in vertical	
347		plane. c.) Beam sizes distribution. . . . .	163
348	5.7	Modeling in MARS code for energy deposition calculation (Striganov,	
349		2009). a.) Sectional view of elliptic jet. b.) Sectional view of	
350		circular jet. c.) Side view of mercury jet. . . . .	164
351	5.8	Influence of magnetic field to the energy deposition distribution	
352		to Hg jet considering experimentally measured jet parameters.	165

353	5.9	Radial energy deposition distribution along jet axis interacting	
354		with 24 GeV proton beam. a.) Along jet axis. b.) Along radial	
355		angle in jet cross section. . . . .	166
356	5.10	Radial energy deposition distribution along jet axis interacting	
357		with 14 GeV proton beam. a.) Along jet axis. b.) Along radial	
358		angle in jet cross section. . . . .	167
359	5.11	Energy deposition distribution per proton according to the variation	
360		of beam spot size along jet axis. . . . .	168
361	5.12	Simulation of peak energy deposition per proton and total energy	
362		deposition per proton according to the beam spot sizes by beam	
363		intensities. Fits of model fits to Striganov's calculation results.	
364		a.) Peak energy deposition per proton and fit of model using	
365		Eqn. (5.6). b.) Total energy deposition per proton and fit of	
366		model using Eqn. (5.7). . . . .	169
367	5.13	Simulation of peak energy deposition and total energy deposition	
368		in total number of protons. Fits of model fits to Striganov's	
369		calculation results. a.) Peak energy deposition and fit of model	
370		using Eqn. (5.8). b.) Total energy deposition and fit of model	
371		using Eqn. (5.9). . . . .	170
372	5.14	Photographs of the Hg jet interaction with 16 Tp, 14 GeV	
373		proton beam at 5 T. Captured at Viewport 3 at 500 $\mu$ s frame	
374		rate (continued). . . . .	171
375	5.14	Photographs of the Hg jet interaction with 16 Tp, 14 GeV	
376		proton beam at 5 T. Captured at Viewport 3 at 500 $\mu$ s frame	
377		rate (continued). . . . .	172

378	5.14 Photographs of the Hg jet interaction with 16 Tp, 14 GeV	
379	proton beam at 5 T. Captured at Viewport 3 at 500 $\mu$ s frame	
380	rate. . . . .	173
381	5.15 Qualitative comparison of the jet response incident by interaction	
382	of low intensity (3 Tp) of 24 GeV beam at 5 T. a.) Calculated	
383	averaged energy deposition profile to mercury jet according to	
384	the distance from jet center. b.) Jet response by captured image.	174
385	5.16 Qualitative comparison of the jet response incident by interaction	
386	of high intensity (10 Tp) of 24 GeV beam at 10 T. a.) Calculated	
387	averaged energy deposition profile to mercury jet according to	
388	the distance from jet center. b.) Jet response by captured image.	175
389	5.17 Standard deviation of disruption length as a function of disruption	
390	length and fit of model. The fitted curve is $\sigma_{disruption} = 1.9352$	
391	$L_{disruption}^{0.3}$ . . . . .	176
392	5.18 Proton beam pulse structure of harmonic 8 and harmonic 16 in	
393	14 GeV and 6 Tp. . . . .	177
394	5.19 Disruption length of Hg jet depending on the beam pulse structure	
395	as a function of 14 GeV beam intensity in 5 T. $Tp=10^{12}$ protons.	
396	a) Global fit of harmonic 8 and 16 using Eqn. (5.13). b.)	
397	Independent fit of harmonic 8 and 16 using Eqn. (5.13). . . . .	178
398	5.20 Disruption length of Hg jet as a function of 14 GeV beam	
399	intensity and magnetic field. Harmonic 16 with 16 bunches	
400	is used. . . . .	179

401	5.21	Disruption length of Hg jet and its estimation as a function of	
402		24 GeV beam intensity and magnetic field. The estimation of	
403		disruption length by energy deposition calculation is compared	
404		by using disruption model of Eqn. (5.14). . . . .	180
405	5.22	Validation of disruption measurement for the evaluation of evolution	
406		of disruption length from Viewport 3. a) Disruption length at	
407		Viewport 3. b.) Disruption length at Viewport 4. c.) Difference	
408		of the disruption length at Viewport 3 and Viewport 4. . . .	181
409	5.23	Disruption length measurement in same conditions. Pump-probe	
410		conditions with harmonic 8 and 16 bunches are used. The	
411		conditions of each group in pump-probe events are given in	
412		Table A.4. a.) Histogram of disruption length in each group.	
413		b.) Disruption length of each group. . . . .	182
414	5.24	Disruption of mercury jet in magnetic fields as a function of	
415		total energy deposition and fit of model using Eqn. (5.15). . .	183
416	5.25	Disruption of mercury jet in magnetic fields as a function of	
417		fluence and fit of model using Eqn. (5.15). . . . .	184
418	5.26	Disruption of mercury jet in magnetic fields as a function of	
419		peak energy deposition and fit of model using Eqn. (5.15). . .	185
420	6.1	Schematic geometry of viewing mercury filaments (McDonald,	
421		2008). . . . .	211
422	6.2	Time delay estimation of devices for triggered image calibration.	
423		a.) Measurement of characteristic response of 25 laser used for	
424		high speed camera at Viewport 2 (Tsang, 2006). b.) Time	
425		structures between light source enabling and proton beam arrival.	212



426	6.3	Photographs of filament evolution on the Hg jet surface as a	
427		function of time at 25 $\mu$ s frame rate. The beam is 10 Tp,	
428		24 GeV. The magnetic field is 10 T. The red circle on the 4 <sup>th</sup>	
429		image of the top row points the filament that is used for velocity	
430		measurement in Fig. 6.8 (b). . . . .	213
431	6.4	Location on the Hg jet surface for velocity measurement of 18	
432		points of filament. The shot condition same with Fig. 6.3. The	
433		numbers above red circles points the filament that is used for	
434		velocity estimation in Fig. 6.6 and Fig. 6.7. . . . .	214
435	6.5	Illustration of bilinear fit for parameters estimation. a.) Multiple	
436		data points. b.) 3 data points. . . . .	215
437	6.6	Estimation of velocity and onset time of filaments shown in	
438		Fig. 6.3. The beam is 10 Tp, 24 GeV. The magnetic field	
439		strength is 10 T. a.) Estimation of filament velocity. b.) Estimation	
440		of onset time of filaments. . . . .	216
441	6.7	Time response of instantaneous filament velocity at jet surface	
442		for various filaments shown in Fig. 6.4. The beam is 10 Tp,	
443		24 GeV. The magnetic field is 10 T. a.) Upper surface. b.)	
444		Lower surface. . . . .	217
445	6.8	Time response of instantaneous filament velocity as a function of	
446		magnetic field. Equation (6.33) is used for measuring instantaneous	
447		filament velocity. The half of elapsed time between each frame is	
448		used to indicate the time at each filament velocity. a.) 14 GeV,	
449		20 Tp beam. b.) 24 GeV, 10 Tp beam. . . . .	218

450	6.9	Maximum observed filament velocity as a function of 14 GeV	
451		beam intensity in various magnetic field. a.) Maximum observed	
452		filament velocity. b.) Onset time of that filament. . . . .	219
453	6.10	Maximum observed filament velocity as a function of 24 GeV	
454		beam intensity in various magnetic field. a.) Maximum observed	
455		filament velocity. b.) Onset time of that filament. . . . .	220
456	6.11	Filament velocity measurement in same conditions. Pump-probe	
457		conditions with harmonic 8 and 16 bunches are used. The	
458		conditions of each group in pump-probe events are given in	
459		Table A.4. a.) Histogram of maximum filament velocity in	
460		each group. b.) Maximum filament velocity of each group. . .	221
461	6.12	Maximum observed filament velocity as a function of peak energy	
462		deposition in various magnetic fields and fit is according to	
463		Eqn. (6.34). . . . .	222
464	6.13	Maximum observed filament velocity as a function of total energy	
465		deposition in various magnetic fields and fit is according to	
466		Eqn. (6.34). . . . .	223
467	B.1	Shot number is 11004. Photo of sequence of 15 frames of captured	
468		image, where the timing for the 1 <sup>st</sup> image is given in column 8	
469		in Table B.1. . . . .	257
470	B.2	Location on the Hg jet surface for velocity measurement of	
471		filaments. Red circles indicate the location of filaments analysis.	
472		Shot number is 11004. a.) Illustration of measured filaments.	
473		b.) Measured velocity onset time. . . . .	258
474	B.3	Shot number is 11007. . . . .	259

475	B.4 Shot number is 11007. a.) Illustration of measured filaments.	
476	b.) Measured velocity onset time. . . . .	260
477	B.5 Shot number is 11010. . . . .	261
478	B.6 Shot number is 11010. a.) Illustration of measured filaments.	
479	b.) Measured velocity onset time. . . . .	262
480	B.7 Shot number is 11021. . . . .	263
481	B.8 Shot number is 11021. a.) Illustration of measured filaments.	
482	b.) Measured velocity onset time. . . . .	264
483	B.9 Shot number is 11032. . . . .	265
484	B.10 Shot number is 11032. a.) Illustration of measured filaments.	
485	b.) Measured velocity onset time. . . . .	266
486	B.11 Shot number is 12031. . . . .	267
487	B.12 Shot number is 12031. a.) Illustration of measured filaments.	
488	b.) Measured velocity onset time. . . . .	268
489	B.13 Shot number is 12032. . . . .	269
490	B.14 Shot number is 12032. a.) Illustration of measured filaments.	
491	b.) Measured velocity onset time. . . . .	270
492	B.15 Shot number is 12033. . . . .	271
493	B.16 Shot number is 12033. a.) Illustration of measured filaments.	
494	b.) Measured velocity onset time. . . . .	272

## List of Tables

496	3.1	Specifications of high speed cameras. . . . .	88
497	3.2	Effects of irradiation up to an equivalent radiation dose of 1 Mrad	
498		on the reflectance and transmittance of the components of the	
499		optical diagnostic system. Reflectance is inferred on the Au-coated	
500		mirror and transmittance is inferred on all other components.	89
501	4.1	Error estimation of fiducial length at each viewport. . . . .	115
502	4.2	Pressure head losses by geometry in pipe for mercury loop. . .	115
503	4.3	Parameterized coefficients, its error, and statistics summary of	
504		fit function in figures. . . . .	116
505	5.1	Measurement of vertical distances of center of jet from magnetic	
506		axis and jet size for modeling in MARS code for the cases of	
507		elliptic and circular jet sectional shape. . . . .	156
508	5.2	Parameterized coefficients, its error, and statistics summary of	
509		fit function in figures. . . . .	157
510	6.1	Parameterized coefficients, its error, and statistics summary of	
511		fit function in figures. . . . .	210

512	A.1	Specifications of optical components in optical diagnostics. . .	240
513	A.2	Properties of mercury. . . . .	242
514	A.3	Features of pressure transducer (Swagelok PTI-S-AG400-15AW). 243	
515	A.4	Measurement of disruption and filament velocity in pump-probe	
516		conditions with 8 and 16 harmonic bunches. . . . .	244
517	A.5	Measured disruption length and beam shot program. Item	
518		1 is shot number. The first digit represents experiment run	
519		day and last 2 ~ 3 digits represent shot numbers of the day.	
520		For example, in shot 2003, 2 represents experiment day 2 and	
521		3 represents shot number 3 of experiment day 2. Item 2 is	
522		number of bunches. Item 3 is number of protons (Tp). Item	
523		4 is magnetic field (T). Item 5 is jet velocity (m/s). Item 6 is	
524		$L_{disruption}$ (m). Item 7 is $\sigma_{disruption}$ ( $\pm$ m). . . . .	245
525	B.1	Properties of shots used for filaments velocity analysis. Item 1	
526		is shot number. Item 2 is camera frame rate ( $\mu$ s). Item 3 is	
527		beam energy (GeV). Item 4 is number of bunches. Item 5 is	
528		number of protons (Tp). Item 6 is magnetic field (T). Item 7	
529		is nominal jet velocity (m/s). Item 8 is lag time between peak	
530		laser emission and proton beam arrival ( $\mu$ s). . . . .	256

## ACKNOWLEDGEMENTS

531       The author greatly appreciates the indispensable guide and constant encouragements  
532       from Dr. Harold Kirk at Brookhaven National Laboratory and Prof. Foluso  
533       Ladeinde, who served as the author's dissertation advisor.

534       The author would like to express a special appreciation to Prof. Kirk  
535       McDonald at Princeton University and Dr. Thomas Tsang at Brookhaven  
536       National Laboratory for their contribution to the procedures used in this work.

537       The author would also like to thank Prof. Thomas Cubaud for agreeing to  
538       be the Chair of his dissertation committee, Prof. James Glimm, for agreeing  
539       to serve on the dissertation committee, Prof. Roman Samulyak, for valuable  
540       suggestions on the analysis of the experimental results.

541       This work was supported in part by the United States Department of  
542       Energy Contract No. DE-AC02-98CH10886. The experiment was carried out  
543       at CERN (European Organization for Nuclear Research) in Geneva, Switzerland  
544       and the analysis performed at Brookhaven National Laboratory. The text  
545       of this dissertation in part is a reprint of the materials as it appears in  
546       Review of Scientific Instruments **79**, 045111(2008). The co-authors listed in  
547       the publication directed and supervised the research that forms the basis for  
548       this dissertation.

## Nomenclature

<b>B</b>	Magnetic induction field, $T$ ( $Wb/m^2$ )
<b>B<sub>o</sub></b>	Applied magnetic field, $T$ ( $Wb/m^2$ )
<b>D</b>	Electric displacement field, $C/m^2$ ; Energy dissipation, $J/s$
<b>E</b>	Electric field, $N/C$ ( $V/m$ ); Global kinetic energy, $J$
<b>H</b>	Magnetic field, $A/m$
<b>J</b>	Current density, $A/m^2$ ; Jacobian matrix
<b>M</b>	Magnetization density, $J/(T \cdot m^3)$
<b>P</b>	Polarization density, $C/m^2$ ; Probability; Particle momentum, $J \cdot s/m$
<b>V</b>	Electric potential, $V$
<b>A</b>	Cross sectional area, $m^2$
<b>C</b>	Contraction coefficient; Discharge coefficient; Constant; Circumference, $m$
<b>D</b>	Diameter of jet, $m$ ; Vertical jet height, $m$
<b>E<sub>dep</sub></b>	Energy deposition, $J/g$
<b>G</b>	Pressure ratio; Gruneisen coefficient
<b>I<sub>T</sub></b>	Intensity of light, $cd$
<b>K</b>	Loss coefficient; Bulk modulus, $N/m^2$
<b>L</b>	Characteristic length, $m$ ; Pipe length, $m$ ; Disruption length, $m$
<b>M</b>	Mass, $kg$ ; Molar mass, $g/mol$
<b>Q</b>	Flow rate, $m^3/s$
<b>R</b>	Gas constant, $J/(K \cdot mol)$ ; Radius of curvature of the centerline of the elbow, $m$
<b>T</b>	Temperature, $^{\circ}C$ ( $K$ ); Time, $s$
<b>U</b>	Mean velocity in the $x$ coordinate direction, $m/s$
<b><math>\alpha_v</math></b>	Volume coefficient of thermal expansion, $K^{-1}$

$\beta$	Ratio of diameter
$\gamma$	Ratio of specific heats, $c_p/c_v$
$\Gamma$	Surface tension, $N/m$
$\delta$	Kronecker delta; Boundary layer thickness, $m$
$\epsilon$	Amplitude of a sinusoidal wave, $m$ ; Random error
$\varepsilon$	Electrical permittivity, $F/m$ ( $C^2/(N \ m^2)$ )
$\varepsilon_o$	Electrical permittivity of free space, $F/m$ ( $C^2/(N \ m^2)$ )
$\zeta$	Intermittency factor
$\eta$	Absolute viscosity, $kg/(m \ s)$
$\theta$	Angle, degree
$\kappa$	Compressibility, $m^2/N$
$\lambda$	Wavelength of a sinusoidal wave, $m$
$\mu$	Magnetic permeability, $H/m$ ( $N/A^2$ )
$\mu_o$	Magnetic permeability of free space, $H/m$ ( $N/A^2$ )
$\nu$	Kinematic viscosity, $\eta/\rho$ , $m^2/s$
$\xi$	free surface perturbation, $m$
$\rho$	Density, $kg/m^3$
$\sigma$	Electrical conductivity, $S/m$ ; Standard deviation
$\tau$	Joule damping term; Wall shear stress, $N/m^2$
$\phi$	Velocity potential, $m^2/s$ ; Angle, degree
$\phi_E$	Electric potential, $V$
$\chi_e$	Electrical susceptibility
$\chi_m$	Magnetic susceptibility
$\psi$	Stream function, $m^2/s$
$\omega$	Vorticity, $s^{-1}$



$a$	Radius of circular pipe, $m$ ; Radius of jet, $m$
$c$	Local speed of sound, $m/s$ ; Distance $m$ ; Wave velocity, $m/s$
$c_p, c_v$	Specific heat capacity, $J/(g\ K)$
$d$	Diameter of circular pipe, $m$ ; Diameter of nozzle, $m$ ; Distance, $m$
$e$	Specific internal energy, $J/kg$ ; Surface roughness, $m$ ; Error, %
$f$	Focal length, $m$ ; Force, $N$ ; Friction factor
$g$	Gravitational constant, $m/s^2$
$h$	Head loss, $m$
$k$	Boltzmann constant; Number of parameters
$n$	Index of refraction; Experimental data points
$p$	Pressure, $N/m^2$ ; Probability
$r$	Residual; Radial coordinates
$s$	Position
$t$	Time, $s$
$x, y, z$	Cartesian coordinates, $m$
$v$	Directional fluid velocity, $m/s$ ; Mean velocity, $m/s$
Al	Alfvén Number
Fr	Froude number
Ha	Hartmann number
N	Stuart number; Number of events; Augmented Jacobian matrix
Re	Reynolds number
$Re_m$	Magnetic Reynolds number
We	Weber number
$\nabla \cdot$	Divergence operator
$\nabla \times$	Curl operator

$\times$	Cross product operator
$\cdot$	Inner product operator; Multiplication

### ***Superscripts***

$'$	Differentiation with respect to variable; Perturbation; Fluctuation
$\cdot$	Differentiation with respect to time

### ***Subscripts***

$I$	Ion thermal
$R$	Reference location
$T$	Transpose of matrix
$a$	Air
$b$	Beam
$c$	Compression
$e$	Electron thermal
$l$	Liquid
$o$	Component mean value; Initial value at the nozzle
$x, y, z$	Component values over the cartesian coordinates

# Chapter 1

## Introduction

Accelerator-based sources of exceptionally intense, tightly focused beams of X-rays and ultraviolet radiation make possible both basic and applied research in fields from physics to biology to technology that are not possible with more conventional equipment. The development of a high-intensity source of muons can be useful for the production of high-energy neutrino, thereby opening the door for a broad range of important new physics experiments such as neutrino oscillation. The concept is to use a high-intensity proton beam incident on a mercury jet to produce pions which decay to give the muons. These muons is magnetically captured, accelerated, and then inserted into a storage ring.

## 1.1 Neutrino Factory For High Power Neutrino Beam

### 1.1.1 The concept of neutrino factory

Accelerators are used to accelerate primary particle beams such as protons and electrons. The required statistics in the collision processes demand a very

high flux of primary particles. On interaction of the primary particles with a target, it is possible to produce secondary beams of elementary particles like pions, neutrons, and gammas. Primary protons pass through a linear accelerator and further through a synchrotron, bunch compressors, and accumulators to achieve a beam with a certain energy, intensity and beam structure. This beam is directed toward a target. On interaction with the target, secondary particles of different kinds are produced. A neutrino factory is the ultimate tool for producing a high-intensity neutrino beam to study neutrino oscillations. The neutrino factory is based on a new concept of an accelerator that produces a high-intensity, high-energy beam of muon and electron neutrinos. It will allow an investigation of a new domain in neutrino physics such as

- High intensity. Its flux is  $10^3$  times greater than conventional neutrino beams.
- High energy. It features a very high beam energy of 20 to 50 GeV.
- In a neutrino factory, the muon sign can be selected. Thus, it is possible to deliver particles and anti-particles.

The basic concept of the Neutrino Factory is the production of muon neutrinos and anti-electron neutrinos from the decay of muons that are circulating in a storage ring. An intense proton beam is delivered to a target, where pions are produced. These pions are collected in a solenoidal magnetic field, which can capture both charged states of pions. The pions decay into muons in a decay channel. The muon beam has both a large energy spread and

transverse emittance. The energy spread is reduced using a phase rotation, while emittance is improved by ionization cooling. The cooled beam is accelerated to energies of 20 to 50 GeV and injected into a storage ring.

### 1.1.2 Neutrino physics

Muons cannot be produced directly, so pions have to be produced first. The first stage of a neutrino factory is thus a high-power proton driver that deliver protons onto a target, where pions are produced. These pions have to be collected and transported. After about 20 m, most of the pions decay into muons. A neutrino beam can be produced from the decay of high-energy muons:

- Pions from  $\text{Proton} + \text{Material} \longrightarrow \pi^\pm + X$

- Muons from  $\pi^\pm \longrightarrow \mu^\pm \nu_\mu (\overline{\nu}_\mu)$

- Neutrinos from  $\mu^\pm \longrightarrow e^\pm \overline{\nu}_\mu \nu_e (\nu_\mu \overline{\nu}_e)$

At this stage, the muon beam has a low phase space density and resembles more a cloud than a beam. Phase rotation as well as ionization cooling is applied to reduce the energy spread and the emittance of the muon beam.

Once the beam is cooled, it can be accelerated to a final energy of 20 to 50 GeV. In the final stage of a neutrino factory, the accelerated muons are injected into a storage ring with long straight sections.

## **1.2 A High Power Target For Neutrino Factory**

### **1.2.1 Material consideration for a high power target**

The intensity of muon beam is directly proportional to the power of the proton beam which initiates the process. Considering that a high intensity proton beam is required in order to generate the required muons, the choice of the target material becomes a particularly important issue. Modeling studies (Osaki, Palmer, Zisman, Gallardo, 2001) point to high-Z materials being more efficient at producing pions of both signs, whereas low-Z materials are better at preventing the absorption of the produced pions. The pion yield per proton increases with the atomic number of the target, as shown in Fig. 1.1 from MARS calculation. A high-Z material is desirable because the pion production cross-section increases with increasing Z. However, the intense proton beam would melt a target made of a solid high-Z material. A target system using a flowing stream of mercury could recycle the spent target. Several types of target material have been proposed including copper, graphite, and mercury.

Since these targets are envisaged as being stationary, one must consider the problem of removing the energy deposited by the beam without interfering with the production of the particles.

### **1.2.2 Moving metallic target for pion production**

While schemes for moving solid targets can be envisaged (Thieberger, Kirk, Weggel, McDonald, 2003), a flowing liquid target is simpler, and mercury as a high Z material presents itself as the liquid metal. The liquid target

should be in the form of a free jet, rather than being confined in containment, since the beam-induced cavitation of the liquid metal can be destructive to solid walls in the immediate vicinity of the interaction region. Another issue associated with the proton beam is the effect of the energy that it deposits in the target. The temperature of the target rises almost instantaneously after the beam pulse, resulting in large internal stresses that might crack a solid target or disperse a liquid target (Kirk *et al.*, 2001). In the case of a liquid jet target, the dispersal of the jet by the beam should not be destructive to the surrounding target system components and should not adversely affect pion production during subsequent beam pulses, either on the microsecond scale, if several micro-pulses are extracted from a proton synchrotron, or on the scale of the macro-pulse period. The operation of a liquid metal jet inside a strong magnetic field raises several magnetohydrodynamic issues such as possible deformation of the jet's shape and trajectory, as well as the effect of the magnetic field on the beam-induced dispersal of the jet.

### **1.2.3 Free mercury jet flow in magnetic field for a high power target**

The free mercury jet in magnetic field is proposed for a high power target to overcome the issues described in the above Chapter. The concept is to use a high intensity proton beam incident on a Hg jet to produce pions which decay to give the muons (Gabriel *et al.*, 2001). The key elements of the target system are an intense proton source, mercury jet, and capture of the generated pions

in a high field solenoidal magnet (McDonald, 2001). The schematics of the key elements of the target system is described in Fig. 1.3.

Previous studies (Osaki, Palmer, Zisman, Gallaro, 2001) indicated that pion yield is maximized with a mercury target in the form of a 1 cm diameter at the interacting center, tilted by about 150 milliradian with respect to the magnetic axis. The target is tilted with respect to the axis of the capture solenoid, thus permitting the pions, whose trajectories are spirals, to leave the side of the target with a minimal probability for re-entering the target volume. The pion yield per proton increases with the atomic number of the target, as shown in Fig. 1.1 from MARS calculation. For 24 GeV protons, a high-Z target is superior in yield. As the pions emerge from the target at large angles to the beam, and follow helical paths that may intersect the target at more than one point, it is advantageous for the target to be in the form of a narrow rod, tilted at a small angle to the magnetic axis. As shown in Fig. 1.2, suitable parameters for a mercury target are a tilt angle of 150 milliradian and a target radius of 5 mm.

Based on the previous studies described in the above, the experimental setup parameters are determined. The layout of experimental setup is briefly described in the below and will be more discussed in Chapter 3. Figure 1.4 shows the detailed schematic of the overlap between key components of the experiment. The velocity of the jet is 15 m/s, where the trajectory of mercury jet overlaps with the proton beam over 30 cm. The facility is a closed piping loop, constructed primarily of 316 stainless steel, and designed to circulate



liquid mercury. The parameters of the proton beam and solenoid system are determined by the required conditions of particle production rates (Bennett *et al.*, 2004). Basic system parameters consist of proton energy 24 GeV, 14 GeV, and number of protons in one pulse  $\approx 3 \times 10^{13}$ , which was extracted from the CERN(European Organization for Nuclear Research) PS(Proton Synchrotron) in 2007. The solenoid length is 100 cm, inside radius is 7.5 cm, and a maximum magnetic field is 15 T. The solenoid magnet is titled at 67 milliradian angle with respect to the beam. The beam arrives at an angle 34 milliradian with respect to the jet which has a radius  $\approx 0.5$  cm, as schematically shown in Fig. 1.4. The angle between moving mercury jet and magnetic axis induces currents, which generates Lorentz force with a component of magnetic field. Thus, it is expected that the optimal 150 milliradian of jet axis with respect to magnetic axis distorts jet shape (Gallardo *et al.*, 2002). Therefore, 33 milliradian of jet axis with respect to magnetic axis was designed for experiment to yield minimum distortion of jet shape. The 24 GeV proton beam is directed on to the solenoid at 67 milliradian off the solenoid axis, so that most high momentum particles do not travel straight down the beam line (Gallardo *et al.*, 2001). If there are no magnetic and gravitational effects on the mercury jet trajectory, the beam should enter at the bottom surface of Hg jet at Viewport 1, which is located at approximately 30 cm from the nozzle and the beam should exit on the top surface of Hg jet at Viewport 3, which is located at approximately 60 cm from the nozzle. The required jet velocity is determined by two conditions: 1), the need to replenish the target before the arrival of

subsequent proton beam pulse, and 2), it should be high enough to overcome the deceleration force induced by Lorentz force (Hassanein, Kinkashbaev, 2001).

Initial tests involving the interaction of proton beams on mercury targets were performed at the Brookhaven Alternating Gradient Synchrotron (AGS) (Kirk *et al.*, 2001), and continued at the CERN ISOLDE facility (Lettry *et al.*, 2003). The BNL test featured a 24 GeV proton beam interacting with a free mercury jet with a nozzle diameter of 1 cm and a velocity of 2.5 m/s. The delivered proton bunch was focused to  $<1$  mm radius, resulting in a peak energy deposition of 80 J/g, delivering 24 GeV proton beam at 15 Hz (Tsoupas *et al.*, 2003). These initial tests did not have a magnetic field on the target. A parallel effort was undertaken to study the effects of high velocity mercury jets in the presence of high-magnetic fields, but with no proton beam (Fabich, 2002).

#### **1.2.4 Impact of the MHD mercury jet experiment for an intense proton target**

The previous experiments did not perform the mercury jet in a high magnetic field interacting with an intense proton beam. In this work, we integrated the mercury jet, solenoid magnet, and intense proton beam all together. The performance and feasibility of utilizing liquid metal jet as a target for an intense proton beam is explored experimentally, which is an explicit objective of the experiment. The liquid jet target concept is recyclability otherwise the target would be destroyed. Therefore, the power of the target has to be

evaluated in terms of the replacing capability and validated experimentally. In order to validate the performance of the target, the MHD jet behavior in a strong magnetic field has to be investigated. The response of the mercury jet due to the energy deposition by interacting with an intense proton beam has to be studied and the magnetic field effect to the disruption of mercury jet has to be studied, as well. The experimental results reveals that the effect of the Lorentz force to the jet stabilization as well as the deflection of jet. The experimental results provide feasibility of utilizing liquid metal jet as a target for an intense proton beam. Also, the results validates the phenomenology of conduction flow in magnetic field based on the MHD theory.

## **1.3 Mercury Target Issues**

### **1.3.1 Mercury jet disruption by energy deposition from an intense proton beam**

The production of large fluxes of particles using high energy, high intensity proton pulses impinging on solid or liquid targets presents unique problems which have not yet been entirely solved. The large amount of power deposition required in the material coupled with the short pulse duration produce large, almost instantaneous local heating. The interaction of the proton beam with the mercury target leads to very high heating rates in the target, where the heat from the beam could melt or crack a high-Z target. Sudden energy deposition into mercury jet causes increase in temperature by specific heat capacity. Increase in temperature causes volumetric changes by the volumetric

thermal expansion coefficient, which results in pressure rise analogous Young's Modulus relationship between stress and strain. Thus, strain energy is built up in the mercury jet. This strain energy is released as kinetic energy such as filaments development on jet surface. The resulting sudden thermal expansion can result in damage causing stresses in solids and in the violent disruption of liquid jets. The volume expansion initiates vibrations in the material. The amplitude of these vibrations is such that stresses that exceed the strength of the material can be generated, causing mechanical failure (Thieberger *et al.*, 2003).

### 1.3.2 Magnetohydrodynamic issues in mercury jet target

Liquid metal jets are proposed as potential target candidates because the heat energy can be removed along with the moving liquid. For mercury, heat conduction is very effective compared to convection: thermal diffusivity is dominant. In heat transfer, the Prandtl number indicates the relative thickness of the momentum and thermal boundary layers. When Prandtl number is small such as mercury, it means the heat diffuses very quickly compared to the velocity. However, there are two important problems that are associated with the use of liquid metal targets in these environments. First, as the liquid jet penetrates the magnetic field, instabilities in jet motion and deceleration may occur because of the large field gradients at the entrance and exit of the solenoid. The designed jet velocity is  $\sim 15$  m/s  $\sim 20$  m/s, considering the repetition rate of target and avoidance of bending jet trajectory in order to

have 2 interaction length between proton beam and jet. These instabilities may change the jet shape into one that is significantly less efficient for pion production (Hassanein, Konkashbaev, 2001). Second, during the intense pulse of energy deposition in a short time, the resultant stress could break up the target, where the liquid jet can develop surface instabilities such as filaments after beam interaction. These filaments may damage to surrounding facility under operation of target because of similar characteristics of mercury to metal.

Mercury flow in a magnetic field experiences induced currents, which cause the jet to produce transverse forces normal to jet axis direction resulting deflection normal to jet axis (Gallardo *et al.*, 2001, 2002). In addition, axial currents are induced if the jet axis does not coincide with the magnetic field axis. These axial currents produce elliptical distortions of the mercury jet. Faraday's law can be used to obtain the azimuthal current density from changing the axial field in the local coordinate system of the Hg jet. The transverse component of the magnetic field normal to the jet axis also varies along the trajectory of the mercury jet. The axial current density can be related to the changing transverse component of the magnetic field normal to the jet axis. These axial currents produce a magnetic force. This force will be balanced by a restoring force from the surface tension of the mercury, and with the condition that the mercury is an incompressible liquid, will produce an elliptic deformation of the mercury jet (Oshima, 1987).

### 1.3.3 Overview of experimental investigation of MHD flow and discussion

A proof-of-principle experiment performed at the CERN(European Organization for Nuclear Research) PS(Proton Synchrotron), which combined a free mercury jet target with a 15 T solenoid magnet and a 24 GeV primary proton beam. (Bennett *et al.*, 2004). The disruption of jet could be much longer than beam-jet interaction length, which must be investigated experimentally and a key purpose of experiment. The experiment validates the liquid type of target for producing an intense secondary source of muons by showing the jet repetition rate to replace the disrupted target by the energy deposition from an intense proton beam. Also, due to the energy deposition in jet by an interaction of proton beam, the filaments development on jet surface could damage and eventually break the facility of surrounding wall. The filament velocity could be much high, which must be investigated experimentally and another key purpose of experiment. For the investigation of feasibility, various behavior of mercury jet in magnetic field interacting with proton beam is reported based on experimental measurement.

The PS runs in a harmonic 16 mode and can fill up to  $2 \times 10^{12}$  protons/bunch (2 Tp/bunch), where the term “harmonic” means sinusoidal pulse shape, the term “8(16)” means number of bunches, and the term “bunch” means sub-pulse in a pulse. Note that Tp(Tera protons) means  $1 \times 10^{12}$  protons. This allows up to  $30 \times 10^{12}$  protons per pulse on the mercury target, generating a peak energy deposition of  $\sim 130$  J/g with  $\sim$  beam spot size of  $5.7 \text{ mm}^2$  at

beam energy 24 GeV, which is a key design parameter of single pulse at CERN for a target system capable of supporting proton beam with powers of 4 MW. Note that CERN could provide requirement of this key design parameter.

For this experiment, a high magnetic field pulsed solenoid with a bore of 15 cm was designed (Titus, 2007). This magnet is capable of delivering a pulsed peak field of 15 T. The pulsed solenoid incorporates a magnetic induction field ramp up of 10 seconds and is capable of sustaining its peak field for a duration of approximately 1 second. A 5.5 MW, 700 V power supply delivers 7500 A of current to pulse the solenoid (Michael, 2005, Martins, 2005, Kirk, 2008). Figure 1.6 shows the calculated behavior of the 15 T magnet during a pulse. Approximately 30 MJ of energy is dissipated in the magnet, which raises its temperature from 80 to 120 K. Note that CERN could provide requirement of this key component for experiment. The magnet is cryogenically cooled by liquid nitrogen to 77 K prior to operation and warms up by 30 K during pulsing due to 30 MJ coil heating (Haug, 2009). Figure 1.7 shows cryogenic process of cooling 15 T solenoid magnet. Therefore, a 30 minute cooling time is needed for each single shot. The magnetic axis is positioned at an angle of 67 milliradian with respect to the proton beam, with the tilt provided by a common baseplate supporting all the equipment (see Fig. 1.5(a)). It was found that the maximum magnetic induction field reached 15 T at Plasma Science and Fusion Center in Massachusetts Institute of Technology (Titus, 2007).

The Hg jet delivery system generates a mercury jet from 1 cm diameter nozzle with velocities up to 15 m/s (Graves, 2007). The primary diagnostic

of the beam-jet interaction is optical. A set of four view-ports along the interaction region is connected by imaging fiber-optic bundles to four high speed cameras. The cross-section and actual equipment for the mercury system with high field solenoid magnet is shown in Fig. 1.5. The horizontal line in Fig. 1.5(a) represents the proton beam. The Hg jet, which is ejected from right to left in Fig. 1.5(a), co-propagates with the proton beam. Four Viewports are shown within the solenoid bore, which represent viewing locations for observation of the Hg jet within its primary containment vessel (see Fig. 1.3). The Hg system provides for double containment vessel of the hazardous liquid metal, and can be inserted or removed from the solenoid bore without disassembly. Figure 1.8 shows schematics of mercury loop system for experiment. A hydraulic syringe pump, with a piston velocity of 3 cm/s was used to pulse the mercury jet. This pump minimizes the heat added to Hg as opposed to a centrifugal pump. The syringe pump also reduces the discharge pressure which is the limitation of a centrifugal pump. The Hg system provides a jet duration of a  $\sim 3$  seconds of constant velocity profile. A total of 180 kg of Hg is loaded in the system. A 30 kW, 200 bar hydraulic power unit drives the syringe pump (Graves, 2007).

Each pulse of the proton beam delivered to this system constitutes a separate experiment. About 360 beam pulses are utilized in a beam-on-demand mode at CERN. These pulses span a range of intensities and time intervals between the multiple extracted bunches per pulse. The magnet operates over a range of field strengths of  $0 \sim 15$  T.



855 In Chapter 2, the full MHD governing equation using Maxwell's equations  
856 are presented. Various modeling of conducting flow in a magnetic field are  
857 formed, where the contribution of Lorentz force to the hydrodynamic equations  
858 is presented and discussed. The formulated and reviewed equations are introduced  
859 to explain and understand MHD experimental results.

860 In Chapter 3, the detailed layout of experimental setup and its installation  
861 are presented. The design of each key component for the experiment is presented.  
862 As a primary diagnostics, the scientific development of optical diagnostics  
863 employing the high speed cameras and infrared lasers to freeze the transient  
864 motion of mercury jet is presented and the performance of the scientific instrument  
865 as well as the methodology to capture images are discussed.

866 In Chapter 4, 5, and 6, MHD behavior of mercury jet in various magnetic  
867 field are discussed based on the observation from experiment. Also, the  
868 characteristics of mercury jet in magnetic field interacting with an intense  
869 proton beam are presented, where the effect of magnetic field to suppress of  
870 disruption of jet and reducing of filament velocity are investigated to validate  
871 the performance and feasibility of utilizing mercury jet as a high power target.  
872 The key result to validate the feasibility of the high-Z liquid target is addressed  
873 based on the experimental measurements and the beam pulse structures.

874 To conclude, discussion based on understanding of MHD flow in various  
875 literatures and various experimental results is summarized in Chapter 7.

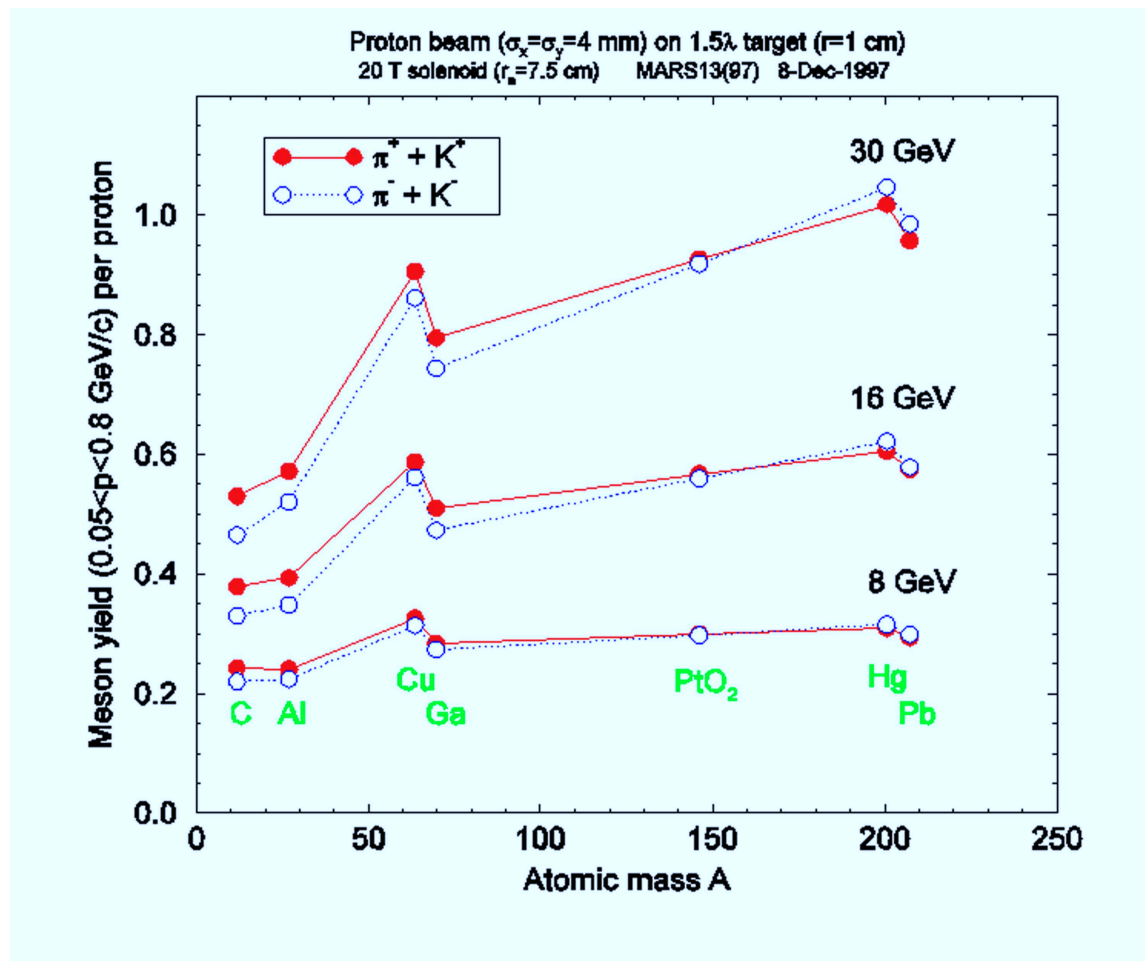


Figure 1.1: Pion yield versus atomic mass number of the target at three proton beam energies (Osaki, 2001 and Mokhov, 2000).

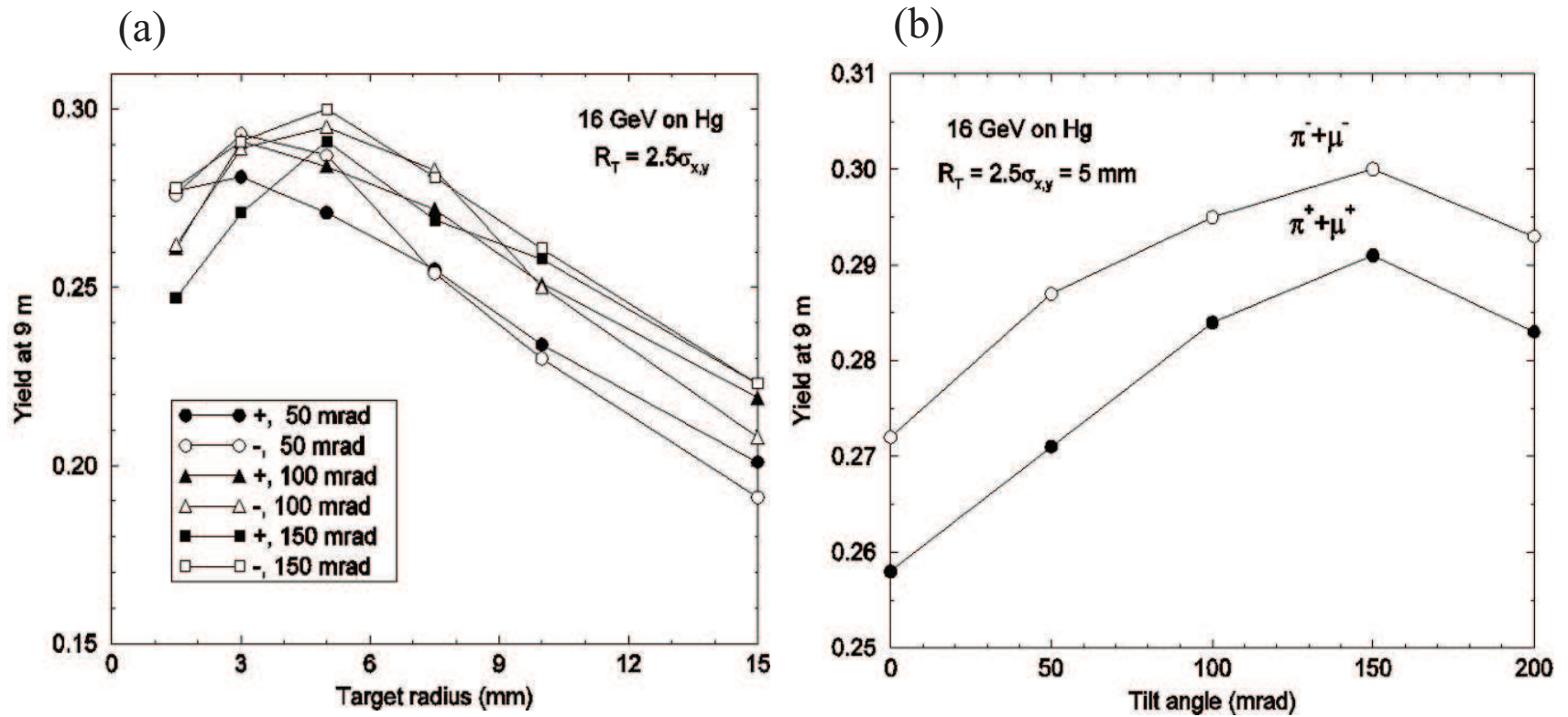


Figure 1.2: Pion yield from Hg targets versus tilt angle between the target/beam axis and the solenoid axis and versus the radius of the target (Osaki, 2001 and Mokhov, 2000). a.) Pion yield versus tilt angle. b.) Pion yield versus target radius.

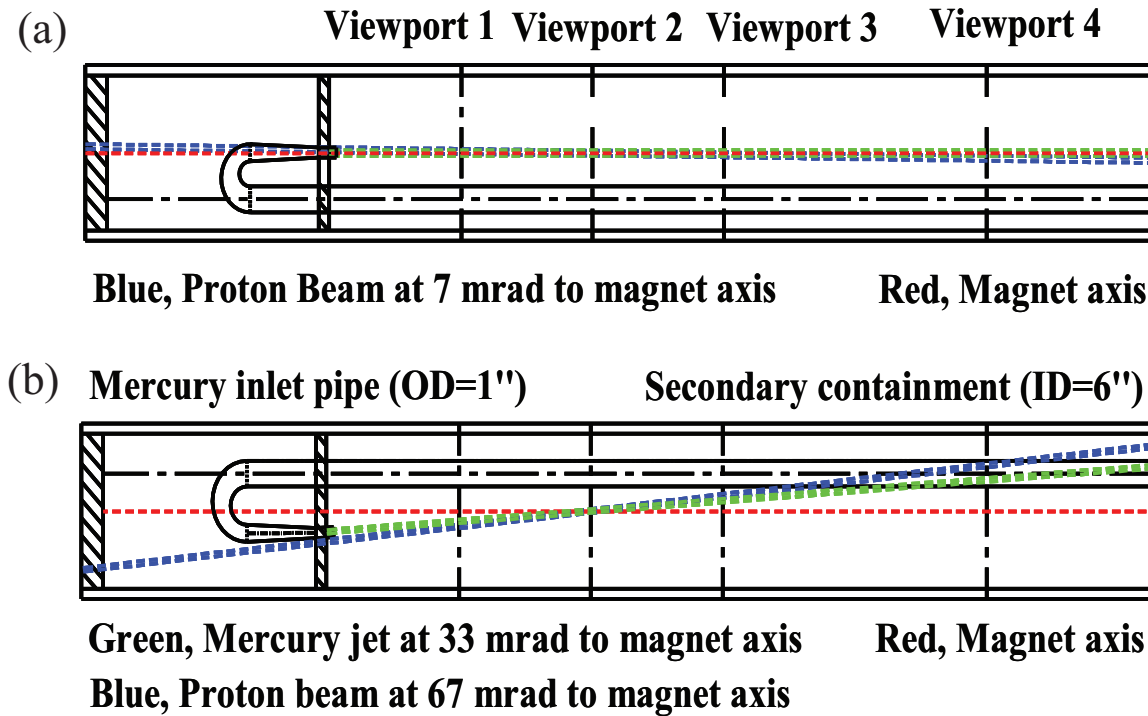


Figure 1.3: Geometry of key elements of target system and Viewports, showing the overlap between the mercury jet, magnetic axis, and the proton beam. a.) Top view. b.) Side view.

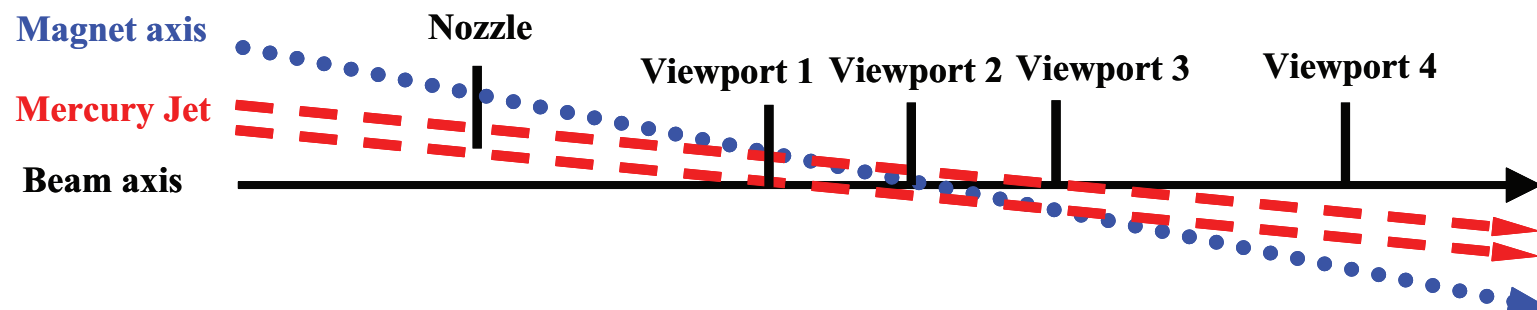


Figure 1.4: Schematics of the relative overlap between proton beam axis, Hg jet axis , and solenoid magnet axis.

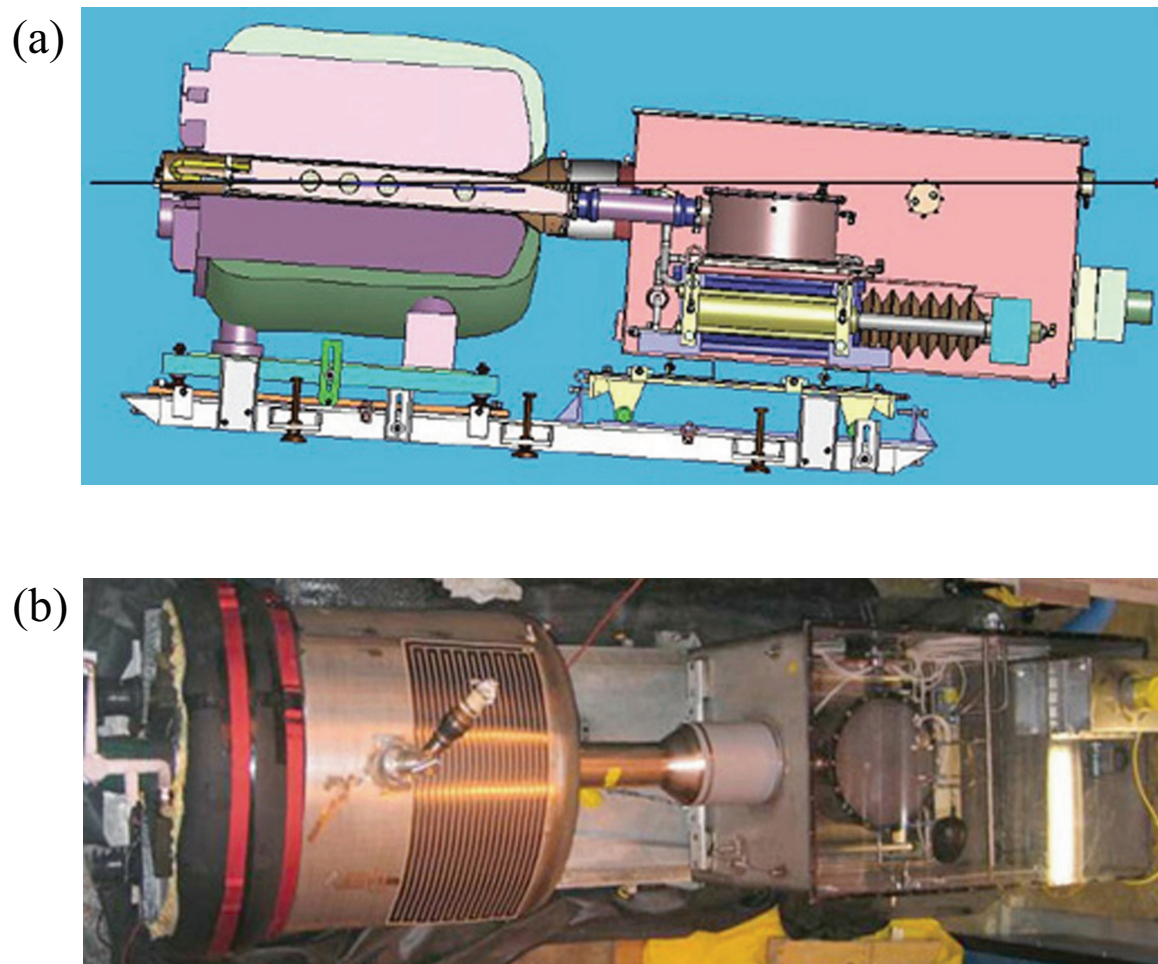


Figure 1.5: Photographs of the entire MERIT experiment. a.) Sectional side view of mercury loop system integrated with 15 T solenoid magnet. b.) Fabricated mercury loop system assembled with 15 T solenoid magnet (Top view).

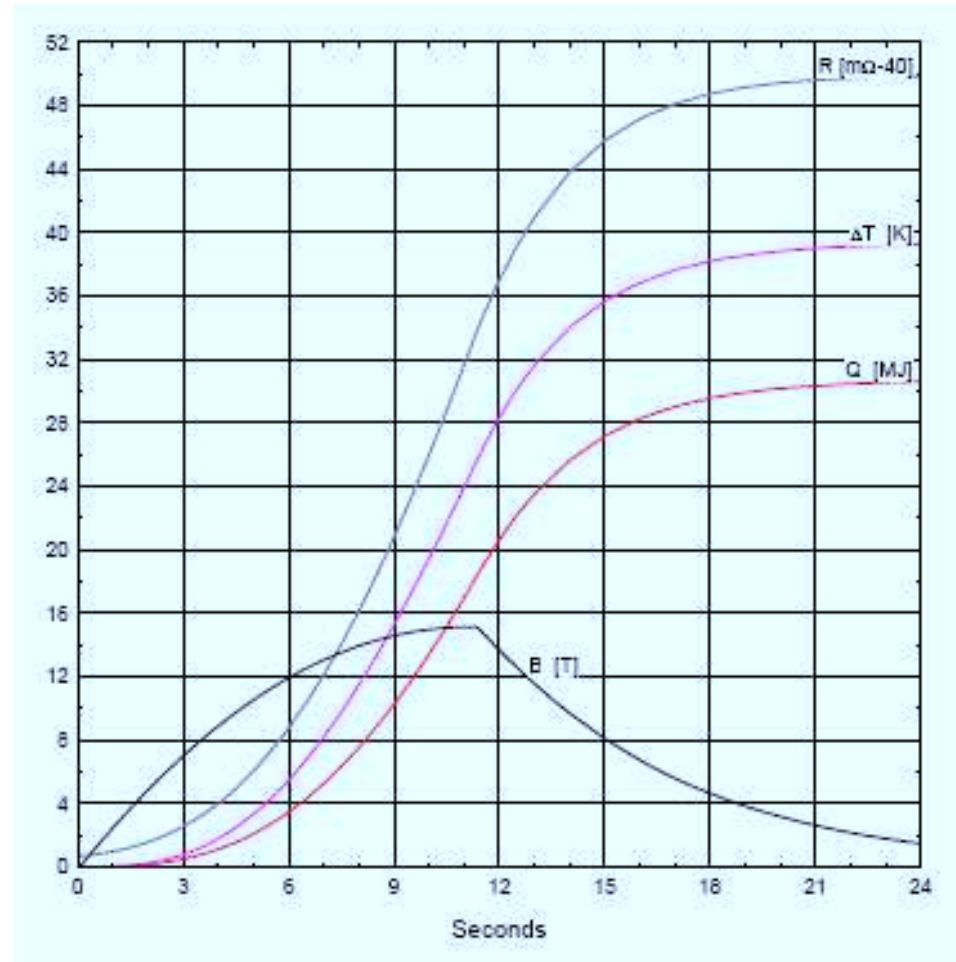


Figure 1.6: Calculated behavior of the 15 T magnet during a pulse.

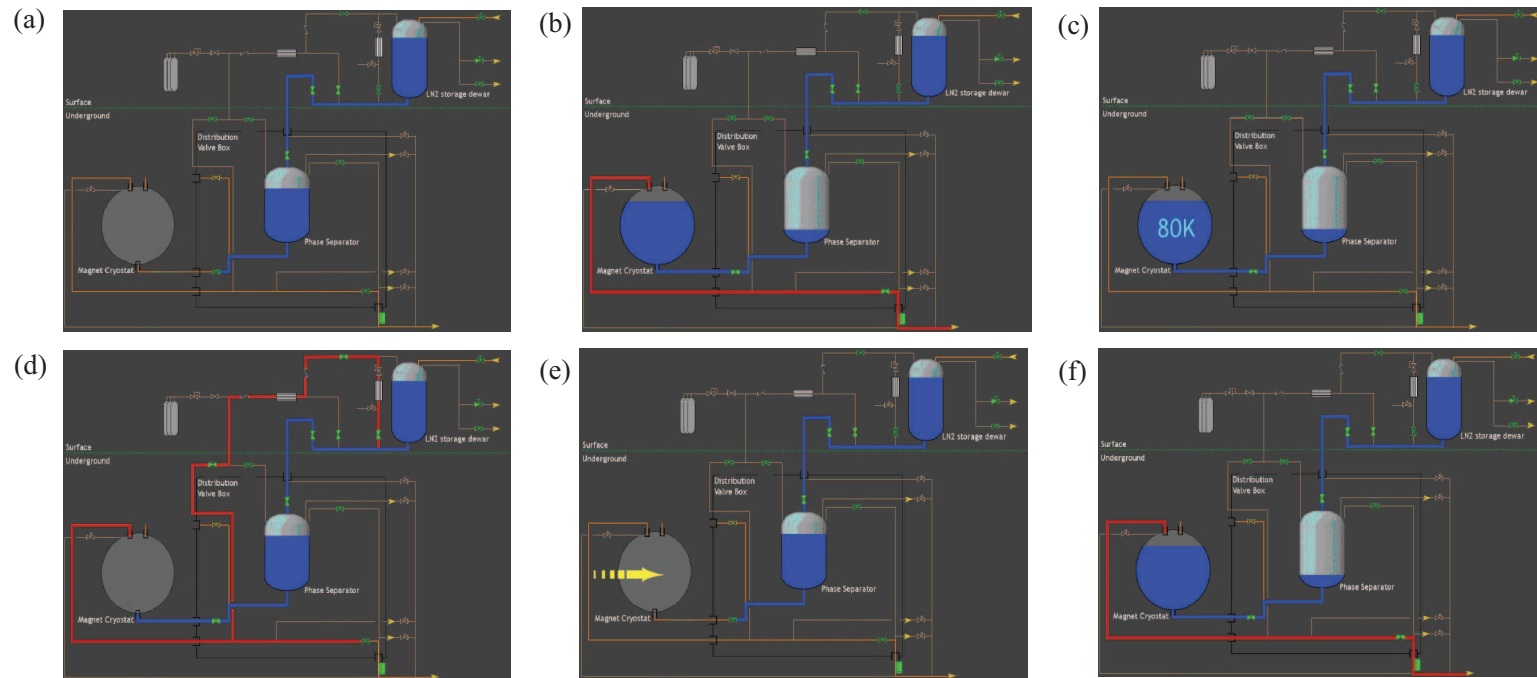


Figure 1.7: Cryogenic process of cooling 15 T solenoid magnet (Haug, 2009). a.) Cooling of proximity cryogenics. b.) Magnet cooldown. c.) Magnet at 80 K. d.) Emptying of the magnet cryostat. e.) Magnet pulse. f.) Re-cooling of magnet.



Figure 1.8: Schematics of mercury loop system for MERIT experiment (Graves, 2007).

## Chapter 2

# Magnetohydrodynamics of Conducting Flow in Magnetic Field

In this chapter, the issues of electrically conducting fluid in a pipe and jet flow in a magnetic field are presented. The governing equations for magnetohydrodynamics, based on electrodynamic relations of Maxwell's equation and hydrodynamic Navier-Stokes equation, are given and the effects of Lorentz force induced by magnetic field are discussed. The review of previous work provides a basis for these studies. Hartmann (1937) considered the flow between two parallel, infinite, non-conducting walls, with magnetic field applied normal to the walls. An exact solution was obtained for this case by Hartmann (1937). Shercliff (1953) solved the more general problem of three dimensional flow in a rectangular duct. Exact solutions demonstrated the fact that for large Hartmann number, the velocity distribution consists of a uniform core with a boundary layer near the walls. This result enabled the solution of the corresponding problem for a circular pipe in an approximate manner for large

894 Hartmann numbers, assuming walls of zero conductivities (Shercliff, 1956).  
 895 Chang and Lundgren (1961) considered the effects of wall conductivity for  
 896 the same problem. Gold (1962) considered a steady one-dimensional flow  
 897 of an incompressible, viscous, electrically conducting fluid through a circular  
 898 pipe in the presence of a uniform transverse field. A no-slip condition on  
 899 the velocity is assumed at the electrically non-conducting wall because if  
 900 the walls are conducting, there is a electromagnetic force on the wall and  
 901 a corresponding force on the fluid. The flow is along the  $z$ -axis, which  
 902 coincides with the axis of the cylinder, and the uniform applied magnetic  
 903 field is along the  $x$ -axis, which is normal to the flow direction. The solution is  
 904 exact and valid for all values of the Hartmann number. The conducting liquid  
 905 jet inside a strong magnetic field raises several magnetohydrodynamic(MHD)  
 906 issues, such as the possible deformation of the jet's shape and trajectory, as  
 907 well as the effect of the magnetic field on the beam-induced dispersal of the  
 908 jet. The electrically conducting flow moving in a magnetic field experiences  
 909 induced currents (Gallardo, 2002). These induced currents cause the jet to  
 910 experience anisotropic pressure distribution with respect to the major and  
 911 minor axis of jet cross section normal to the jet flowing axis while the jet  
 912 penetrates the nonuniform magnetic field (Gallardo, 2002). In addition, axial  
 913 currents are induced if the jet axis does not coincide with the magnetic field  
 914 axis. These currents in turn produce transverse elliptical distortions of the  
 915 mercury jet. Finally, the liquid jet can develop surface instabilities such as  
 916 surface wavelength growing and jet breakup during both liquid motion in a

inhomogeneous magnetic field and after the interaction of intense proton beam, because of the Rayleigh instabilities in a magnetic field and the sudden energy deposition leading to jet breakup. These instabilities can change the jet shape into a significantly less efficient target for pion production. The analytical approach to describe the behaviors of MHD conducting flow in a magnetic field is provided in this chapter.

## 2.1 Governing Equations for MHD Flow

### 2.1.1 Electromagnetic equations

In this section, we describe the electromagnetic relations that have been used in the derivation of the MHD governing equations. The following properties are defined as follows:

- polarization density  $\mathbf{P}$ : the vector field that expresses the density of permanent or induced electric dipole moments in a dielectric material. It is defined as the dipole moment per unit volume.
- magnetization density  $\mathbf{M}$ : the magnetic dipole moment per unit volume.
- electrical susceptibility  $\chi_e$ : a measure of how easily a dielectric material polarizes in response to an electric field. This determines the electric permittivity of the material. It is defined as the constant of proportionality when relating an electric field  $\mathbf{E}$  to the induced dielectric polarization density  $\mathbf{P}$ .

- 938        • magnetic susceptibility  $\chi_m$ : the degree of magnetization of a material in  
939        response to an applied magnetic field.
- 940        • electric displacement field **D**: It accounts for the effects of bound charges  
941        within materials. It is the macroscopic field average of electric fields from  
942        charged particles that make up otherwise electrically neutral material.  
943        It can be considered the field after taking into account the response of a  
944        medium to an external field such as reorientation of electric dipoles.
- 945        • magnetic field strength **H**: A vector field that permeates space and which  
946        can exert a magnetic force on moving electric charge and on magnetic  
947        dipoles such as permanent magnets.
- 948        • electric field **E**: the electric force per unit charge. The direction of the  
949        field is taken to be the direction of the force it would exert on a positive  
950        test charge.

#### 951    2.1.1.1    *electromagnetic relation in a linear material*

952        In a linear material, the polarization density **P** and magnetization density  
953        **M** are given by

$$955 \qquad \qquad \qquad \mathbf{P} = \chi_e \varepsilon_o \mathbf{E} \ , \qquad \qquad \qquad (2.1)$$

$$956 \qquad \qquad \qquad \mathbf{M} = \chi_m \mathbf{H} \ , \qquad \qquad \qquad (2.2)$$

where  $\chi_e$  is the electrical susceptibility and  $\chi_m$  is the magnetic susceptibility of the material. Electric displacement field,  $\mathbf{D}$ , and magnetic induction field,  $\mathbf{B}$ , are related to electric field,  $\mathbf{E}$ , and magnetic field  $\mathbf{H}$  by

$$\mathbf{D} = \varepsilon_o \mathbf{E} + \mathbf{P} = \varepsilon \mathbf{E} , \quad (2.3)$$

$$\mathbf{B} = \mu_o (\mathbf{H} + \mathbf{M}) = \mu \mathbf{H} , \quad (2.4)$$

where  $\varepsilon$  is the electrical permittivity and  $\mu$  is the magnetic permeability of the material.

#### 2.1.1.2 *Maxwell's equations*

The solenoidal condition for the magnetic induction, indicating that there are no magnetic monopoles, is given by

$$\nabla \cdot \mathbf{B} = 0 , \quad (2.5)$$

That is there are no sources and sinks for magnetic field lines.

Faraday's law of magnetic induction is given by

$$\nabla \times \mathbf{E} = -\partial \mathbf{B} / \partial t \quad (2.6)$$

showing that a spatially varying electric field can induce a magnetic field.

Charge conservation gives

$$\nabla \cdot \mathbf{E} = \rho^* / \varepsilon_o , \quad (2.7)$$

where  $\rho^* = \varepsilon_o (n^+ - n^-)$  is the charge density,  $n^+$  is the number of ions, and  $n^-$  is the number of electrons.

Ampère's law is given by

$$\nabla \times \mathbf{B} = \mu \mathbf{j} + \mu \varepsilon \partial \mathbf{E} / \partial t , \quad (2.8)$$

where the last term on the right hand side is the displacement current. Introducing the fundamental units of mass M, length L, velocity  $v$ , and time t, we consider the dimensions of the displacement current in Eqn. (2.8). The dimensions of the magnetic field B, electric field E, and the speed of light  $c$  itself respectively are considered for simplicity.

$$\nabla \times \mathbf{E} \sim \frac{E}{L}, \frac{\partial \mathbf{B}}{\partial t} \sim \frac{B}{t} \text{ gives } E = v B . \text{ From the speed of light, } c = \frac{1}{\sqrt{\mu \varepsilon}},$$

$$\mu \varepsilon \partial \mathbf{E} / \partial t = \frac{1}{c^2} \partial \mathbf{E} / \partial t \sim \frac{1}{c^2} \frac{E}{t} = \frac{v}{c^2} \frac{B}{t} = \frac{B}{L} \frac{v^2}{c^2}.$$

Therefore, The displacement current in Ampère's law can be neglected if the flow velocity is much less than the speed of light.

By assuming the flow obeys charge neutrality,  $n^+ - n^- \ll n$ , where  $n$  is the total number density, the charge density in Eqn. (2.7) can be neglected.

Finally, Ohm's law without Hall effect is given by

$$\mathbf{j} = \sigma (\mathbf{E} + \mathbf{v} \times \mathbf{B}) . \quad (2.9)$$

This is the generalization of the relation between voltage and current in a moving conductor. It provides the link between the electromagnetic equations and the fluid equations.

The electric charge is conserved, which is given by Kirchhoff's law:

1003

1004

$$\nabla \cdot \mathbf{j} = 0. \quad (2.10)$$

1005

### 2.1.2 The Navier Stokes and magnetic induction equations in a conducting liquid flow

1006

1007

1008

1009

1010

1011

The motion of an electrically conducting fluid in the presence of magnetic field obeys the equations of magnetohydrodynamics. The fluid is treated as a continuum and the classical results of fluid dynamics and electro-dynamics are combined in the derivation of the equations. The first equation is from mass conservation:

1012

1013

$$\rho \frac{\partial \rho}{\partial t} + \nabla \cdot (\rho \mathbf{v}) = 0. \quad (2.11)$$

1014

Next, Newton's second law of motion gives

1015

1016

$$\rho \frac{D\mathbf{v}}{Dt} = -\nabla p + \mathbf{F}, \quad (2.12)$$

1017

1018

1019

1020

where the external force  $\mathbf{F}$  consists of several terms, such as the Lorentz force, given by  $\mathbf{j} \times \mathbf{B}$ , the gravitational force  $\rho \mathbf{g}$ , and the viscous force. The viscous term is given by a kinematic viscosity of the form  $\rho \nu \nabla^2 \mathbf{v}$  for an incompressible flow. Thus, Equation (2.12) becomes

1021

1022

$$\rho \frac{\partial \mathbf{v}}{\partial t} + \rho(\mathbf{v} \cdot \nabla) \mathbf{v} = -\nabla p + \rho \mathbf{g} + \eta \nabla^2 \mathbf{v} + \mathbf{j} \times \mathbf{B}. \quad (2.13)$$

1023

1024

Note that the Lorentz force couples the fluid equations to the electromagnetic equations. Equation (2.13) can be reduced to a dimensionless form.



1025

1026 
$$\frac{\partial \mathbf{v}}{\partial t} + \mathbf{v} \cdot \nabla \mathbf{v} = -\nabla p + \frac{\mathbf{g}}{\text{Fr}^2} + \frac{1}{\text{Re}} \nabla^2 \mathbf{v} + \text{Al}(\mathbf{j} \times \mathbf{B}) , \quad (2.14)$$

1027 where  $\text{Fr} = v/\sqrt{gL}$ ,  $\text{Re} = \rho vL/\eta$ ,  $\text{Re}_m = \mu \sigma vL$ , and  $\text{Al} = B_o^2/\mu \rho v^2$  denote the  
 1028 Froude, Reynolds, magnetic Reynolds, and Alfvén numbers, respectively. The  
 1029 Hartmann number gives the ratio of magnetic forces to viscous forces. Thus,  
 1030 this number is the important parameter in cases where the inertial effects are  
 1031 small. On the other hand, the Stuart number gives the ratio of magnetic forces  
 1032 to inertial forces, Thus, this number is the important parameter where dealing  
 1033 with inviscid or turbulence. The Hartmann number  $\text{Ha}$  and Stuart number  
 1034  $N$  are related through  $\text{Ha}^2 = \text{ReRe}_m\text{Al}$  and  $N = \text{Re}_m\text{Al}$ . Note that the ratio  
 1035 of Hartmann number and Reynolds number represents a mixture parameters  
 1036 and involving viscous, magnetic, and inertial forces and can be thought of the  
 1037 square root of the product of the viscous and magnetic forces divided by the  
 1038 inertial forces.

1039 We consider components of the magnetic induction field  $B_x, B_y, B_z$ . Note  
 1040 that the longitudinal magnetic field along the jet axis  $x$  and the transverse  
 1041 magnetic field normal to the jet axis are given by  $B_x = B_X \cos\theta - B_Y \sin\theta$ ,  $B_y =$   
 1042  $-B_X \sin\theta + B_Y \cos\theta$  respectively, where  $B_X$  is axial magnetic field and  $B_Y$  is  
 1043 radial magnetic field. Also note that the  $(x, y, z)$  coordinate system is related  
 1044 with the dynamics of jet dynamics and the  $(X, Y, Z)$  coordinate system is  
 1045 related with the magnetic field direction in solenoid. The nondimensionalized  
 1046 momentum equations in the  $(x, y, z)$  coordinate system in Fig. 2.1 is represented  
 1047 as Eqn. (2.15) using Ohm's equation:

1048

$$\begin{aligned}
& \frac{\partial v_x}{\partial t} + v_x \cdot \nabla v_x = -\nabla p + \frac{1}{\text{Re}} \nabla^2 v_x - \frac{\text{Ha}_y^2}{\text{Re}} v_x + \frac{\text{Ha}_x \text{Ha}_y}{\text{Re}} v_y , \\
& \frac{\partial v_y}{\partial t} + v_y \cdot \nabla v_y = -\nabla p + \frac{1}{\text{Re}} \nabla^2 v_y - \frac{\text{Ha}_x^2}{\text{Re}} v_y + \frac{\text{Ha}_x \text{Ha}_y}{\text{Re}} v_x , \\
1049 \quad & \frac{\partial v_z}{\partial t} + v_z \cdot \nabla v_z = -\nabla p + \frac{1}{\text{Re}} \nabla^2 v_z - \frac{\text{Ha}_x^2}{\text{Re}} v_z - \frac{\text{Ha}_y^2}{\text{Re}} v_z . \tag{2.15}
\end{aligned}$$

1050

1051

1052

1053

In MHD, to eliminate the electric field  $\mathbf{E}$  and the electric current density  $\mathbf{j}$ , we use the Ampere's law and Ohm's law. Then, the Faraday's law gives the magnetic induction equation:

$$1054 \quad \frac{\partial \mathbf{B}}{\partial t} = \nabla \times (\mathbf{v} \times \mathbf{B}) - \frac{1}{\mu\sigma} \nabla \times \nabla \times \mathbf{B} = \nabla \times (\mathbf{v} \times \mathbf{B}) + \frac{1}{\mu\sigma} \nabla^2 \mathbf{B}. \tag{2.16}$$

1055

### 2.1.2.1 *magnetic Reynolds number*

1056

1057

1058

1059

In Eqn. (2.16), the dimension of the term on the left hand side is  $\frac{B}{t}$  and the second term on the right hand side is  $\frac{B}{\sigma\mu L^2}$ . Therefore,  $\sigma\mu \sim \frac{t}{L^2}$ . The magnetic induction equation can be reduced to a dimensionless form.

$$1060 \quad \frac{\partial \mathbf{B}}{\partial t} = \nabla \times (\mathbf{v} \times \mathbf{B}) + \sigma\mu Lv \nabla^2 \mathbf{B}, \tag{2.17}$$

1061

1062

1063

1064

1065

where the quantity  $\sigma\mu Lv$  is a dimensionless number,  $\text{Re}_m$ , called the magnetic Reynolds number.  $\text{Re}_m$  is a measure of the size of the advection term,  $\nabla \times (\mathbf{v} \times \mathbf{B})$ , relative to the diffusion term,  $\sigma\mu Lv \nabla^2 \mathbf{B}$ . Reynolds number  $\text{Re}$  measures the extent to which a convective process prevails over a diffusive one. In viscous flow, the viscosity causes vorticity to diffuse in the face of

1066 convection and the Reynolds number measures the power of convection over  
 1067 diffusion of vorticity. In MHD, the conductivity causes convection to overcome  
 1068 diffusion of the magnetic field to a degree measured by the magnetic Reynolds  
 1069 number  $Re_m$ . If  $Re_m$  is large, convection dominates over diffusion and magnetic  
 1070 boundary layer near the fields are to be expected. The magnetic Prandtl  
 1071 number measures the ratio of viscous diffusivity and magnetic diffusivity and  
 1072 is defined as  $Re_m/Re$ . When it is small, magnetic fields diffuse much more  
 1073 rapidly than vorticity and magnetic boundary layers are much thicker than  
 1074 viscous layers. This makes for simplifications such as the neglect of viscosity  
 1075 in the magnetic boundary layer.

1076 In any region of length scale  $\delta$  where convection and diffusion are equally  
 1077 important,  $\delta$  must be of order  $1/\mu\sigma v$ . Only within limited regions where  $B$   
 1078 changes significantly in a distance  $\delta$  can the gradients be high enough for  
 1079 diffusion and dissipation to matter. The characteristic time in the flow is the  
 1080 transit time  $L/v$ , during which a field disturbance diffuses a distance of order  
 1081  $(L/\mu\sigma v)^{1/2}$ . This is much less than  $L$  if  $Re_m \gg 1$ , in which case diffusion  
 1082 is negligible. It will diffuse a distance of order  $(t/\mu\sigma)^{1/2}$ , which is negligible  
 1083 in comparison with the length scale  $L$  if  $L^2\mu\sigma/t \gg 1$ . This is the required  
 1084 criterion for the perfect conductivity approximation to be valid. At the other  
 1085 extreme case where diffusion is dominant is that the medium diffuses to the  
 1086 form it would be in stationary fluid, where no induced magnetic field would  
 1087 occur. The ratio of the induced magnetic field and the imposed magnetic field  
 1088 is of order  $\mu\sigma vL$ , which is  $Re_m$ . The low  $Re_m$  approximation is to ignore the

1089 induced field, to replace  $\mathbf{B}$  by the known field  $\mathbf{B}_o$  in all MHD equations.

### 1090 **2.1.2.2 *frozen-in theorem in magnetic induction equation***

1091 If  $\text{Re}_m \gg 1$ , the induction equation Eqn. (2.16) is approximated by

1092

1093 
$$\frac{\partial \mathbf{B}}{\partial t} = \nabla \times (\mathbf{v} \times \mathbf{B}). \quad (2.18)$$

1094 The timescale with changes due to the fluid motion from Eqn. (2.18) is  
1095 given by  $t_{motion} \sim \frac{L}{v}$ . In the case  $t_{motion} \ll t_{diffusion}$ , which corresponds to  
1096  $\text{Re}_m \gg 1$ , the diffusion term is negligible. According to the frozen-flux theorem  
1097 of Alfvén, in a perfectly conducting fluid, where  $\text{Re}_m \rightarrow \infty$ , the magnetic  
1098 field lines move with the fluid: the field lines are ‘frozen’ into the fluid. This  
1099 theorem states that motions along the field lines do not change the field but  
1100 motions transverse to the field carry the field with them. If the area of the flux  
1101 tube is small, the field strength will be approximately constant across the area  
1102 of the tube. Thus, the  $|\mathbf{B}| \times \text{cross sectional area}$  is constant so that the field  
1103 strength becomes stronger if the cross sectional area is reduced by the fluid  
1104 motion. The vorticity flux through any loop moving with the fluid is constant  
1105 and the particles which initially lied on a vorticity line continue to do so. All  
1106 the fluid particles which initially lie on a magnetic field line continue to do so  
1107 in a perfect conductor.

### 1108 **2.1.2.3 *the diffusion limit in induction equation***

1109 If  $\text{Re}_m \ll 1$ , the induction equation Eqn. (2.16) is approximated by

1110

1111

$$\frac{\partial \mathbf{B}}{\partial t} = \frac{1}{\mu\sigma} \nabla^2 \mathbf{B}. \quad (2.19)$$

1112

1113

1114

1115

1116

The timescale with changes due to field diffusion from Eqn. (2.19) is given by  $t_{diffusion} \approx \sigma\mu L^2$ . The diffusion equation indicates that any irregularities in an initial magnetic field will diffuse away and be smoothed out. The field will tend to be a simpler uniform field. This process of smoothing out will occur on the given diffusion timescale.

1117

## 2.2 The Energy Equation in MHD

1118

1119

1120

$$\frac{\rho^\gamma}{\gamma - 1} \frac{D}{Dt} \left( \frac{p}{\rho^\gamma} \right) = -\mathbf{D} , \quad (2.20)$$

1121

1122

1123

1124

1125

1126

1127

1128

1129

where  $\mathbf{D}$  is the total energy loss function,  $\gamma$  is the ratio of specific heats,  $c_p/c_v$ . The energy loss function consists of thermal conduction, radiation, and heating. The heating consists of several terms, such as small scale magnetic wave heating, ohmic heating, and viscous heating. However, such losses (gains) can be neglected if the medium is either isentropic or adiabatic. There are cases where no energy is added to the flow and no energy losses occur. The adiabatic term can be represented as follows, using Eqn. (2.11):

$$\rho^\gamma \frac{D}{Dt} \left( \frac{p}{\rho^\gamma} \right) = \frac{\partial p}{\partial t} + \mathbf{v} \cdot \nabla p + \gamma p \nabla \cdot \mathbf{v} = -(\gamma - 1)\mathbf{D}. \quad (2.21)$$

1130 To close the system of equations, an equation of state is needed, which is  
 1131 taken as ideal gas law:

1132

$$1133 \quad p = \frac{\rho}{M}RT , \quad (2.22)$$

1134 where  $M$  is molar mass and  $R$  is the gas constant ( $8.3 \text{ J} \cdot \text{mol}^{-1} \text{ K}^{-1}$ ).

### 1135 **2.2.1 Energetics and effects of Lorentz force**

1136 The energy equation that contains all the various types of energy, including  
 1137 kinetic energy, gravitational energy, the internal energy, and the magnetic  
 1138 energy is obtained using the MHD governing equations. The gravitational  
 1139 potential  $\Phi$  is defined by  $-\nabla\Phi = \mathbf{g}$ . The kinetic energy is obtained by  
 1140 multiplying Eqn. (2.11) by  $v^2/2$  and dotting Eqn. (2.12) with  $\mathbf{v}$ . The energy  
 1141 equation can then be written as

1142

$$1143 \quad \frac{\partial}{\partial t}(\frac{1}{2}\rho v^2) + \nabla \cdot (\frac{1}{2}\rho v^2 \mathbf{v}) = -\mathbf{v} \cdot \nabla p + \mathbf{v} \cdot (\mathbf{j} \times \mathbf{B}) - \mathbf{v} \cdot \rho \nabla \Phi + \mathbf{v} \cdot \eta \nabla^2 \mathbf{v} . \quad (2.23)$$

1144 The gravitational term can be expressed as follows using Eqn. (2.11) and  
 1145 the fact that  $\partial\Phi/\partial t = 0$ .

1146

$$1147 \quad \mathbf{v} \cdot \rho \nabla \Phi = \nabla \cdot (\rho \Phi \mathbf{v}) + \frac{\partial}{\partial t}(\rho \Phi) . \quad (2.24)$$

1148 Equation (2.24) gives the flux of the gravitational potential energy and the  
 1149 rate of change of gravitational potential energy in time. The Lorentz force  
 1150 term can be expressed as follows using Eqn. (2.9):

1151

1152 
$$\mathbf{v} \cdot (\mathbf{j} \times \mathbf{B}) = -\mathbf{j} \cdot (\mathbf{v} \times \mathbf{B}) = -\frac{j^2}{\sigma} + \mathbf{j} \cdot \mathbf{E} . \quad (2.25)$$

1153 Equation (2.25) is rearranged using Eqn. (2.6):

1154

1155 
$$\mathbf{v} \cdot (\mathbf{j} \times \mathbf{B}) = -\frac{j^2}{\sigma} - \nabla \cdot \left( \frac{\mathbf{E} \times \mathbf{B}}{\mu} \right) - \frac{\partial}{\partial t} \left( \frac{B^2}{2\mu} \right) . \quad (2.26)$$

1156 The pressure gradient term gives

1157

1158 
$$-\mathbf{v} \cdot \nabla p = -\nabla \cdot (p\mathbf{v}) + p\nabla \cdot \mathbf{v} . \quad (2.27)$$

1159 Equation (2.27) can also be expressed as follows using Eqn. (2.21):

1160

1161 
$$p\nabla \cdot \mathbf{v} = -\frac{\partial}{\partial t} \left( \frac{p}{\gamma - 1} \right) - \nabla \cdot \left( \frac{p}{\gamma - 1} \mathbf{v} \right) - \mathbf{D} . \quad (2.28)$$

1162 Substituting the foregoing relations, the full energy equation can be expressed

1163 as

1164

1165 
$$\frac{\partial}{\partial t} \left[ \frac{1}{2} \rho v^2 + \rho \Phi + \frac{p}{\gamma - 1} + \frac{B^2}{2\mu} \right] + \nabla \cdot \left\{ \left[ \frac{1}{2} \rho v^2 + \rho \Phi + \gamma \frac{p}{\gamma - 1} \right] \mathbf{v} + \frac{\mathbf{E} \times \mathbf{B}}{\mu} \right\} = -\frac{j^2}{\sigma} - \mathbf{D} . \quad (2.29)$$

## 1166 **2.2.2 Proton beam induced energy deposition and equation** 1167 **of state**

1168 Due to the sudden energy deposition by proton beam, it is worthy to

1169 consider the components of added energy and the state of energy from compressible

density variation as well as ionization to the right hand side of full energy equation Eqn. (2.29). The instantaneous beam energy deposition is

$$E_{beam}(r) = E_{beam}(r) \cdot \delta(t - t_{beam}), \quad (2.30)$$

where

$$E_{beam}(r) = E_o \exp\left[-\frac{r}{a}\right] \quad (2.31)$$

and

$$E_o = \frac{E_{beam}}{\pi r_{beam}^2}. \quad (2.32)$$

$E_{beam}(r)$  is radial energy density distribution of the beam and the proton beam energy is assumed to be deposited as a  $\delta$  function at time  $t = t_{beam}$ .  $E_{beam}$  is the peak energy deposition corresponding to the beam spot radius  $r_b$ . The equation of state (EOS) is considered as the sum of compression, ion thermal, and electron thermal terms. The EOS can be expressed for simplification. The compressible pressure  $P_c$  and energy  $E_c$  are

$$P_c = P_{co} \left[ \left( \frac{\rho}{\rho_o} \right)^\gamma - 1 \right], \quad (2.33)$$

$$E_c = E_{co} \left[ \left( \frac{\rho}{\rho_o} \right)^{\gamma-1} - 1 \right] \frac{\rho}{\rho_o} + P_{co} \left( 1 - \frac{\rho}{\rho_o} \right), \quad (2.34)$$

where



1191

$$1192 \quad P_{co} = \frac{\rho c^2}{\gamma} \quad , \quad E_{co} = \frac{P_{co}}{\gamma - 1}. \quad (2.35)$$

1193 Ion and electron thermal pressure and energy are

1194

$$1195 \quad E_I = 3nk(T - T_o) \quad , \quad P_I = G_I E_I \quad , \quad (2.36)$$

1196

$$1197 \quad E_e = \frac{1}{2}\beta(T - T_o)^2 \quad , \quad \beta = \beta_o\left(\frac{\rho_o}{\rho}\right)^{2/3} \quad , \quad P_e = G_e E_e, \quad (2.37)$$

1198 where  $n = \frac{\rho}{M}$  and  $k$  is Boltzmann's constant. Thus, the total energy and  
1199 pressure are

1200

$$1201 \quad E = E_c + E_I + E_e \quad , \quad P = P_c + P_I + P_e \quad , \quad (2.38)$$

1202 where subscripts c, I, and e correspond to compression, ion thermal, and  
1203 electron thermal components, respectively.  $G_I$  and  $G_e$  are the Gruneisen  
1204 coefficients for the ion and electron.  $c$  is the speed of sound in the material.  
1205 Initial mercury pressure  $P$  is 0 at  $T = T_o = T_{melting}$  and normal density  $\rho = \rho_o$ .  
1206 At higher temperatures, the mercury can be ionized and the resulting energy  
1207 and pressure by free-electron component is added to the EOS. Accordingly,  
1208 the solid state partition of the electron thermal energy and pressure decreases  
1209  $(1 - f_z)$  times, where  $f_z$  is the ionization fraction.

### 1210 **2.2.3 Magnetic damping with joule dissipation**

1211 It is known that a static magnetic field can suppress motion of an electrically  
1212 conducting liquid. If a conducting liquid moves through an imposed static

magnetic field, electric currents are generated. These, in turn, lead to ohmic heating such as Joule dissipation. As the thermal energy of the fluid rises, there is a corresponding drop in its kinetic energy, and so the fluid decelerates. This is to suppress the motion of liquid jets. In many applications, it is believed that the imposition of a static magnetic field is used as one means of suppressing unwanted motion. Considering the uniform perpendicularly imposed magnetic field to the flow direction for simplicity, the damping effect of Lorentz force can be quantified. If the magnetic field is uniform, the Faraday' law requires that  $\nabla \times \mathbf{E} = 0$ . Using Ohm's law and the fact that the current density is solenoidal, the current relationship is given by

$$\nabla \cdot \mathbf{J} = 0 \quad , \quad \nabla \times \mathbf{J} = \sigma \mathbf{B} \cdot \nabla \mathbf{v} . \quad (2.39)$$

Thus,  $\mathbf{J}$  is zero if  $\mathbf{v}$  is independent of the magnetic field direction. By doing cross product of  $\mathbf{J}$  and  $\mathbf{B}$  and using the vector identity, Lorentz force per unit mass is given by

$$\mathbf{F} = -\frac{\mathbf{v}}{\tau} + \frac{\sigma(\mathbf{B} \times \nabla \phi_E)}{\rho} , \quad (2.40)$$

where  $\tau = \rho/\sigma B^2$  is Joule damping term and  $\phi_E$  is electrical potential, which is given by the divergence of Ohm's law:  $\phi_E = \nabla^{-2}(\mathbf{B} \cdot \omega)$ . The Lorentz force then simplifies to  $-\mathbf{v}/\tau$  when the magnetic field and the vorticity field are mutually perpendicular. Thus, the perpendicular  $\mathbf{v}$  to magnetic field declines on a time scale of  $\tau$ , which clearly explains the mechanism of magnetic damping. The ratio of the damping time  $\tau$  to the characteristic time  $L/v$  gives

the interaction parameter  $N = \sigma B^2 L / \rho v$ , which is also used for the indication of the ratio of the magnetic and inertial forces.

To investigate the role of Joule dissipation, consider the fully derived energy equation in inviscid flow.

$$\frac{dE}{dt} = -\frac{1}{\sigma \rho} \int \mathbf{J}^2 dV = -\mathbf{D} , \quad (2.41)$$

where  $\mathbf{D}$  is joule dissipation and  $E$  is global kinetic energy.

$\mathbf{J}^2$  from Eqn. (2.39) was estimated (Davidson, 1999) and is given.

$$\frac{dE}{dt} \sim -\left(\frac{L_{min}}{L_{\parallel}}\right)^2 \frac{E}{\tau} , \quad (2.42)$$

from which

$$E \sim E_o \exp \left( -\tau^{-1} \int_0^t (L_{min}/L_{\parallel})^2 dt \right) , \quad (2.43)$$

where  $L_{\parallel}$  is the characteristic length for the flow, parallel to the magnetic field. Fig. 2.3 (a) shows the decay of energy depending on the Joule damping term with various magnetic field. The energy is dissipated as a result of energy decay by Joule dissipation. So, the time constant required for energy dissipation is getting smaller as the magnetic field strength increases. As a result, the magnetic field affect to the integration of energy, which is shown in Fig. 2.3 (b). It indicates that the flow decays on a time scale of  $\tau$  provided that  $L_{min}$  and  $L_{\parallel}$  are of the same order. However, the Lorentz force can not create or destroy linear (angular) momentum despite the Joule dissipation. This indicates that the flow can not be decayed on a time scale of  $\tau$  and the

Eqn. (2.42) and (2.43) infer that  $L_{min}/L_{\parallel}$  must increase with time. Therefore, it is expected that these flow will experience anisotropy, with  $L_{\parallel}$  increasing as the flow evolves.

## 2.3 Vorticity Equations in MHD flow

The possibility of using an electromagnetic field for vortices control in conducting fluids needs to be investigated. Electromagnetic force can influence the stability of a flow, thus prevents its transition to turbulence by suppressing disturbances or changing mean velocity profiles. A significant drag reduction is possible when the surface boundary condition is modified to suppress the vortices. Transverse magnetic field does not reduce drag because the magnetic field increases the skin friction drag by directly altering the mean flow, so called Hartmann flow, even though turbulent fluctuations are significantly reduced. The longitudinal magnetic field does not directly interact with the mean flow although it can reduce turbulent fluctuations. Thus it is possible that the longitudinal magnetic field can result in drag reduction.

### 2.3.1 Governing equations for vorticity

It is useful to transform the governing equations in terms of vorticity transport. The equation for the vorticity  $\omega$  of an incompressible conducting fluid in MHD is

1277

$$\begin{aligned}
& \frac{\partial \omega}{\partial t} + (\mathbf{v} \cdot \nabla) \omega - (\omega \cdot \nabla) \mathbf{v} \\
& = \nu \nabla^2 \omega + \frac{1}{\rho} \nabla \times (\mathbf{j} \times \mathbf{B}) \\
& = \nu \nabla^2 \omega + \frac{1}{\rho} \{ (\mathbf{B} \cdot \nabla) \mathbf{j} - (\mathbf{j} \cdot \nabla) \mathbf{B} \} .
\end{aligned} \tag{2.44}$$

1278

1279 The term  $(\omega \cdot \nabla) \mathbf{v}$  in Eqn. (2.44) expresses the effect of stretching and  
1280 turning vorticity lines. From the Faraday's law and  $\partial \mathbf{B} / \partial t = 0$ , the electric  
1281 field in terms of an electric potential,  $\phi_E$ , is

1282

$$1283 \quad \mathbf{E} = -\nabla \phi_E . \tag{2.45}$$

1284 From the Ohm's law, Kirchhoff's law, and Eqn. (2.45), the electromagnetic  
1285 equation can be simplified as Eqn. (2.47) using nondimensionalized Ohm's law  
1286 Eqn. (2.46).

1287

$$1288 \quad \mathbf{j} = \text{Re}_m (-\nabla \phi_E + \mathbf{v} \times \mathbf{B}) . \tag{2.46}$$

1289

$$1290 \quad \nabla^2 \phi_E = \nabla \cdot (\mathbf{v} \times \mathbf{B}) . \tag{2.47}$$

1291 The important parameter in vortices dynamics is the Stuart number  $N$   
1292  $(= \text{Re}_m \text{Al} = \sigma \mathbf{B}^2 L / \rho v)$ , which is the ratio of the electromagnetic force to the  
1293 inertial force. Therefore, one can fix the Reynolds number and change the  
1294 Stuart number to see the effect of magnetic field over the vortices strength.  
1295 The Hartmann numbers,  $\text{Ha} = \sqrt{\text{Re} N}$ , can be determined correspondingly.

1296 The Stuart number gives the ratio of Ha to Re. Thus, the Stuart number will  
 1297 indicate the stabilizing effect of magnetic field to the unique characteristic of  
 1298 transition to turbulence.

## 1299 2.3.2 Vorticity suppression

1300 The vorticity is suppressed by the magnetic field, transverse to the vorticity.  
 1301 The result is altered if the conductivity  $\sigma$  is nonuniform and varies with  
 1302 coordinates, in which case vorticity will be created. When a conducting liquid  
 1303 flows along a pipe with an axial magnetic field, there will be no magnetic effect  
 1304 if the motion is laminar, though the vorticity is perpendicular to the magnetic  
 1305 field, but if the flow is turbulent, adding the field damps the turbulence and  
 1306 reduces the Reynolds stresses and the frictional drag. Adding the field also  
 1307 raises the critical Reynolds number for instability of flow (Shercliff, 1965).

### 1308 2.3.2.1 *spanwise magnetic field effect to vorticity suppression*

1309 For a spanwise magnetic field,  $B = (0, 0, B_z)$ , the corresponding Lorentz  
 1310 force,  $f = (f_x, f_y, f_z)$  can be represented as follows.

1311

$$\begin{aligned} f_x &= N\left(-\frac{\partial\phi_E}{\partial y}B_z - B_z^2v_x\right) , \\ f_y &= N\left(\frac{\partial\phi_E}{\partial x}B_z - B_z^2v_y\right) , \\ f_z &= 0 . \end{aligned} \tag{2.48}$$

1312

1313 Introducing the stream function  $\psi$ ,

1314

1315 
$$\frac{\partial^2 \psi}{\partial x^2} + \frac{\partial^2 \psi}{\partial y^2} = -\omega_z , \quad (2.49)$$

1316 where the spanwise vortex  $\omega_z = \partial v_y / \partial x - \partial v_x / \partial y$ . The Ohm's law Eqn. (2.47)

1317 yields

1318

1319 
$$\frac{\partial^2 \phi_E}{\partial x^2} + \frac{\partial^2 \phi_E}{\partial y^2} = \omega_z , \quad (2.50)$$

1320 where unity quantity of  $B_z$  is assumed.

1321 From Eqn. (2.47) and (2.50),  $\phi_E = \psi + \text{const.}$  Correspondingly this

1322 relation yields  $\mathbf{f} = 0$ . Therefore, the spanwise vortex flow is not affected by

1323 the spanwise magnetic field (Lim, 1998). However, it can reduce turbulent

1324 fluctuations without directly interacting with the mean flow.

1325 **2.3.2.2 longitudinal and transverse magnetic field effect to vorticity**  
 1326 **suppression**

1327 For longitudinal and transverse magnetic field  $\mathbf{B} = (B_x, B_y, 0)$  in a two

1328 dimensional flow, Eqn. (2.47) yields  $\nabla^2 \phi_E^2 = 0$  assuming that there is no

1329 velocity ( $v_z$ ) onto the normal to the flow direction. The corresponding forces

1330 can be represented as follows:

1331

1332 
$$\begin{aligned} f_x &= N(B_y \frac{\partial \phi_E}{\partial z} - B_y^2 v_x + B_x B_y v_y) , \\ f_y &= N(-B_x \frac{\partial \phi_E}{\partial z} - B_x^2 v_y + B_x B_y v_x) , \\ f_z &= N(-B_y \frac{\partial \phi_E}{\partial x} + B_x \frac{\partial \phi_E}{\partial y} - B_x^2 v_z - B_y^2 v_z) . \end{aligned} \quad (2.51)$$

1333 The effect of the longitudinal and transverse magnetic field on the strength  
 1334 of spanwise vortices can be shown from the vorticity equation where additional  
 1335 vortices term  $\omega_{Lorentz} = \nabla \times \mathbf{f}$  caused by the Lorentz force has been added.

1336

$$1337 \quad \frac{\partial \omega_z}{\partial t} + (\mathbf{v} \cdot \nabla) \omega_z = (\omega_z \cdot \nabla) \mathbf{v} + \frac{1}{\text{Re}} \nabla^2 \omega_z + N \left( -B_x \frac{\partial^2 \phi_E}{\partial x \partial z} \right. \\ \left. - B_y \frac{\partial^2 \phi_E}{\partial y \partial z} + B_x B_y \left( \frac{\partial v_x}{\partial x} - \frac{\partial v_y}{\partial y} \right) - B_x^2 \frac{\partial v_y}{\partial x} + B_y^2 \frac{\partial v_x}{\partial y} \right) . \quad (2.52)$$

1338 If we consider the longitudinal magnetic field  $\mathbf{B} = (B_x, 0, 0)$  and the  
 1339 transverse magnetic field  $\mathbf{B} = (0, B_y, 0)$  independently, the corresponding force  
 1340 can be shown in Eqn. (2.53), Eqn. (2.54) respectively.

1341

$$1342 \quad \begin{aligned} f_x &= 0 , \\ f_y &= N(-B_x \frac{\partial \phi_E}{\partial z} - B_x^2 v_y) , \\ f_z &= N(B_x \frac{\partial \phi_E}{\partial y} - B_x^2 v_z) . \end{aligned} \quad (2.53)$$

1343

$$1344 \quad \begin{aligned} f_x &= N(B_y \frac{\partial \phi_E}{\partial z} - B_y^2 v_y) , \\ f_y &= 0 , \\ f_z &= N(-B_y \frac{\partial \phi_E}{\partial x} - B_y^2 v_z) . \end{aligned} \quad (2.54)$$

1345 Equations. (2.53) and (2.54) clearly show that the Lorentz force retards  
 1346 the local velocity. The vorticity equation is shown as Eqn. (2.55), Eqn. (2.56).

1347

$$1348 \quad \frac{\partial \omega_z}{\partial t} + (\mathbf{v} \cdot \nabla) \omega_z = (\omega_z \cdot \nabla) \mathbf{v} + \frac{1}{\text{Re}} \nabla^2 \omega_z + N(-B_x \frac{\partial^2 \phi_E}{\partial x \partial z} - B_x^2 \frac{\partial v_y}{\partial x}) . \quad (2.55)$$



1349

1350 
$$\frac{\partial \omega_z}{\partial t} + (\mathbf{v} \cdot \nabla) \omega_z = (\omega_z \cdot \nabla) \mathbf{v} + \frac{1}{\text{Re}} \nabla^2 \omega_z + N(-B_y \frac{\partial^2 \phi_E}{\partial y \partial z} + B_y^2 \frac{\partial v_x}{\partial y}) . \quad (2.56)$$

1351 The Lorentz force is negatively correlated with the spanwise vorticity.

1352 Therefore, the Lorentz force induced by the longitudinal and transverse magnetic

1353 field reduces the strength of the spanwise vorticity effectively.

## 1354 2.4 One Dimensional Pipe Flow in Transverse 1355 Magnetic Field

1356 In one-dimensional problem, the governing equations and the boundary

1357 conditions are assumed that there is only one component of the velocity,  $v_z$ ,

1358 and only one component of the induced magnetic field,  $\mathbf{B}_z$ , along with the

1359 applied field  $\mathbf{B}_o$ , so that the total velocity and magnetic fields are given by

1360

$$v_r = v_\theta = 0, \quad v_z = v_z(r, \theta), \quad B_r = B_o \cos \theta ,$$

1361 
$$B_\theta = -B_o \sin \theta, \quad B_z = B_z(r, \theta) . \quad (2.57)$$

1362 Substituting these expressions into Eqn. (2.13) using cylindrical coordinates,

1363 we obtain

1364

1365 
$$p(r, \theta, z) = -(1/2\mu)B_z^2 + O_1 z + O_2 , \quad \partial p / \partial z = O_1 = \text{constant} , \quad (2.58)$$

1366

1367 
$$O_1 = \eta \left[ \frac{\partial^2 v_z}{\partial r^2} + \left( \frac{1}{r} \right) \frac{\partial v_z}{\partial r} + \left( \frac{1}{r^2} \right) \frac{\partial^2 v_z}{\partial \theta^2} \right] + \left( \frac{1}{r} \right) B_\theta \frac{\partial B_z}{\partial \theta} + B_r \frac{\partial B_z}{\partial r} , \quad (2.59)$$

1368 where  $O_2$  is a constant.

1369 Equation (2.5), Equation (2.11), and Equation (2.57) are identically satisfied  
 1370 and Eqns. (2.16) becomes

1371

1372 
$$\frac{1}{\mu\sigma} \left[ \frac{\partial}{\partial r} \left( r \frac{\partial B_z}{\partial r} \right) + \left( \frac{1}{r} \right) \frac{\partial^2 B_z}{\partial \theta^2} \right] + \left[ B_r \frac{\partial}{\partial r} (r v_z) + \frac{\partial}{\partial \theta} (v_z B_\theta) \right] = 0 . \quad (2.60)$$

## 1373 2.4.1 Non-dimensional form of the governing equations 1374 using cylindrical coordinates

### 1375 2.4.1.1 *uncoupled governing equations*

1376 The modified non-dimensional form of Navier-Stokes equations and the  
 1377 magnetic induction equations using cylindrical coordinates is expressed as  
 1378 follows:

1379

1380 
$$\nabla^2 v_z - \left( \frac{\text{Ha}^2}{\text{Re}_m} \right) \left[ \left( \frac{\sin \theta}{r} \right) \frac{\partial B_z}{\partial \theta} - \cos \theta \frac{\partial B_z}{\partial r} \right] = O , \quad (2.61)$$

1381

1382 
$$\nabla^2 B_z - \text{Re}_m \left[ \left( \frac{\sin \theta}{r} \right) \frac{\partial v_z}{\partial \theta} - \cos \theta \frac{\partial v_z}{\partial r} \right] = 0 , \quad (2.62)$$

1383 where  $\nabla^2 \equiv \frac{\partial^2}{\partial r^2} + \left( \frac{1}{r} \right) \frac{\partial}{\partial r} + \left( \frac{1}{r^2} \right) \frac{\partial^2}{\partial \theta^2}$ ,  $\text{Ha} = B_o a (\sigma / \eta)^{1/2}$ ,  $\text{Re}_m = \sigma \mu v a$ , and  
 1384  $O = O_1 a^2 / v \eta$ .

1385 Equations (2.61) and (2.62) apply to any general incompressible, steady  
 1386 magnetohydrodynamic duct flow. The restriction as to geometry and the  
 1387 conditions at the wall enters through the boundary conditions.



1407

$$v_z = \frac{-Kv}{4\alpha} [e^{-\alpha \frac{r}{a} \cos \theta} \sum_{n=0}^{\infty} \epsilon_n \frac{I'_n(\alpha)}{I_n(\alpha)} I_n(\alpha \frac{r}{a}) \cos n\theta + e^{\alpha \frac{r}{a} \cos \theta} \sum_{n=0}^{\infty} (-1)^n \epsilon_n \frac{I'_n(\alpha)}{I_n(\alpha)} I_n(\alpha \frac{r}{a}) \cos n\theta] , \quad (2.67)$$

1408

1409

$$B_z = \frac{-\text{Re}_m K B_o}{8\alpha^2} [e^{-\alpha \frac{r}{a} \cos \theta} \sum_{n=0}^{\infty} \epsilon_n \frac{I'_n(\alpha)}{I_n(\alpha)} I_n(\alpha \frac{r}{a}) \cos n\theta - e^{\alpha \frac{r}{a} \cos \theta} \sum_{n=0}^{\infty} (-1)^n \epsilon_n \frac{I'_n(\alpha)}{I_n(\alpha)} I_n(\alpha \frac{r}{a}) \cos n\theta - 2 \frac{r}{a} \cos \theta] , \quad (2.68)$$

1410

1411 where  $\alpha = \frac{1}{2} \text{Ha}$ ,  $I_n$  is the modified Bessel function of order  $n$ ,  $\epsilon_n = 1$  for  
 1412  $n=0$ , and  $\epsilon_n = 2$  for  $n>0$ . Equation (2.65) and (2.66) are used to obtain the  
 1413 electric field  $\mathbf{E}$ :

1414

$$E_r = (\frac{a\mu v}{\text{Re}_m r}) \frac{\partial B_z}{\partial \theta} - v_z B_o \sin \theta . \quad (2.69)$$

1415

1416  $I_n$  identities are given by

1417

$$1418 \quad I_n(\alpha) = I_{-n}(\alpha) , I_n(-\alpha) = (-1)^n I_n(\alpha) , I_n(\alpha)' = \frac{1}{2} (I_{n+1}(\alpha) + I_{n-1}(\alpha)) , \quad (2.70)$$

1419 and

1420

$$1421 \quad I_n(x) = \frac{1}{\pi} \int_0^\pi e^{x \cos \theta} \cos n\theta d\theta - \frac{1}{\pi} \int_0^\infty e^{-x \cosh u - nu} du . \quad (2.71)$$

## 1422    **2.5    Stability of Conducting Flow in a Magnetic** 1423    **Field**

1424        The problem of the flow of liquid metal jets in magnetic field arises in  
1425        certain applications of magnetohydrodynamics. The stability of the flow of a  
1426        conducting film in the presence of two components of the magnetic field (in  
1427        the direction of the flow and normal to the surface) was investigated by B.A.  
1428        Kolovadin (1965) using the approximation of small Reynolds numbers: The  
1429        ratio of transverse magnetic field to longitudinal magnetic field changes due  
1430        to the finite inclination of jet axis to the magnetic field axis. The magnitude  
1431        of the inclination angle affects the stability of the liquid jets.

1432        These instabilities can change the jet shape into one that makes the jet  
1433        a significantly less efficient target for particle production. As described in  
1434        Chapter 1, the particle production depends on several parameters such as jet  
1435        size and jet angle. Thus, the unstable behaviors of jet in a magnetic field yields  
1436        less or unexpected production of particle. In addition, the larger inclination  
1437        of jet axis makes the jet size become bigger than the nominal jet size due to  
1438        the increased magnetic field. Thus, the mercury jet interacting with beam  
1439        will have different energy deposition leading to different particle production.  
1440        Therefore, the stable motion of mercury jet is required for stable particle  
1441        production and it then needs to be investigated.

### 2.5.1 Propagation of waves at an interface separating two flows in magnetic field

To investigate the surface wave motion of free jet in magnetic field, we followed the procedure of a direct extension of Currie (1993) to the case with a magnetic field. The detailed procedures and derivations are described in Appendix C.2.

We consider the  $(x, y, z)$  coordinate system in Fig. 2.1. The magnetic field along and normal to the Hg jet axis can be derived from the solenoid magnetic field map. From trigonometry, the longitudinal magnetic field along the jet axis and the transverse magnetic field normal to the jet axis are given by  $B_x = B_X \cos\theta - B_Y \sin\theta$ ,  $B_y = -B_X \sin\theta + B_Y \cos\theta$ , respectively, where  $B_X$  is the axial component of the magnetic field and  $B_Y$  is the radial component. To investigate the effect of sinusoidal wave perturbation at the interface, the equation of the interface is chosen to be  $\xi(x, t) = \epsilon e^{i(2\pi/\lambda)(x-ct)} + a$ , where  $\epsilon$  is the wave amplitude,  $\lambda$  is the wavelength, and  $c$  is the wave propagation speed. Small perturbations from the basic flow in the form  $v_{xi} = U_i + v'_{xi}$ ,  $v_{yi} = v'_{yi}$ ,  $p_i = P_i + p'_i$ ,  $v'_{xi} = \frac{\partial \phi_i}{\partial x}$ ,  $v'_{yi} = \frac{\partial \phi_i}{\partial y}$  are assumed, where  $\phi_i$  is the velocity potential for the perturbation to the uniform wavy flows at the interface. Substituting the perturbed expressions into the equations of motion, neglecting second order terms in the perturbed quantities, and making use of the fact that U, P satisfy the flow equations and the current density in Lorentz force term can be represented using Ohm's law, we have the linearized equations governing the motion of disturbance, which yields the Rayleigh's stability equation of

conducting flow in a magnetic field by replacing the perturbed quantities with the equation of motion. The Rayleigh's equation must be solved subject to the boundary conditions. The dynamic boundary condition at interface yields the effect of a magnetic field and the conditions of interfacing flows such as flow velocity and density to the wave velocity and wave number. Without a magnetic field, the quantity  $c$  has an imaginary part that results in the interfacial wave growing exponentially with time. Thus, the interface at the shear layer is unstable. However, the magnetic effects to the wave propagation velocity to reduce the wave amplitude and correspondingly the wavelength increases due to the magnetic field.

Several investigations have suggested that magnetic field suppresses turbulent fluctuations in conducting liquid by stabilizing the flow (Shercliff 1956, Gold 1962, Kozyrev 1981, Bernshtam 1982) and the stabilizing action of the longitudinal component of a magnetic field is considerably weaker than that of the transverse component, where stabilization is judged by an increase in the characteristic wavelength of the flow and  $Re_{cr}$ .

## 2.5.2 Magnetic pressure and tension

Once the jet surface is stabilized and flattened by a magnetic field, the magnetic pressure caused by the Lorentz force is contributing to the hydrodynamic pressure. It gives rise to deflect the jet in directions perpendicular to the magnetic field. Considering that the continuity condition has to be satisfied, the Lorentz force makes the jet shape change elliptically. Therefore, the

contributions of each magnetic pressure components to the isotropic hydrodynamic pressure needs to be investigated.

Lorentz force is  $\mathbf{F} = \mathbf{J} \times \mathbf{B} = \frac{1}{\mu}(\nabla \times \mathbf{B}) \times \mathbf{B} = \frac{1}{\mu}(\mathbf{B} \cdot \nabla)\mathbf{B} - \frac{1}{2\mu}\nabla\mathbf{B}^2$ . Suppose the Maxwell stress tensor  $T_{ij} = \frac{1}{\mu}(B_{ij} - \frac{1}{2}\delta_{ij}B^2)$ , which represents the deviatoric stress tensor of magnetic field. The divergence of the Maxwell stress tensor is represented as follows, which gives the same expression with Lorenz force.

$$\begin{aligned} \nabla \cdot T &= \frac{1}{\mu} \begin{bmatrix} \frac{\partial}{\partial x} & \frac{\partial}{\partial y} & \frac{\partial}{\partial z} \end{bmatrix} \begin{bmatrix} \frac{B_x^2 - B_y^2 - B_z^2}{2} & B_x B_y & B_x B_z \\ B_y B_x & \frac{B_y^2 - B_x^2 - B_z^2}{2} & B_y B_z \\ B_z B_x & B_z B_y & \frac{B_z^2 - B_x^2 - B_y^2}{2} \end{bmatrix} \\ &= \frac{1}{\mu}((\mathbf{B} \cdot \nabla)\mathbf{B} + (\nabla \cdot \mathbf{B})\mathbf{B} - \nabla(\frac{\mathbf{B}^2}{2})) \end{aligned} \quad (2.72)$$

T has units of pressure. The shear is given by the off-diagonal elements of T and the diagonal elements of T correspond to the pressure acting on a differential area element. Total force on a volume is represented as follow.

$$F = \int \int \int_V \nabla \cdot T dV = \oint_S T \cdot dS \quad (2.73)$$

The conservation of momentum in inviscid flow is represented as follow.

$$\begin{aligned} &\frac{d}{dt} \int \int \int_V \rho \mathbf{v} dV + \oint_S \rho \mathbf{v} (\mathbf{v} \cdot \hat{n}) dS \\ &= - \oint_S p \hat{n} dS + \int \int \int_V \rho \mathbf{g} dV + \int \int \int_V \nabla \cdot T dV \end{aligned} \quad (2.74)$$



1504

1505

$$\frac{d\mathbf{v}}{dt} + (\mathbf{v} \cdot \nabla)\mathbf{v} = -\frac{1}{\rho}\nabla p + \mathbf{g} + \frac{1}{\rho}\nabla \cdot T = -\frac{1}{\rho}\nabla \mathbb{P} + \mathbf{g} \quad (2.75)$$

1506

,where

$$\mathbb{P} = \begin{bmatrix} p - \frac{B_x^2 - B_y^2 - B_z^2}{2\mu} & -B_x B_y & -B_x B_z \\ -B_y B_x & p - \frac{B_y^2 - B_x^2 - B_z^2}{2\mu} & -B_y B_z \\ -B_z B_x & -B_z B_y & p - \frac{B_z^2 - B_x^2 - B_y^2}{2\mu} \end{bmatrix} \quad (2.76)$$

1507

1508

1509

1510

1511

1512

Note that the magnetic field increases the pressure by an amount  $\mathbf{B}^2/2\mu$ , in directions perpendicular to the magnetic field and decreases the pressure by the same amount in the parallel direction. Thus, the magnetic field gives rise to a magnetic pressure  $\mathbf{B}^2/2\mu$ , acting perpendicular to field lines, and a magnetic tension  $\mathbf{B}^2/2\mu$ , acting along field lines.

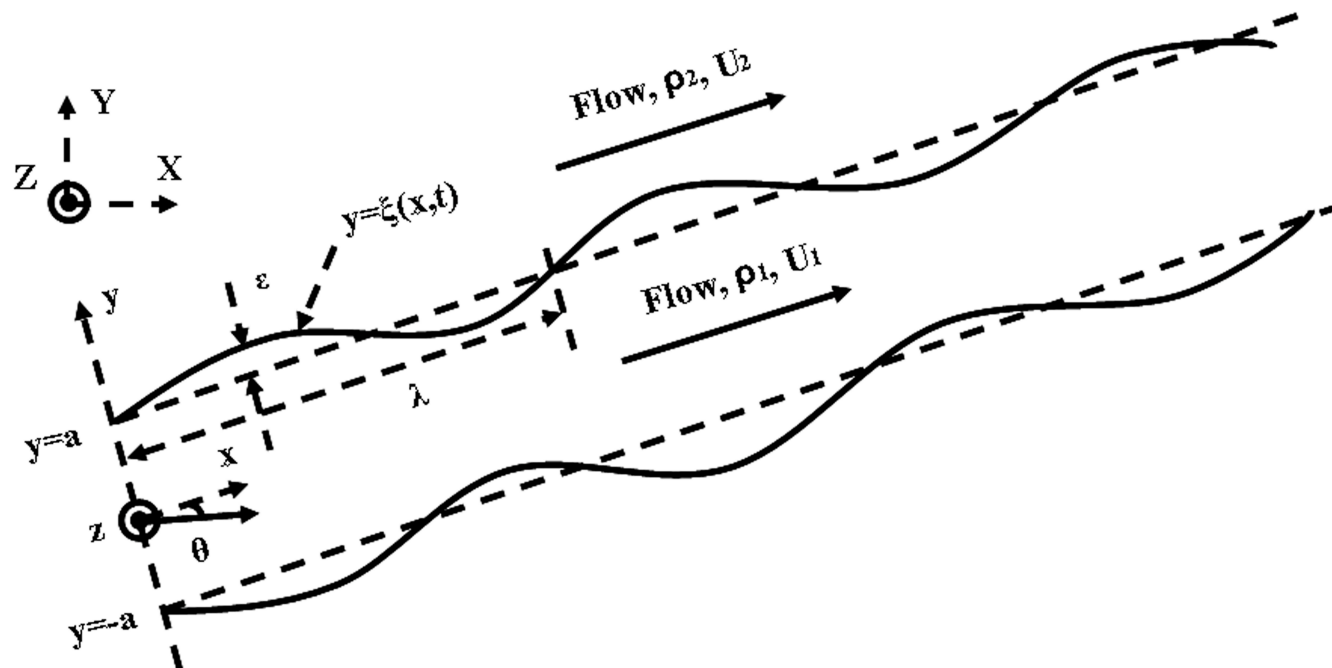


Figure 2.1: Wave-shaped interface separating two different fluids traveling at different average speeds.

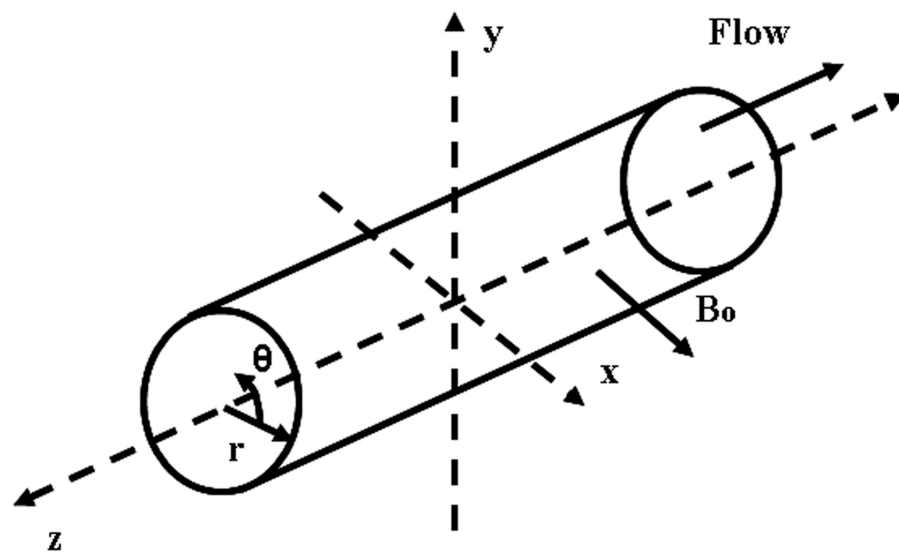


Figure 2.2: Axes and electrodes of circular duct.

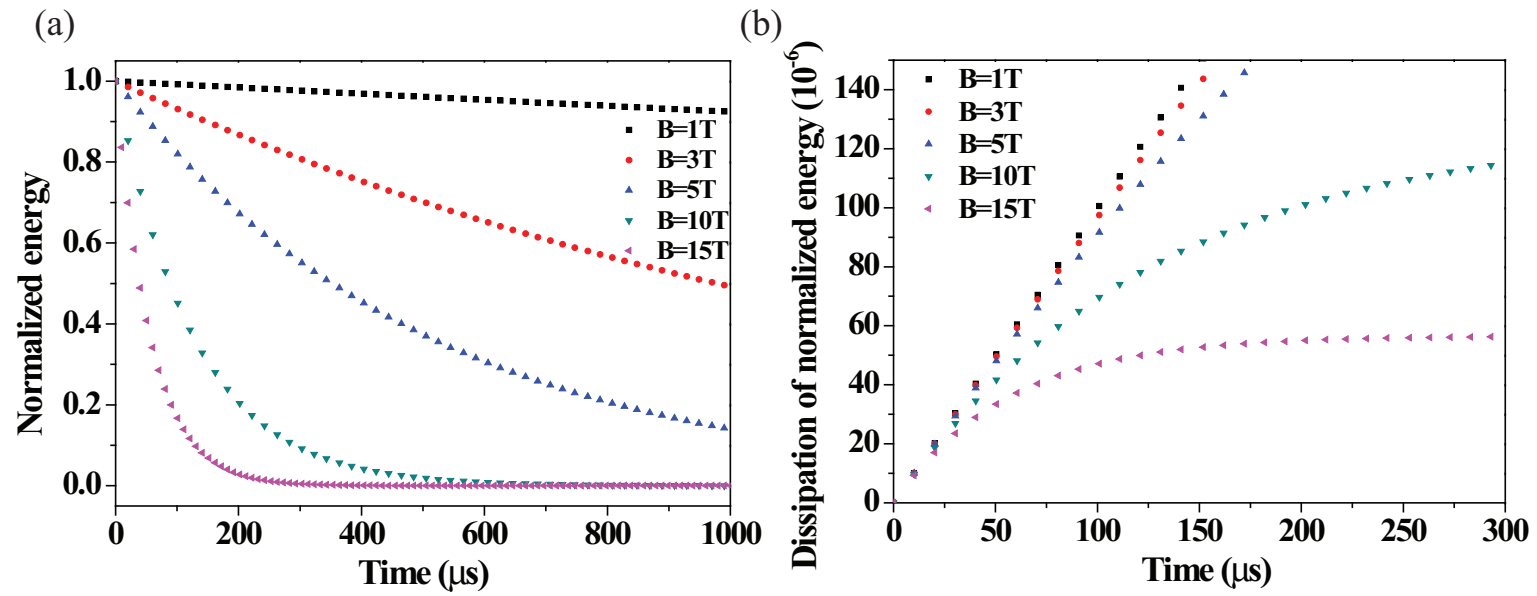


Figure 2.3: Energy decay in magnetic field. a.) Normalized energy decay. b.) Dissipation of normalized energy.

## Chapter 3

# Experimental Method for Investigation of Magnetohydrodynamic Mercury Jet Flow

The optical method is considered to investigate MHD processes. Optical methods have considerable advantages over other measurement techniques: they do not introduce any perturbations into the medium being investigated, they possess high sensitivity and accuracy, their response is practically instantaneous, which enables them to be used to investigate turbulent flows and transition states, since they provide the possibility of visually following the phenomenon being investigated, and they enable one to obtain the physical characteristics for the whole space being investigated at the same instant of time. Unlike other probeless methods, optical methods possess high spatial resolution. All these features enable optical methods to be widely employed in MHD experiments and underlie the need to search for new ways of using modern optical methods which have not yet been employed.

Direct visualization techniques for hydrodynamic examination have often been employed to investigate the dynamics of MHD flows. In this method, one measures the time taken for the particles to traverse a given path. Because no quantitative results can be deduced from direct visualization methods and difficulties often arise when investigating thin boundary layers in liquids, attention has turned to the use of optical techniques for the investigations of fluid dynamics and MHD (Fedin, 1973).

It should be noted that visualization is usually employed for qualitative investigations, but this method can also be used to measure the average flow velocity and a change in the velocity profile. To do this one measures merely the time taken for the particles to traverse a given path or the path traversed in a given time.

## **3.1 Optical Diagnostics as a Principal Diagnostics of High Power Target Experiment**

### **3.1.1 Working principle of shadowgraph for optical diagnostics**

Optical measurements have many advantages over other techniques. The major one is the absence of an instrument probe that could influence the flow field. The light beam can also be considered as essentially inertialess, so that very rapid transient effects can be studied.

Shadowgraph is often employed in studying shock and flame phenomena, in which very large density gradients are present. It integrates the quantity

measured over the length of the light beam. For this reason they are well suited to measurements in two dimensional fields, where there is no index of refraction or density variation in the field along the light beam.

In a shadowgraph system the linear displacement of the perturbed light is measured. Consider the illumination at the exit of the test section. Figure 3.1 shows the displacement of a light beam for shadowgraph. If the illumination is uniform entering the test section, it should still be closely uniform there. The beam is deflected by an angle  $\theta$ , which is a function of  $y$ . The illumination within the region defined by  $\Delta y$  at this position is within the region defined by  $\Delta y_{sc}$  at the screen. If the initial intensity of light is  $I_T$ , then at screen,

$$I_o = \frac{\Delta y}{\Delta y_{sc}} I_T . \quad (3.1)$$

If  $Z_{sc}$  is the distance to the screen, then the contrast is

$$\frac{\Delta I}{I_T} = \frac{I_o - I_T}{I_T} = \frac{\Delta y}{\Delta y_{sc}} - 1 \simeq -z_{sc} \frac{\partial \theta}{\partial y} , \quad (3.2)$$

$$\frac{\Delta I}{I_T} = -\frac{z_{sc}}{n_a} \int \frac{\partial^2 n}{\partial y^2} dz = -\frac{z_{sc}}{n_a} \int \frac{\partial^2 \rho}{\partial y^2} \cdot \frac{\partial n}{\partial \rho} dz , \quad (3.3)$$

where  $n$  is the index of refraction of a homogeneous transparent medium and  $n_a \simeq 1$  for the ambient air.

For gas, Eqn. (3.4) could be substituted into Eqn. (3.3). Equation (3.3) is integrated twice to determine the density distribution. (Goldstein, 1991)

1574

1575 
$$\frac{\partial^2 n}{\partial y^2} = C \left[ -\frac{\rho}{T} \frac{\partial^2 T}{\partial y^2} + \frac{2\rho}{T^2} \left( \frac{\partial T}{\partial y} \right)^2 \right], \quad (3.4)$$

1576 where the constant C, called the Gladstone-Dale constant, is a function of  
1577 the particular gas and T is temperature of medium on Kelvin scale.

1578 Shadowgraph is used principally for qualitative descriptions of a density  
1579 field. Because it yields information on the first and second derivatives of  
1580 density, its application can be found in systems with steep gradients of density  
1581 and temperature, such as flame fronts and shock waves.

1582 Optical techniques are non-invasive and do not cause any perturbation of  
1583 the subject being investigated. Furthermore, their sensitivity increases with  
1584 photon intensity and the resolution of the subject can reach the diffraction-limited  
1585 resolution. The optical response of fluid dynamics and MHD are practically  
1586 instantaneous, enabling the optical technique to study details of turbulent  
1587 flows and transition states. Coupled to a state-of-the art high-speed camera  
1588 and the long interaction path length of a light beam with a field of view  
1589 adjustable to arbitrary dimensions, the optical technique enables one to obtain  
1590 the physical characteristics for the entire subject being investigated in a short  
1591 period of time.

### 1592 3.1.2 Development of optical diagnostic system

1593 An optical diagnostic system is designed and constructed for imaging a free  
1594 mercury jet interacting with a high intensity proton beam in a pulsed high-field  
1595 solenoid magnet. The optical imaging system employs a back-illuminated,



laser shadow photography technique. Object illumination and image capture are transmitted through radiation-hard multi-mode optical fibers and flexible coherent imaging fibers. A retro-reflected illumination design allows the entire passive imaging system to fit inside the bore of the solenoid magnet. A sequence of synchronized short laser light pulses are used to freeze the transient events and the images are recorded by several high speed charge coupled devices.

#### **3.1.2.1 *the optical imaging system and Viewports design***

Laser back-illuminated shadow photography technique is employed in experiment to capture the dynamics of the interaction of the proton beam with a moving free mercury jet. The design of the optical imaging system is based on a few essential criteria which are described below. The entire optical imaging head has to fit inside a small portion of a 1 meter long, 150 mm diameter bore magnet. Figure 3.2 shows the conceptual back illuminated optics design, the installation of 4 Viewports on the primary containment vessel, and the schematic layout of optical components, respectively.

Note that all optics placed inside the interaction beam tunnel are required to be radiation-hard because of high radiation levels in the beam tunnel and the activation of the mercury after proton beam interactions. In our setup, all cameras, lasers, and all other associated electronics are placed in an adjacent beam tunnel controlled locally by several desktop computers. Remote control of the entire system is achieved through designated control desktops located in the control room via MS Window XP remote desktop connections from the

1619 ethernet network (see Fig. 3.7).

1620 A Viewport is located at the beam interaction center and two additional  
1621 Viewports are located at  $\pm 152.4$  mm up/down stream locations. Viewport 4  
1622 is positioned at  $+457.2$  mm and is designed to capture the residual dynamics of  
1623 the proton interaction. Because of limited space inside the magnet bore, object  
1624 illumination and image capture are transmitted through multi-mode optical  
1625 fibers and coherent imaging fibers, respectively, all positioned on one side  
1626 exterior to the primary containment vessel. Figure 3.3 shows the fabricated  
1627 and assembled optical head containing the integration of ball lens, imaging  
1628 lens, illumination fiber, and imaging fiber.

1629 The arrangement resembles a compact endoscope design but with a different  
1630 illumination scheme. Illumination light pulses are coupled into a 15 meter  
1631 long multi-mode fiber (ThorLabs BFL22-200). It has a numerical aperture of  
1632 0.22,  $25^\circ$  cone angle, with a core diameter of  $200\ \mu\text{m}$  that matches that of the  
1633 fiber-coupled lasers. To provide a  $\sim 55$  mm illumination area at the center  
1634 of the primary containment vessel over a limited short working distance of  $<$   
1635 100 mm, the illumination cone angle has to be opened up to a  $43^\circ$  full cone  
1636 angle. This is achieved by placing a tiny  $\sim 0.5$  mm diameter sapphire ball lens  
1637 (Edmund Optics M46-117) at the tip of the illumination fiber and secured  
1638 by a thin stainless steel plate. At the heart of the illumination arrangement  
1639 is a 76 mm diameter Au-coated concave spherical retro-reflector that has a  
1640 short radius of curvature of 124 mm (Rainbow Research Optics). When the  
1641 much diverged illumination fiber is placed at the radius of curvature and

shined onto the optical axis of the reflector, a retro-reflected beam returns back to the illumination fiber providing the back-illumination scheme. Again, because of the tight environment inside the primary, a Au-coated 90° prism mirror turns the optical path from longitudinal to transverse onto the center of the primary. Two anti-reflection coated sapphire windows (Swiss Jewel Company) are mounted on the primary with airtight seals tested up to 1.4 bar pressure. The diameter and the thickness of the window is 100 mm and 6 mm respectively, sufficiently large enough for the observation of a 1 cm diameter jet and mechanically strong enough to withstand the momentum of a direct impact from mercury jet with a mean velocity of 20 m/s (Simos, 2005). Based on this optical arrangement, a mercury jet in front of the reflector naturally makes a shadow on the retro-reflected beam. The shadow is collected by a 1 mm diameter AR-coated cylindrical grin objective lens (GrinTech, GT-IFRL-100-inf-50-CC) which has an optical path length of 2.43 mm. The grin lens is coupled onto a coherent image fiber. This flexible coherent imaging fiber is the key optical element of the imaging system. It is a 10 meter long Sumitomo IGN-08/30 fiber with 30,000 picture elements (pixels). Each individual fiber has a core diameter of  $\sim 4 \mu\text{m}$  with a total fiber diameter of merely 0.96 mm including coating. It has a bending radius of 40 mm, sufficiently small to allow curving and arching inside the primary containment vessel. All imaging fiber ends are hand polished in-house to optical finished quality to allow high quality images with maximum light intensity transmission. Figure 3.4 shows the final finished end of an imaging fiber after polishing with

0.3  $\mu\text{m}$  lapping film (ThorLabs, LFG03P). The surface quality and the flatness of the imaging fibers are inspected under a microscope. The imaging fibers are jacketed in-house with reinforced furcation tubing (ThorLab FT030-BK). One end of the imaging fiber is finished with an SMA 905 fiber-optics connector to facilitate coupling to a CCD camera. The other ends of the illumination and imaging fibers are positioned next to each other with  $\sim 2$  mm separation inserted inside a specially fabricated plastic ferrule. The integrated optical head is shown in Fig. 3.3, where a red laser diode is used to illuminate the optical head. The integrated all-in-one ferrule (ball lens, illumination fiber, objective lens, and imaging fiber bundle) is placed at the radius of curvature as well as on the optical axis of the reflector so that it allows both the illumination and the imaging collection to work on one side of the primary. The liquid mercury target is enclosed in a stainless steel primary containment vessel which is placed in the primary beam tunnel (TT2A). A total of four optical imaging heads for each Viewport are mounted on the exterior of the primary, designated as channels 1 to 4. All fibers are routed through a  $\sim 150$  mm diameter, 2 meter long concrete passage to an adjacent beam tunnel (TT2), where radiation is much reduced. All electronics control for the optical diagnostic as well as all other electronics control for the solenoid magnet operation and hydraulic power unit used to generate the mercury jet are also placed in the adjacent tunnel. The exit end of each imaging fiber is coupled to an SMA fiber adaptor (ThorLabs SM1SMA) mounted on an x-y translator (ThorLab LM1XY). Four  $40\times$  infinitely corrected microscope objective (Newport M-40x) relay the  $\sim$

1688 0.96 mm image outputs of each imaging fiber onto each corresponding CCD  
1689 with appropriate lens tubes to fully expand the images onto a typical 10  
1690  $\times$  10 mm CCD array. A non-rotating adjustable lens tube zoom housing  
1691 (ThorLabs SM1ZM) provides fine and accurate adjustment of image focus on  
1692 CCD.

1693 **3.1.2.2 *the consideration for focusing and tilting alignment of***  
1694 ***optics***

1695 A retro-reflective mirror captures the output beam of the laser diode and  
1696 focuses it through the field of view at the target onto the lens of the telescope.  
1697 The CCD camera views the target through the telescope. Tilting alignment by  
1698 using fine adjustments on the side of the retro-reflecting mirror can be made  
1699 and the field of view can be adjusted by moving the imaging lens forwards or  
1700 backwards. The system is designed to make 6 possible alignment adjustments.  
1701 After the retro-reflecting mirror is moved forward or backward, the field of  
1702 view can also be adjusted. The maximum field of view that we can obtain is  
1703  $\sim 5.0$  cm diagonally. The distance  $d$  from the objective lens to the imaging  
1704 lens is related to the field of view at the target. For target to be in focus, one  
1705 must obey the lens formula,

1706  
1707 
$$\frac{1}{f} = \frac{1}{c} + \frac{1}{d}, \quad (3.5)$$

1708 where  $c$  is the distance from the target to the objective lens and  $d$  is the  
1709 distance from the objective lens to the camera.

### 3.1.2.3 *high speed cameras and light sources*

Table 3.1 gives the specifications of high speed cameras in terms of some selected attributes. Two FastVision cameras with CCD size of  $15.4 \times 12.3$  mm run with a full  $1280 \times 1000$  pixel resolution at a 0.5 kHz frame rate. One Olympus Encore PCI 8000S camera with 1/3 inch CCD size runs with a  $480 \times 420$  pixel resolution at a 4 kHz recording rate. A high speed "Silica Mountain Devices (SMD)" 64KIM camera with a CCD size of  $13.4 \times 13.4$  mm runs with a reduced single frame size of  $(960 \times 960)/4$  pixel resolution at up to 1 MHz frame rate. For the three slower cameras, images collected by each individual imaging fiber overfill the CCD pixels by a factor of  $\sim 6$  and  $\sim 3$ , respectively, i.e. one fiber projected onto  $6 \times 6$  and  $3 \times 3$  CCD pixel area, respectively. However, for the SMD camera, each imaging fiber slightly underfills the CCD pixels by a factor of 0.83, i.e. one fiber projected onto nearly a single CCD pixel area. Due to the nature of spatial superposition, an array of imaging fibers imaged by an array of CCD pixels, some images might compose of a honeycomb pattern caused by this pixelation artifact. However, the artifact can be minimized by slightly defocusing the image on the CCD. However, the FastVision and Olympus CCDs are capable of recording at a frame rate higher than 500 Hz, the architecture for binning at reduced resolution requires a change of the zoom ratio on the image head doom. The SMD camera has a different but fixed binning architecture so that the full field of view is taken at a high speed frame rate with reduced resolution. Except for the SMD camera where images are frozen by the short 150 ns illumination laser pulses, all other

1733 images are arrested by the short adjustable electronic exposure time of  $10 \sim$   
 1734  $50 \mu\text{s}$  set on the CCDs.  
 1735 Synchronized short laser light pulses are used to illuminate the target and  
 1736 freeze the motion of the jet after the impact of the proton beam. For SMD  
 1737 camera, the mask reduces the photosensitive area to 0.03 of the nominal pixel  
 1738 area. The quantum efficiency of the photo-resistive area is 0.18 at 800 nm,  
 1739 and the pixel fill is 200000 electrons. Therefore, a full exposure of a frame of  
 1740 the CCD therefore requires  $(960)^2 \times 200000 / 0.03 / 0.18 \approx 3.4 \times 10^{13}$  photons  
 1741 or 10 Watts for 800 nm photons. For FastVision camera, the sensor is  $1280$   
 1742  $\times 1024$  pixel (1.03 megapixel) of CCD of total area  $15.36 \times 12.29 \text{ mm}^2$  in 8  
 1743 bits at 500 frames per second (10 bits at 400 frames per second). Maximum  
 1744 frame rate is 500,000 at  $1 \times 1280$ . The mask reduces the photosensitive  
 1745 area to 0.4 of the nominal pixel area. Based on the estimation of required  
 1746 photons, a full exposure of a frame of the CCD therefore requires  $1280 \times 1024$   
 1747  $\times 200000 / 0.4 / 0.18 \approx 3 \times 10^{12}$  photons or 1 Watts for 800 nm photons.  
 1748 Optical light pulses are sent through 15 meters of multi-mode illumination  
 1749 fibers. The light sources used in the experiment are all Class 4 lasers, emitting  
 1750 at wavelengths of 808 to 850 nm. Three lasers are capable of emitting a  
 1751 peak optical power of 1 Watt (JDS Uniphase SDL-2300-L2) driven by three  
 1752 independent current drivers (ThorLabs LDC220C). These 1 Watt lasers can be  
 1753 operated from CW to a minimum programmable pulse width of  $1 \mu\text{s}$  limited by  
 1754 the trigger logic pulse. The 4<sup>th</sup> laser emits at a peak optical power of 25 Watt  
 1755 (Bright Solution BDL20-808-F6) limited by the pulsed current driver (Avtech

AXOZ-A1A-B). It provides a current pulse of 150 ns and is capable of running at the maximum 1 MHz repetition rate, i.e. a frame rate of 1  $\mu$ s/frame.

The complete transmission of the imaging system is  $\sim 0.2$  per Viewport channel, including 0.85 for the 15 meter long illumination fiber, 0.86 for the sapphire ball lens, 0.86 for each pass of the sapphire Viewport, 0.91 for the retro-reflector, 0.67 for the 10 meter long imaging fiber, and 0.86 for the grin lens and the relay lens. For the SMD camera, the imaging circle filled  $\pi/4$  of the CCD array. A measured output energy of 3.5  $\mu$ J/pulse is obtained from the Bright Solution (BDL20-808-F6) laser illumination light source for Viewport 2. Therefore the calculated number of photons impinging on the SMD camera reaches  $4.2 \times 10^6$  photons/pixel. After taking into account the 18% quantum efficiency of the CCD,  $7.5 \times 10^5$  photoelectrons are generated at the full illumination intensity. Since the SMD camera has full well capacity of  $2.2 \times 10^5 e^-$ , there is a factor of  $\sim 3$  on the optical power budget reserved for unanticipated optical power loss and for overcoming the possible attenuation due to ionization radiation. Similar calculations for Viewport channels 1 and 3 give a factor of  $\sim 10$  on the optical power budget. This larger factor is mostly due to the long, 10  $\mu$ s, exposure time set on the FastVision cameras. Overall, the imaging system is designed to have sufficient optical power budget for the illumination of each Viewport throughout the entire experiment.



#### 3.1.2.4 *radiation-hardness*

Because of the high radiation level in the beam tunnel and the activation of the mercury after the proton beam interactions, all optics placed inside the interaction beam tunnel are required to be radiation-hard. One complete set of optics was selected for radiation resistance test done at CERN. This complete set of optics included an Au-coated reflector, sapphire window, illumination fiber, imaging fiber, and Grin objective lens. The experiment has anticipated a total of 200 proton pulses at 14 and 24 GeV with a total of  $\sim 3 \times 10^{15}$  protons. The calculated total radiation reaches  $\sim 1$  Mrad equivalent radiation dose. Therefore, all optics except the grin objective lens were irradiated at CERN to a lower energy 1.4 GeV proton beam but up to an equivalent radiation dose of  $5 \times 10^{15}$  protons. Because we missed an opportunity to deliver the grin lens to the CERN irradiation facility, the grin objective lens was instead irradiated at BNL using a Co-60 source up to a total dose of  $\sim 3$  Mrad. The reflectance of the Au-coated reflector and the transmittance of all other optics are measured at the wavelength of 830 nm before and after irradiation. Table 3.2 shows the effects of irradiation up to an equivalent radiation dose of 1 Mrad on the reflectance and transmittance of the components of the optical diagnostic system. No noticeable change in the reflectance was observed on the Au-coated reflector even though the substrate of the reflector has turned nearly opaque. The sapphire, 5 meter long of illumination fiber, and 0.3 meter long of imaging fiber do not show any additional insertion loss. They are all radiation hard up to a 1 Mrad dose. However, the small grin objective lens did suffer

radiation damage resulting in a 0.73 transmission. This tiny grin objective lens is made of silver-ion exchanged index modification internal to a glass substrate. Therefore it was not anticipated to have a high radiation resistance. However, it is well known that although glass (and silica fibers) lose its transmission in the visible wavelengths, near infrared (NIR) light can still has adequate light throughput for some applications (Kakuta, 1999). This is one of the reason we select NIR rather than visible laser light for back-illumination of the mercury jet. Since the back-illuminated NIR light passes the grin objective only once, the 0.27 transmission loss over the entire experiment is tolerable and can be recovered with the present designed laser capability. We should note that the integrity of the imaging properties of the grin lens was unchanged, i.e. no image distortion was observed after the 1 Mrad radiation resistance test.

### **3.1.2.5 *scintillating fiber channel***

A jacketed 2 meter long 1 mm diameter blue emitting scintillating fiber is attached along with the imaging head to register gamma emission during the proton beam and mercury jet interaction. A 12 meter long 1 mm diameter fiber patch-cord (ThorLabs BFH37-1000) carries the blue scintillated light signal and is fiber-coupled to an Avalanche photodiode (ThorLabs APD210), designated as channel 0. The overall transmission at the center wavelength of 480 nm of the fiber patch-cord is measured to be 0.77. The scintillating signal trace is displayed on an oscilloscope and data can be retrieved remotely from the control room. This scintillating signal serves to confirm the arrival of the

proton beam and has the potential to extract the proton intensity from the scintillating signal pulse level.

### 3.1.3 Schematic of electronic trigger and high speed camera control

Because we are using several high speed cameras from different vendors, we must use separate camera control software for each camera. The limitation on their exposure time also requires two different set of illumination laser pulse trains. A master trigger pulse, synchronized to the arrival of the proton bunch, is delivered to trigger the mercury loop system, the solenoid magnet system, and the optical diagnostic system together. The mercury jet reaches its steady state for 1 second when the solenoid magnet reaches the highest magnetic induction field of 15 T. However, there is a significantly long time lag of  $\sim 10$  seconds for the solenoid system to power up to its full capacity. Therefore, the master trigger signal is first sent to a digital delay generator (Stanford Research DG535) to provide a sufficient long delay to synchronize with all other electronic components. These relative and absolute delays are measured by an oscilloscope. By adjusting each independent delay channel, complete synchronization of all cameras with the pulsing of the laser light sources can be achieved and verified by comparing the bright/dark image intensities of each frame of each CCD.

Figure 3.5 shows the two sets of pulse sequences used to simultaneously trigger all cameras. The 25W infrared laser consisted of a 17 pulse sequence

with a pulse width of 150 ns. This determines the exposure time of the SMD camera on the Viewport 2. The laser pulse period is set to match the frame rate of the images. The SMD camera collects 16 frames of image. Figure 3.6 shows the traced signals on an oscilloscope when the beam and the beam triggering are delivered. After the master trigger from the synchrotron is delivered at time  $t = 0$ , the proton beam comes in  $\sim 3 \mu\text{s}$ . The photodiode response from scintillating fiber has a 20 ns rise time and the level indicates the beam intensity and beam position. The scintillating fiber signal gives the beam arrival time. Therefore, it is possible to set the trigger timing for the cameras and laser driver inputs, which is  $\sim 2 \mu\text{s}$  after the master trigger from the proton synchrotron.

Three 1 Watt lasers pulsed to a 0.5 second duration are used to independently illuminate Viewport 1, Viewport 3, and Viewport 4, respectively. Typically the FastVision and Olympus cameras continuously collect 220 frames of images. The exposure times on the cameras are set at  $10 \sim 50 \mu\text{s}$  respectively to give a sharp image quality. Although the sharpness of images increases with reduced exposure time, much more light is required for illumination. Therefore, a trade off between exposure time and laser intensity is made. On the contrary, the exposure time for SMD camera is determined by the laser pulse width. As the pulse width of the laser decreases, the laser intensity also decreases. In order to utilize the maximum allowable intensity of the 25 W laser, the maximum pulse width of  $0.15 \mu\text{s}$  is used. This pulse width should not seriously jeopardize the image quality even running at its highest frame rate of  $1 \mu\text{s}/\text{frame}$ . A

schematic diagram linking all cameras, triggering electronics, and controlling computers is shown in Fig. 3.7. 2 desktops reside in the control room to master the optical diagnostics system. All other electronics and desktops are placed in the TT2 tunnel adjacent to the interaction beam tunnel TT2A.

## **3.2 Windows Consideration as Viewports for Observation**

The mercury jet target is observed through four windows. These windows must contain any possible spray of mercury due to intense beam energy deposition, and remain transparent after a radiation dose from the interaction of beam and mercury.

### **3.2.1 Fiducial mark on windows**

We put fiducial mark on each sapphire window to use the magnitude of the referenced length. The size of fiducial on the back and front windows is varying on images according to the changing field of view. i.e, the back fiducial looks smaller than the front fiducial. Figure 3.8 shows the artificially marked fiducial on the sapphire window. It gives referencing length scale when we measure the size of jet, velocity, rotation of windows, and the location of magnetic axis on images.

### 3.2.2 Impact resistance test

We used sapphire windows to obtain enough strength and did surface coating on both sides for anti-reflection at 800 nm wavelength. In order to check the survival from mercury droplet impact, we tested sapphire window using a paint ball gun. A paint ball is a 2.7 gram sphere of radius 8.6 mm containing a colored gel that readily “splats” on impact. The velocity of a paint ball was 95 m/s. The ratio of the force from a paint ball to that due to the dispersal of the entire mercury jet by the proton beam is

$$\frac{F_{\text{paintball}}}{F_{\text{mercury}}} = \frac{m_{\text{paintball}} v_{\text{paintball}}^2 r_{\text{mercury}}}{m_{\text{mercury}} v_{\text{mercury}}^2 r_{\text{paintball}}} . \quad (3.6)$$

The momentum of the paint ball is the same as that of a 7 mm diameter mercury drop at 95 m/s. The sapphire window survived in the test.

### 3.2.3 Pressure leaking test of sapphire windows

The primary containment is mostly welded and the window ports are sealed with rubber gaskets (BUNA-N). Each window is sealed with two sheets of rubber gaskets per port. 21 psi is loaded inside the primary containment to check the sealing of the primary containment. To locate leaks, a Metheson 8850 flammable gas sniffer, which has a 5 ppm sensitivity, and Ar/Methane (90 % / 10 % ) was used. All of 8 windows survived the 21 psi pressure for over 17 hours.

### **3.3 Integrated Experimental Setup for High Power Target**

#### **3.3.1 Mercury loop system in solenoid magnet**

The cross-section and actual equipment for the mercury system with high field solenoid magnet is shown in Fig. 1.5. The horizontal line in Fig. 1.5(a) represents the proton beam. The Hg jet, which is ejected from right to left in Fig. 1.5(a), co-propagates with the proton beam. Four Viewports are shown within the solenoid bore, which represent viewing locations for observation of the Hg jet within its primary containment vessel (see Fig. 1.3). Viewport 2 is positioned at the center of the solenoid and is the location where the center of the proton beam interacts with the Hg jet. The pulsed solenoid incorporates a magnetic field ramp up of 10 seconds and is capable of sustaining its peak field for a duration of approximately 1 second. The magnetic axis is positioned at an angle of 67 milliradian with respect to the proton beam, with the tilt provided by a common baseplate supporting all the equipment (see Fig. 1.5(a)). The applied magnetic induction field has been measured with a gaussmeter placed both perpendicular and parallel to the magnetic induction field. The relationship between the measured magnetic induction field and the applied solenoid current was mapped to deduce the maximum magnetic induction field at the center of the solenoid.

### 3.3.1.1 *the considerations in nozzle design*

Better yields of low energy pions are obtained from the mercury jet target when the proton beam and target are tilted with respect to the axis of the capture solenoid magnet. Monte Carlo simulations have indicated that a tilt angle of about 100 milliradian between the mercury jet and the proton beam is optimal (Mokhov, 2000). However, jet motion in a magnetic induction field behaves differently, depending on the angle between the axis of the magnet and that of the jet, as a result of the differences in the magnitude of the components of the magnetic induction field (Samulyak, 2006). As the crossing angle increases, the transverse component of the magnetic induction field increases, but with no significant change in the longitudinal component. The increase in the transverse component of the magnetic field raises the induced current on the Hg jet. Therefore, the angle of the Hg jet is launched at 33 milliradian with respect to the axis of the magnet, resulting in an interaction region about 30 cm long in case of a 1 cm diameter mercury jet with a 1.5 mm RMS diameter of proton beam. Since the proton beam in TT2A beamline at CERN is horizontal, the mercury jet should make a 34 milliradian angle with respect to the proton beam axis, and the magnetic axis should make an angle of 67 milliradian with respect to the proton beam. The mercury will flow from the upstream end of the magnet to the downstream end of the magnet. The jet velocity is designed to be 20 m/s and the center of the jet to intersect the center of the proton beam at center of magnet.



### 1946      **3.3.2    Water jet observation for nozzle performance test**

1947            Prior to mercury injection in the primary at Oak Ridge National Laboratory(ORNL),  
1948    extensive optical diagnostics were carried out by pulsing water jets in the  
1949    system using 4 different types of nozzle configurations. One nozzle showed  
1950    the most stable shape of jet motion with fairly uniform velocity,  $\sim 10$  mm  
1951    diameter and 20 m/s respectively.

1952    Due to the spray and wetting of water on the interior of windows, only  
1953    ambiguous shadow of the water jet was observed. A clear surface motion  
1954    is required in order to obtain accurate velocity measurement. Therefore, only  
1955    qualitative diagnostics was made on the water jet. The field of view of each  
1956    Viewport is  $\sim 50$  mm. The diameter of the jet is measured by overlaying a  
1957    grid of referenced field of view onto the images. The time lapse of each frame  
1958    is read from the camera frame rates. The trajectory of the jet between several  
1959    frames can then be measured and the velocity of the jet surface motion is  
1960    estimated.

1961    These measurements of the water jet tests were done at ORNL. The observations  
1962    led us to select the design of the final nozzle for the subsequent jet runs. It  
1963    was fabricated from Titanium and the assembly was anodized for electrical  
1964    insulation.

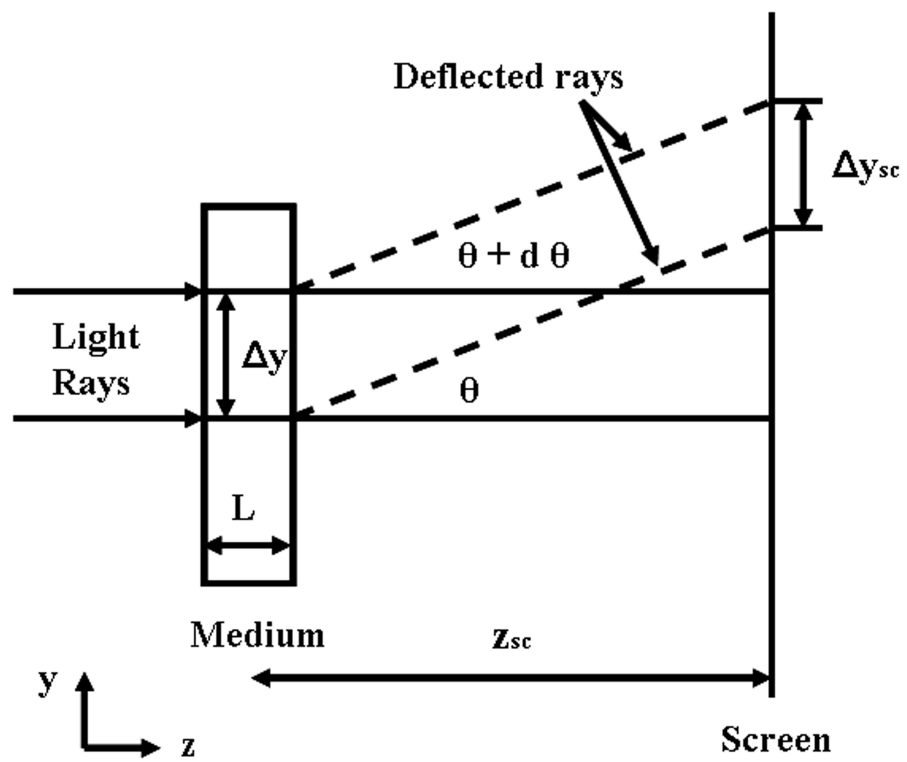


Figure 3.1: Displacement of light beam for shadowgraph.

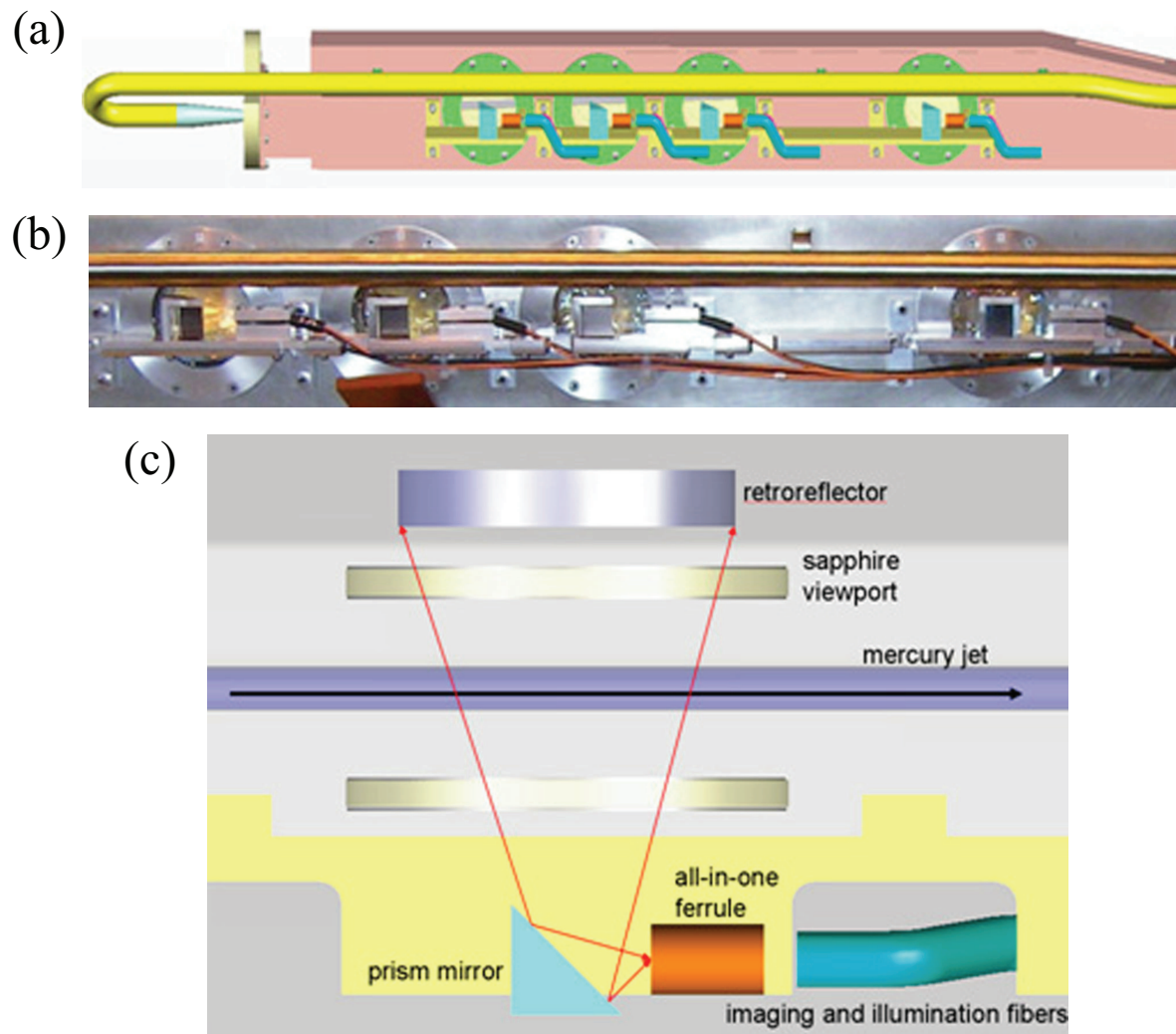


Figure 3.2: Design of optical layout and installation of 4 Viewports of primary containment vessel. a.) Conceptual integration of optics to primary containment vessel. b.) Photograph of installation of optics to primary containment vessel. c.) Schematic layout of optical components.

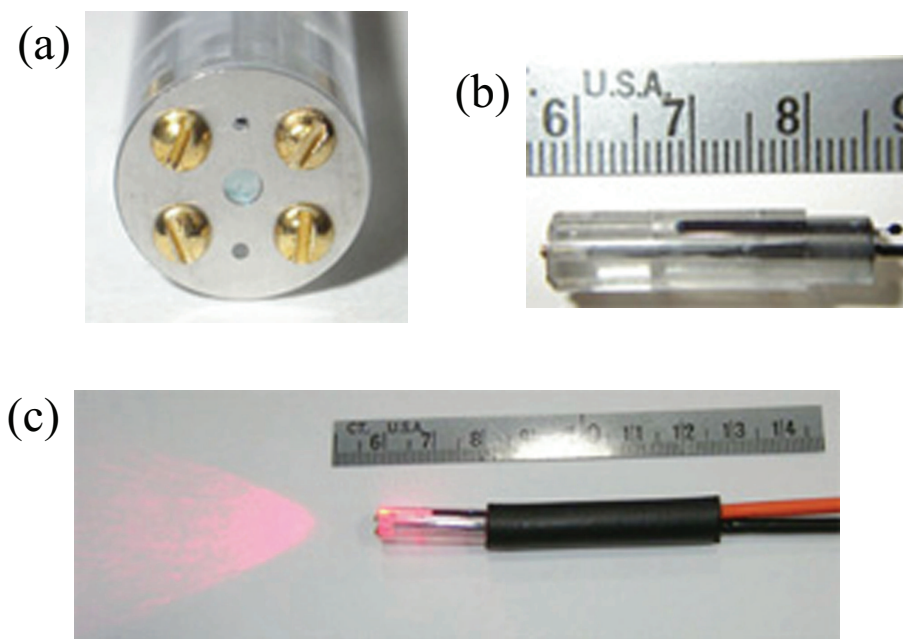


Figure 3.3: Photograph of optical head assembly and its illumination of laser. a.) Front view of optical head assembly. b.) Side view of optical head assembly. c.) Illumination of fiber-optics head assembly.

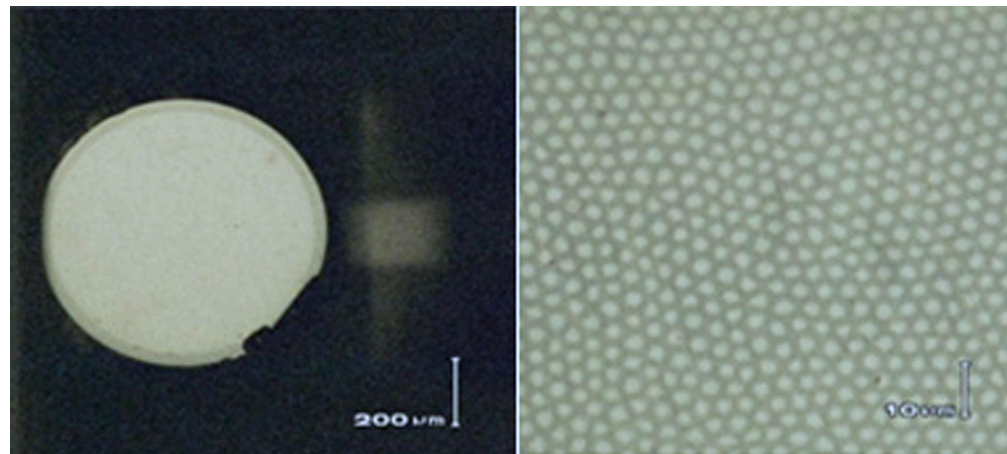


Figure 3.4: Polished fiber end, 50 X and 800 X magnifications, respectively

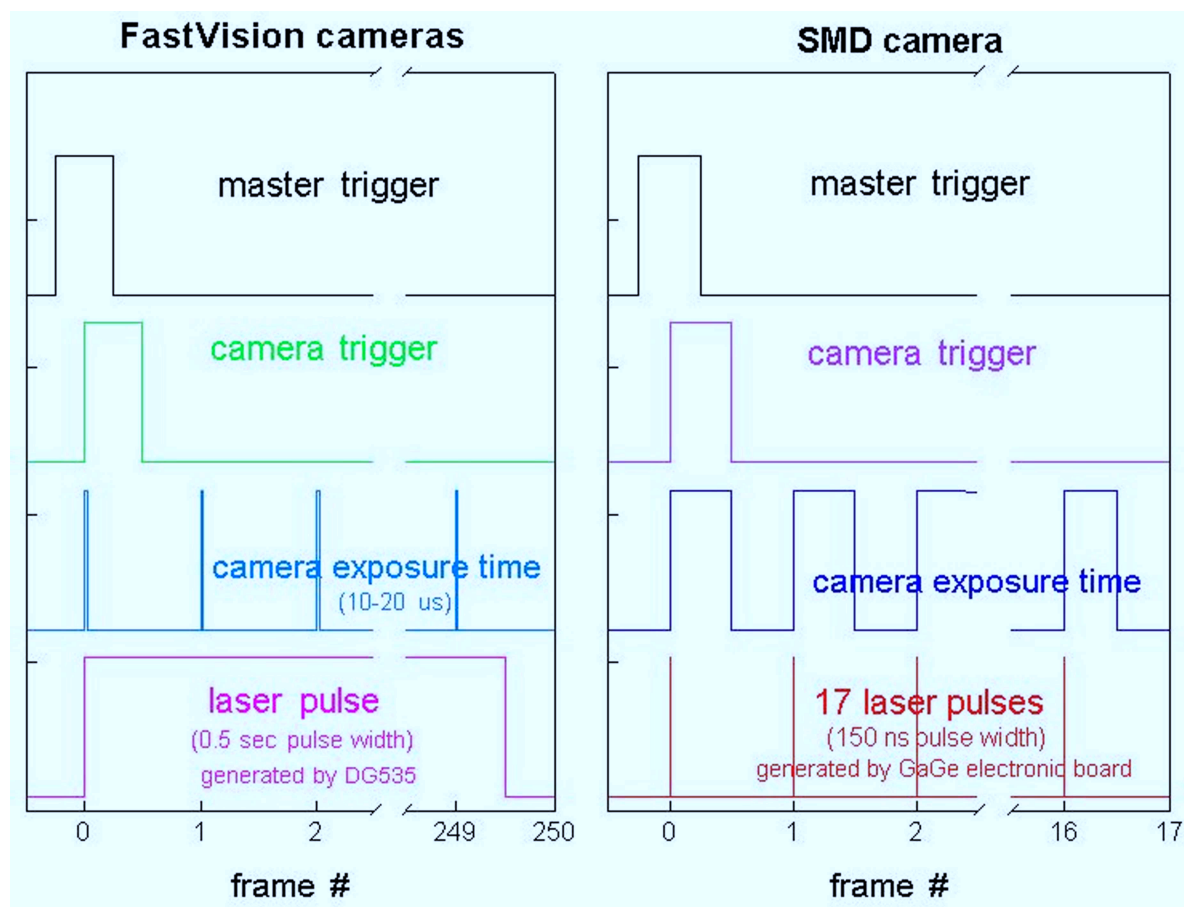


Figure 3.5: Schematic of synchronized signal of high speed camera and laser pulse.

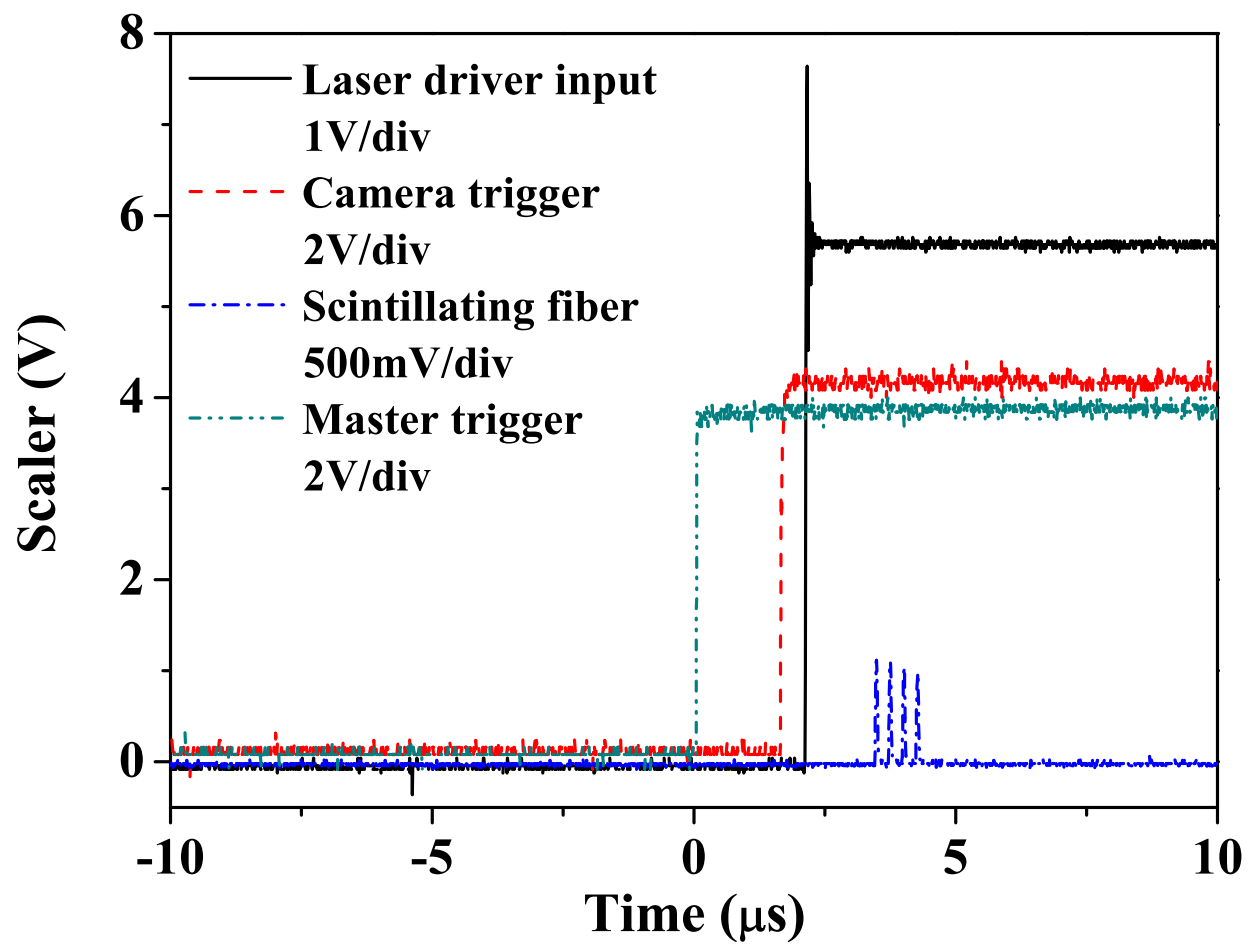


Figure 3.6: The triggering time for high speed camera upon beam arrival.

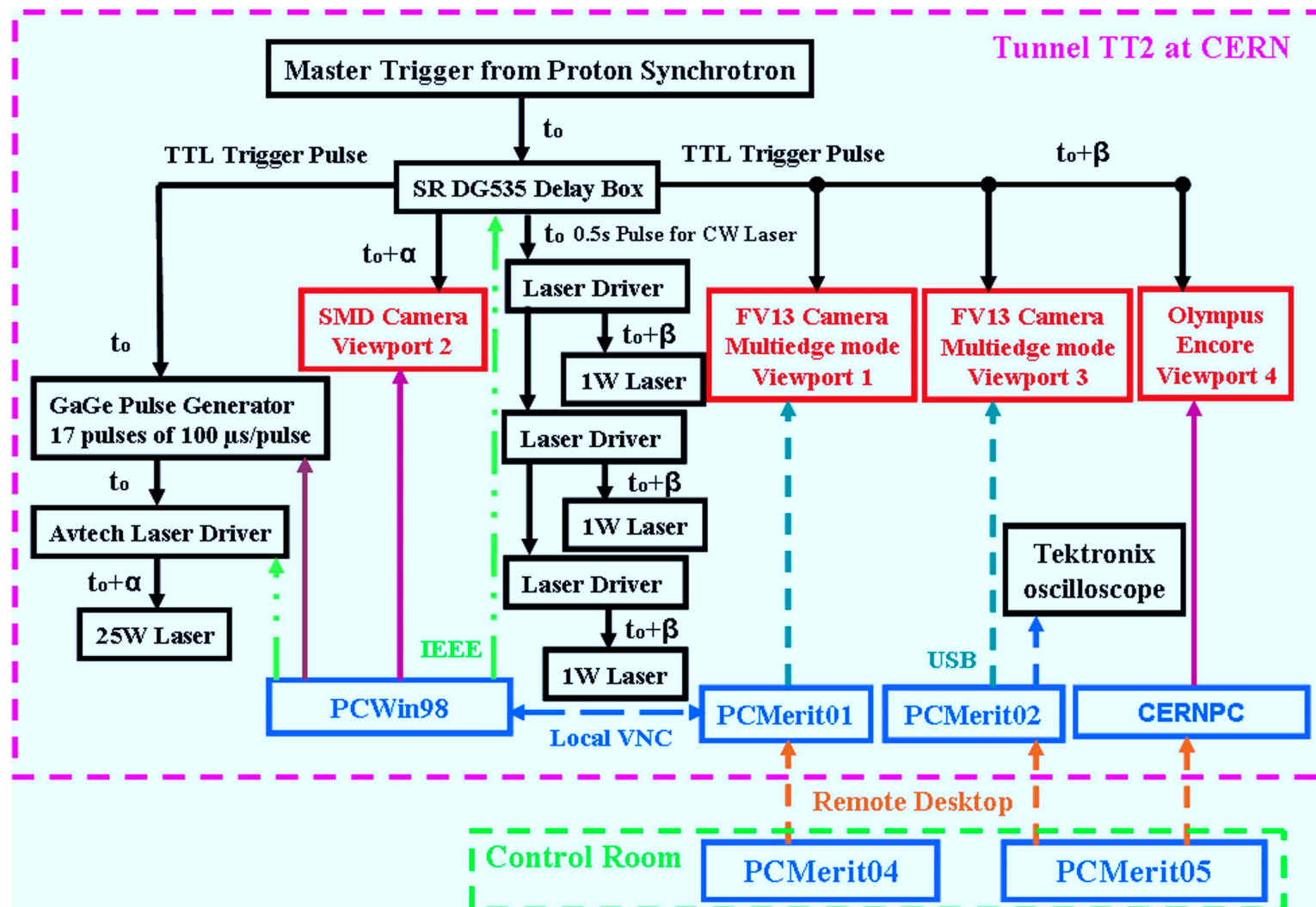


Figure 3.7: Schematic of electrical triggering and high speed camera control in tunnel for experiment.



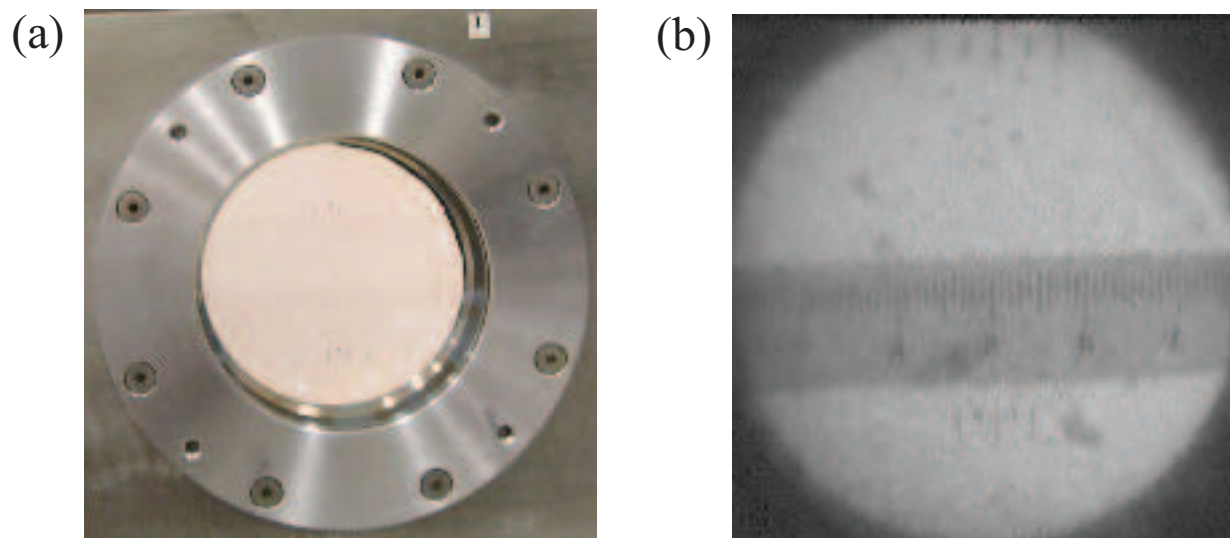


Figure 3.8: Top fiducial on the front window and bottom fiducial on the rear window. a.) Photo of fiducial on the sapphire window assembled in Viewport. b.) Image of fiducial captured by camera.

Table 3.1: Specifications of high speed cameras.

Attributes	SMD 64KIM	FastVision	Olympus Encore PCI 8000S
CCD chip size	13.4 mm $\times$ 13.4 mm	15.4 mm $\times$ 12.3 mm	1/3 inch
Pixels	960 $\times$ 960	1280 $\times$ 1024	480 $\times$ 420
Pixel size	14 $\mu$ m	12 $\mu$ m	13 $\mu$ m
Single frame	240 $\times$ 240	1280 $\times$ 1000	480 $\times$ 420
Maximum frame rate	1 MHz <sup>1</sup>	0.5 kHz <sup>2</sup>	4 kHz <sup>3</sup>
Full well Capacity	220,000 $e^-$	$\sim$ 1000 LSB/lux-sec	-
ADC	12 bit	8 bit	8 bit

---

<sup>1</sup> 16 frames.

<sup>2</sup> at full resolution.

<sup>3</sup> 12.5  $\mu$ s electronic shutter, with reduced frame size.

Table 3.2: Effects of irradiation up to an equivalent radiation dose of 1 Mrad on the reflectance and transmittance of the components of the optical diagnostic system. Reflectance is inferred on the Au-coated mirror and transmittance is inferred on all other components.

Optical component	Before radiation	After radiation	% difference
Large Au-coated mirror	0.91	0.92	no change
Sapphire window(1 mm)	0.86	0.87	no change
Illumination fiber(5 m)	1	1.02	no change
Imaging fiber (30 cm)	0.67	0.71	no change
Grin lens	0.90	0.66	73 %

## 1965 Chapter 4

# 1966 Experimental Investigation of 1967 Mercury Jet Flow in Magnetic 1968 Fields

1969

1970 In this chapter, the jet behavior in magnetic field are investigated. To  
1971 do this, the collected images are read digitally and the characteristic jet  
1972 parameters are evaluated based on the probability approach. It effectively  
1973 diagnoses the jet condition on each collected image. Jet deformation such  
1974 as the free jet surface deformation and surface stabilization is investigated by  
1975 measuring the pixels on the collected images based on 2-D shadow photography.  
1976 As a result, we will discuss the magnetic field effect to the dynamic behavior of  
1977 freely moving jet in a solenoid magnetic field. The driving pressure of mercury  
1978 flow entering inlet pipe is measured to monitor the effect of the magnetic field  
1979 and assure if the input condition for driving the jet is affected. In order to  
1980 diagnose the flow rate, the flow velocity in magnetic field is discussed and the  
1981 deflection of jet size in various magnetic field is investigated. Based on the  
1982 observed flow rate of jet, the shape of jet is suggested for the energy deposition

1983 calculation by proton beam interaction with Hg jet target.

## 1984 4.1 Image Analysis for Data Reduction

### 1985 4.1.1 Image acquisition

1986  $\sim 360$  complete integrated tests (i.e., with magnet, proton beam, Hg loop  
1987 system, and optical diagnostic system) were conducted at CERN (European  
1988 Organization for Nuclear Research) with various values of the proton beam  
1989 structure (8 harmonic and 16 hamonic) and the beam intensity up to  $30 \times 10^{12}$   
1990 protons and the beam energy (14 Gev and 24 GeV) and the the magnetic field  
1991 (0 T, 5 T, 7 T, 10 T, and 15 T) and two Hg jet velocities (15 m/s and 20 m/s).  
1992 Figure 4.3 and 4.4 are representative optical diagnostic results collected by  
1993 the 3 cameras, with and without a magnetic induction field at Plasma Science  
1994 and Fusion Center in Massachusetts Institute of Technology. Note that the  
1995 Olympus Encore PCI 8000S camera for Viewport 4 was integrated in the beam  
1996 interacting target study done at CERN.

1997 The current in the magnet system generates heat, which is cryogenically  
1998 removed using liquid nitrogen. As the magnet cools down, all Viewports  
1999 become foggy up due to condensation. It was found out that  $\sim 0.5 \ell$  of  
2000 water (from nozzle performance test at Oak Ridge National Laboratory) was  
2001 not removed from the system prior to loading Hg. Flexible heater strips were  
2002 installed both on the exterior of the primary containment vessel and on the  
2003 snout in order to prevent the condensation of the humid air on the Viewports.  
2004 Although residual Hg droplets in sizes less than 1 mm often adhere to the

2005 sapphire Viewports after every shot, jet motion with adequate image quality  
2006 could still be collected.

#### 2007 4.1.2 Image processing

2008 To measure the shape of the jet, 8 and 12 bit grey scaled TIF images are  
2009 converted into digital forms. Background images are subtracted to reject the  
2010 noise in the image digitization process. The residual data is then transformed  
2011 into a 2 bit scaled image. Figure 4.1 shows the collected image and its  
2012 transformed 2 bit scaled image. Only the black and white colored pixels in  
2013 the 2 bit depth images are used to differentiate the shadow of the jet and the  
2014 background. Due to the image quality caused by the Hg droplet on window and  
2015 the quality in fiber optic system, the noise such as black dots exists. A threshold  
2016 is adjusted according to Otsu's method to highlight the interface between the  
2017 mercury and background (Otsu, 1979). Otsu's method selects the threshold  
2018 by minimizing the within-class variance and maximizing the between-class  
2019 variance of the two groups of pixels separated by the thresholding operator.  
2020 Otsu's method, which relies on the assumption that all image pixels belong to  
2021 one of two classes, background or foreground, has been shown to be efficient  
2022 in image segmentation for bi-level thresholding.

2023 Figure 4.2(a) shows the sensitivity of 2 bit scaled image conversion to the  
2024 measurement of jet height with respect to the level of 8 bit threshold using  
2025 Otsu's method. As the threshold level increases, the mean value of the jet  
2026 height as well as the  $\sigma$  value of the jet height in measurement is approaching

an asymptotic level. The optimally selected threshold value by the Otsu's method in this example is 0.35.

The Hg jet was observed at upstream (Viewport 1), midstream (Viewport 2), and downstream (Viewport 3) locations from the nozzle exit. 220 images are collected at each run for both the upstream and downstream locations, with an image size of  $1280 \times 1000$  pixels. The most probable transverse jet height within the longitudinal pixel range of 300 to 1000 is shown in the histogram of Fig. 4.2(b). Note that within this range, the transverse jet height probability  $P$  could be obtained by counting the number of longitudinal pixel events in the jet image. Let  $z$  denotes the transverse direction (in terms of pixels).

The number of background events (i.e., outside of the jet) is always larger than that within the jet because the portion of bright background on each image is larger than that of the black jet shadow. The distribution on the left in Fig. 4.2(b) (i.e.,  $0 < z < 200$ ) represents the background pixels. Then, the number of pixels corresponding to the jet height is counted within the longitudinal pixel range of 300 to 1000. Each counted pixel numbers are directly average to give a jet height measurement and then added up over  $\sim 200$  images for 1 jet shot, where the time elapse corresponds to  $\sim 0.4$  s at Viewport 1 and 3. Multiple shots are then used to add up all of the counted vertical jet height. The average of the individually counted vertical pixels is given to indicate the nominal jet height. In a mathematical form, the direct averaging method is described as Eqn. (4.1) as follow:

2049

2050

$$D_{jet} = \frac{1}{i + j + k} \sum_1^i \sum_1^j \sum_1^k N_{vertical} , \quad (4.1)$$

2051

2052

2053

2054

where  $D_{jet}$  and  $N_{vertical}$  denote the averaged vertical jet height and a individually counted number of vertical pixels respectively.  $i, j, k$  represent the number of shots, images in a shot, and vertical lines in a image respectively. Note that jet height measurement using Eqn. (4.1) is shown at Fig. 4.6.

2055

2056

2057

2058

2059

2060

2061

2062

On Viewport 2, 16 image files are collected at each run, with an image size of  $316 \times 316$  pixels. The images are analyzed in the same manner as described above. Viewports 1 and 3 give the same resolution for the images:  $1280 \times 1000$ . Thus, no image re-scaling is needed when comparing the pixel size for these images. However, Viewport 2 gives a resolution of  $316 \times 316$ . Based on the 1 cm scale fiducial mark on the exterior of all Viewports, all images taken on this Viewport are re-scaled to match the resolution of Viewport 1 prior to comparison.

2063

2064

### 4.1.3 Study on the scaling length and the location of center of window

2065

2066

2067

2068

2069

2070

In order to relate the lengths on the collected images at each Viewport, the pixel length on the images has to be investigated. Since the image size corresponds to the CCD size, any discrepancy in horizontal and vertical pixel size is not considered. Viewports 1 and 3 give the same resolution for the images:  $1280 \times 1000$ . Thus, no image re-scaling is actually needed when comparing the pixel size for these images but did the scaling to see any



difference on the image length of Viewport 1 and Viewport 3. The fiducial length on the top front window and the bottom back window is measured and then interpolated to get the length at the mid-span on the primary containment. The interpolated pixel length at the mid-span corresponds to 1 cm at the mid-span of primary containment. Thus, in Viewport 3, a pixel length at the mid-span where the jet is moving is approximated  $\sim 0.05$  mm. Same scaling was done at images in Viewport 3. The ratio of the pixel length in Viewport 3 to Viewport 1 is 1.06.

Viewport 2 gives a resolution of  $245 \times 252$ . Based on the 1 cm scale fiducial mark on the exterior of all Viewports, all images taken on this Viewport are re-scaled to match the resolution of Viewport 1 prior to comparison. A pixel length at the mid-span is approximated  $\sim 0.21$  mm. Viewport 4 gives a different resolution of images depending on the frame rate setting but typically the resolutions of  $320 \times 280$  was used. A pixel length at the mid-span is approximated  $\sim 0.21$  mm, which is same with Viewport 2.

The distance of the center position between the fiducial and the window is 0.75 inch apart. In order to locate the center of the window at the mid-span, the positions where 0.75 inch is apart from the top fiducial and bottom fiducial is found on each image and then the averaged difference in the located position is considered as the center of window.

Based on these scaling study, the measurement is performed for the following investigation. The measurement is averaged for  $\sim 200$  images to give a result of the following investigation and the standard deviation is also calculated

for the individual measurement respectively. Based on the standard deviation and the number of events, the error bar,  $\sigma/\sqrt{N}$ , is calculated to give error estimation for each measurement.

## 4.2 Motion of Mercury Jet and Stability in Magnetic Field

### 4.2.1 Jet deflection and surface flattening

When the jet is injected without an applied magnetic field, it is difficult to discern the jet surface because of blockage by Hg droplets on the window. Therefore, some errors in the measurement exists (see images in Fig. 4.3(a) through Fig. 4.3(c) and 4.4(a) through 4.4(c)). On the contrary, when a magnetic field is applied, the measurement errors are significantly reduced, leading to significantly less intermittent jet boundaries.

The inertial forces appear to dominate the jet movement when the jet velocity is 15 m/s. The turbulent jet motion is unstable but becomes stabilized as the magnetic field approaches 5 T. It has been reported that the radial force induced by the transverse component of magnetic field caused by the axially induced current due to the tilted jet angle can significantly increase the jet height (Gallardo *etal.*, 2002). The phenomena of increasing jet thickness with high magnetic induction field is observed for the first time when the magnetic field exceeds 10 T.

Figure 4.6 shows the jet height measurement by direct average of vertical jet height from scanned pixels on each image. The standard deviation is used

to give the error bar. This two plot shows the extreme two conditions of evaluation of the measured jet height, but one can effectively observe the fluctuating amount relative to the nominal jet height according to the various magnetic fields.

At a jet velocity of 15 m/s, the relatively low inertial force reduces the extent of turbulent fluctuation. For this case, the magnetic field does not significantly affect the dynamics of the jet until the magnetic field strength of  $\sim 5$  T reaches. Consequently, the height of the jet decreases only slightly until 5 T since the magnetic field reduces the fluctuating surfaces and the jet is more likely to elongate axially to the jet axis. The results shown in Fig. 4.3 and 4.4 clearly suggest that the magnetic field has constrained (stabilized) the Hg jet flow by smoothing out the edges of the otherwise turbulent flow. At large number of the magnetic field ( $>10$  T), stability is maintained at all Viewports. At 15 T, a larger height (cross sectional distortion) is observed on all Viewports.

The fact that the Hg jet size is relatively reduced from 0 T to 5 T but increases from 10 T to 15 T suggests that the Hg jet might encounter a different type of instability at high field, namely a quadrupole effect. The quadrupole effect would alter the jet's circular cross-section to become elliptical. From the data obtained with a 15 m/s jet, the jet height at a 10 T is smaller than that at 15 T, which is manifested in the vertical elongation of the jet. However, the height at a 10 T is smaller than that at 5 T. The issues for such a behavior have to be addressed. There are two possibilities. First, the jet is elongating

2139 axially up to 10 T. The equivalence of hydrodynamic pressure with magnetic  
2140 pressure is more dominantly affecting to the axial elongation of jet than the  
2141 transverse pressure. Equation (2.76) shows the magnetohydrodynamic stress  
2142 tensor, which indicates the ration of the axial pressure and the transverse  
2143 pressure. The increasing axial pressure of jet is more elongating from 0 T  
2144 to 10 T. However, the transverse magnetic pressure becomes significant once  
2145 the magnetic field exceeds 10 T. Thus, the jet at 15 T is experiencing the  
2146 transverse deflection as well as axial deflection, but the the role of transverse  
2147 deflection plays significantly on the behavior of jet. That can explain why  
2148 the reduction of jet is appearing up to 10 T and then the expansion of jet is  
2149 appearing at 15 T.

2150 Second, the optical diagnostics depends only on the side sectional view of  
2151 jet movement. The reduction of jet size on the minor axis of the elliptical core  
2152 has to be accompanied by the gain in jet size on the major axis in order to  
2153 satisfy the continuity condition in flow. In other words, the cross-sectional  
2154 are in flow should be constant. Although the two dimensional nature of  
2155 the image data does not distinguish between an elliptical cross section and  
2156 a circular one, occasional observation of a smaller jet thickness at 15 m/s with  
2157 10 T field as opposed to a 5 T indicates that the jet cross section might vary  
2158 between the major and minor axis of an elliptical core. It is important to note  
2159 that within the axial distance of interest, the jet diameter is approximately  
2160 constant. Therefore, references to "larger jet height" should be interpreted  
2161 to mean larger distortions of the jet cross section. Since the jet and solenoid

field are cylindrically symmetric, it is hard to estimate in what direction the jet is going to be distorted but the ratio of the deflection can be determined experimentally. The ratio also can be compared with the transverse magnetic pressure  $B^2/2\mu$  considering the reversed direction of deflection on each plot. Samulyak (2007) suggested that the deflection ratio of jet size  $\Delta R/R_o$  is proportional to the magnitude  $\mathbf{B}_o^2/U$ . By using the developed MHD code, where the governing MHD equations and free jet boundary condition including Maxwell's equations using low magnetic Reynolds approximation are employed and calculated the Hg jet deflection in magnetic field using a hybrid of Eulerian and Lagrangian method, so called Front tracking method. Figure 4.7(a) shows the deflection ratio of Hg jet along the distance from nozzle at 10 T and 15 T magnetic field. As shown in Fig. 4.3 and Fig. 4.4, the magnetic field stabilizes the Hg jet surface so that the jet surface is getting flattened. In MHD simulation, constant 1 cm diameter of Hg jet is considered. Although the magnetic field causes the jet surface flattening, the nature of turbulence such as growth of jet size is observed in experiment. Therefore, in order to avoid such a turbulent nature between simulation and experiment, the ratio of jet deflection ratio between 10 T and 15 T is evaluated to see the comparison of the magnetic field effect  $\mathbf{B}_o^2/U$  between Fig. 4.7(a) and Fig. 4.6, which is shown in Fig. 4.7(b). It shows somewhat consistency at upstream, but still the ratio diverges as the jet flows to downstream.

As expected, jet motion in a magnetic field behaves differently, depending on the angle between the axis of magnet and the axis of jet, as a result of

the differences in the magnitude of components of magnetic field (Samulyak, 2006). Figure 4.5(a) and (b) show the axial and radial components of the magnetic field in a solenoid. Figure 4.5(c) and (d) show the transverse and longitudinal components of the magnetic field along the jet axis at different crossing angles. As the crossing angle increases, the transverse component of the magnetic field increases, but with no significant change in the longitudinal component of the magnetic field. An increase of the transverse component of the magnetic field raises the induced axial current on the Hg jet. Therefore, the angle of the Hg jet is launched at 33 milliradian with respect to the axis of solenoid magnet.

The jet surface can readily be extracted from each collected image. The jet axis is approximated by fitting the averaged positions between top surface and bottom surface. This jet axis is moved with an offset until it interferes the top surface bottom surface. The amount of fluctuations of surface is measured by getting the difference between the fluctuation surfaces and the interfering jet axis on a RMS scale. Let  $\delta(r, t)$  denotes the probability of turbulence at  $r$ , such that  $\delta$  is 0 in the non-turbulent fluid, where the background is considered here, and is 1 in the turbulent fluid, where the jet is considered here. Time average of  $\delta$  yields  $\zeta(r)$ , the intermittency factor at  $r$ . The turbulent fluctuations are produced by the intermittency effect and these fluctuations are significant for scalar quantities. The intermittency characteristics of the turbulence are the appropriate input to be used in defining rough surface for a scattering analysis. When the intermittency phenomenon is present, the conventional turbulent

fluctuation is modified by the intermittency function and there is an additional contribution depending on the difference between the mean turbulent quantity and the non-turbulent quantity (Yen, 1967). However, the probability of the fluctuating jet surface area is introduced to define the intermittency in the following work. The pixel information along the jet axis by changing the translational offset is added to represent the intermittency of jet on the top and bottom surface. The intermittency within the jet represents 1 and it is gradually decrease to 0 at the background. The intermittency is between 0 and 1 at the jet surface depending on the surface fluctuations. Figure 4.8 shows the intermittency as a function of magnetic field and time. Total evaluated time is 160  $\mu s$ . Without magnetic field, the slope of intermittency at the jet surface is broad and it is oscillating as a function of time. With higher magnetic field, the slope of intermittency at the jet surface is more steep and it keeps same shape with respect to time. This result clearly tells that the magnetic field suppresses the fluctuation of jet surface.

Figure 4.9 shows the measured fluctuations on the jet surface. Surface fluctuations is monotonically decreasing and the surface is flattened approximately at 5 T. The fluctuations at Viewport 3 (downstream) is larger than that at Viewport 1 (upstream) since the tendency to be turbulent grows. The amount of fluctuations at top surface and bottom surface of jet is almost same, though the magnetic field is varied. Thus, the symmetry on the jet surface in terms of the surface variations such as fluctuations and wave amplitude is valid. The amount of difference of surface fluctuations at Viewport 1 and Viewport 3

becomes same. It indicates that the jet surface becomes flattened at 5 T in flow velocity 15 m/s. The decreased amount of surface fluctuation at Viewport 1 and Viewport 3 is  $\sim 0.5$  and 1.5 mm RMS respectively. This explains why the jet height is reducing from 0 T to 5 T in Fig. 4.6. The magnetic field makes the wavelength on the jet surface increases. Correspondingly, the wave propagation speed is increasing. Thus, it causes  $Re_{cr}$  to increase and the flow becomes laminar due to the stabilization by the magnetic field. The transverse component of magnetic field prevails more over the jet stabilization. Though there is some measurement errors due to the saturation in image brightness, the measurement could show the field effect to the reduction of fluctuation on jet surfaces.

The these observations are supported by previous results. For example, several investigations have suggested that magnetic field suppresses turbulent fluctuations in conducting liquid by stabilizing the flow (Shercliff 1956, Gold 1962, Kozyrev 1981, Bernshtam 1982), where stabilization is judged by an increase in the characteristic wavelength of the flow.

#### **4.2.2 Trajectory of mercury jet projectile in magnetic field**

The Hg jet and the beam are launched at 33 and 67 milliradian with respect to the magnetic axis respectively. The trajectory of Hg jet projectile is acted upon by gravity, which is represented as follow:



2252

$$\begin{aligned}
 t &= \frac{x}{v_o \cos \theta} \\
 y &= -\frac{g}{2} t^2 + v_o \sin \theta t + y_{nozzle} \\
 |v| &= \sqrt{v^2 - 2gx \tan \theta + \left(\frac{gx}{v \cos \theta}\right)^2}, \tag{4.2}
 \end{aligned}$$

2253

2254 where  $x$  is the jet traveling distance,  $y$  is the height at  $x$ ,  $y_{nozzle}$  is the  
 2255 vertical position of nozzle,  $v_o$  is the launched velocity, and  $\theta$  is the launched  
 2256 angle of Hg jet. Based on the governing trajectory equation Eqn. (4.2), fit  
 2257 function of the jet flow height can be expressed as

2258

$$y = A_1 + B_1 x - \frac{g(1 + B_1^2)x^2}{2C_1^2}, \tag{4.3}$$

2259

2260 where  $A_1 = y_{nozzle}$ ,  $B_1 = \tan \theta$ , and  $C_1 = v_o$ . The values and error are  
 2261 given in Table 4.3. The distance of jet elevation is determined by measuring  
 2262 the distance from the magnetic axis at center of each window to the jet axis,  
 2263 which is approximated by fitting the averaged positions between top surface  
 2264 and bottom surface. Figure 4.10 shows the trajectory of Hg jet and it's effect  
 2265 by the magnetic field and gravity. The solid line represents the globally fitted  
 2266 value using the trajectory of projectile with different initial launching speed of  
 2267 jet for the case of 15 m/s and 20 m/s respectively. It shows that the trajectory  
 2268 of Hg flow approximately agrees well with the trajectory of projectile for both  
 2269 15 m/s and 20 m/s shots. Experiment shows that the trajectory of the Hg jet  
 2270 is parabolic. The magnetic field caused some elevation of Hg jet closer to the  
 2271 center of magnetic field. As the jet moves to downstream, magnetic field effect

is more clearly observed since the jet is more likely to elongate to the axial direction. The longitudinal magnetic force is more increasing as one can see the magnetic pressure term in the longitudinal direction increasing at Eqn. (2.76). Therefore, it is observed that the jet is behaving more like straight at Viewport 4 with higher magnetic field. At 15 T, the elevation of jet is observed from Viewport 1 to Viewport 4. It shows that the magnetic force is overcoming the inertia force at 15 T similarly as there is the increase in jet height at 15 T. The overall increase of the jet elevation in upstream, midstream, and downstream at 15 T may have been caused by the asymmetric change of jet height. Possibly the stable equilibrium between magnetic force and gravitational force could be varying according to the variation of magnetic field (Geim, 1999).

The beam trajectory is also given to show the overlap with the Hg jet. It is shown that the overlap length is  $\sim 30$  cm when we consider the height of jet at various position with various magnetic field.

Based on the result of the jet trajectory, the angle of jet axis at Viewport 2 (midstream) is determined by the trigonometric approach using the elevation of jet and the distance along the magnetic axis between Viewport 1 and Viewport 3. Figure 4.11 shows the estimation of jet angle at center of magnetic axis (Viewport 2), which is approximately  $7 \sim 11$  milliradian. The jet angle is slightly decreasing with higher magnetic field, which indicates that the jet is more likely to move horizontally following the field line direction.

## 4.3 Dynamics of Liquid Jet Flow From Nozzle

### 4.3.1 Jet flow in surrounding medium

Lee (1977) investigated the phenomenon of air wake caused by a cylindrical jet emerging from a nozzle and showed the boundary layer of jet by applying continuity of jet mass and matching the loss of jet momentum with air drag on the jet. Figure 4.12 depicts schematically the boundary layer of jet emerging from a nozzle. The conservation of axial momentum and the rate of momentum loss to the skin friction on the jet and the continuity of the liquid jet are expressed as follows:

$$2\pi\rho_a \int_0^{\delta(x)} [a(x) + y]v^2(x, y)dy + \rho_l\pi a^2(x)v_l^2(x) = \rho_l\pi a_o^2v_{lo}^2, \quad (4.4)$$

$$\frac{d}{dz}[\pi\rho_l a^2(x)v_l^2(x)] = 2\pi a(x)\mu_a \frac{\partial v}{\partial y}|_{y=0}, \quad (4.5)$$

and

$$\pi a^2(x)v_l(x) = \pi a_o^2v_{lo}, \quad (4.6)$$

where velocity, density, and viscosity are denoted by  $v$ ,  $\rho$ , and  $\mu$ , respectively, with subscripts  $a$  and  $l$  for air and liquid, respectively. The subscripts  $o$  denotes the initial values at the nozzle. For boundary layer analysis of cylindrical objects, because of the diverging flux characteristics in radial direction, a logarithmic profile is the most appropriate (Stewartson, Glanert, 1955). Thus,

the velocity profile of the air induced by the liquid jet is assumed to be as follow:

$$v(x, y) = v_l(z) \left\{ 1 - \frac{1}{\beta(x)} \ln \left[ 1 + \frac{y}{a(x)} \right] \right\} \quad (4.7)$$

and

$$\frac{\delta(x)}{a(x)} = e^{\beta(x)} - 1. \quad (4.8)$$

Substitution of Eqns. (5.15) into Eqns. (5.8) Eqns. (5.13) results in

$$\bar{v}_l(\bar{x}) = \frac{v_l(\bar{x})}{v_{lo}} = \frac{1}{1 - \bar{\rho} \left[ 1 + \frac{1}{\beta} - \frac{1}{2\beta^2} (e^{2\beta} - 1) \right]} \quad (4.9)$$

and

$$\frac{d\beta(\bar{x})}{d\bar{x}} = \frac{\beta^2 - \bar{\rho} [\beta^2 + \beta - \frac{1}{2}(e^{2\beta} - 1)]}{\beta(1 + e^{2\beta}) - (e^{2\beta} - 1)}, \quad (4.10)$$

where  $\bar{x} = \frac{4x}{\text{Re}_e a_o}$ ,  $\text{Re}_e = \frac{2a_o \rho_a v_{lo}}{\mu_a}$ , and  $\bar{\rho} = \frac{\rho_a}{\rho_l}$ . For a given value of  $\rho$ , the stream velocity  $\bar{v}_l(\bar{x})$  and boundary layer thickness  $\bar{\delta}(x)$  are obtained. As seen in Fig. 4.13, the Reynolds number plays its role implicitly and this makes the density ratio  $\bar{\rho}$  to be varied. Since the cylindrical jet has larger volumes, for the initial momentum of the jet to be maintained, the liquid density must be reduced and the value of the density parameter to be used must be modified to  $\bar{\rho} = \rho_a D^2 / (\rho_l d_o^2)$ , where  $D$  and  $d_o$  denote diameter of jet and nozzle, respectively.

### 4.3.2 Pressure loss and magnetic effect to the Hg delivery pipe

Fig. 4.14 (a) and (b) show the pipe inlet pressure for driving jet in various magnetic field strength. The Hg jet is driven by the piston in syringe and the piston velocity is measured by position sensor. The piston velocity determines the flow rate so that the dynamic pressure head at pipe inlet is determined using the conservation of flow rate. The pressure sensor installed at the pipe wall measures the static pressure. No significant pressure drop is observed at the pipe inlet in magnetic field strength. It indicates that the driving pressure in pipe for nozzle is at same condition regardless of the magnetic field variation.

To obtain the jet velocity, the distance traveled by a fixed point on the jet surface is tracked over a given time period. Figure 4.15 (a) shows the jet velocity measured at Viewport 1, Viewport 2, Viewport 3, and Viewport 4 in various magnetic field strength. Note that this velocity does not change with the imposition of a magnetic field. Therefore, considering the measurement error in Fig. 4.15 (a), the averaged flow velocity, regardless of magnetic fields, can reasonably indicate the flow velocity given in Fig. 4.15 (b). This explains why the pressure is approximately constant in the pipe, consistent with the report (Graves, 2007).

Another interesting result is that the cross section of Hg jet is more likely to be elliptical since the longitudinal jet flow velocity is constant from upstream to downstream. Regardless of the magnetic field, the Hg jet does not show jet velocity change. Thus, the jet is changing its shape once it leaves the

nozzle from circular to elliptical. Hence, the result in Fig. 4.6 should be again interpreted by the result in Fig. 4.15 in the manner that the jet height at 5 T is elongated on the minor axis followed by the reduction of jet height on the major axis of the elliptical core, and the jet is deflecting further at 10 T. However, the jet height at 15 T is elongated on the major axis, which is manifested by the comparison between the ratio of the reduction of jet height and the increased ratio of the jet height at 15 T. This approach is already mentioned in the above, but it is examined again.

Considering that the driving pressure and the jet velocity are not significantly changed in various magnetic field, it is concluded that the longitudinal magnetic field does not affect to the pressure loss or velocity degradation while Hg passes the solenoid magnet two times along with the direction of magnetic field line. It is reported that the gradient of longitudinal jet velocity depends on the integration of gradient of longitudinal magnetic field along the magnetic axis plus it's multiplication to longitudinal magnetic field itself. (Gallardo *etal.*, 2002) It is expressed as follow:

$$\Delta v(x) = \frac{\kappa}{\rho} \frac{r_o^2}{8} \left( \int_{x_1}^{x_2} \left( \frac{dB_x}{dx} \right)^2 + \frac{d}{dx} \left( B_x \frac{dB_x}{dx} \right) dx \right), \quad (4.11)$$

where  $r_o$  is the radius of jet and  $\kappa$  is electrical conductivity. Since the gradient of magnetic field is increasing (plus) at entrance and decreasing (minus) at exit, it seems that there is an increasing velocity gradient (acceleration) at upstream and decreasing velocity gradient (deceleration) at downstream but it is  $\leq 0.5$  m/s due to the relatively high density comparing with the

electrical conductivity only if we consider the effect by the magnetic field. The experimental result shows slight effect of magnetic field but is consistent with the reported result in terms of the gradient of longitudinal velocity in magnetic field.

#### 4.3.2.1 *pressure loss in pipe flow*

Schematic pipe geometry is given in Fig. 1.3, where the pipe is connected from the syringe pump to nozzle and it is passing parallel with solenoid magnetic field line next to the primary containment. A loss coefficient is defined as follows:

$$(h_{loss}) = K_1 \frac{v_1^2}{2g} + K_2 \frac{v_2^2}{2g} + \dots + K_N \frac{v_N^2}{2g} ,$$

$$A_1 v_1 = A_2 v_2 = \dots = A_N v_N = A_R v_R , \quad (4.12)$$

where the subscript  $R$  signifies a reference location and  $K$  represents the loss coefficient. The general thermodynamic loss, so called the head loss  $h_{loss}$  is defined as follow:

$$\int_1^2 \delta F = (h_{loss})_{1,2} = \frac{p_1 - p_2}{\rho g} + \frac{v_1^2 - v_2^2}{2g} + (z_1 - z_2) . \quad (4.13)$$

Darcy-Weisbach equation is given to express the head loss of wherever the density is constant as follow:

$$\frac{\Delta p}{\rho g} = f \frac{L}{d} \frac{U^2}{2g} , \quad (4.14)$$

where  $f$ ,  $L$ ,  $d$  are friction factor, the pipe length, and the diameter of pipe respectively. Considering that the  $Re = 1800000$  and  $e/d = 0.002$  for commercial steel in terms of Nikuradse's sand grain scale, turbulent friction factor  $f$  via Moody plot or by Colebrook Eqn. (4.15) is approximated to 0.024. Colebrook simply combined the expressions for the friction factor for smooth and rough pipes into a single transition equation of the equivalent form as follow:

$$\frac{1}{\sqrt{f}} = 1.74 - 2 \log \left( 2 \frac{e}{d} + \frac{18.7}{Re \sqrt{f}} \right) . \quad (4.15)$$

Note that Colebrook's expressions for the friction factor in the transition region reduces to Prandtl's smooth pipe equations when the relative roughness approaches zero, and reduce to von Karman's fully rough pipe equation at very high pipe Reynolds number.

The loss coefficients for elbows are presented as follows, where  $a$  and  $R$  represent the inside radius of the elbow and the radius of curvature of the centerline of the elbow respectively. For  $Re(a/R)^2 > 91$ , the loss coefficient is expressed as follow (Ito, 1960):

$$K_{elbow} = 0.00241 \alpha \theta \left( \frac{R}{a} \right)^{0.84} Re^{-0.17} , \quad (4.16)$$

where  $\theta$  is the bend angle in degrees and  $\alpha$  is an empirical factor given as:

$$\alpha_{\theta=90^\circ} = 0.95 + 17.2 \left( \frac{R}{a} \right)^{-1.96} . \quad (4.17)$$



2423 Inputting  $R=1.942$  and  $a=0.442$ ,  $\alpha = 1.9$  and  $K_{elbow} = 0.1232$ . A correction  
 2424 term is applied to the  $90^\circ$  elbow to determine the loss coefficient for arbitrary  
 2425 angle of elbow (SAE, 1960).

2426

$$2427 \quad K_\theta = (C_\theta)_{elbow} K_{90^\circ} , \quad (4.18)$$

2428 where  $C_{elbow}$  is given in the referenced manual (SAE, 1960). The  $C_\theta$  is 0.28  
 2429 at  $\theta = 23^\circ$  and  $K_\theta = 0.0345$ .

2430 The loss coefficient for the reducer or well-rounded inlet loss is  $K_{reducer} =$   
 2431 0.05 based on the flow area of the smaller piping section (Benedict, 1980).

2432 The loss coefficient for the abrupt enlargement is determined by combining  
 2433 the momentum balance over the area of interest. Then, it yields the Carnot-Borda  
 2434 equation, which shows the head loss in the abrupt enlargement. By equating  
 2435 it to the head loss equation Eqn. (4.12), the loss coefficient is given based on  
 2436 the inlet velocity as follow:

2437

$$2438 \quad K_{enlargement} = \left(1 - \frac{v_2}{v_1}\right)^2 = \left(1 - \frac{A_1}{A_2}\right)^2 = (1 - \beta^2)^2 ,$$

$$\frac{p_1}{p_2} = 1 + \left(\frac{1 - G_1}{G_1}\right)(2\beta^2 - 2\beta^4) , \quad (4.19)$$

2439 where  $G_1$  is the inlet pressure ratio of static pressure to total pressure,  
 2440  $p_t/p_{t1}$ . The fluid experiences pressure loss when going from a piping system  
 2441 to a plenum, so called exit loss. According to Eqn. (4.19), the loss coefficient  
 2442 for exit  $K_{exit}$  is 1, where  $\beta = 0$ . It applies regardless of whether the pipe  
 2443 protrudes into the exit plenum, is well rounded at exit, or is flush.

Finally, the loss coefficient for the abrupt contraction is given based on the velocity at exit as follow (Benedict, 1980):

$$K_{contraction} = \left(\frac{1}{C_D^2} - 1\right)(1 - \beta^4) ,$$

$$C_D = \frac{Q_{acutal}}{Q_{ideal}} , \quad (4.20)$$

where the discharge coefficient  $C_D$  is given in reference (Benedict, 1980). The mean discharge coefficient is given as 0.815 based on the water tests in short pipes. According to Eqn. (4.20), this yields a maximum loss coefficient at  $\beta = 0$  of 0.506. Assuming  $\beta = A_2/A_1 = 0.9$ ,  $K_{contraction}$  yields 0.1738.

The head losses and the contribution of each geometry are given in Table 4.2. Total length of pipe is 87.1 inch. The diameter of inside pipe is 0.884 inch. The diameter of inside nozzle is 0.4 inch. Total pressure head loss is 2.3358 m., which corresponds to  $\sim 16$  % of input pressure head. The main loss is caused by large length with friction by surface roughness inside pipe, which is over  $\sim 50$  %. The loss from pipe bend is somewhat low comparing with others.

Based on the calculated head loss, the jet velocity at nozzle is determined assuming the pressure right after nozzle exit is atmospheric. The pipe inlet pressure is given in Fig. 4.14(a) and (b). The elevation of the pipe inlet and the nozzle is  $\sim 2.9$  inch. The calculated jet velocity from nozzle including the pressure loss in pipe is  $15 \pm 1$  m/s, which is  $\sim 10$  % larger than the measured result in Fig. 4.15, where the jet velocity is  $\sim 13.5$  m/s. Jet velocity in nozzle position was reported in Fig. 4.14(c) with  $\sim 15.8$  m/s by using incompressible constant flow rate between pipe inlet and nozzle exit, where

piston size is 10 inch, nozzle inside size is 0.4 inch, and moving position of piston for injection of mercury jet was measured with respect to 10 Hz of data acquisition rate via NI hardware (Graves, 2007). According to Eqn. (2.76), the magnetic field increases the fluid pressure by an amount of  $B^2/2\mu$ , in directions perpendicular to the magnetic field, and decreases the fluid pressure by the same amount, in the parallel direction of the magnetic field. The fluid pressure including the magnetic pressure has to balance with the atmospheric pressure and surface tension of jet and satisfy the continuity condition. The fluid pressure will find equilibrium point since the fluid pressure perpendicular to the magnetic field line is mutually symmetric. Therefore, the jet is changing to be elliptical in Fig. 4.6. Hence, the pressure drop is not occurred significantly and correspondingly the longitudinal jet velocity is not changed with magnetic field in Fig. 4.15.

#### 4.3.2.2 *the measurement of wall tap pressure*

Wall tap is used in order to sense static pressure, wherein small pressure tap is located at a point on pipe surface so that it does not disturb the fluid. Tap size error arises because of a local disturbances of the boundary layer.

$$\text{Re}_d^* = \frac{v^* d_{tap}}{\nu}$$

$$\text{Re}_d^* = \sqrt{\frac{f}{8}} \left( \frac{d_{tap}}{d} \right) \text{Re} , \quad (4.21)$$

where  $d_{tap}$  is the tap diameter,  $\text{Re}_d^*$  is the tap Re number, and  $v^*$  is the friction velocity. The friction factor is 0.024. The tap inside diameter and pipe

inside diameter are 0.5, 0.884 inch respectively, which yields  $Re_d^* = 55764$ .

At tap  $Re$  greater than 385, the error in static pressure caused by the tap size is given as follow:

$$\frac{e_{tap}}{\tau} = 0.269 (Re_d^*)^{0.353} , \quad (4.22)$$

where  $\frac{e_{tap}}{\tau} = 12.74$ .

Combining the Darcy friction factor with the wall shear stress yields

$$f = 4 \left( \frac{\tau}{\rho v^2 / 2g} \right) . \quad (4.23)$$

Therefore, the error in a static pressure can be expresses as non-dimensionalized form by the dynamic pressure  $p_{dynamic}$  as follow:

$$\frac{e_{tap}}{p_{dynamic}} = \left( \frac{e_{tap}}{\tau} \right) \frac{f}{4} , \quad (4.24)$$

where  $\frac{e_{tap}}{p_{dynamic}} = 0.0764$ . The error of static pressure in Fig. 4.14 (a) is estimated to give 7.64 % uncertainty of the dynamic pressure in Fig. 4.14 (b).

Table 4.1: Error estimation of fiducial length at each viewport.

Viewport number	Fiducial length (cm)	Scaling factor
1	$1.0 \pm 0.095$	1.0 (reference)
2	$1.0 \pm 0.091$	$4.3 \pm 0.81$
3	$1.0 \pm 0.062$	$1.0 \pm 0.16$
4	$1.0 \pm 0.067$	$4.3 \pm 0.70$

Table 4.2: Pressure head losses by geometry in pipe for mercury loop.

Geometry in pipe for mercury loop	Calculated pressure head loss	Percentage in total pressure head loss (%)
Friction by surface roughness	1.4176	60.7
Elbows in pipe bend ( $3 \times 90^\circ$ , $2 \times 23^\circ$ )	0.2629	11.3
Reducer, Contraction in nozzle	0.6553	28

Table 4.3: Parameterized coefficients, its error, and statistics summary of fit function in figures.

Figure	1	2	3	4	5	6	7	8	9	10
4.10(B=0 T,V=15 m/s)	-0.01448	9.97E-04	0.03375	0.00379	-	-	-	-	13.6445	0.85213
4.10(B=5 T,V=15 m/s)	-0.01448	9.97E-04	0.03375	0.00379	-	-	-	-	13.85258	0.89937
4.10(B=10 T,V=15 m/s)	-0.01448	9.97E-04	0.03375	0.00379	-	-	-	-	14.13407	0.96089
4.10(B=15 T,V=15 m/s)	-0.01448	9.97E-04	0.03375	0.00379	-	-	-	-	14.48514	0.99102
4.10(B=15 T,V=20 m/s)	-0.01448	9.97E-04	0.03375	0.00379	-	-	-	-	18.85852	2.2851
Figure	11	12	13	14	15	16	17	18	19	
4.10(B=0 T,V=15 m/s)	-	-	-	-	20	13	25.15504	0.92629	0	
4.10(B=5 T,V=15 m/s)	-	-	-	-	20	13	25.15504	0.92629	0	
4.10(B=10 T,V=15 m/s)	-	-	-	-	20	13	25.15504	0.92629	0	
4.10(B=15 T,V=15 m/s)	-	-	-	-	20	13	25.15504	0.92629	0	
4.10(B=15 T,V=20 m/s)	-	-	-	-	20	13	25.15504	0.92629	0	

---

**1** : A1 value, **2** : A1 standard deviation,

**3** : B1 value, **4** : B1 standard deviation, **5** : B2 value, **6** : B2 standard deviation,

**7** : B3 value, **8** : B3 standard deviation , **9** : C1 value, **10** : C1 standard deviation,

**11** : C2 value, **12** : C2 standard deviation, **13** : C3 value, **14** : C3 standard deviation,

**15** : Number of points, **16** : Degrees of freedom, **17** : Reduced  $\chi^2$ , **18** : Adjusted  $\mathbf{R}^2$ , **19** :  $\chi^2$  probability.

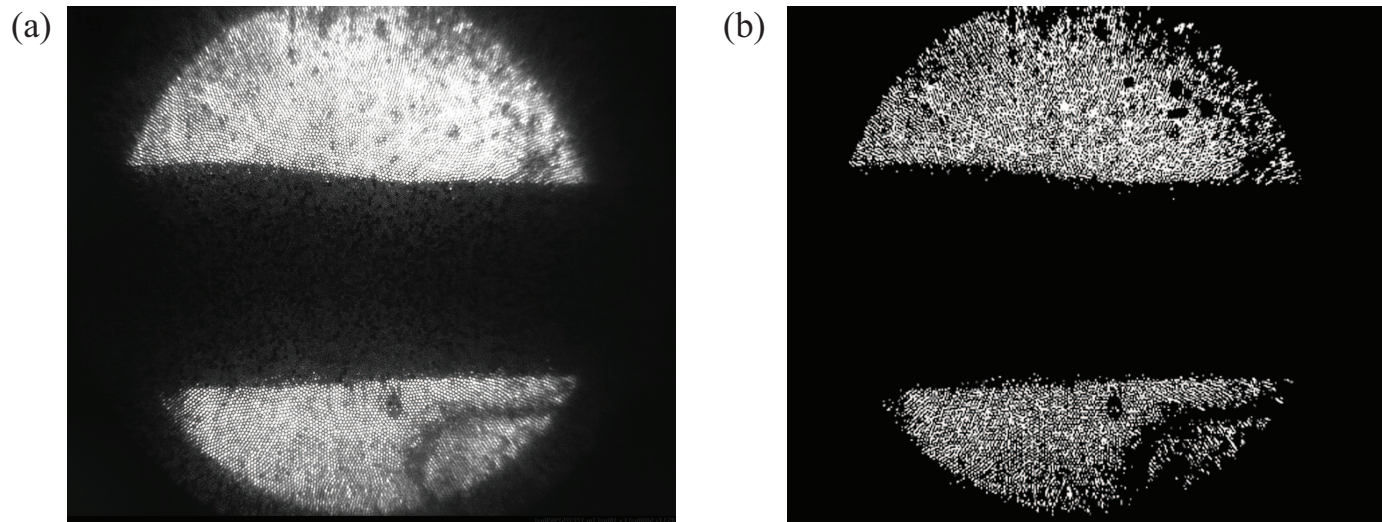


Figure 4.1: Image data conversion for image analysis. a.) Collected image data. b.) 2 bit scaled image data.

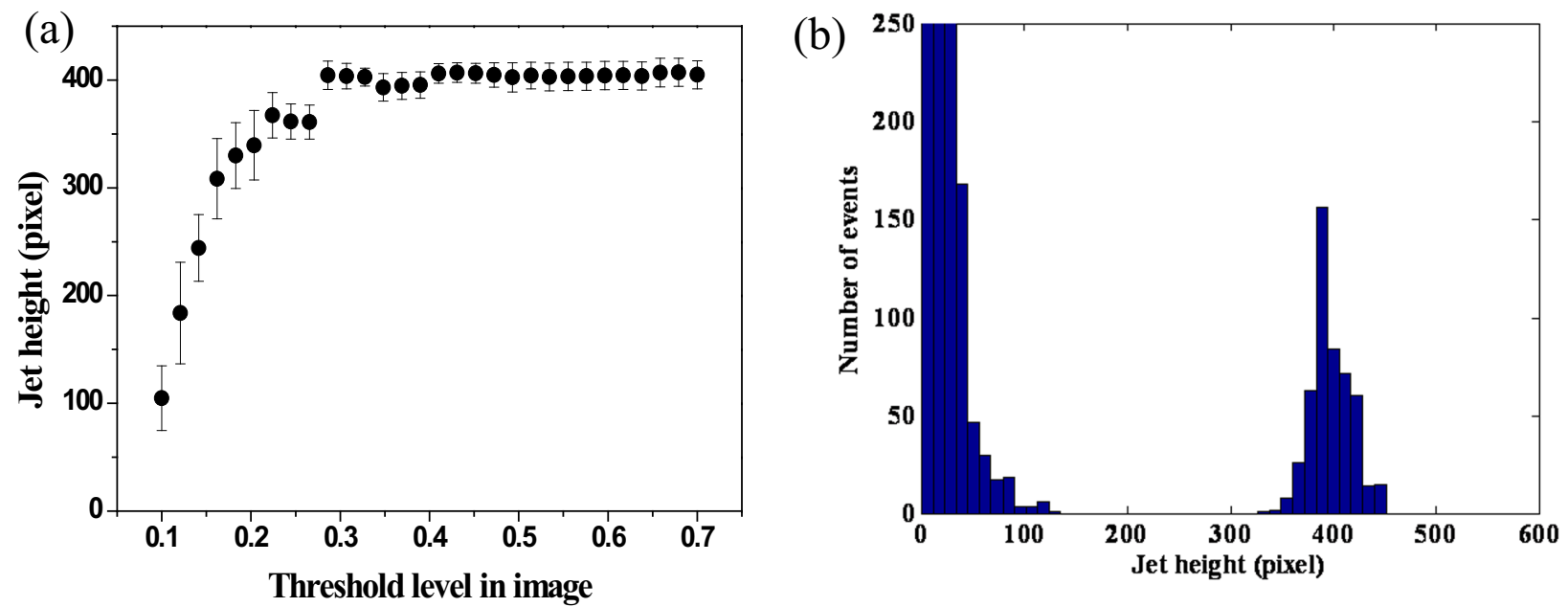


Figure 4.2: Jet height determination from image analysis. a.) Sensitivity of threshold in a 2 bit scaled image conversion. b.) Histogram of number of events in the jet height measurement.



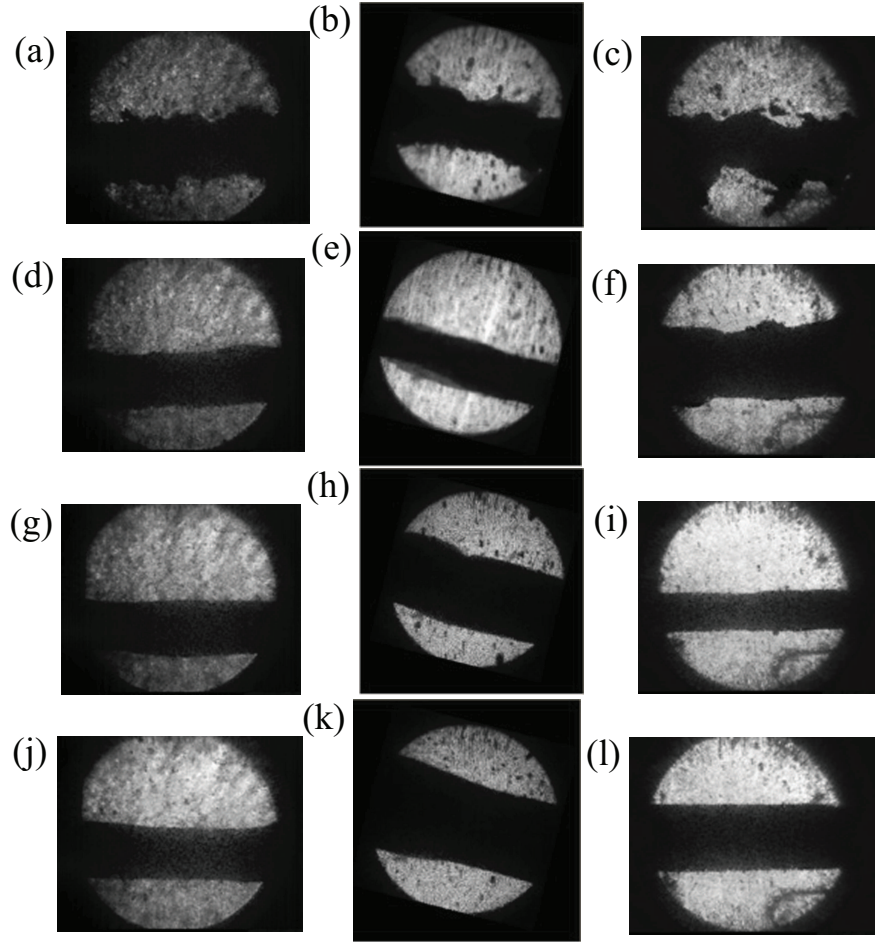


Figure 4.3: Mercury jet flows as observed from the 3 Viewports. The jet flows from left to right on each image. The first, second, and third columns represent Viewport 1, 2, and 3, respectively. The individual caption shows the applied magnetic induction field. The jet velocity is 15 m/s. Images on Viewport 2 has a  $14^\circ$  clockwise rotation due to the SMD software. a.)  $B=0$  T. b.)  $B=0$  T. c.)  $B=0$  T. d.)  $B=5$  T. e.)  $B=5$  T. f.)  $B=5$  T. g.)  $B=10$  T. h.)  $B=10$  T. i.)  $B=10$  T. j.)  $B=15$  T. k.)  $B=15$  T. l.)  $B=15$  T.

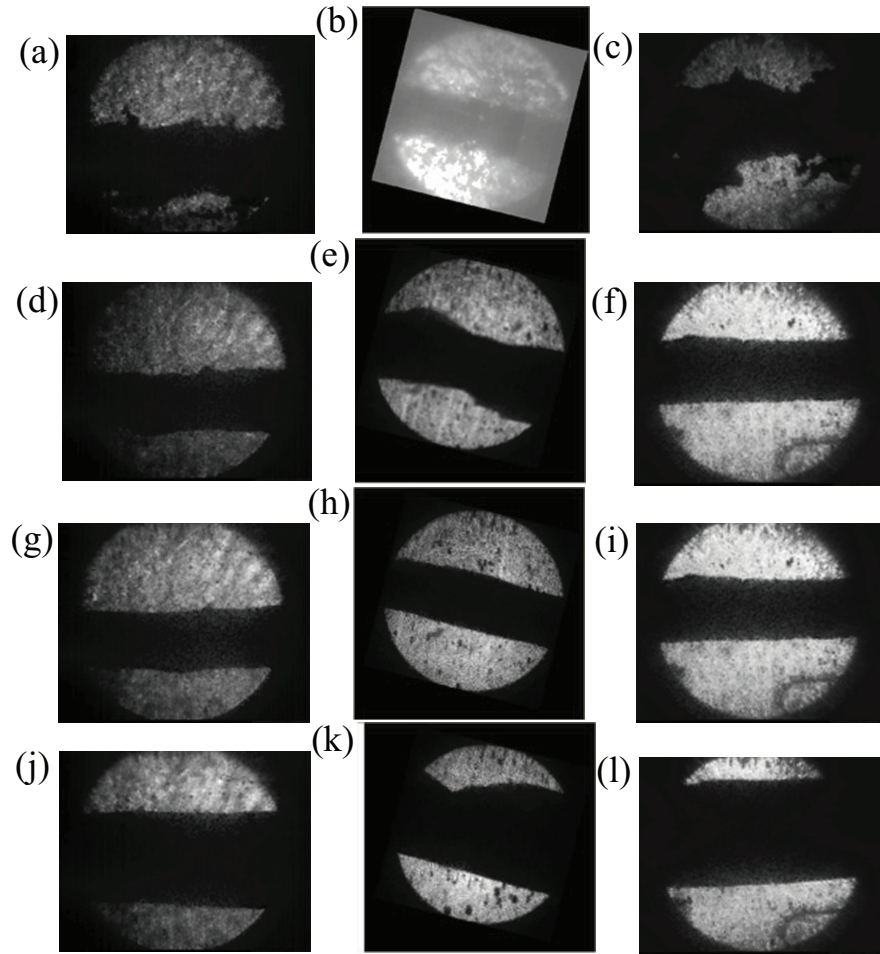


Figure 4.4: Same as Fig. 4.3 but with a jet velocity of 20 m/s. a.)  $B=0$  T. b.)  $B=0$  T. c.)  $B=0$  T. d.)  $B=5$  T. e.)  $B=5$  T. f.)  $B=5$  T. g.)  $B=10$  T. h.)  $B=10$  T. i.)  $B=10$  T. j.)  $B=15$  T. k.)  $B=15$  T. l.)  $B=15$  T.

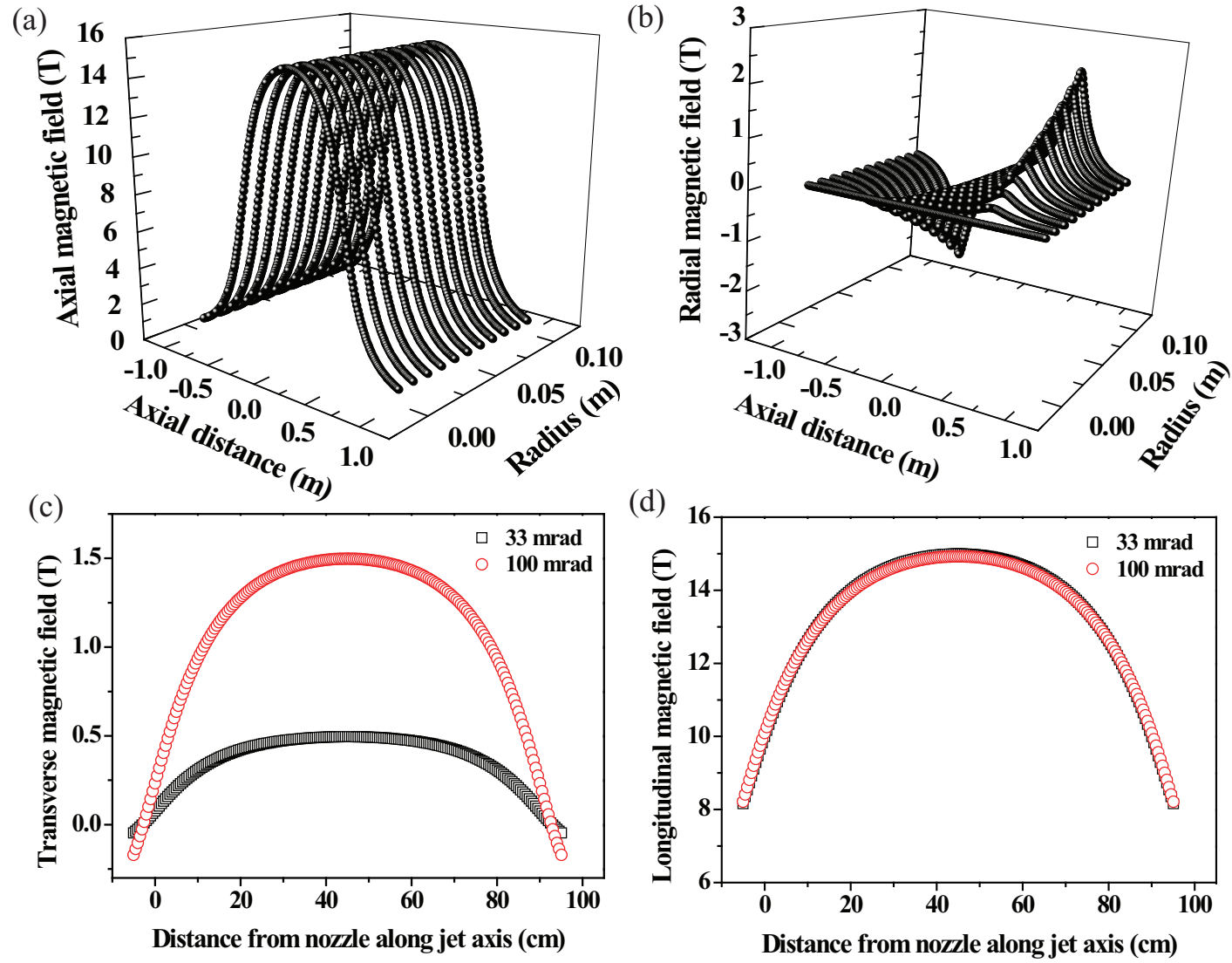


Figure 4.5: Calculated solenoid magnetic induction field map. a.) Radial field map. b.) Axial field map. c.) Transverse component of magnetic induction field along jet axis. d.) Longitudinal component of magnetic induction field along jet axis.

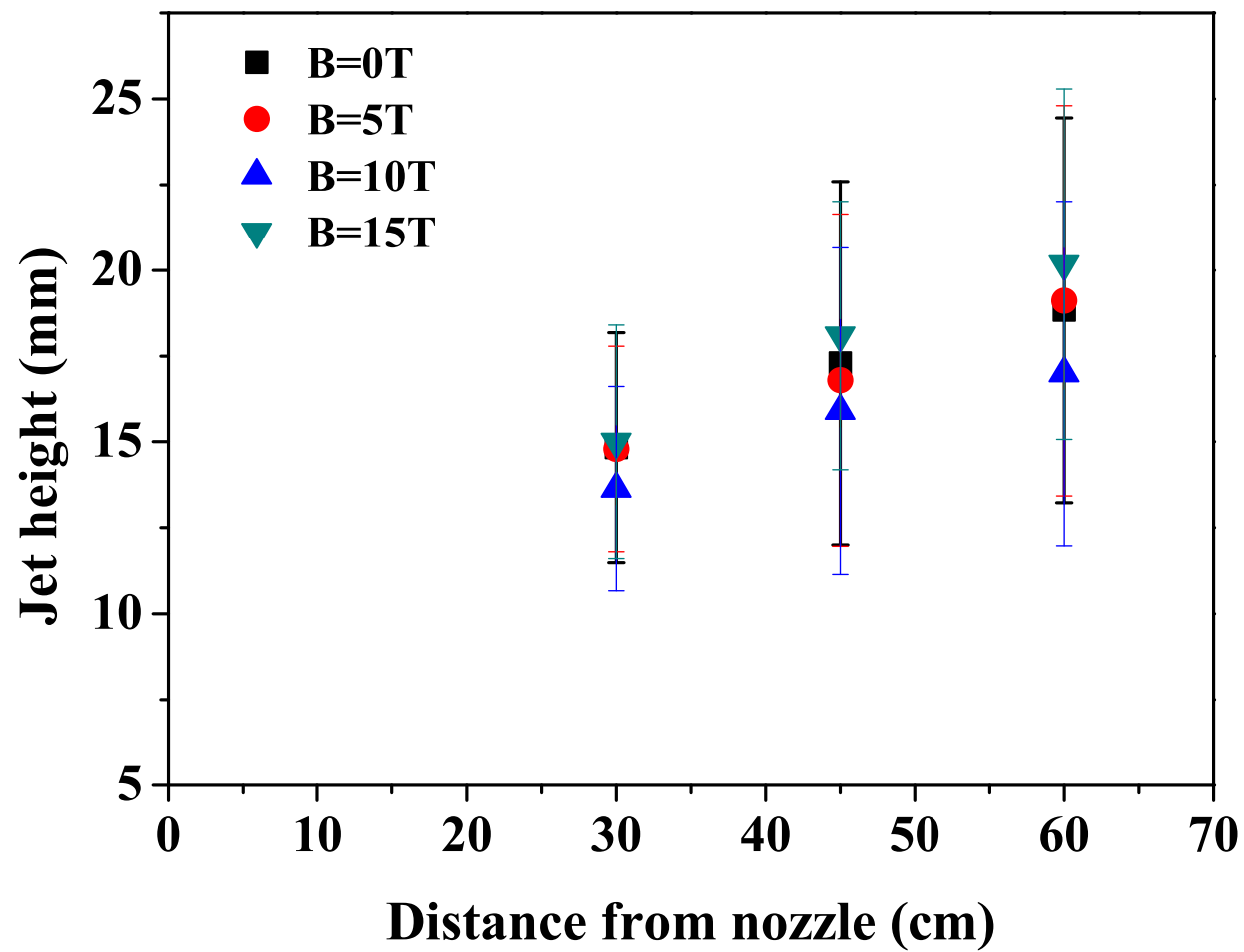


Figure 4.6: Hg jet height measurement from direct average of vertical height in magnetic fields on each image.

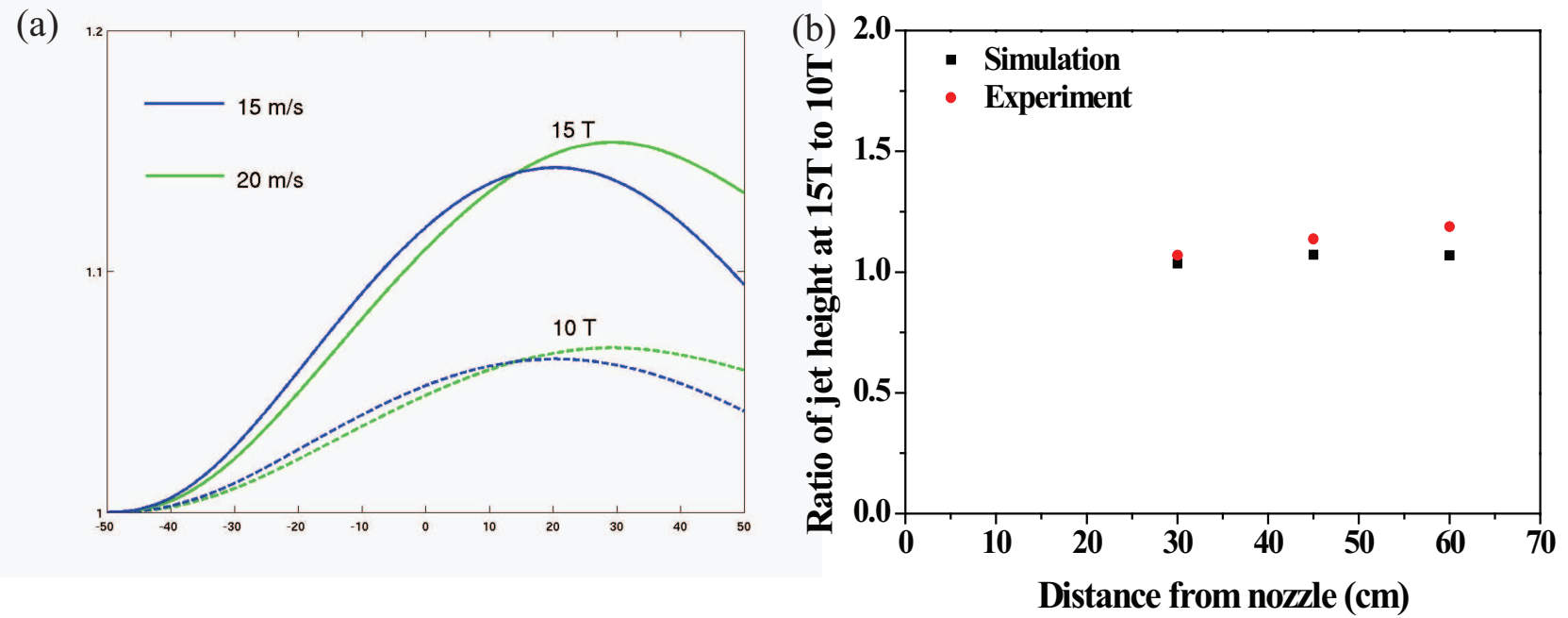


Figure 4.7: Comparison of Hg jet deflection ratio at 15 T to that at 10 T. a.) Numerical calculation of deflection ratio. b.) Comparison of ratio of jet deflection.



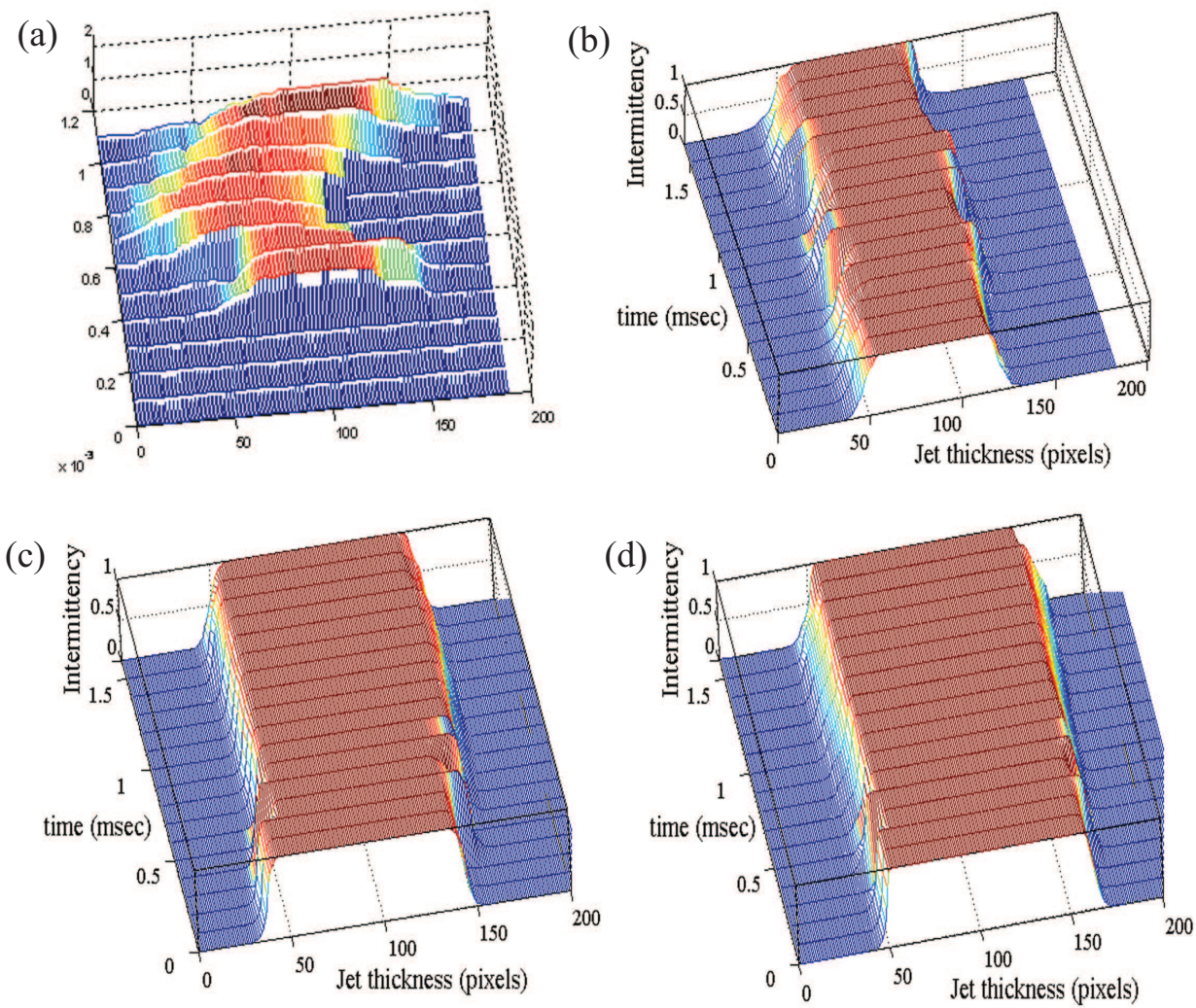


Figure 4.8: Intermittency of Hg jet at Viewport 2. The jet velocity is 15 m/s. a.)  $B=0$  T. b.)  $B=5$  T. c.)  $B=10$  T. d.)  $B=15$  T (continued).

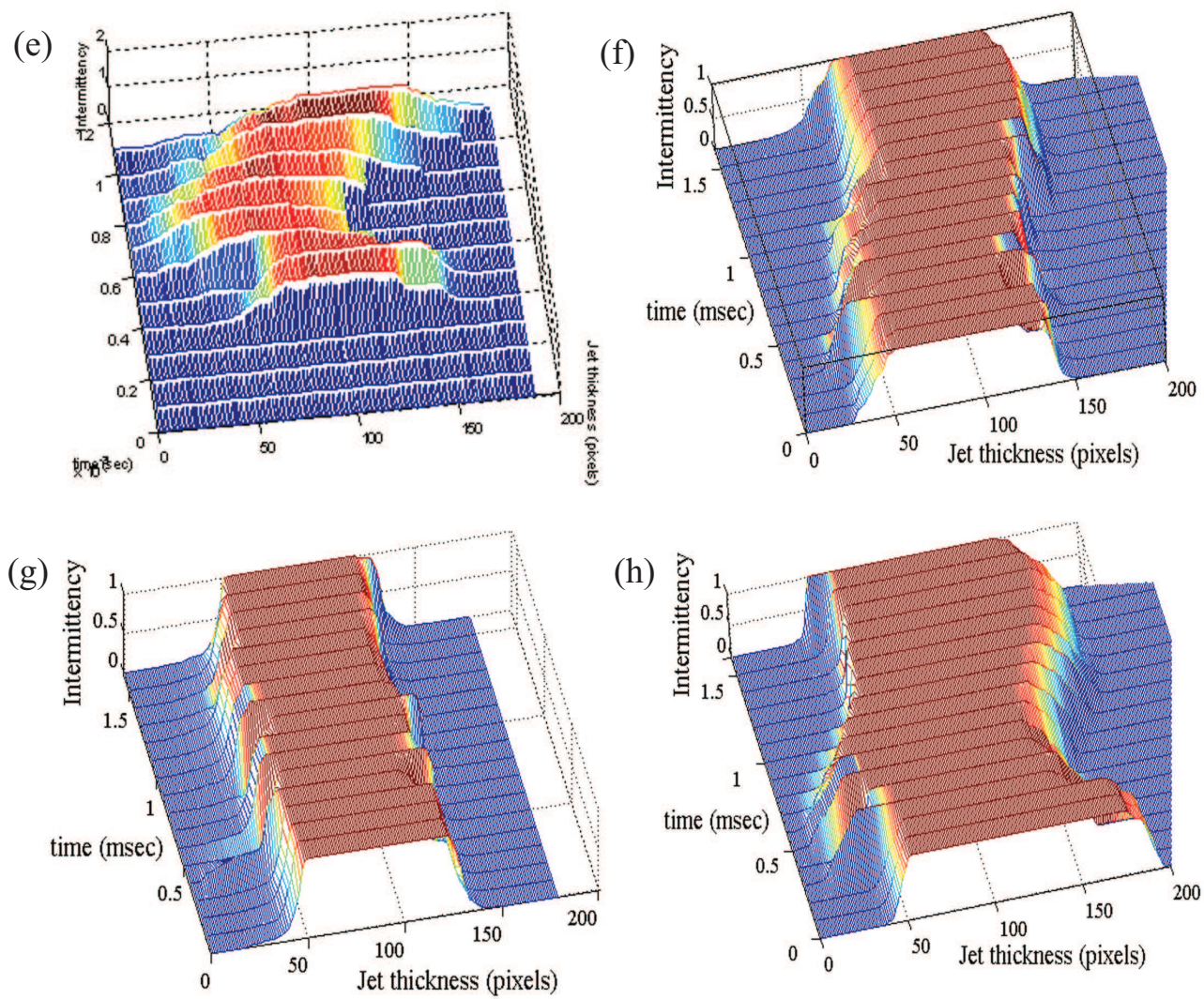


Figure 4.8: Intermittency of Hg jet at Viewport 2. The jet velocity is 20 m/s. e.)  $B=0$  T. f.)  $B=5$  T. g.)  $B=10$  T. h.)  $B=15$  T.

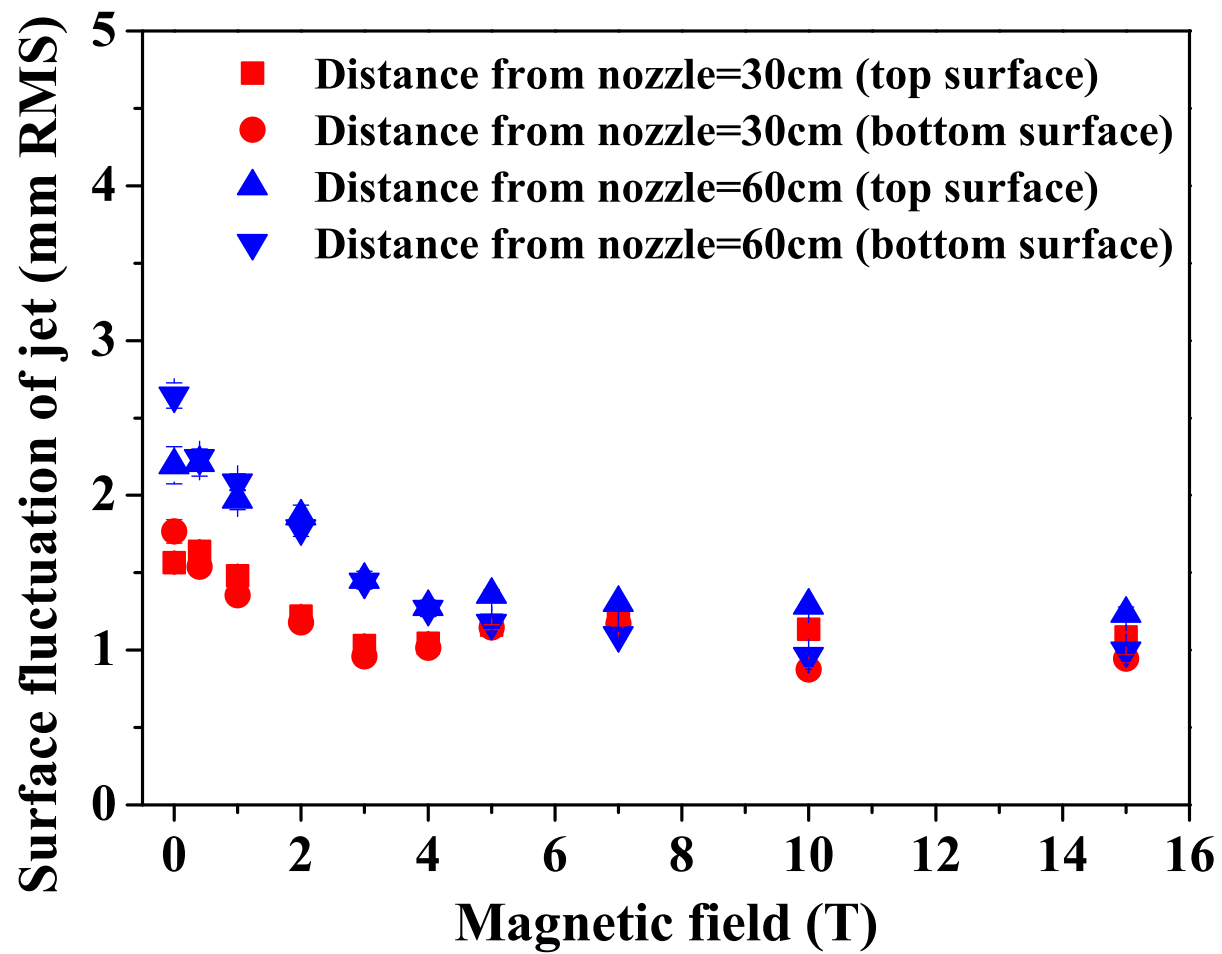


Figure 4.9: Surface fluctuations in a magnetic field.



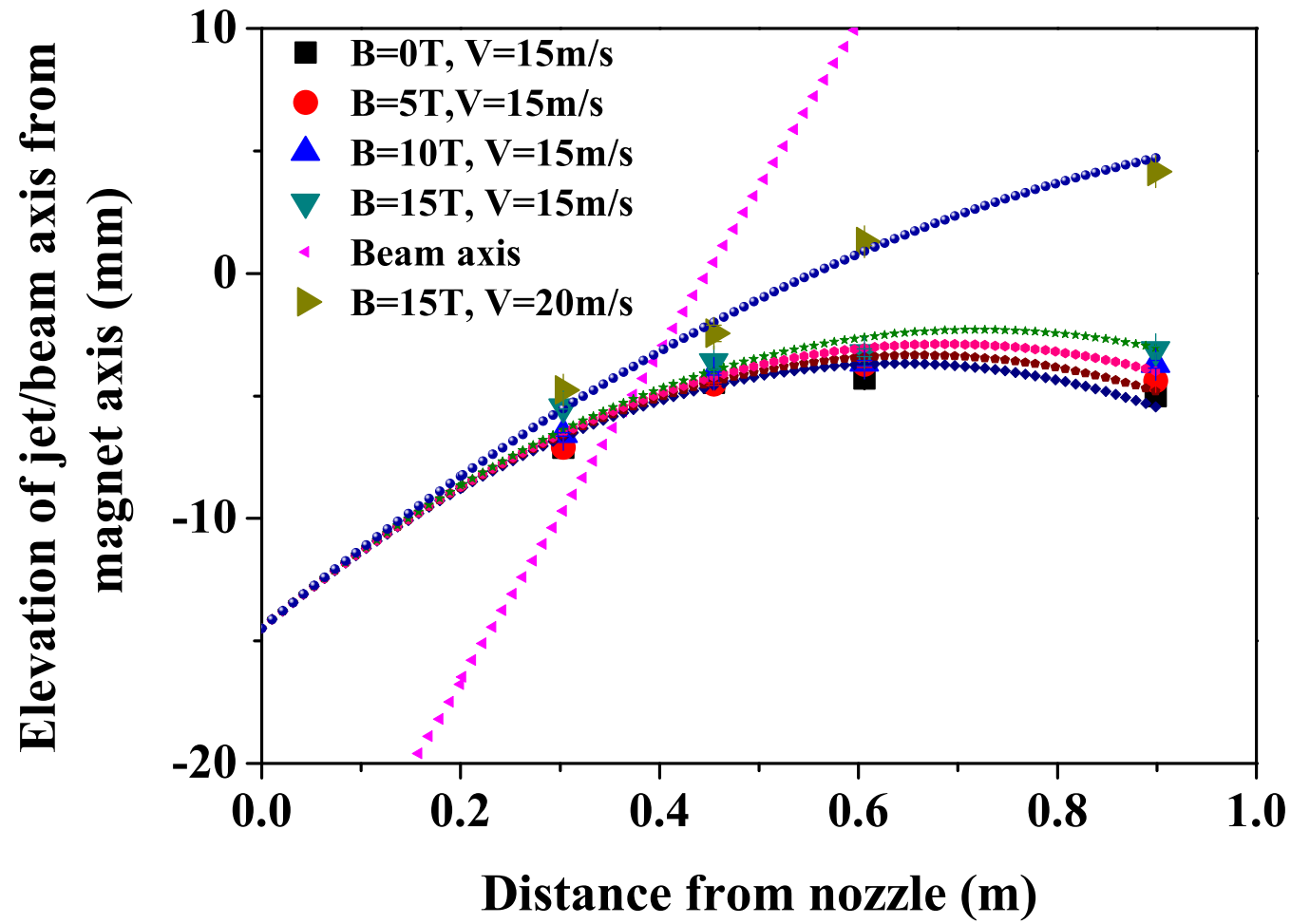


Figure 4.10: Trajectory of beam axis and Hg jet axis projectile with respect to magnetic axis in magnetic field. Solid line represents the simulated value using trajectory of projectile with different velocity.

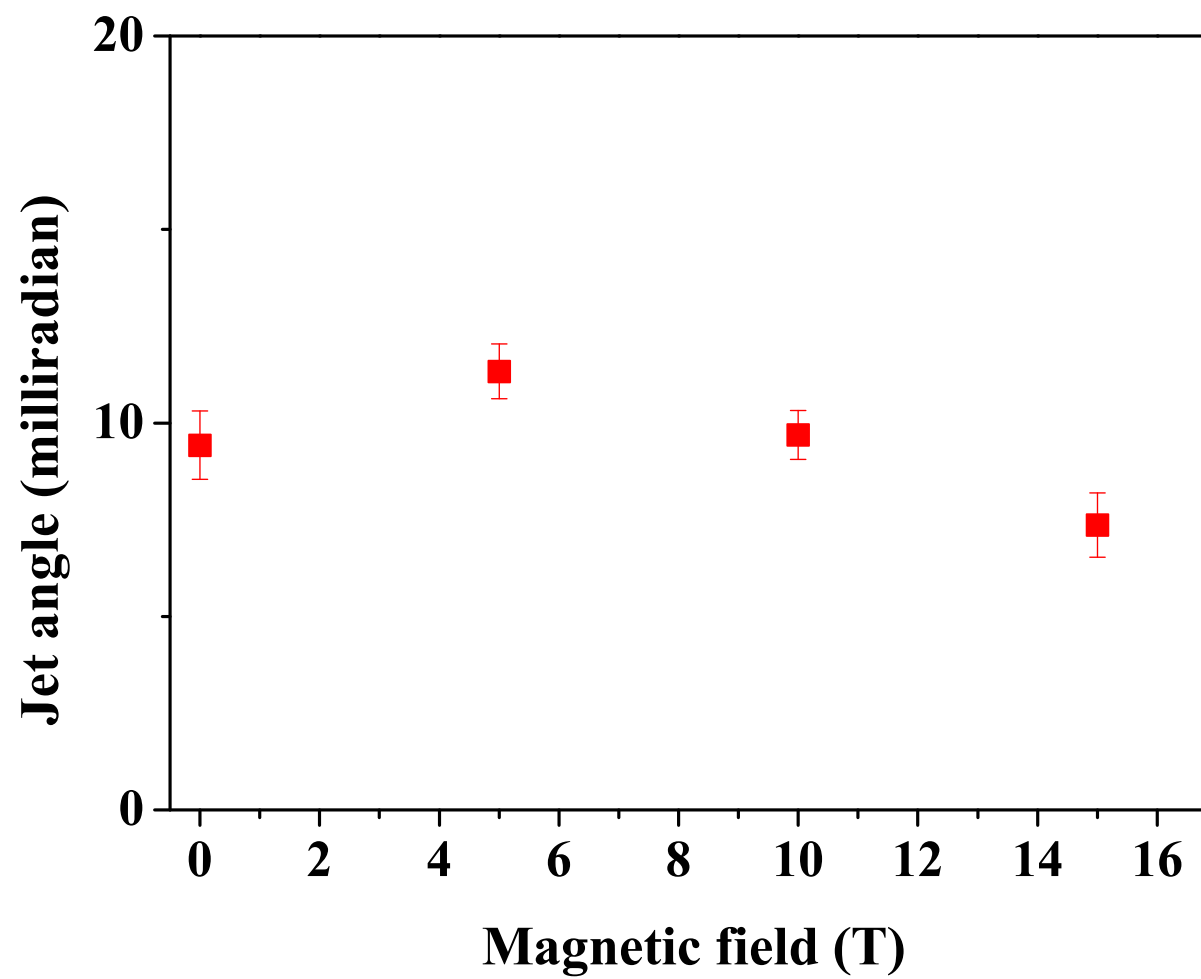


Figure 4.11: Hg jet angle at the center of magnetic axis (Viewport 2) as a function of magnetic field.

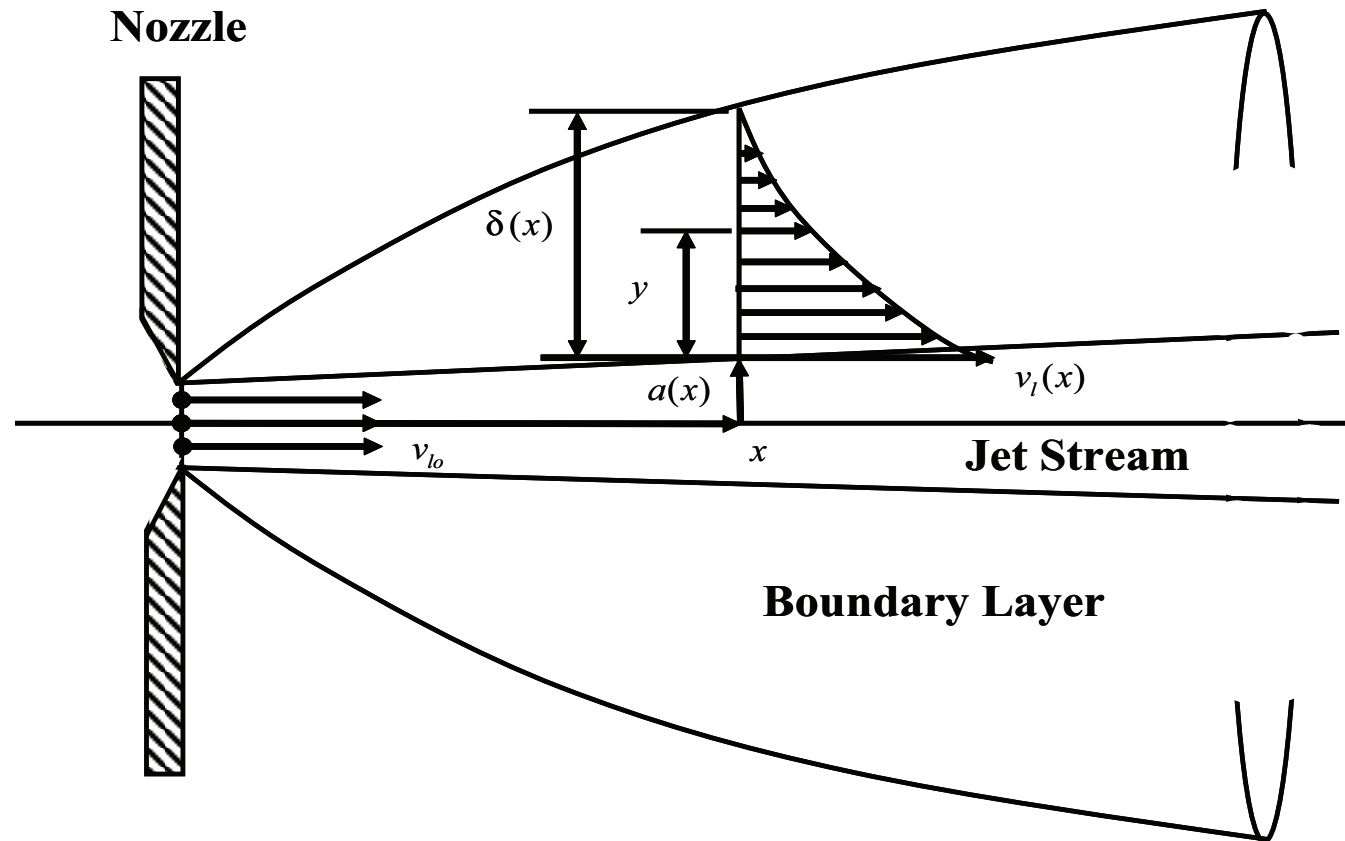


Figure 4.12: Boundary layer induced by a jet emerging from a nozzle.

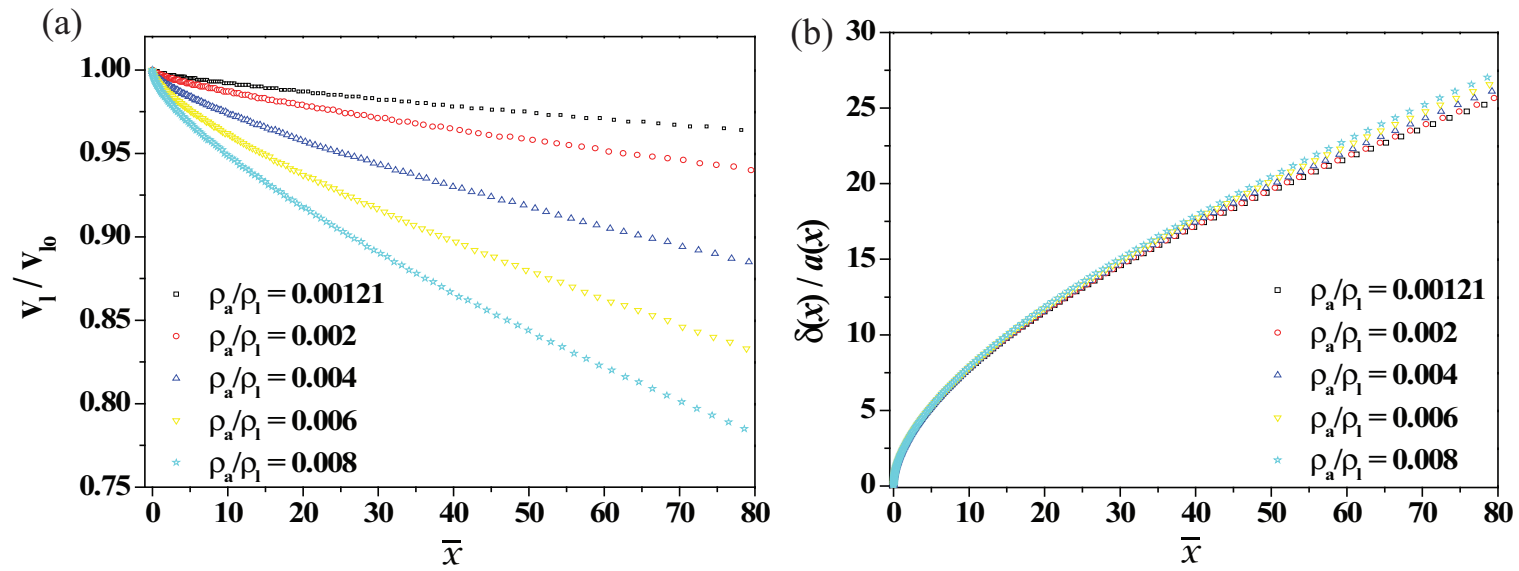


Figure 4.13: Stream velocity and boundary layer thickness for various values of density ratio.

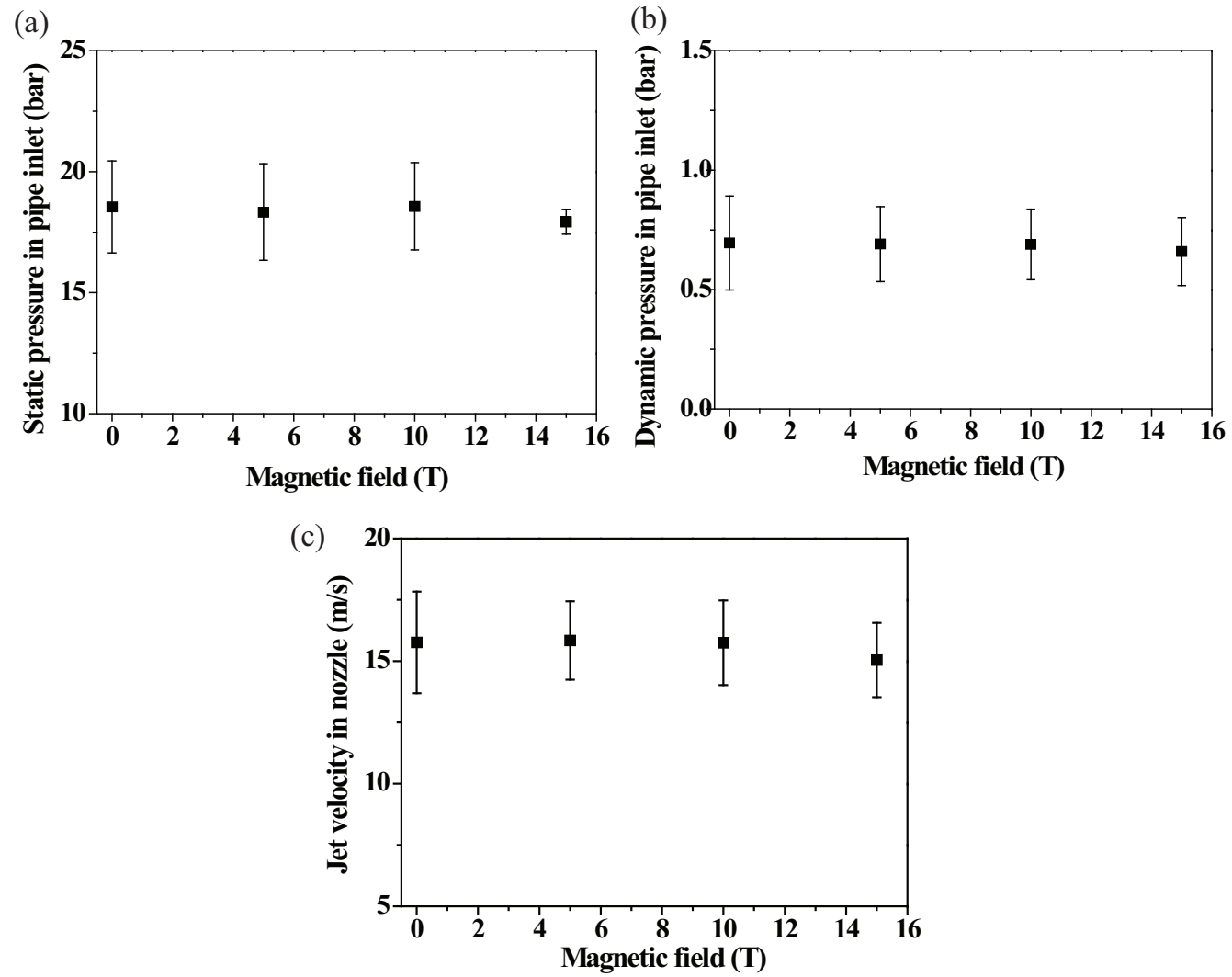


Figure 4.14: Pipe inlet pressure for driving Hg jet. a.) Static pressure. b.) Dynamic pressure. c.) Jet velocity in nozzle (Graves, 2007).

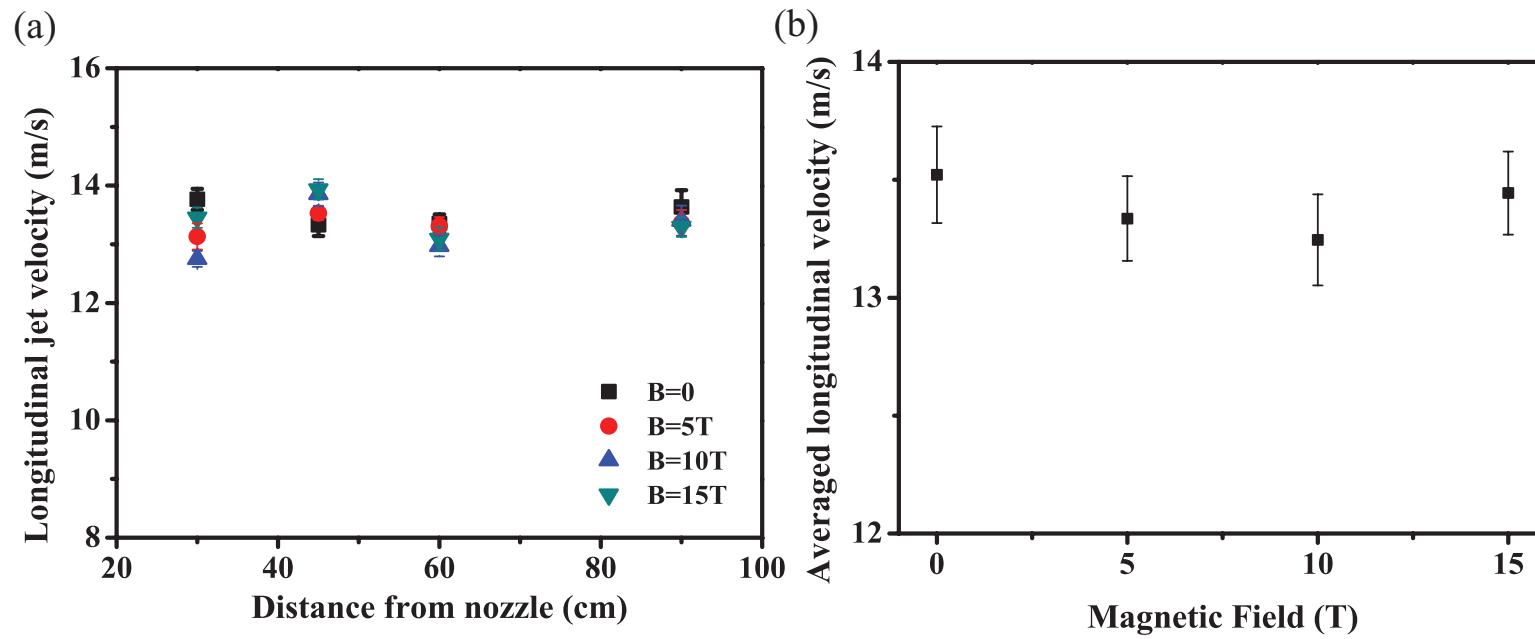


Figure 4.15: Longitudinal Hg jet flow velocity in magnetic field. a.) Velocity at each Viewport dependent of magnetic field. b.) Averaged velocity at each Viewport independent of magnetic field.

## 2502 Chapter 5

# 2503 Interaction of an Intense Proton 2504 Beam with Hg Jet in Magnetic 2505 Field

2506

2507 In this chapter, the jet's interacting characteristics in magnetic field are  
2508 investigated. The disruption of the jet interacting with various beam intensities  
2509 and beam energy is observed and the magnetic suppression to it is discussed.  
2510 The captured images show the mechanism of the beam-jet interaction and the  
2511 qualitative consistency with the distribution of calculated energy deposition  
2512 is discussed. The energy deposition induced by the proton beam generates  
2513 filaments on the Hg jet surface due to thermal stresses. The filaments velocity  
2514 and its reduction by magnetic field are discussed.

2515

## 2516 5.1 High Energy Proton Beam Structure

### 2517 5.1.1 Proton synchrotron machine

2518 Neutrino factories requires a large number of muons, which are obtained  
2519 from the decay of pions. Efficient production of pions can be achieved by

colliding an intense proton beam with a high-Z target. An important consideration is the problem of removing the power deposited by the proton beam without interfering with the process of extracting the end-product, which is the muon beam. The response of a liquid target in a high-magnetic induction field will have beam energy effects, which is investigated experimentally. Experiments on the interaction of a 14 GeV and 24 GeV proton beam with pulse structures of 4 to 16 bunches per pulse and the spot sizes in the order of 2 to 10 mm<sup>2</sup> RMS up to 30 tera-protons(Tp) per pulse in magnetic field up to 15 T has been carried out at CERN. Figure 5.1 (a) shows the infrastructures for experiment at CERN. All equipments for experiment are installed at tunnel TT2/TT2A and these are controlled remotely at control room. The proton beam is delivered from proton synchrotron ring and the beam setup is schematically shown in Fig. 5.1 (b). The PS machine is set up in harmonic 16 bunches and the extracted protons fill the machine in bunch pairs. A bunch in harmonic 8 mode is consisted of a bunch pair. Therefore, a bunch period in harmonic 8 mode is two times of a bunch period in harmonic 16 mode. Each bunch can fill protons up to  $2.5 \times 10^{12}$ . Therefore, the maximum beam intensity can be achieved up to  $32 \times 10^{12}$  protons. Figure 5.2 shows the layout of tunnel at CERN, where equipments for experiment are installed. Electronic equipments for optical diagnostics, hydraulic power unit, and cryogenic system are positioned at tunnel TT2. Hg loop system, solenoid magnet, and beam diagnostic system are positioned at tunnel TT2A. The fibers for optical diagnostics of Hg target in solenoid magnet and cables for controlling the Hg loop system and solenoid



2543 magnet are connected between TT2 and TT2A passing through an artificially  
2544 drilled hole.

### 2545 5.1.2 Proton beam pulse length

2546 In order to produce the design number of  $10^{21}$  muons /year in muon storage  
2547 ring, 4 MW of proton beam power is desired. For our experiment, the CERN  
2548 PS ran typically in a harmonic 16 mode. Hence, it is possible to fill with  $2 \times$   
2549  $10^{12}$  protons/bunch and therefore up to  $32 \times 10^{12}$  protons/spill. One beam  
2550 pulse consists of several beam bunches. The bunch lengths for harmonic 16  
2551 mode are 50 ns and 30 ns at full width at half maximum (FMWH) respectively.  
2552 The bunch lengths for harmonic 8 mode are 70 ns and 40 ns at full width  
2553 at half maximum (FMWH) respectively. The bunch-to-bunch differences for  
2554 harmonic 16 mode and harmonic 8 mode are multiples of 131 ns and 262 ns  
2555 respectively. The proton beam pulse structure of harmonic 8 and harmonic 16  
2556 in 14 GeV, 6 Tp is shown in Fig. 5.18. The spot size at the experiment is in  
2557 the order of 2 to 10 mm<sup>2</sup> RMS. This allows to place up to  $32 \times 10^{12}$  protons  
2558 on the mercury target, generating a peak energy deposition of  $\sim 150$  J/g.  
2559 Power consumption is dominated by the repetition rate. Thus, the capability  
2560 to replace the disrupted jet determines the ultimate beam power. The optimal  
2561 interaction length for the 24 GeV beam energy is in the region of 30 cm which  
2562 corresponds to approximately 2 interaction length for mercury (Kirk *et al.*,  
2563 2008). For a 20 m/s jet velocity, replacing two interaction lengths will be  
2564 taken in 14 ms thus allowing for operations with a repetition rate of up to

70 Hz. The beam energy per pulse is 115 kJ for a beam of  $30 \times 10^{12}$  protons with 24 GeV beam energy. The disruption length at  $30 \times 10^{12}$  protons with 24 GeV beam energy in a magnetic field of 15 T is less than 20 cm at 24 GeV beam energy in Fig. 5.21, thus preserving the 70 Hz beam repetition rate option. It yields the key result that a target system capable of supporting proton beams with powers of up to 8 MW (Kirk *et al.*, 2008).

### 5.1.3 Proton beam envelope by optics and camera screen

The proton beam with 14 GeV and 24 GeV beam energy is employed in the experiment. As the number of protons in a beam pulse increases, it is reported (Efthymiopoulos, 2008) that the beam spot size increases. The beam spot size is calculated by CERN using the measured beam emittance, dispersion, and the momentum spread of the beam particle. The emittance is measured by measuring the beam profile in a position of known beam parameters based on optics. Figure 5.4 shows the estimated  $1 \sigma$  beam spot size at the center of target based on optics (Efthymiopoulos, 2008). Figure 5.5 shows the measured  $1 \sigma$  beam spot size at the phosphor camera screen installed  $\sim 4.2$  m away from the center of magnet before entering the magnet (Skoro, 2008). It is also reported (Skoro, 2008) that the beam spot size increases as the number of protons increases. Due to the saturation of image, the measured size is shown as  $\sim 2$  times larger than the estimated beam spot size from optics. Figure 5.6 (c) shows the beam sizes distribution measured by phosphor screen monitor as a function of time interval between beam shots, where the histogram for events

of beam size in horizontal plane is shown in Fig. 5.6 (a) and the histogram for events of beam size in vertical plane is shown in Fig. 5.6 (b). This plots show that the possible residual saturation of image by phosphor screen monitor is not related with time interval between each beam shot. The distribution of beam spot size is uniform regardless of the possible residual saturation by screen monitor.

## 5.2 MARS Simulation for Energy Deposition to Mercury Jet by Proton Beam

### 5.2.1 Physics model

MARS is a Monte Carlo code for inclusive and exclusive simulation of 3D hadronic and electromagnetic cascades, muon and heavy ion transport in accelerator, detector, and shielding components in the energy range from a fraction of an electronvolt up to 100 TeV. In MARS code, hadron production, neutrino interactions, electromagnetic interactions of heavy particles, and electromagnetic showers are considered. For hadron production, information on the nuclides generated in nuclear collisions is scored, or reported in the results of the simulation, which covers a hadron kinetic energy range up to 100 TeV. For neutrino interactions, the model permits the selection of the energy and angle of each particle ( $\nu, e, \mu$ ) emanating from a simulated interaction. These particles, and the showers initiated by them, are then further processed in the code. Four types of neutrino interactions are distinguished ( $\nu_\mu, \bar{\nu}_\mu, \nu_e, \bar{\nu}_e$ ) and the model identifies all possible types of neutrino interactions with nuclei. The

corresponding formulas for these processes as well as results of Monte Carlo simulations are considered. For electromagnetic interactions of heavy particles, electromagnetic interactions of muons and charged hadrons in arbitrary materials are simulated. Radiative processes and atomic excitation and ionization with energy transfer are considered. The electromagnetic showers are based on the physics of electromagnetic interactions and it gives electron and photon interactions in composite solid, liquid and gaseous materials (Mokhov, 2000).

### 5.2.2 Mercury jet modeling in MARS code

Using MARS code, Calculation of energy deposition is performed at Fermi National Accelerator Laboratory (Striganov, 2009). For the modeling of jet in MARS, the experimentally measured Hg jet size and trajectory in magnetic field with assumption of sectionally elliptic jet shape and circular jet shape with equivalent reduced mass density to the initial flow rate from nozzle. The proton beam is passing through the center of magnetic axis. For simplicity, the z coordinate of modeling in MARS defines as 0 at the center of magnetic axis along the direction of magnetic field. Accordingly, the x coordinate of modeling in MARS defines as the vertical direction perpendicular to the direction of magnetic field. The experimentally measured jet size and vertical position to the center of magnetic axis is shown at Fig. 4.6 and Fig. 4.10. The experimental measurement of vertical distance between magnetic axis and the center of jet is given in Table 5.1, where the experimentally measured jet size as well as approximated mass density for the simulation of circular jet case are also given.

2631 The vertical distance in cm in MARS code between center of jet and magnetic  
 2632 axis is employed as follow:

2633

$$x_{vert} = -1.4522 - 3.65 \times 10^{-2} \times zz - 3.1672 \times 10^{-4} \times zz^2 + 5.4206 \times 10^{-9} \times zz^4, \quad (5.1)$$

2634

2635 where  $zz = z - 46$  in cm.

2636 Figure 5.7 (a) and (b) show the sectional view of elliptic/circular jet and  
 2637 Fig. 5.7 (c) shows the side view of jet interacting with proton beam in magnetic  
 2638 field, which is indicated as arrows. Using MARS code, Calculation of energy  
 2639 deposition with various magnetic field strength and beam intensity is performed  
 2640 at Fermi National Accelerator Laboratory (Striganov, 2009).

## 2641 5.2.3 Energy deposition to mercury jet

### 2642 5.2.3.1 *energy deposition in magnetic field*

2643 Figure 5.8 shows the averaged energy deposition along the jet axis for  
 2644 the case of 2 Tp according to the variation of magnetic field. Calculated  
 2645 energy deposition in each meshed volume is averaged along the jet axis using  
 2646 Eqn. (5.2):

2647

$$E(z) = \frac{1}{N_{\theta}^r} \sum_r \sum_{\theta=0}^{2\pi} E_{\theta}^r(r, z, \theta), \quad (5.2)$$

2648

2649 where  $N_{\theta}^r$ ,  $E_{\theta}^r$  represent the number of meshes along radial angle at each  
 2650 radial distance and its energy deposition respectively. As the magnetic field

increases, the distribution of energy deposition over the jet increases. This indicates interaction of charged particles with magnetic field, so that more atomic excitation and ionization with energy transfer occurs in higher magnetic field. Also, the electromagnetic shower produced by a particle that interacts via the electromagnetic force gives electron and photon interactions in mercury. From the equation of particle motion and Lorentz force in Eqn. (5.3), the momentum of charged particle has an influence of the intensity of magnetic field followed by Maxwell's equations.

$$\frac{d\mathbf{p}}{dt} = e[\mathbf{E} + \mathbf{v} \times \mathbf{B}], \quad (5.3)$$

where  $e$  is the charge on the particle and  $\mathbf{v}$  is the particle velocity.

### 5.2.3.2 *geometric distribution of energy deposition in elliptic Hg jet cross section*

Figure 5.9 (a) shows the radially averaged energy deposition over the orientation in sectional jet area along the jet axis for the case of 2 Tp in 5 T. Calculated energy deposition in each meshed volume is averaged along the jet axis using Eqn. (5.4):

$$E(z, \theta) = \frac{1}{N_{\theta}^r} \sum_r E_{\theta}^r(r, z, \theta). \quad (5.4)$$

The larger distribution of energy deposition occurs at bottom ( $\sim 270^\circ$ ) of jet where the beam enters. Gradually the larger distribution moves to the top ( $\sim 90^\circ$ ) of jet where the beam leaves. It again gives the consistent result with

Fig. 5.15 (a) and Fig. 5.16 (a), where the profile of energy deposition shows its changes along with the beam path through Hg jet.

Figure 5.9 (b) shows the axially averaged energy deposition over the variation of magnetic field along the orientation in sectional jet area for the case of 2 Tp in 5 T. Calculated energy deposition in each meshed volume is averaged along the orientation in sectional jet area using Eqn. (5.5):

$$E(\theta) = \frac{1}{N_z^r} \sum_z \sum_r E_z^r(r, z, \theta), \quad (5.5)$$

where  $N_z^r$ ,  $E_z^r$  represent the number of meshes along axial jet axis at each radial distance and its energy deposition respectively. The larger axially averaged energy deposition is at bottom ( $\sim 270^\circ$ ) of jet and the distribution of energy deposition increases as the magnetic field increases. The geometrical distribution of energy deposition depending on the applied magnetic field does not change but keeps uniform profile of distribution, which indicates that the profile of distribution is most likely dependent to the shape of Hg jet.

### 5.2.3.3 *proton beam spot size to the energy deposition*

Figure 5.11 shows the averaged energy deposition per proton along the jet axis using Eqn. (5.2) according to the variation of number of protons in 10 T. As shown in Fig. 5.4, the beam spot size increases as the number of protons increase. As a result, the energy deposition per proton decreases due to the decrease of beam intensity caused by increasing beam spot size. Figure 5.12 shows the variation of peak energy deposition per proton and total energy

deposition to mercury jet with respect to the number of protons at both 14 GeV and 24 GeV beam energy in magnetic fields. The total energy deposition amounts to  $\sim 6 \sim 8$  % of the incident beam energy and the total energy deposition is slightly decreasing depending on the variation of beam spot size. However, the total energy deposition increases as the magnetic field increases. As discussed in Fig. 5.8, it again indicates interaction of charged particles with magnetic field, so that more atomic excitation and ionization with energy transfer occurs in higher magnetic field. However, the peak energy deposition is determined by the incident number of protons regardless of magnetic field strength. The solid line in Fig. 5.12 (a) and (b) represent the fit of calculated peak energy deposition per proton using Eqn. (5.6) and Eqn. (5.7) respectively, shown as

$$z = (A_1 + B_1 x^{B_2}) w^{C_1} \quad (5.6)$$

and

$$z = A_1 (y - B_1)^{B_2} w^{C_1} + x B_3 w^{C_2}, \quad (5.7)$$

where  $x$ ,  $y$ ,  $z$ , and  $w$  denote number of protons, magnetic field, energy deposition, and beam energy respectively. Note that the parameterized values of coefficients and errors of the fit functions for energy deposition with respect to number of protons, magnetic field, and beam energy are given in Table 5.2. The energy deposition is estimated by using fit function and error. The peak energy deposition decreases with square rooted power of number of protons,



and it increases with  $\sim 1.5$  power of beam energy between 14 GeV and 24 GeV. The ratio of beam energy between 14 GeV and 24 GeV is  $\sim 1.7$ . The total energy deposition decreases slightly linearly with number of protons and increases with 0.06 power of magnetic field strength. Thus, the total energy deposition has an increase with  $\sim 1.4$  power of beam energy as an offset between 14 GeV and 24 GeV, and  $\sim 0.9$  power of beam energy as an slope in fit function , which indicates possibly that the absolute ratio of power  $\sim 1.5$  due to the beam energy difference is separated into two coefficient terms ratio of  $C_1$  to  $C_2$  in fit function.

Based on the result in Fig. 5.12, the number of protons are multiplied to the peak energy deposition per proton, which yields the result in Fig. 5.13 on logarithmic scale. The peak energy deposition with respect to the number of protons increases parabolically due to the increase of parabolically approximated beam cross sectional area, which directly influences to the peak energy deposition to Hg jet. Also, the higher magnetic field again results in larger total energy deposition to Hg jet.

The solid line in Fig. 5.13 (a) and (b) represent the fit of calculated peak energy deposition using Eqn. (5.8) and Eqn. (5.9) respectively, shown as

$$z = A_1 x^{B_1} w^{C_1} \quad (5.8)$$

and

$$z = A_1 x^{B_1+B_2 y^{B_3}} w^{C_1}. \quad (5.9)$$

2741 The fit result from Eqn. (5.8) shows that the peak energy increases with  $\sim$   
 2742 0.8 power of number of protons on linear scale. As one expects, on logarithmic  
 2743 scale, it can be rephrased as a linear relation with  $\sim 0.8$  between number  
 2744 of protons and peak energy deposition, and  $\sim 1.6$  between beam energy and  
 2745 number of protons. The fit result from Eqn. (5.9) shows that the total energy  
 2746 deposition increases with  $\sim 0.9$  power of number of protons, but it slightly  
 2747 increases with  $\sim 0.4$  power of magnetic field. Again, on logarithmic scale,  
 2748 total energy deposition increases linearly with  $\sim 1.4$  times of beam energy.  
 2749 This study is useful since it allows one to extrapolate the trend for estimation  
 2750 of profile of energy deposition, so that one can approximate the profile of  
 2751 energy deposition over all of the region of Hg jet based on the characteristics  
 2752 of relations in energy deposition to magnetic field, beam intensity, and Hg jet  
 2753 shape.

## 2754 **5.3 Observation of Interaction and Hg Jet Response** 2755 **to The Energy Deposition by Proton Beam**

### 2756 **5.3.1 Hg jet pressurization by energy deposition of proton** 2757 **beam**

2758 The energy deposition  $E_{dep}$  due to ionization losses of the protons is  $\sim$   
 2759 33 J/g and additional ionization due to secondary particles from interactions  
 2760 of the protons in the target raises this to a peak of  $\sim 100$  J/g at 10 cm into the  
 2761 target (McDonald, 2000). The energy deposition,  $E_{dep}$ , leads to peak pressure  
 2762  $P$  that can be estimated as follow:

2763

2764

$$P \approx K \alpha_v \Delta T = \frac{\alpha_v K E_{dep}}{c_p} , \quad (5.10)$$

2765

2766

2767

2768

2769

2770

2771

2772

2773

2774

2775

$$E_{strain} = \frac{K}{2} (\alpha \Delta T)^2. \quad (5.11)$$

2776

2777

2778

2779

where  $\alpha_v$  is the thermal volumetric expansion coefficient, which corresponds to 3 times of thermal linear expansion coefficient,  $K$  is the bulk modulus,  $E_{dep}$  is the energy deposition, and  $c_p$  is the specific heat capacity. For mercury,  $\alpha_v = 180 \times 10^{-6}/K$ ,  $K = 25$  GPa,  $c_p = 138$  J/(K kg). A peak value of  $E_{dep}=100$  J/g corresponds to a peak stress of  $\sim 3000$  MPa. The mercury target will be disrupted by the proton beam, leading to a breakup into droplets. The strain energy is built up in the jet due to compression (Sievers and Pognat, 2000). The strain energy per unit volume can be estimated as follow based on the relationship between pressure thermal expansion:

This deposited strain energy will be released as kinetic energy such as the generation of filaments on the jet surface. Hence, it indicates that the thermal volumetric expansion is possibly proportional to the jet expansion velocity with the coefficient of compressibility of jet material.

2780

2781

### 5.3.2 Observation of proton beam interaction and jet breakup

2782

2783

2784

Figure 5.14 is the photographs of the typical Hg jet interacting mechanism with a 16 Tp, 14 GeV proton beam at 5 T captured at Viewport 3 at a  $500 \mu s$  frame rate, which shows clearly how the Hg jet is responding from the sudden

energy deposition by the proton beam. The beam hits the Hg jet at the bottom surface, passing through the center of jet at Viewport 2, leaving the Hg jet on the top surface. The captured photos show the response of the Hg jet upstream, midstream, and downstream with the interaction of proton beam. There are filaments on the top surface of jet downstream, where the beam is leaving, and on the bottom surface of the jet upstream, where the proton beam is hitting, entering the target. The jet break up voids midstream where the beam is passing through, possibly caused by the cavitations from energy deposition.

### 5.3.2.1 *energy deposition calculation with low intensity of proton beam and its observation*

Figure 5.15 (a) shows the distribution of energy deposition by 24 GeV, 3 Tp intensity of proton beam in 5 T. Calculated energy deposition in each meshed volume is averaged along the jet axis and vertical radius of jet using Eqn. (5.12):

$$E(z, r) = \frac{1}{N_{\theta}^r} \sum_{\theta=0}^{2\pi} E_{\theta}^r(z, r, \theta), \quad (5.12)$$

where  $N_{\theta}^r$  and  $E_{\theta}^r$  represent the number of meshes along radial angle at each radial distance and its energy deposition respectively.

The spot size from optics is used. The energy density distribution is plotted depending on the radial position of Hg jet from jet center. Therefore, the peak of energy density exists respectively depending on the radial position in

analysis. It shows that the maximum energy deposition density is obtained at the bottom surface of jet at  $\sim 13$  cm from the center of magnet, where Viewport 1 is actually positioned, and the peak energy deposition density moves to the center of the Hg jet followed by the larger energy deposition density is located at the top surface of the Hg jet. The peak energy deposition density is moving corresponding to the beam crossing trajectory in Hg jet. The most dense energy deposition is distributed at the center of Hg jet between upstream and midstream, where the Hg jet breaks. The collected photos in Fig. 5.15 (b) clearly supports these simulation results, where the frame rate is 2 ms and measured disruption length at Viewport 3 is 11 cm.

### 5.3.2.2 *energy deposition calculation with high intensity of proton beam and its observation*

Figure 5.16 (a) shows the distribution of energy deposition by 24 GeV, 10 Tp intensity proton beam in 5 T. Averaged energy deposition is also calculated using Eqn. (5.12). The distribution profile of energy deposition throughout Hg jet is similar with low intensity of beam. The collected photos in Fig. 5.16 (b) clearly supports these simulation results again, where the frame rate is 2 ms and measured disruption length at Viewport 3 is 17 cm. However, the jet breakup voids the midstream where the beam is passing through, which is different with comparing with the observation of low intensity beam. These voids are not observed at 3 Tp intensity of beam, possibly indicates threshold of the existence of cavitation induced by energy deposition.

### 5.3.3 Hg jet disruption and magnetic suppression of the disruption

The disruption length is determined by counting the number of frames at Viewport 3 where the complete disruption of the jet is observed. The time delay between Viewport 2 and Viewport 3 is 10 ms. Thus, the disruption generated at Viewport 2 by the beam could be observed at Viewport 3 after 10 ms, where the jet is moving with a velocity of 15 m/s. Each image is separated into 10 segments vertically in order to locate the position of disruption. Thus, the accuracy of the measurement to define the location of starting(ending) disruption in measurement could be increased. The disruption length is given by multiplying the frame rate by the counted number of images and investigated with the beam energy, beam intensity, and magnetic field. 230 events out of 360 beam shots are evaluated for the disruption length. About 130 events out of 360 beam shots are evaluated for the detection of particles without Hg jet. Thus, the images for these events are not collected. Figure 5.17 shows the standard deviation of the evaluated disruption lengths with respect to the disruption length. The solid line represents the curve fitted approximation of the reduced data distribution, where the line asymptote logarithmic. This curve fitted line is used for estimation of the standard deviation of the disruption length at respective disruption length. Correspondingly, the error bar is determined by dividing the the estimated standard deviation by the root square of the number of samples N for each data point.

### 5.3.3.1 *characteristics of beam structure in disruption length, harmonic 8 and 16*

The proton beam pulse structure of harmonic 8 and harmonic 16 in 14 GeV, 6 Tp is shown in Fig. 5.18. A pulse carries same number of protons with doubled bunch structures. Fig. 5.19 shows the dependence of the disruption length of the Hg jet on the proton beam pulse structure with a 14 GeV beam in 5 T. The solid line in Fig. 5.18 (a) and (b) show the global fit and independent fit of disruption length with both harmonic 8 and harmonic 16 bunches as a function of total energy deposition respectively. A liner fit function is used as follow:

$$z = A_1(x - B_1), \quad (5.13)$$

where  $x$  and  $z$  denote the total energy deposition and disruption length respectively. The  $\chi^2$  probability of global fit in Fig. 5.18 (a) is 0.056. The  $\chi^2$  probability of each independent fit in Fig. 5.18 (b) by using the sum of  $\chi^2$  and degrees of freedom of each independent fit yields 0.051. From this point of view, there is no statistical difference between the two ways of fitting, so that one could conclude that the disruption length does not depend on harmonic number. The disruption of Hg jet is affected by the number of protons, resulted from energy deposition of interaction of number of protons. The short time in each bunch structure is negligible. The disruption on the Hg jet surface disappears when the beam intensity is less than  $\sim 4$  Tp in Fig. 5.20. The threshold of beam intensity is  $\sim 4$  Tp at 14 GeV in 5 T.

### 5.3.3.2 *disruption length with 14 GeV proton beam*

Fig. 5.20 shows the disruption length with beam intensities up to 30 Tp for a 14 GeV beam. The peak and total energy deposition to Hg with 14 GeV beam energy at 30 Tp and 15 T is  $\sim 52$  J/g and 3700 J by approximating it from Fig. 5.13, where the disruption length corresponds to  $\sim 23$  cm  $\pm$  5 cm for 10 T to  $\sim 18$  cm  $\pm$  5 cm for 15 T respectively. At high intensities of beam, the disruption length appears to be approaching an asymptotic level. The magnetic field suppresses weak disruption such as onset of generation of the filaments on the jet surface. The threshold of the disruption for beam intensity is around 4 Tp at 5 T and the magnetic field can increase it, though the effect is not clear in Fig. 5.20 due to the difficulty in quantifying and judging to measure the small amount of the disruption length.

### 5.3.3.3 *disruption length with 24 GeV proton beam*

Figure 5.21 shows the disruption length with the beam intensities up to 30 Tp for a 24 GeV proton beam. The estimation of disruption length is performed by estimating the extent of energy in Hg jet along jet axis larger than the energy deposition experimentally determined by threshold intensity of beam as follow :

$$L_E^{disruption}(z) = z_2 - z_1, \quad E(z) \geq E_{threshold}^{peak}(z), \quad L_{E_{threshold}^{peak}}^{disruption}(z) = 0, \quad (5.14)$$

where  $L^{disruption}$  and  $E_{threshold}^{peak}$  represent the length of disruption and peak energy of thresholding intensity of beam experimentally determined for jet



disruption. For example, Fig. 5.16 (a) shows the profile of energy deposition along jet axis. Therefore, energy in mercury jet is known. By using Eqn. (5.8), one can estimate peak energy deposition at  $3.7 \text{ Tp}$ , which is the experimentally determined threshold intensity of beam. Now, in Fig. 5.15 (a), find the extent of length along jet axis where the energy in Hg jet is larger than the peak energy at threshold intensity of beam. The jet length determined here is judged as disruption length of jet and it is plotted in Fig. 5.21.

According to Fig. 5.13, the peak and total energy deposition to Hg with 24 GeV beam energy at 30 Tp in 10 T is  $\sim 125 \text{ J/g}$  and 8200 J, where the disruption length corresponds to  $\sim 22 \text{ cm} \pm 5 \text{ cm}$  for 10 T to  $\sim 17 \text{ cm} \pm 5 \text{ cm}$  for 15 T respectively. The results again show that the magnetic field suppresses the disruption length. The disruption length appears to be approaching an asymptotic level. If there is no magnetic field, the disruptions are always generated by proton beam regardless of the beam intensities, though very weak disruptions on the Hg jet surface are observed with low beam intensities. The threshold of the disruption for beam intensity is  $\sim 1 \text{ Tp}$  at 5 T but the higher magnetic field increases it. The estimation of disruption length in 10 T based on the calculation of energy deposition using the beam spot size from optics is well agreed with the experimental measurement, but the estimation in 0 T based on the beam spot size from optics underestimates the experimental results. Possibly, the difference in MARS model may cause the difference of energy deposition calculation and the beam spot size is more likely to be larger at 0 T. Therefore, possibly the estimation by energy

deposition from larger beam spot size is more likely to be fit to the experimental measurement. For these estimations, the independent threshold of beam intensity is chosen individually from the experimental results depending on the conditions of individual cases for estimation. Therefore, the energy for threshold is differently used for each case of estimation using the beam size from optics and camera. For the case of estimation of 0 T, 5 T, and 10 T, 0.8 Tp, 1.5 Tp, and 3.7 Tp of threshold beam intensity are chosen respectively.

#### 5.3.3.4 *validation of measurements of Viewport 3 through comparison with Viewport 4*

In order to validate measurements of the disruption length at Viewport 3, measurements of disruption lengths at Viewport 4 are also performed. Fig. 5.22 (a) shows the disruption length at Viewport 3 for 23 events with a harmonic 16 beam structure, 16 Tp, 14 GeV beam energy in 5 T. Figure 5.22 (b) shows the disruption length at Viewport 4 for the same events. Figure 5.22 (c) shows the difference of disruption length between Viewport 3 and Viewport 4 for the same events. The solid line represents the average and distribution of the disruption length difference based on gaussian distribution approximation. The difference of measured disruption length between Viewport 3 and Viewport 4 is  $1.3 \pm 3.5$  cm. The reason for the difference of the disruption length measurement between Viewport 3 and Viewport 4 is mainly caused by the fluctuation of the proton beam and the Hg jet in a magnetic field. The reduction of surface instabilities by the presence of a static magnetic field is a consequence of magnetic damping. Also, surface structure is frozen by magnetic field.

Therefore, the same disrupted shape on the jet surface at Viewport 3 is observed at Viewport 4 without variation of the disruption length.

### 5.3.3.5 *disruption measurement in pump-probe condition as a check of experiment*

Figure 5.23 shows the measured disruption length of multiple events with pump-probe conditions as a check of experiment. The conditions of each group in pump-probe events are given in Table A.4. There are 4 groups at 14 GeV and each group has different number of bunches and time delay between pump and probe. Figure 5.23 (a) shows the histogram of disruption length and Fig. 5.23 (b) shows statistics summary such as average, minimum, maximum, and median value. In group 2, qualitatively meaningful distribution of measurements are shown, which is  $19.8 \pm 6.1$  cm. In sub-category of group 2, 3 different time delay between 6 bunches and 2 bunches does not show significant difference in disruption length. This check is agreed with the result provided in both Fig. 5.20 and Fig. 5.24.

## 5.4 Disruption of Hg Jet By Energy Deposition

Fig. 5.24 shows the disruption of mercury jet in magnetic fields as a function of total energy deposition and fit of model using Eqn. (5.6) up to 25 T. Figure 5.25 shows the disruption of mercury jet in magnetic fields as a function of fluence and fit of model using Eqn. (5.6) up to 25 T, where fluence is defined as  $Tp/(\sigma_x\sigma_y)$  and the beam intensity is normalized with beam spot area. Figure 5.26 the disruption of mercury jet in magnetic fields as a function of

peak energy deposition and fit of model using Eqn. (5.6) up to 25 T.  $\chi^2$  values indicate somewhat comparison of goodness of fit for Fig. 5.24, Figure 5.25, and Figure 5.26, where fit of model as a function of total energy deposition yields the lowest  $\chi^2$  value. In addition to that, as discussed, the extent of disruption of jet is dominated by the distribution of energy deposition interacting with proton beam. Therefore, the total energy deposition is more likely to play a role in determining of the extent of disruption of Hg jet. The total energy deposition in magnetic fields is investigated. The total energy deposition depending on colliding number of protons at both 14 GeV and 24 GeV beam energy is calculated by Fig. 5.13 (b). Thus, Fig. 5.20 and Fig. 5.21 are combined as a function of total energy deposition, which shows the results of experiment in disruption length at a glance. As a finally important result for experiment, Fig. 5.24 shows the disruption of mercury jet in magnetic fields as a function of total energy deposition and its extrapolation up to 25 T. The employed global fit with multi-variables for disruption length using the measured disruption length is:

$$z = A_1(x - (B_1 + B_2y^{B_3}))^{\frac{1}{C_1+C_2y+C_3y^2}}, \quad (5.15)$$

where  $x$  and  $y$  are total energy deposition and magnetic field respectively. Note that the parameterized values of coefficients and errors of the fit functions are provided in Table 5.2. The threshold of disruption increases in 0.8 power of magnetic field, and it is 338 J of total energy deposition with no magnetic field. Also, the threshold of disruption is  $\sim 10$  J of peak energy deposition

2987 with no magnetic field, and it increases in 1.2 power of magnetic field. The  
2988 disruption length increases in square root power of total energy deposition  
2989 with no magnetic field, but it is suppressed in  $\sim 1/(2 + 0.04B)$  power of total  
2990 energy deposition with magnetic field.

2991 In Fig. 5.24, the disruption length at 15 T is less than 20 cm and the total  
2992 energy deposition is  $\sim 8000$  J. According to Fig. 5.13 (b), approximately 6  $\sim$   
2993 8 % of beam energy is deposited into mercury target. Therefore, 100  $\sim$  133 kJ  
2994 of beam energy can be recycled with a 70 Hz repetition rate for 20 m/s jet.  
2995 This result validates that a target system capable of supporting proton beams  
2996 with powers of up to 8 MW, which is a key result for this experiment.

Table 5.1: Measurement of vertical distances of center of jet from magnetic axis and jet size for modeling in MARS code for the cases of elliptic and circular jet sectional shape.

<b>1</b> (T)	<b>2</b> (mm)	<b>3</b> (mm)	<b>4</b> (mm)	<b>5</b> (mm)	<b>6</b> (mm)	<b>7</b> (mm)	<b>8</b> ( $g/cm^3$ )
Elliptic jet shape							
0	7.11	4.46	4.28	5.01	8.65	2.9	13.55
5	7.1	4.52	3.7	4.38	8.4	3.0	13.55
10	6.57	4.08	3.66	3.71	7.95	3.15	13.55
15	5.45	3.6	3.24	3.11	9.05	2.76	13.55
Circular jet shape							
0	7.11	4.46	4.28	5.01	8.65	8.65	4.50
5	7.1	4.52	3.7	4.38	8.4	8.4	4.77
10	6.57	4.08	3.66	3.71	7.95	7.95	5.32
15	5.45	3.6	3.24	3.11	9.05	9.05	4.11

- 
- 1** : Magnetic field  
**2** : Vertical distance at Viewport1  
**3** : Vertical distance at Viewport2  
**4** : Vertical distance at Viewport3  
**5** : Vertical distance at Viewport4  
**6** : Vertical radius of jet  
**7** : Horizontal radius of jet  
**8** : Hg density

Table 5.2: Parameterized coefficients, its error, and statistics summary of fit function in figures.

Figure	1	2	3	4	5	6	7	8	9	10
5.12(a)	0.74078	0.03855	-0.06864	0.01598	0.50641	0.05307	-	-	1.48078	0.0158
5.12(b)	0.02228	8.60E-04	-1.09835	0.36388	0.0613	0.00759	-5.49E-04	1.62E-04	1.36185	0.01097
5.13(a)	0.06023	0.0073	0.80386	0.0105	-	-	-	-	1.5568	0.04025
5.13(b)	3.52931	0.3187	0.88872	0.01003	0.02553	0.01138	0.3758	0.16582	1.4208	0.02953
5.19(a)	1.43E-04	1.86E-05	647.56071	89.38814	-	-	-	-	-	-
5.19(b)(H8)	1.70E-04	3.77E-05	638.26526	126.57444	-	-	-	-	-	-
5.19(b)(H16)	1.39E-04	2.18E-05	680.28969	113.41709	-	-	-	-	-	-
5.24	0.00649	0.00348	338.24297	15.76037	115.38009	47.56862	0.82899	0.22938	1.92463	0.29005
5.25	0.09242	0.01457	1.56733	0.12275	0.66907	0.18602	0.71351	0.14258	1.59393	0.26343
5.26	0.04119	0.01018	9.93998	0.48595	0.98744	0.0975	1.21081	0.07709	1.74961	0.25844
Figure	11	12	13	14	15	16	17	18	19	
5.12(a)	-	-	-	-	32	28	14.67464	0.99691	0	
5.12(b)	0.91711	0.10273	-	-	32	26	256.24604	0.99909	0	
5.13(a)	-	-	-	-	32	29	95.44974	0.99168	0	
5.13(b)	-	-	-	-	32	27	3972.28821	0.99628	0	
5.19(a)	-	-	-	-	11	9	1.84	0.85406	0.056	
5.19(b)(H8)	-	-	-	-	5	3	1.97369	0.82927	0.1155	
5.19(b)(H16)	-	-	-	-	6	4	1.77779	0.88853	0.1301	
5.24	0.03939	0.01079	0	0	36	30	1.82037	0.88724	0.0039	
5.25	0.06785	0.03317	0	0	36	30	2.18746	0.86451	0.0001	
5.26	0.05655	0.02131	0	0	36	30	2.86591	0.82248	2.6019e-7	

---

**1** : A1 value, **2** : A1 standard deviation,

**3** : B1 value, **4** : B1 standard deviation, **5** : B2 value, **6** : B2 standard deviation,

**7** : B3 value, **8** : B3 standard deviation , **9** : C1 value, **10** : C1 standard deviation,

**11** : C2 value, **12** : C2 standard deviation, **13** : C3 value, **14** : C3 standard deviation,

**15** : Number of points, **16** : Degrees of freedom, **17** : Reduced  $\chi^2$ , **18** : Adjusted  $\mathbf{R}^2$ , **19** :  $\chi^2$  probability.

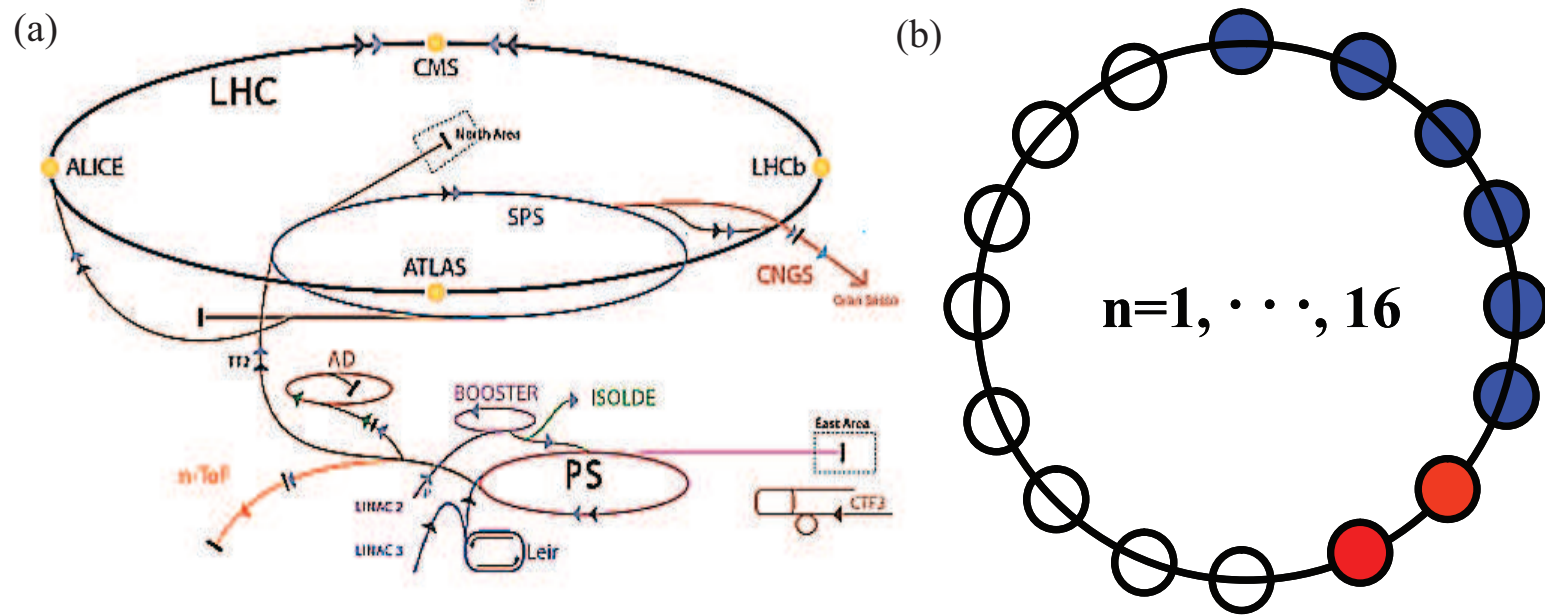


Figure 5.1: Infrastructures for experiment at CERN. a.) CERN accelerator complex and TT2 tunnel for experiment. b.) 16 harmonics of beam extraction in proton synchrotron.



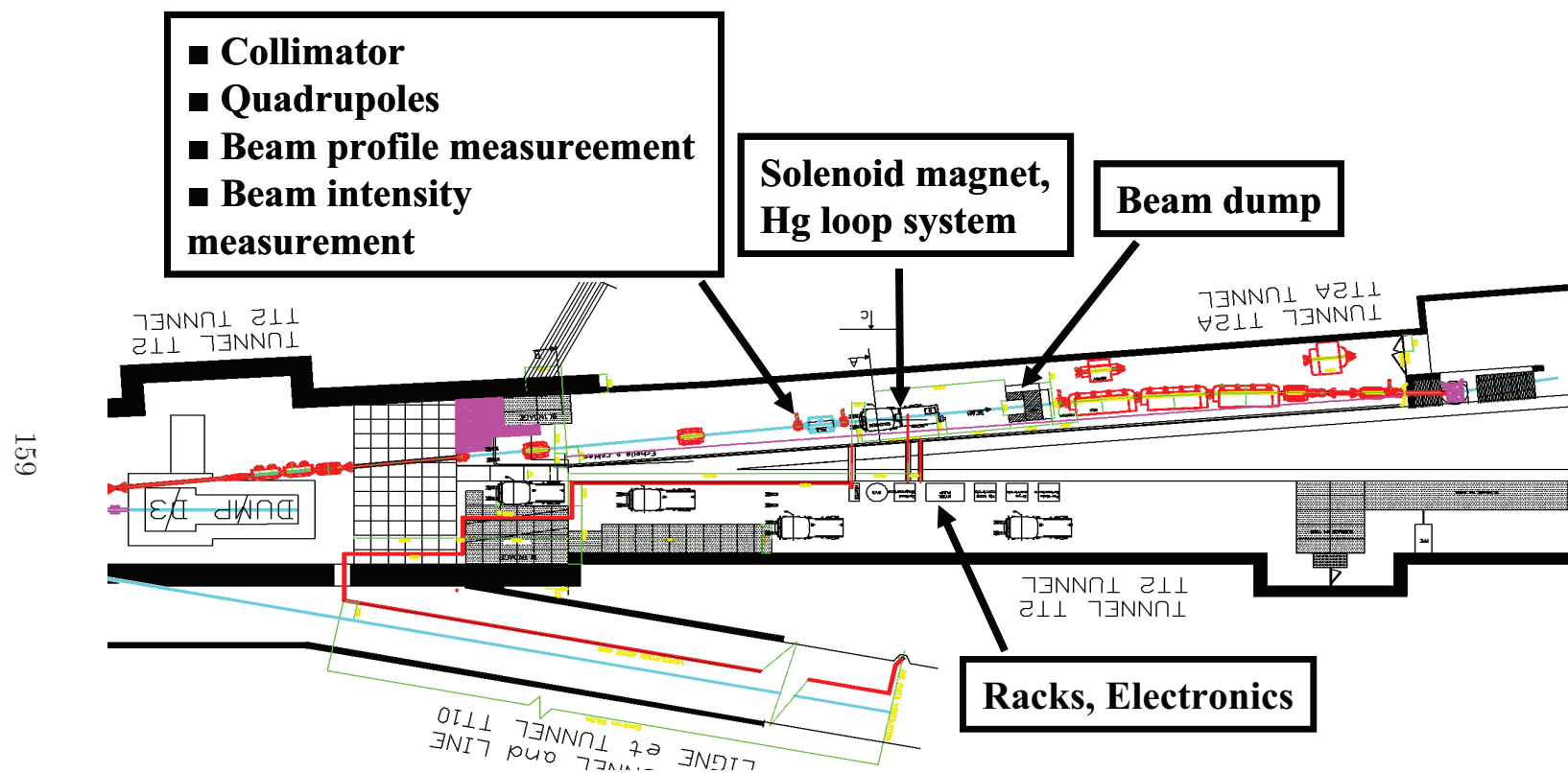


Figure 5.2: Installation of integrated experimental components in tunnel TT2/TT2A for high power target experiment. Extracted proton beam comes from left to right in tunnel TT2A.

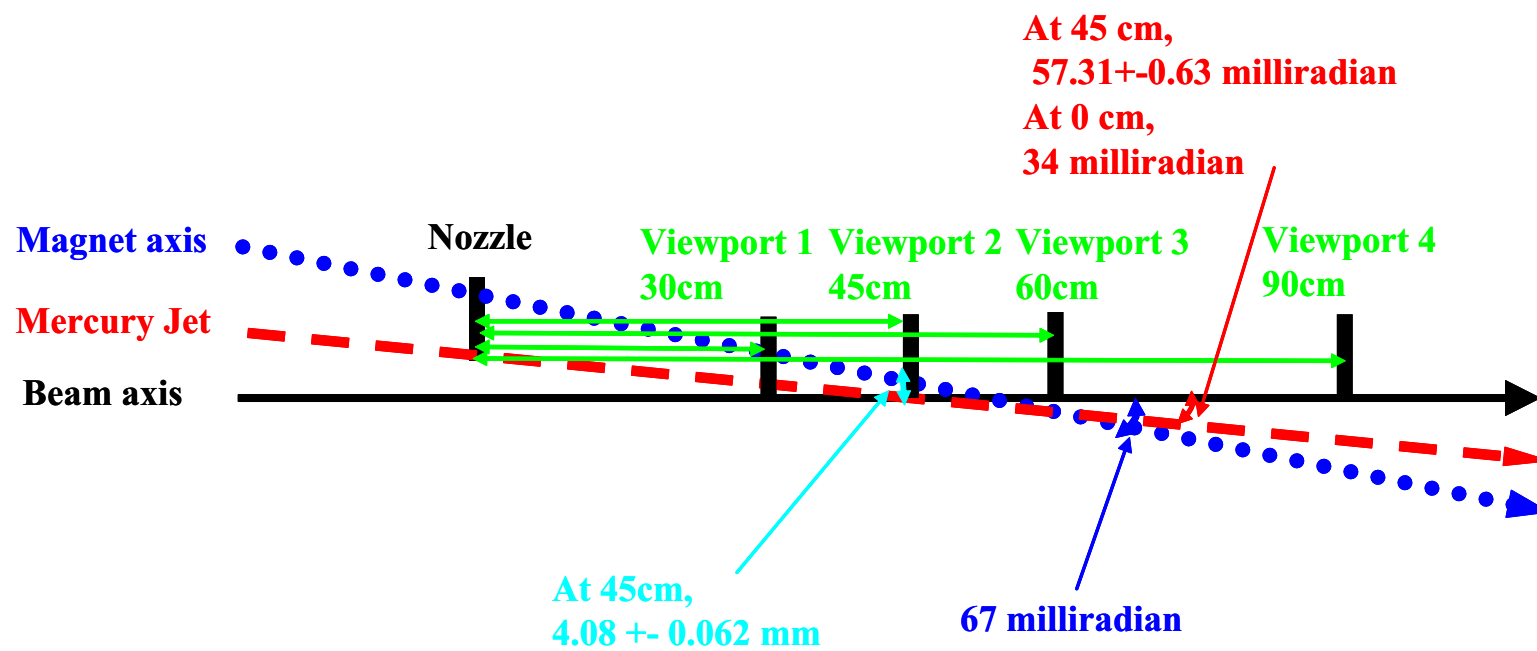


Figure 5.3: Schematics of beam to jet interaction in magnetic field and the location of each Viewport.

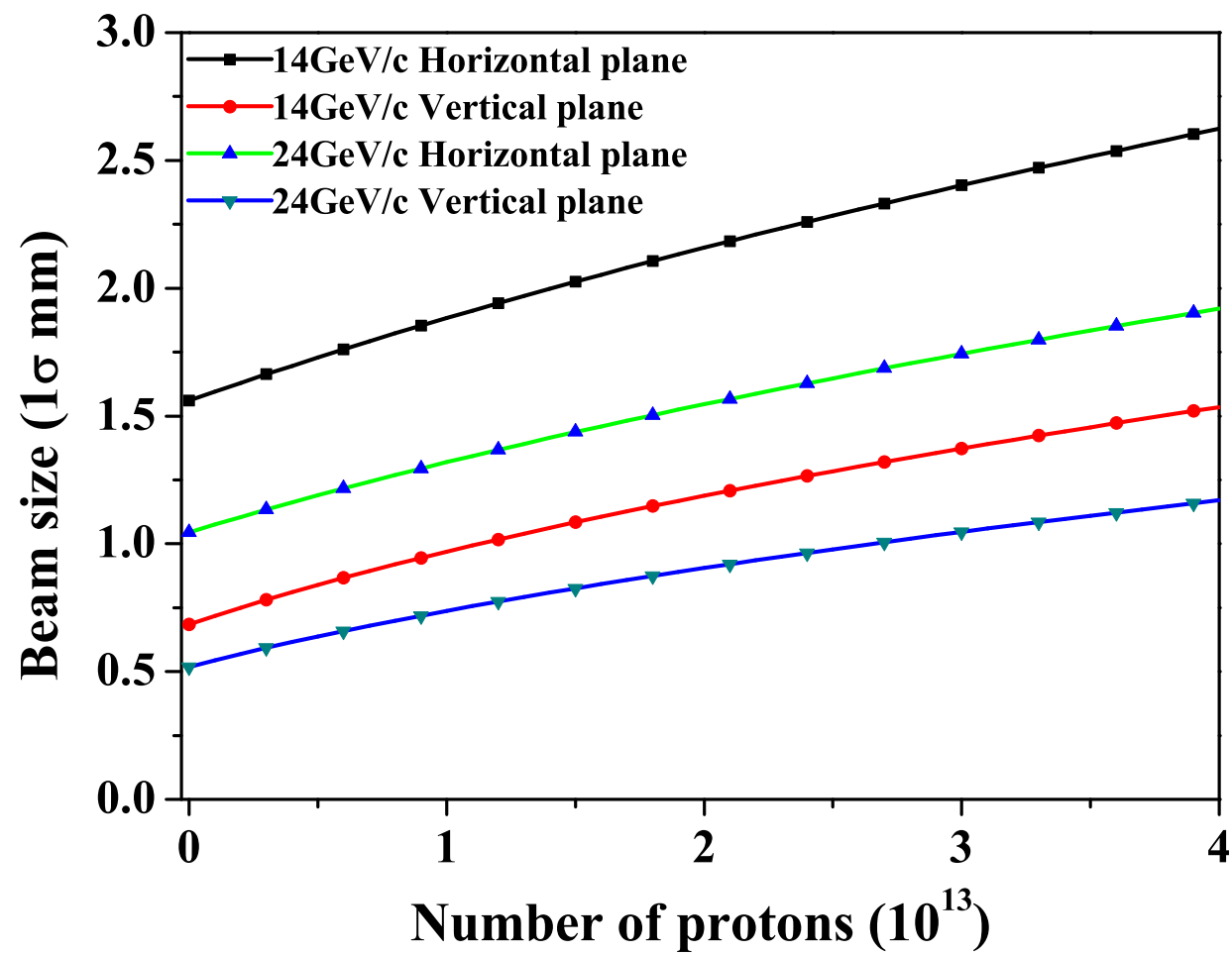


Figure 5.4:  $1\sigma$  proton beam size at the center of magnet by optics (Efthymiopoulos, 2008).

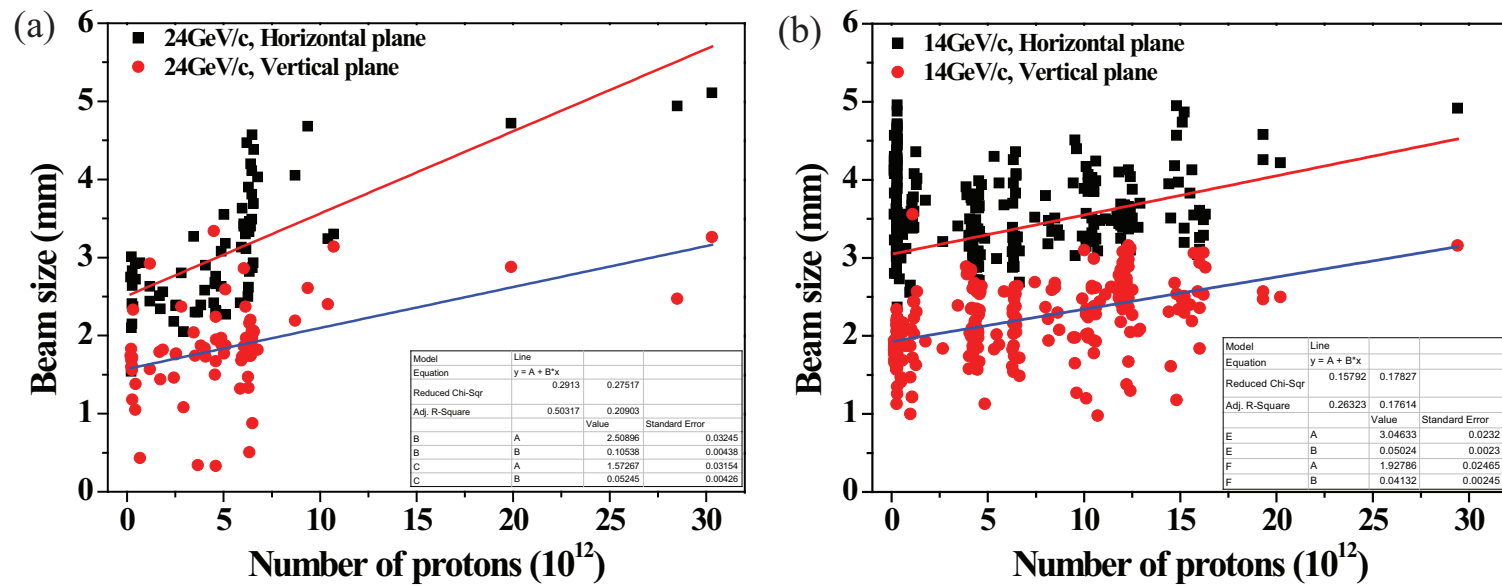


Figure 5.5:  $1\sigma$  proton beam size by camera screen (Skoro, 2008). a.) 14 GeV beam. b.) 24 GeV beam.

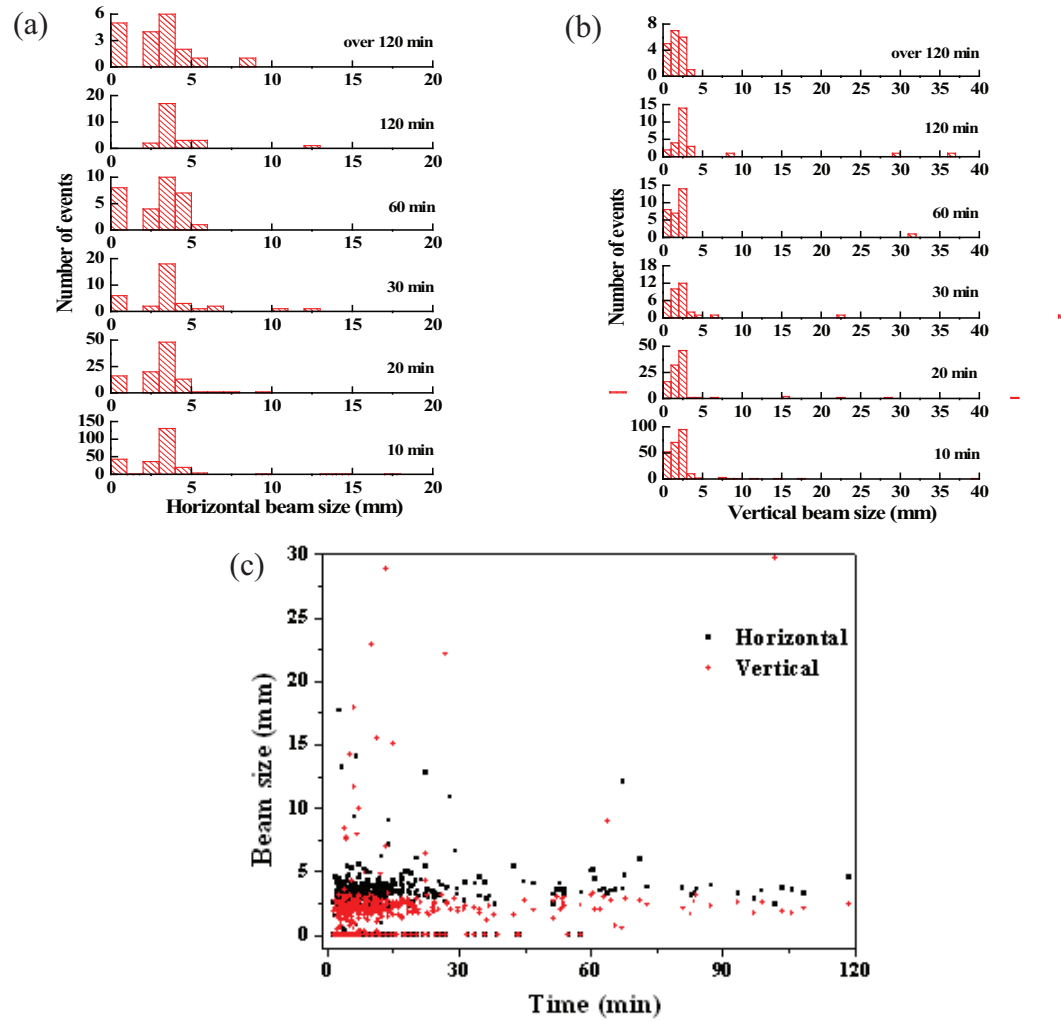


Figure 5.6: Beam size measured by phosphor screen monitor as a function of time interval between beam shots. a.) Histogram of beam size in horizontal plane. b.) Histogram of beam size in vertical plane. c.) Beam sizes distribution.

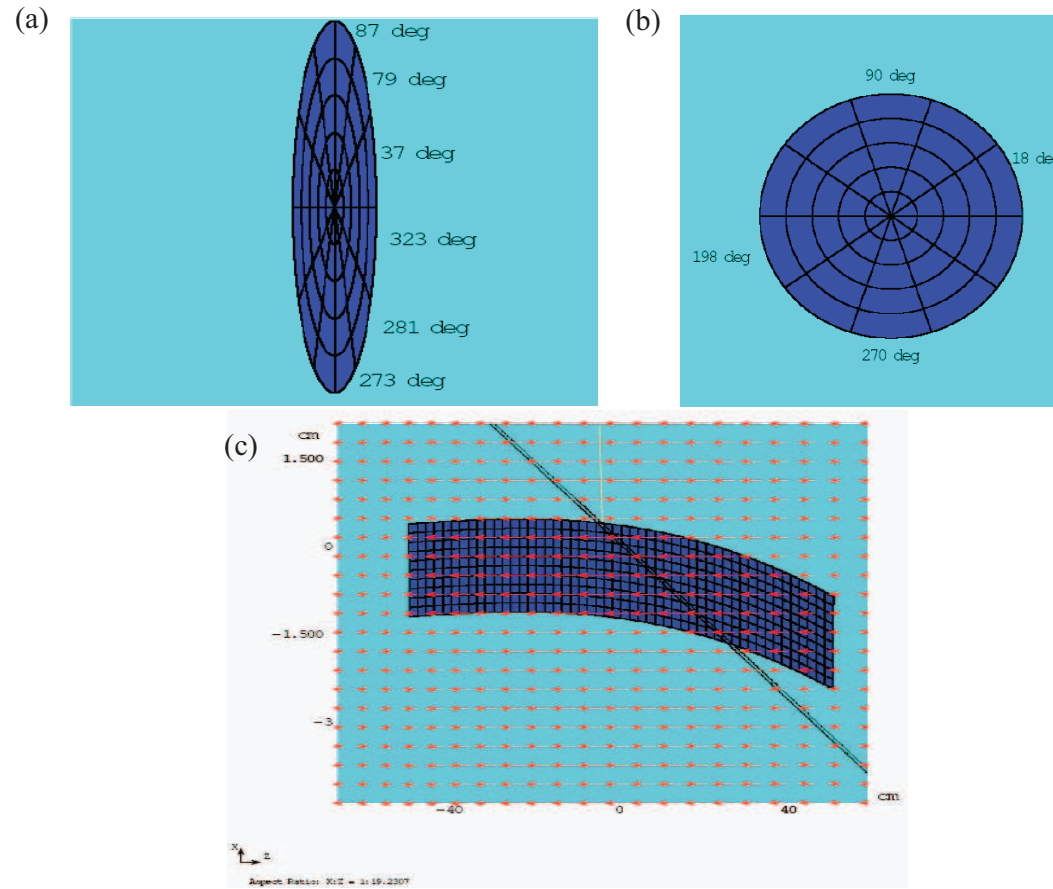


Figure 5.7: Modeling in MARS code for energy deposition calculation (Striganov, 2009). a.) Sectional view of elliptic jet. b.) Sectional view of circular jet. c.) Side view of mercury jet.

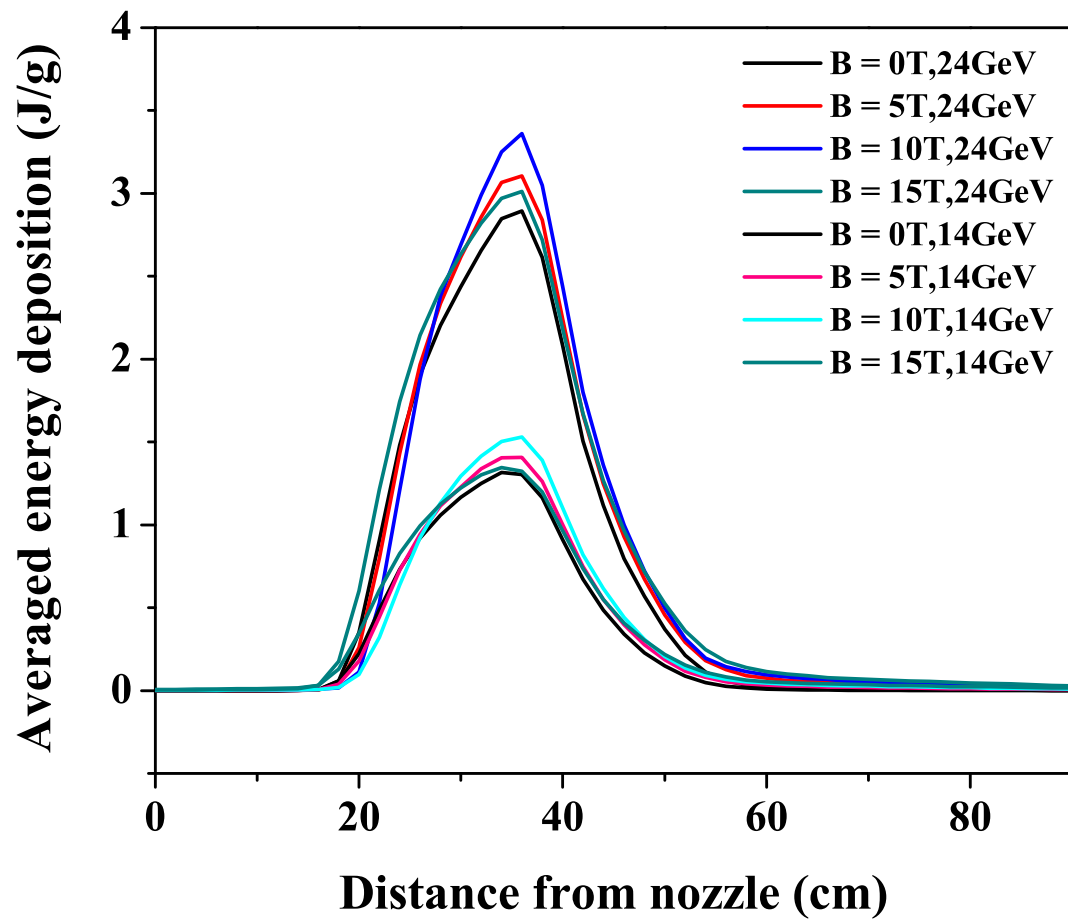


Figure 5.8: Influence of magnetic field to the energy deposition distribution to Hg jet considering experimentally measured jet parameters.

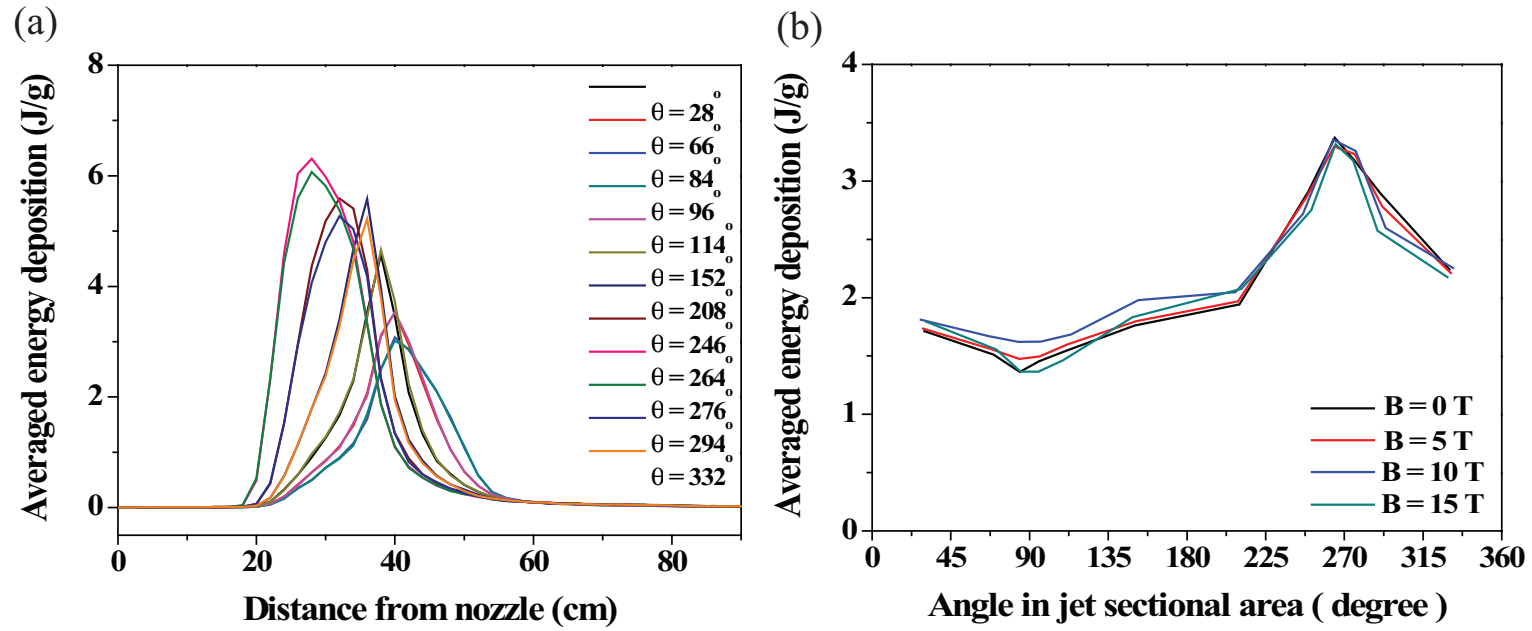


Figure 5.9: Radial energy deposition distribution along jet axis interacting with 24 GeV proton beam. a.) Along jet axis. b.) Along radial angle in jet cross section.



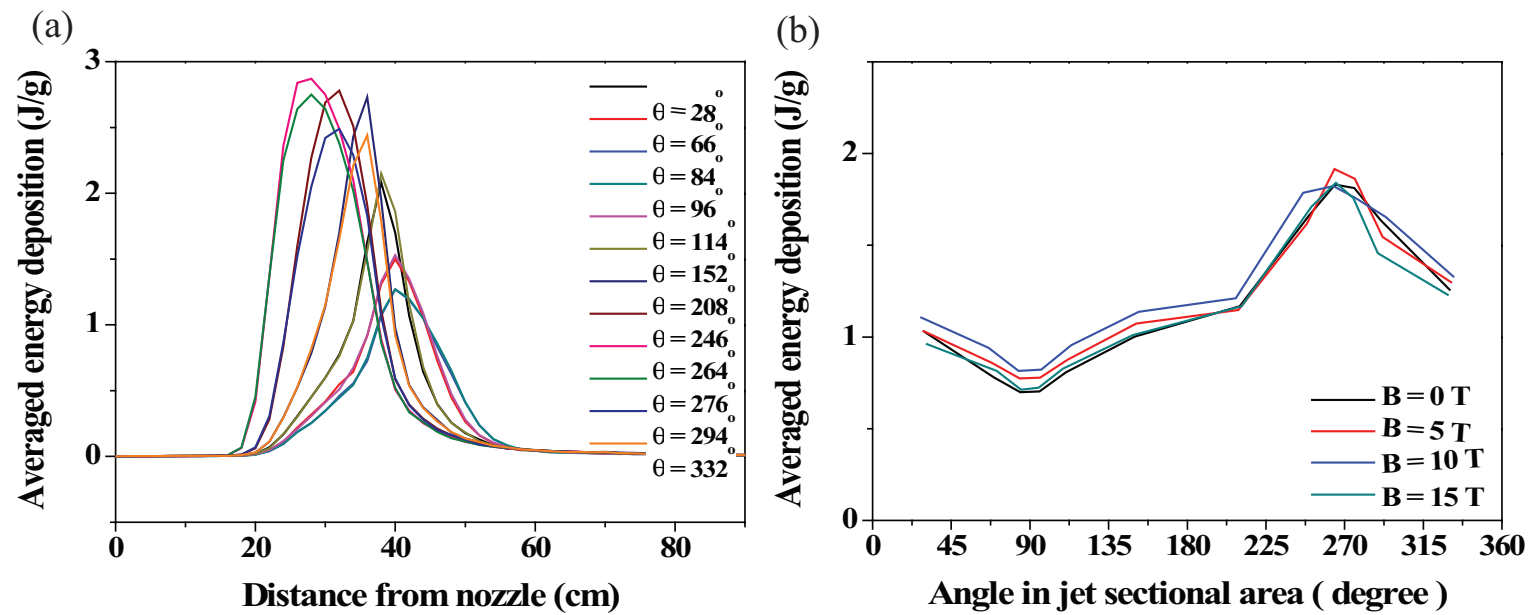


Figure 5.10: Radial energy deposition distribution along jet axis interacting with 14 GeV proton beam. a.) Along jet axis. b.) Along radial angle in jet cross section.

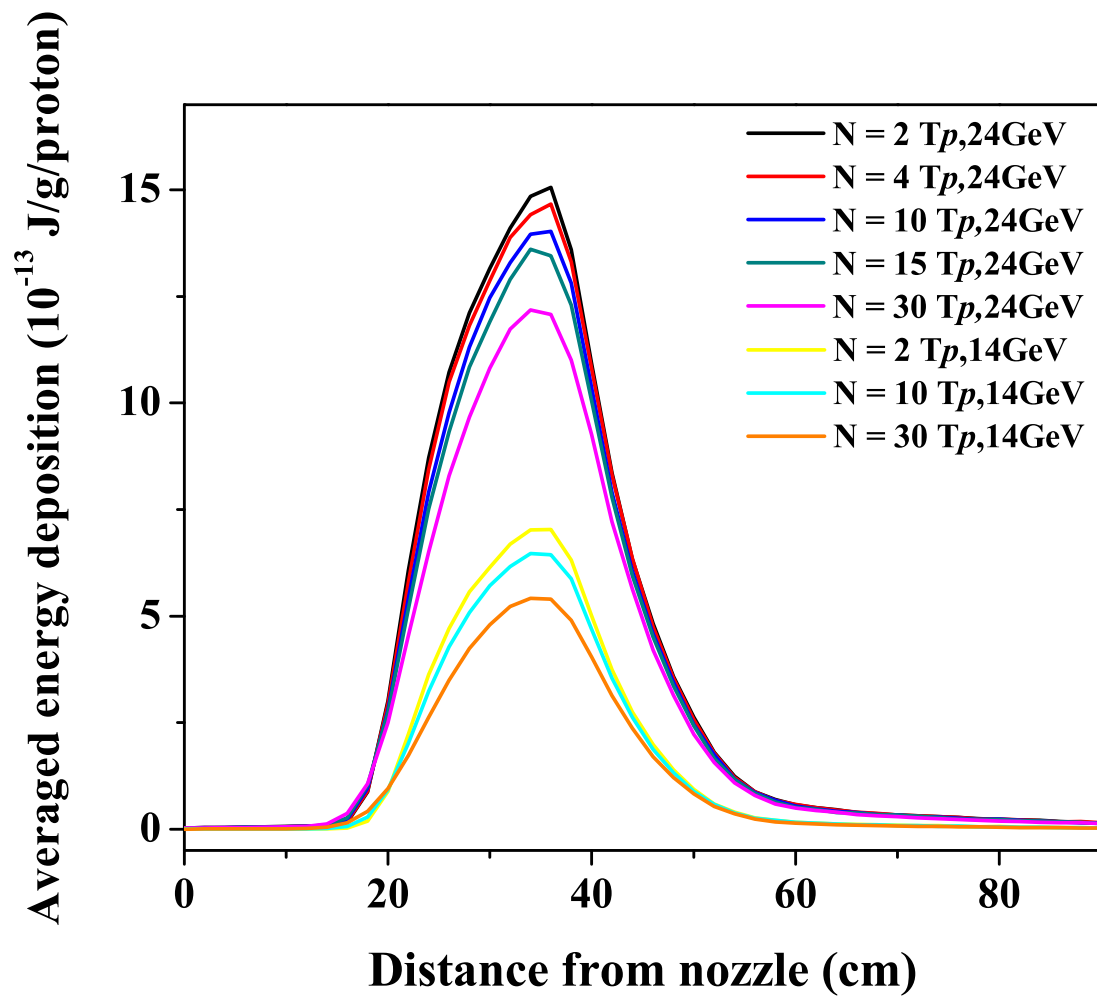


Figure 5.11: Energy deposition distribution per proton according to the variation of beam spot size along jet axis.

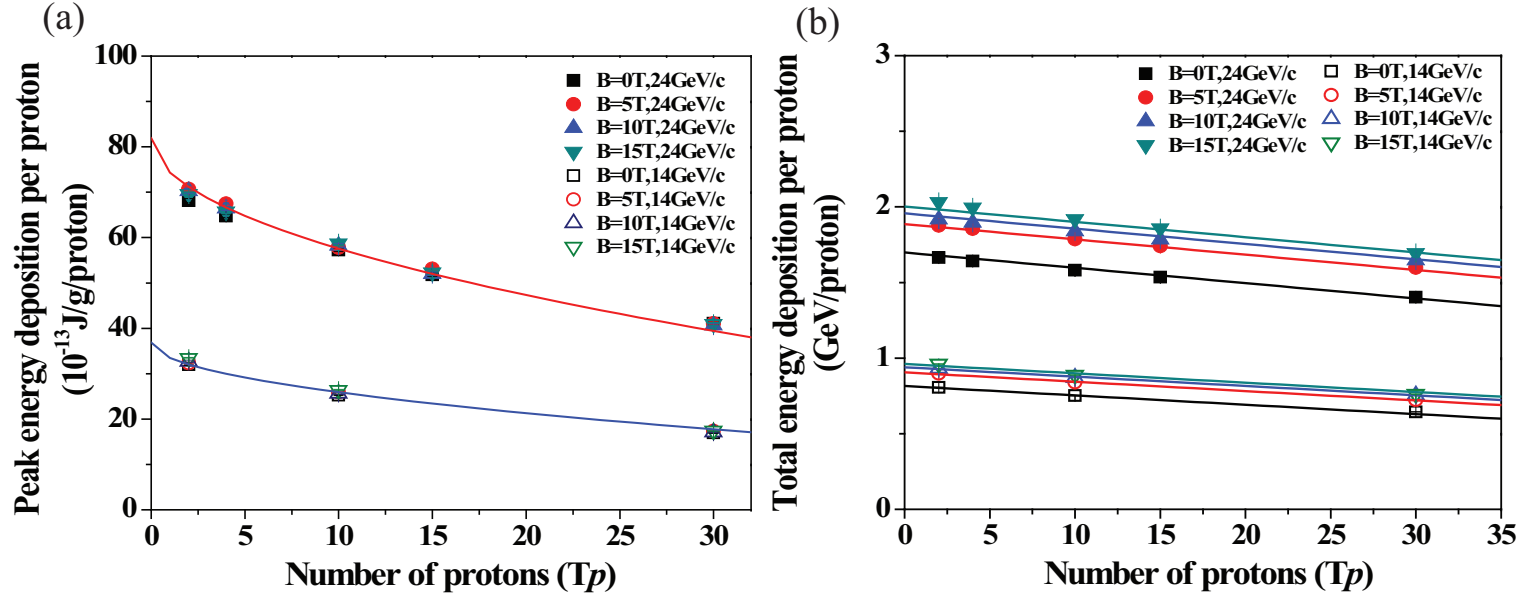


Figure 5.12: Simulation of peak energy deposition per proton and total energy deposition per proton according to the beam spot sizes by beam intensities. Fits of model fits to Striganov's calculation results. a.) Peak energy deposition per proton and fit of model using Eqn. (5.6). b.) Total energy deposition per proton and fit of model using Eqn. (5.7).

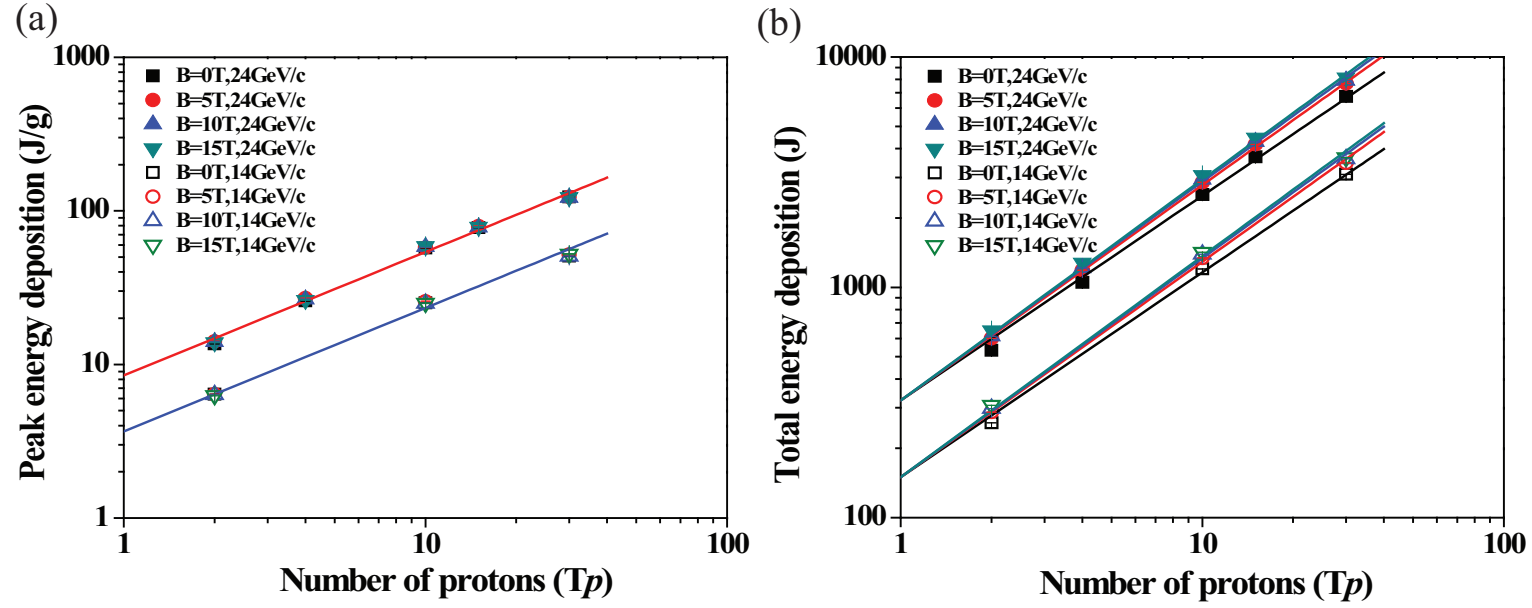


Figure 5.13: Simulation of peak energy deposition and total energy deposition in total number of protons. Fits of model fits to Striganov's calculation results. a.) Peak energy deposition and fit of model using Eqn. (5.8). b.) Total energy deposition and fit of model using Eqn. (5.9).

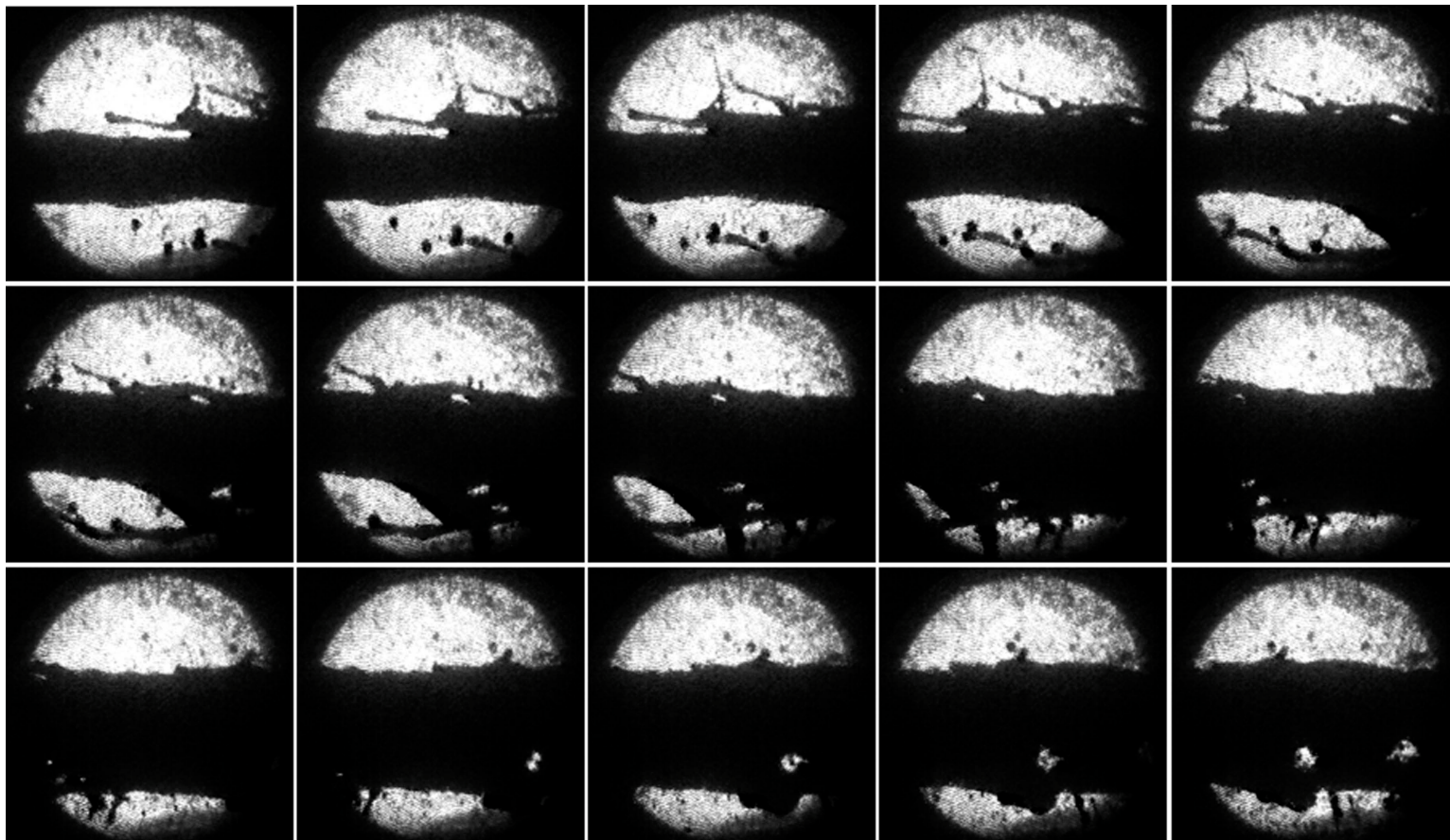


Figure 5.14: Photographs of the Hg jet interaction with 16 Tp, 14 GeV proton beam at 5 T. Captured at Viewport 3 at  $500 \mu\text{s}$  frame rate (continued).

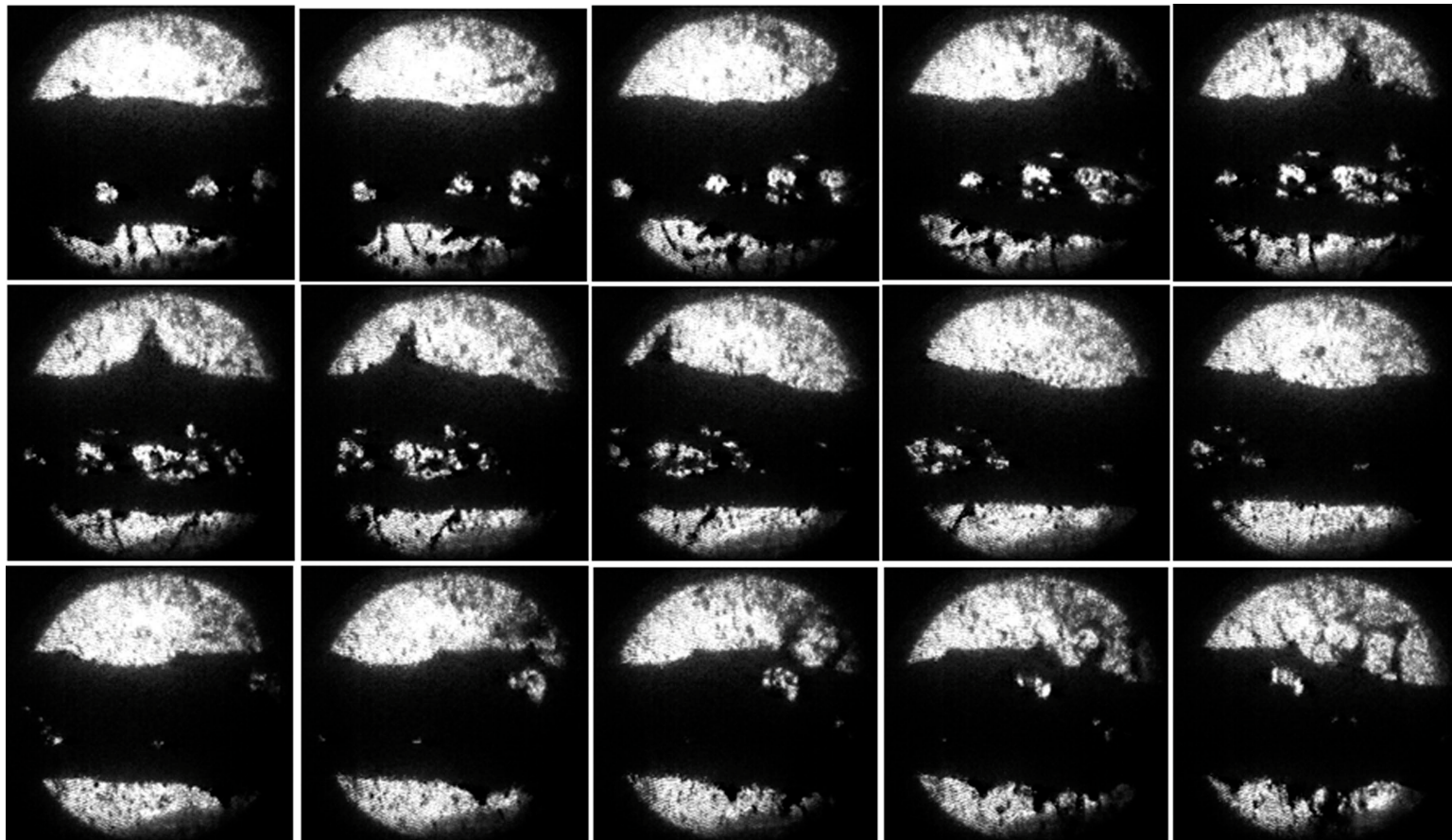


Figure 5.14: Photographs of the Hg jet interaction with 16 Tp, 14 GeV proton beam at 5 T. Captured at Viewport 3 at  $500 \mu\text{s}$  frame rate (continued).



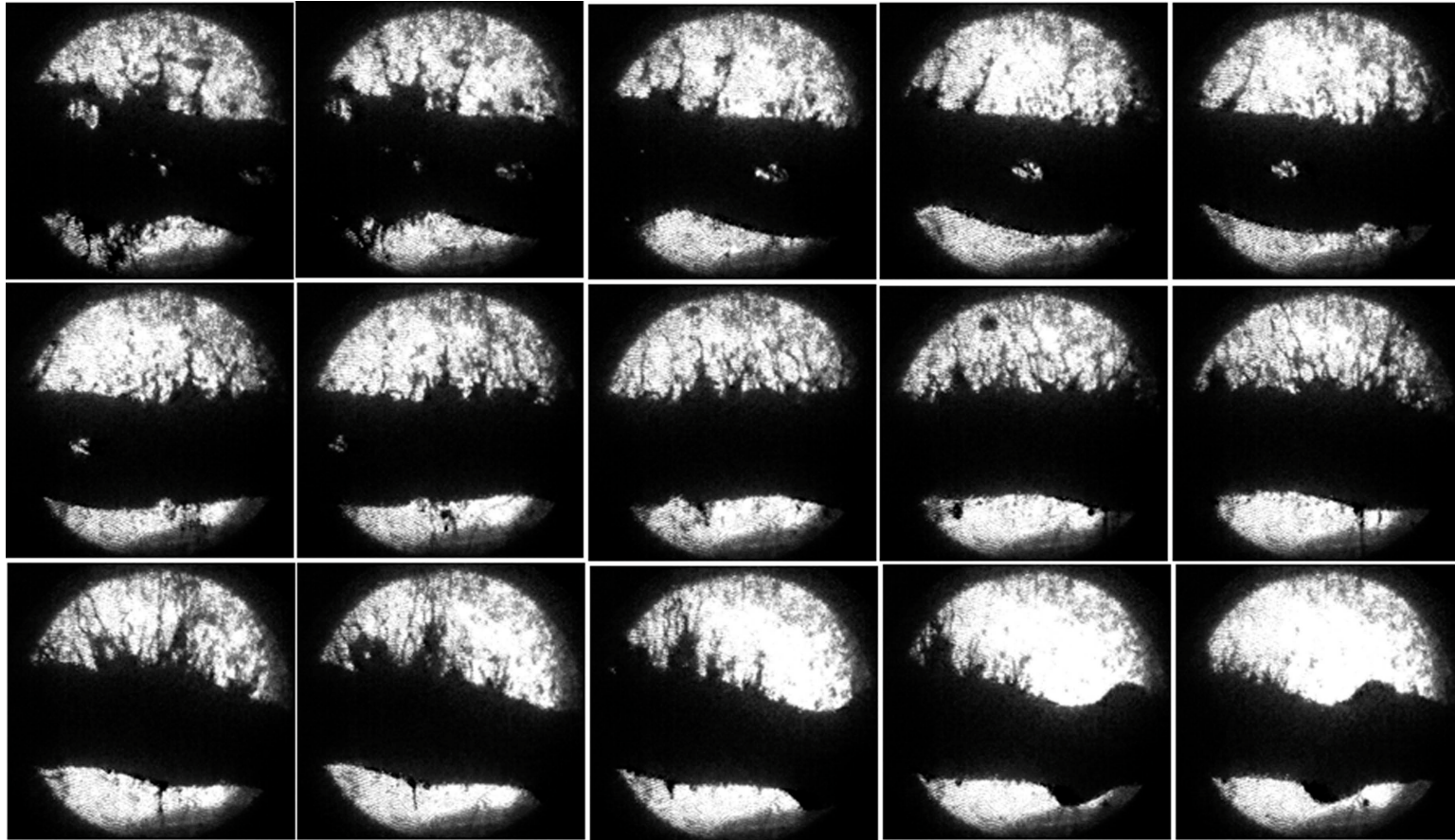


Figure 5.14: Photographs of the Hg jet interaction with 16 Tp, 14 GeV proton beam at 5 T. Captured at Viewport 3 at  $500 \mu\text{s}$  frame rate.

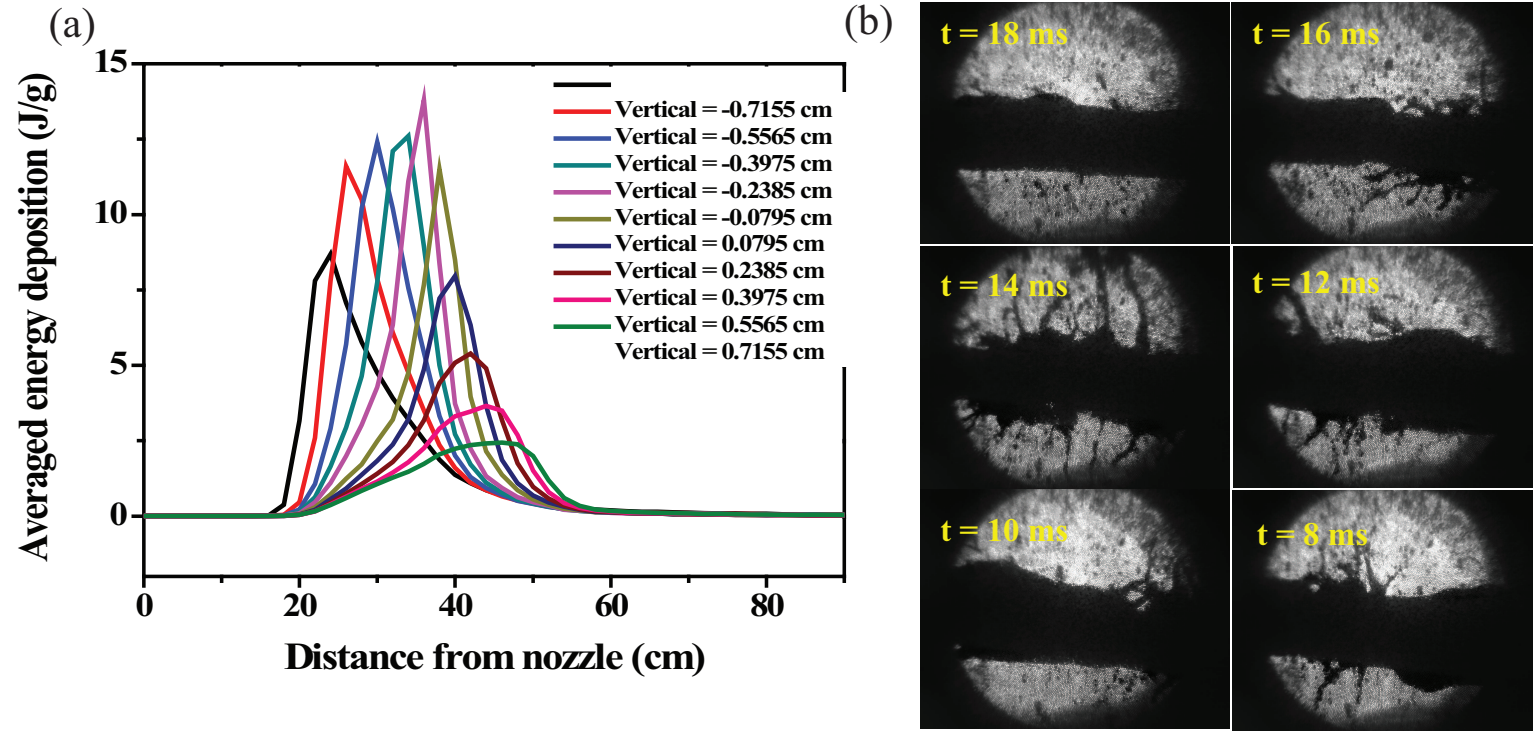


Figure 5.15: Qualitative comparison of the jet response incident by interaction of low intensity (3 Tp) of 24 GeV beam at 5 T. a.) Calculated averaged energy deposition profile to mercury jet according to the distance from jet center. b.) Jet response by captured image.



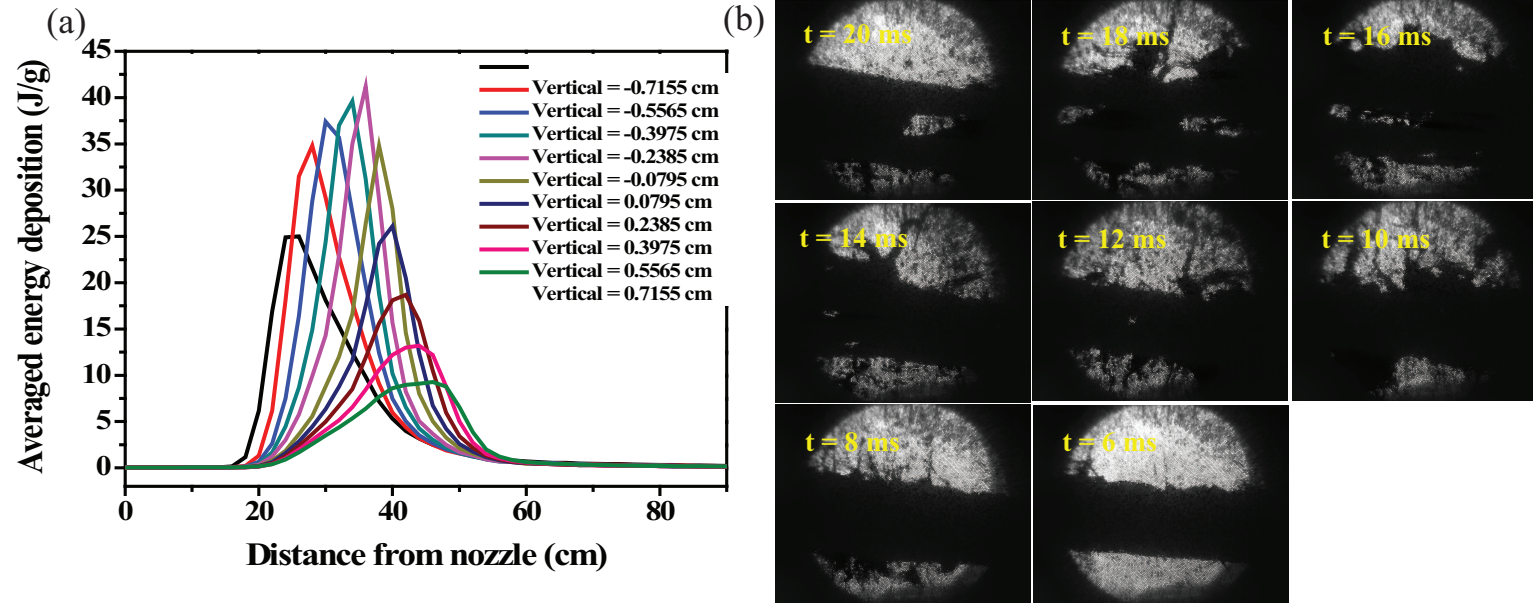


Figure 5.16: Qualitative comparison of the jet response incident by interaction of high intensity (10 Tp) of 24 GeV beam at 10 T. a.) Calculated averaged energy deposition profile to mercury jet according to the distance from jet center. b.) Jet response by captured image.

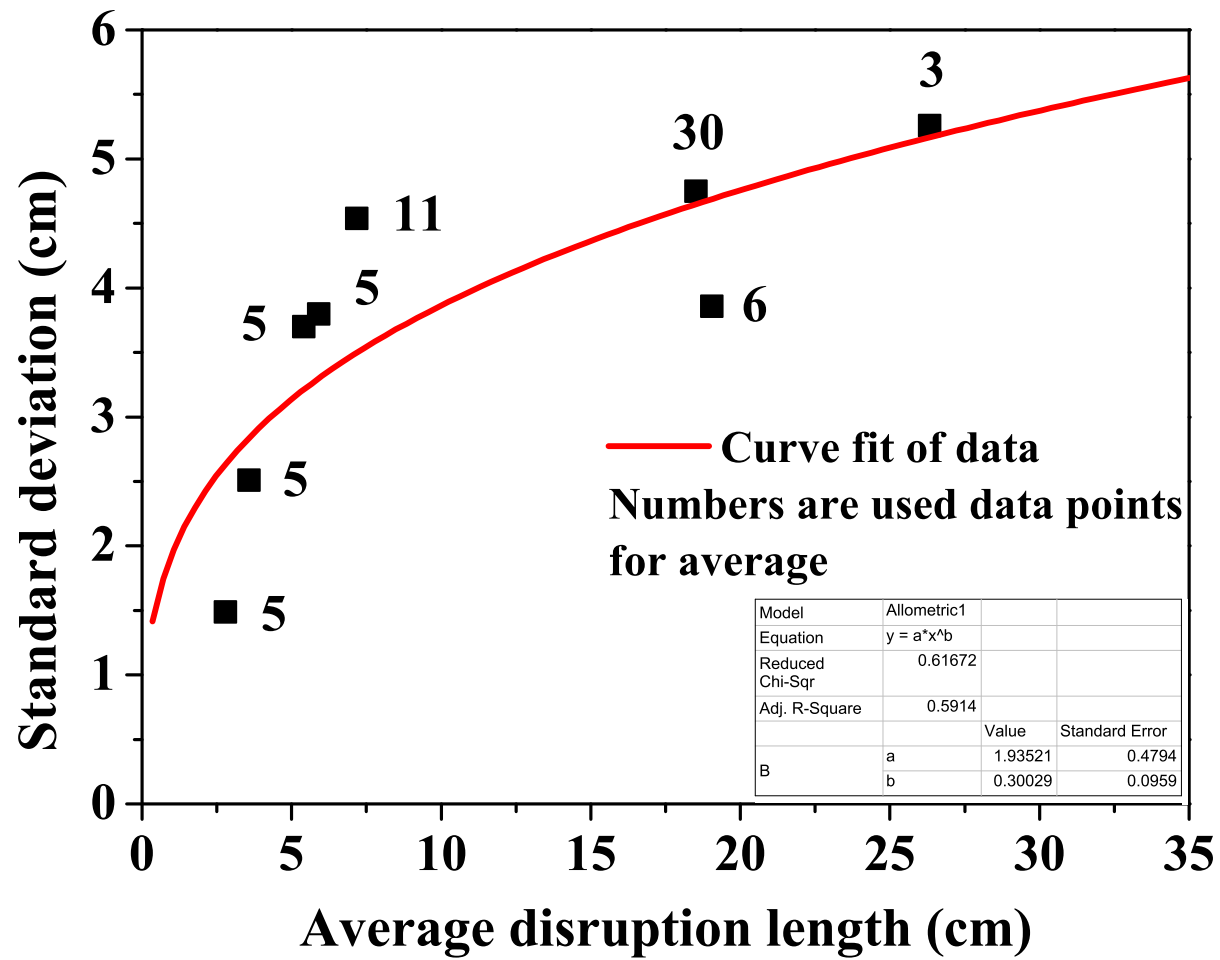


Figure 5.17: Standard deviation of disruption length as a function of disruption length and fit of model. The fitted curve is  $\sigma_{disruption} = 1.9352 L_{disruption}^{0.3}$ .

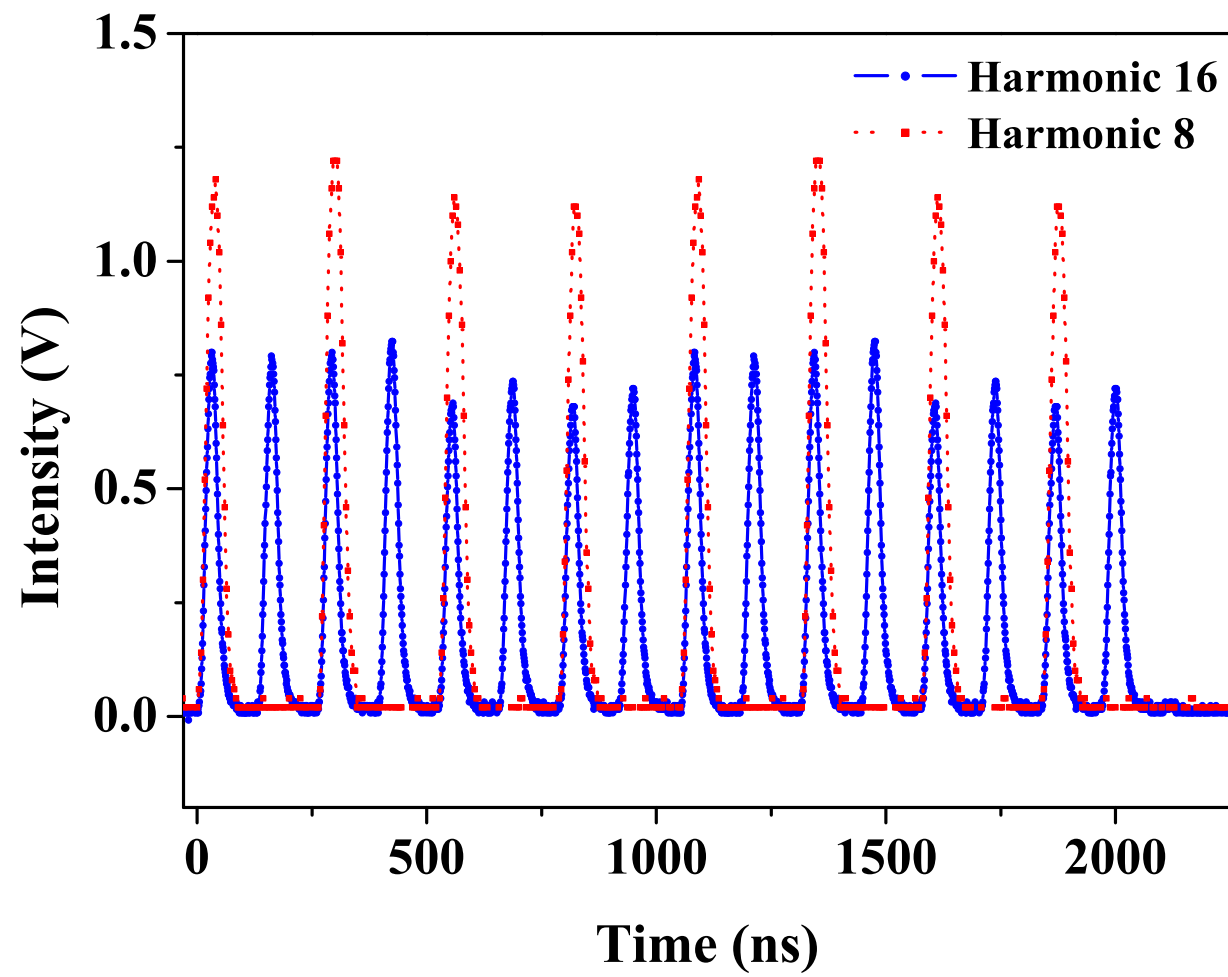


Figure 5.18: Proton beam pulse structure of harmonic 8 and harmonic 16 in 14 GeV and 6 Tp.

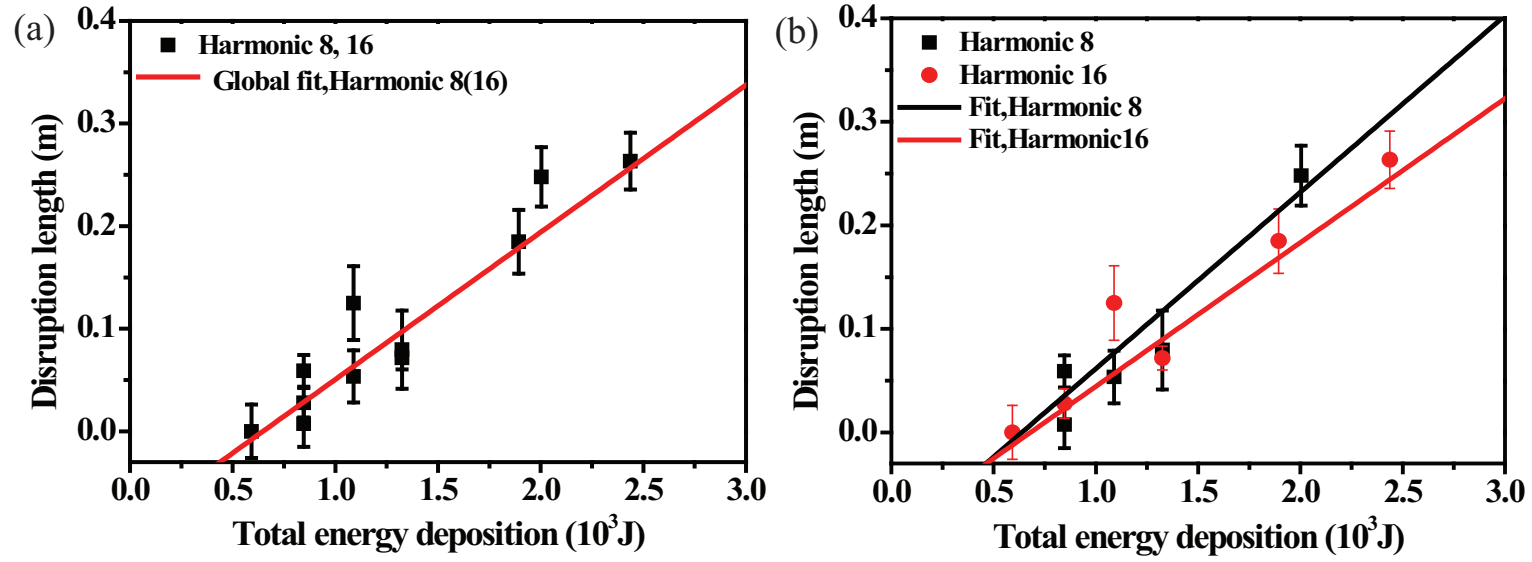


Figure 5.19: Disruption length of Hg jet depending on the beam pulse structure as a function of 14 GeV beam intensity in 5 T.  $Tp=10^{12}$  protons. a) Global fit of harmonic 8 and 16 using Eqn. (5.13). b.) Independent fit of harmonic 8 and 16 using Eqn. (5.13).

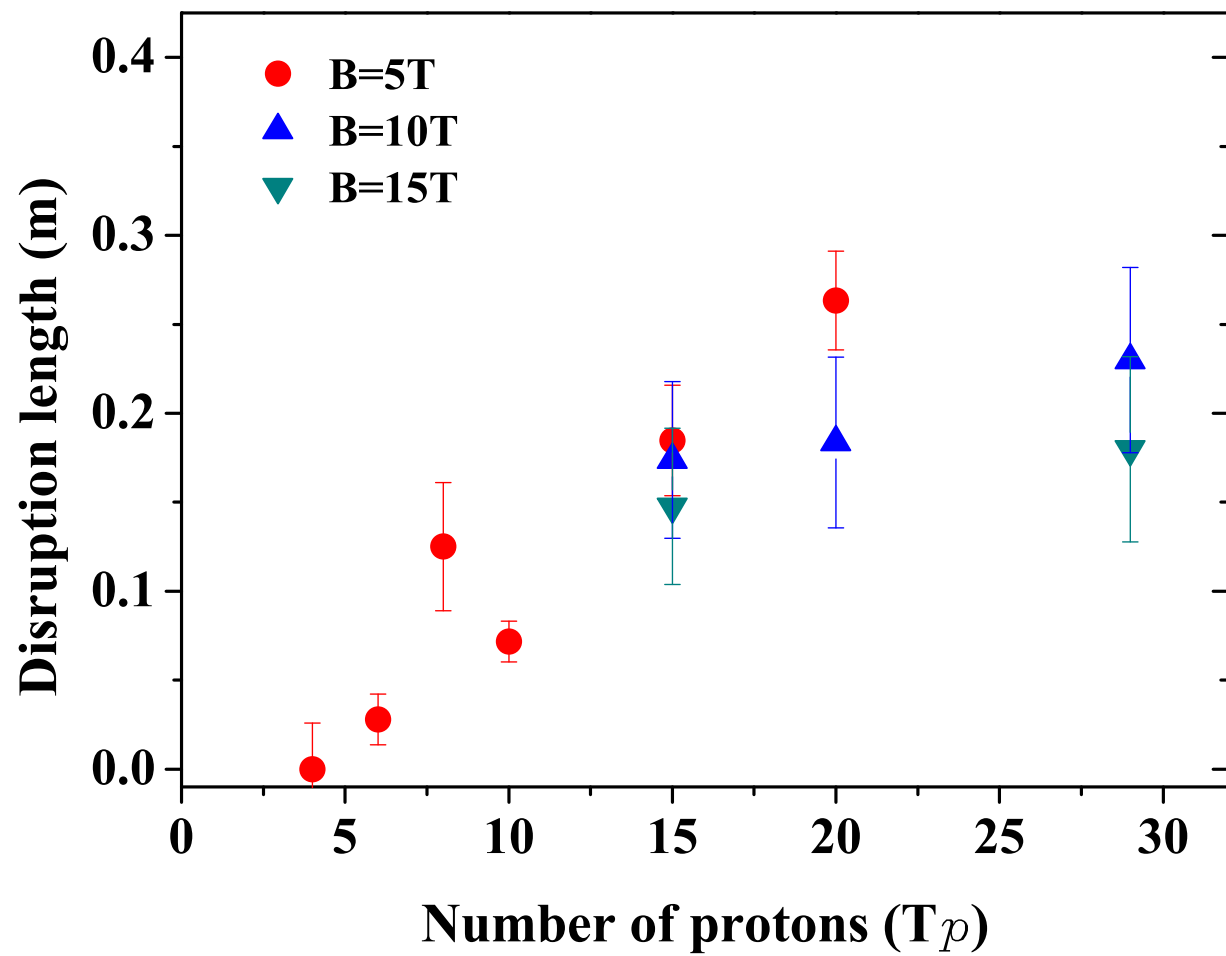


Figure 5.20: Disruption length of Hg jet as a function of 14 GeV beam intensity and magnetic field. Harmonic 16 with 16 bunches is used.

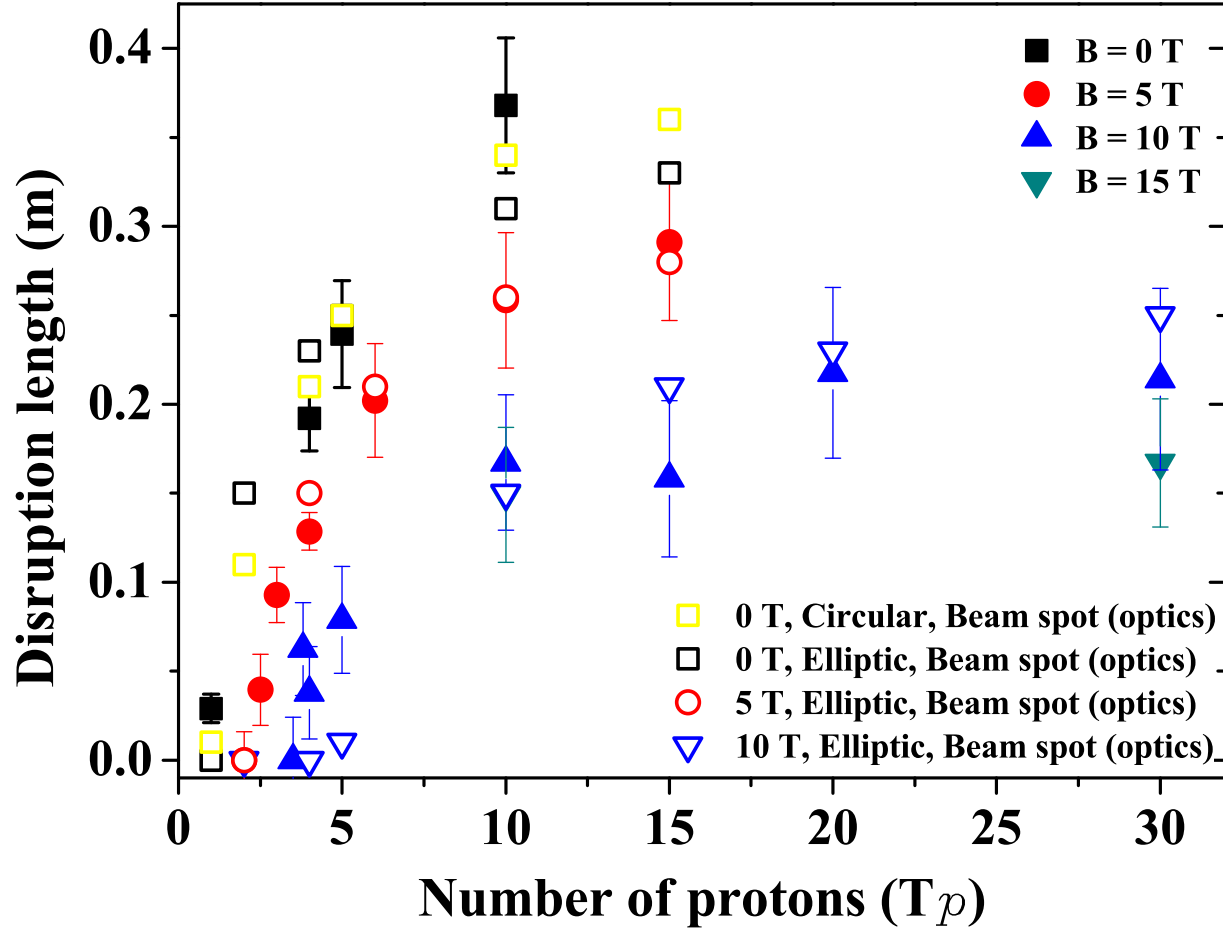


Figure 5.21: Disruption length of Hg jet and its estimation as a function of 24 GeV beam intensity and magnetic field. The estimation of disruption length by energy deposition calculation is compared by using disruption model of Eqn. (5.14).

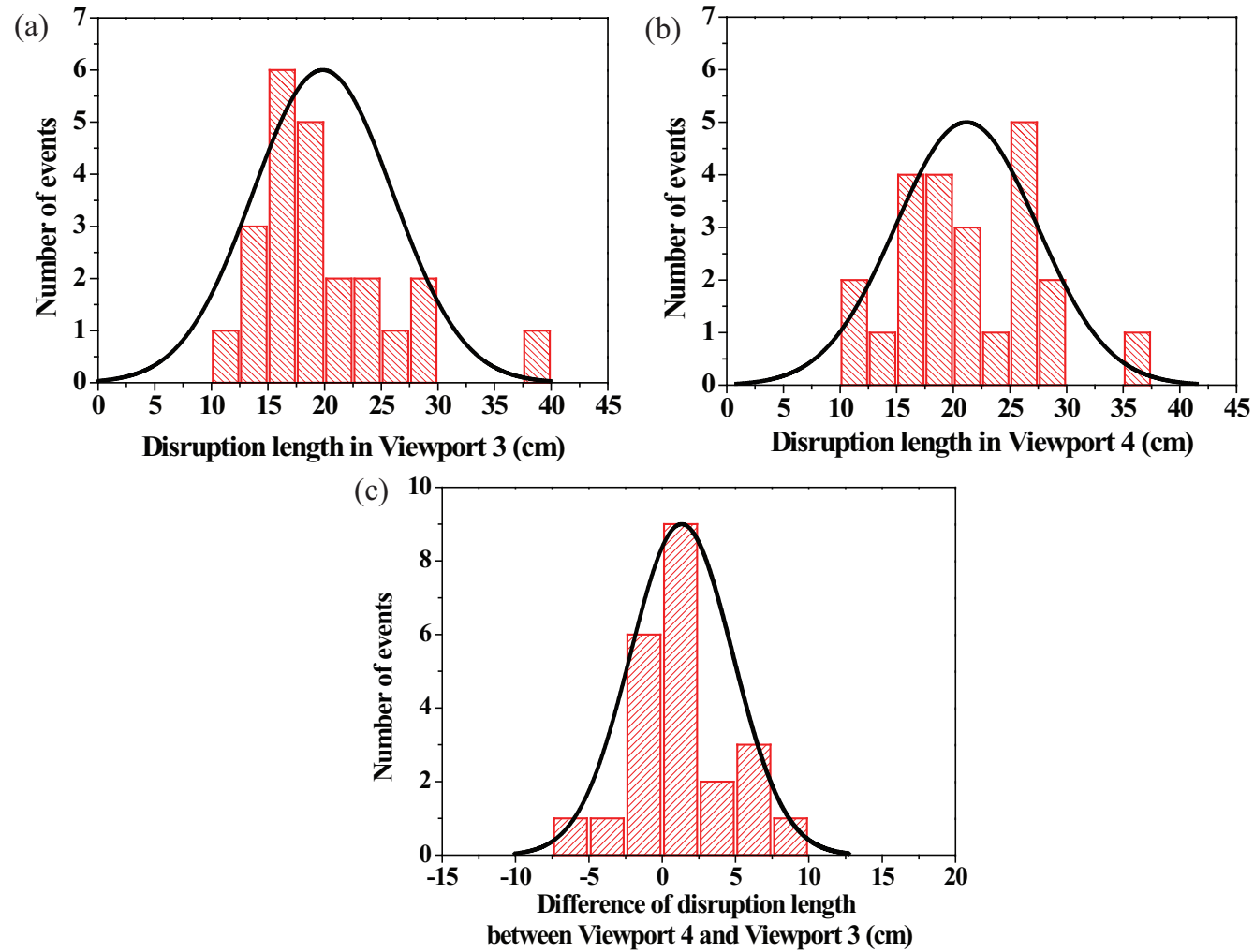


Figure 5.22: Validation of disruption measurement for the evaluation of evolution of disruption length from Viewport 3. a) Disruption length at Viewport 3. b.) Disruption length at Viewport 4. c.) Difference of the disruption length at Viewport 3 and Viewport 4.

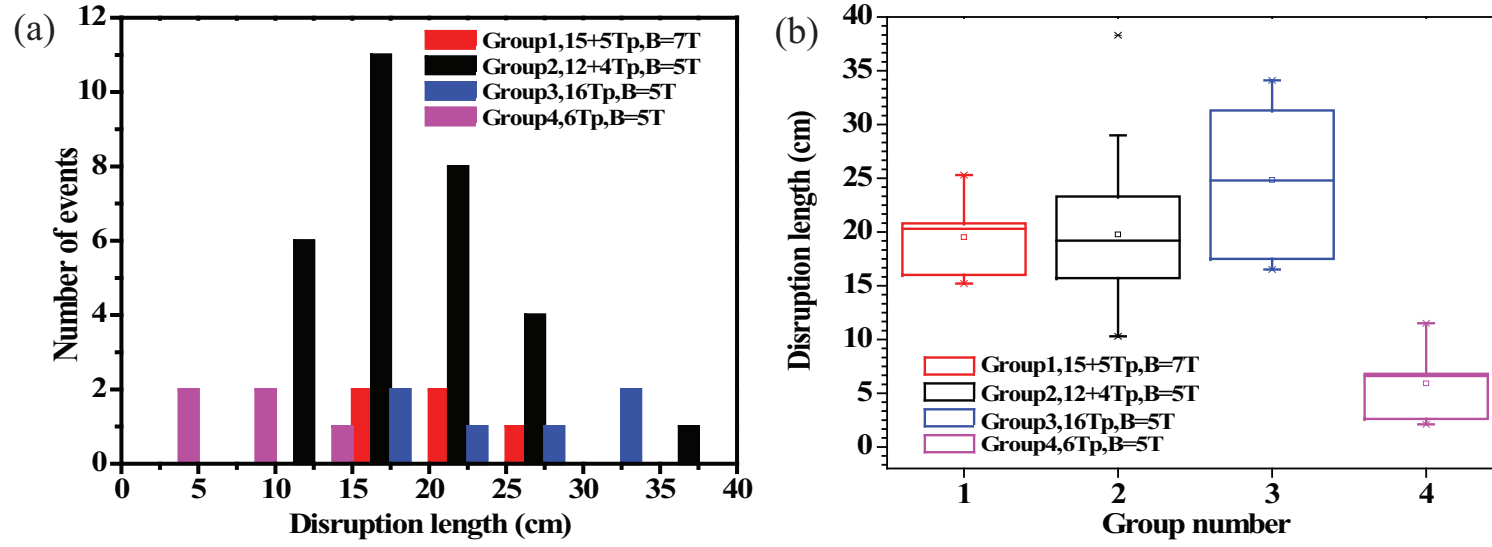


Figure 5.23: Disruption length measurement in same conditions. Pump-probe conditions with harmonic 8 and 16 bunches are used. The conditions of each group in pump-probe events are given in Table A.4. a.) Histogram of disruption length in each group. b.) Disruption length of each group.



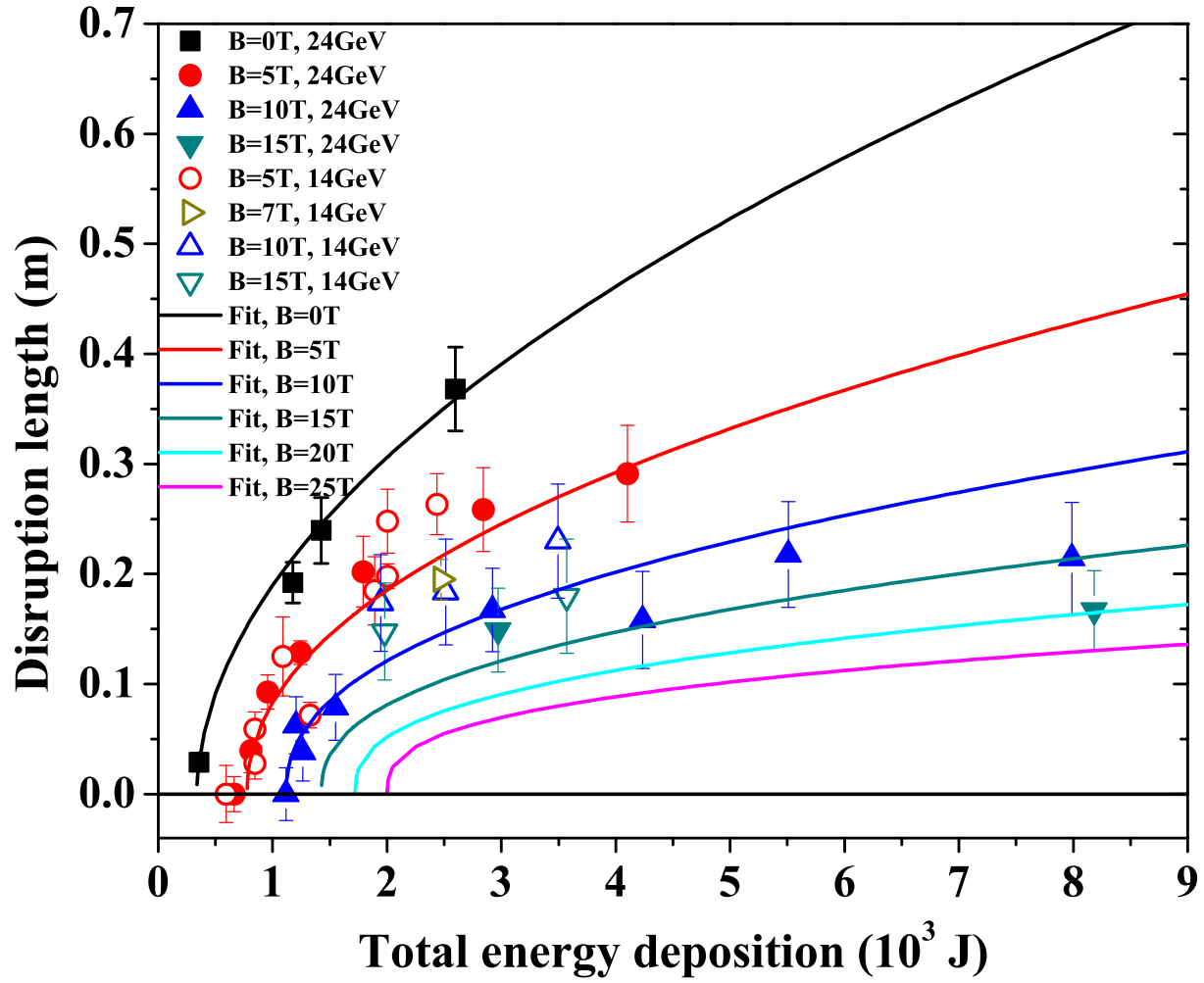


Figure 5.24: Disruption of mercury jet in magnetic fields as a function of total energy deposition and fit of model using Eqn. (5.15).

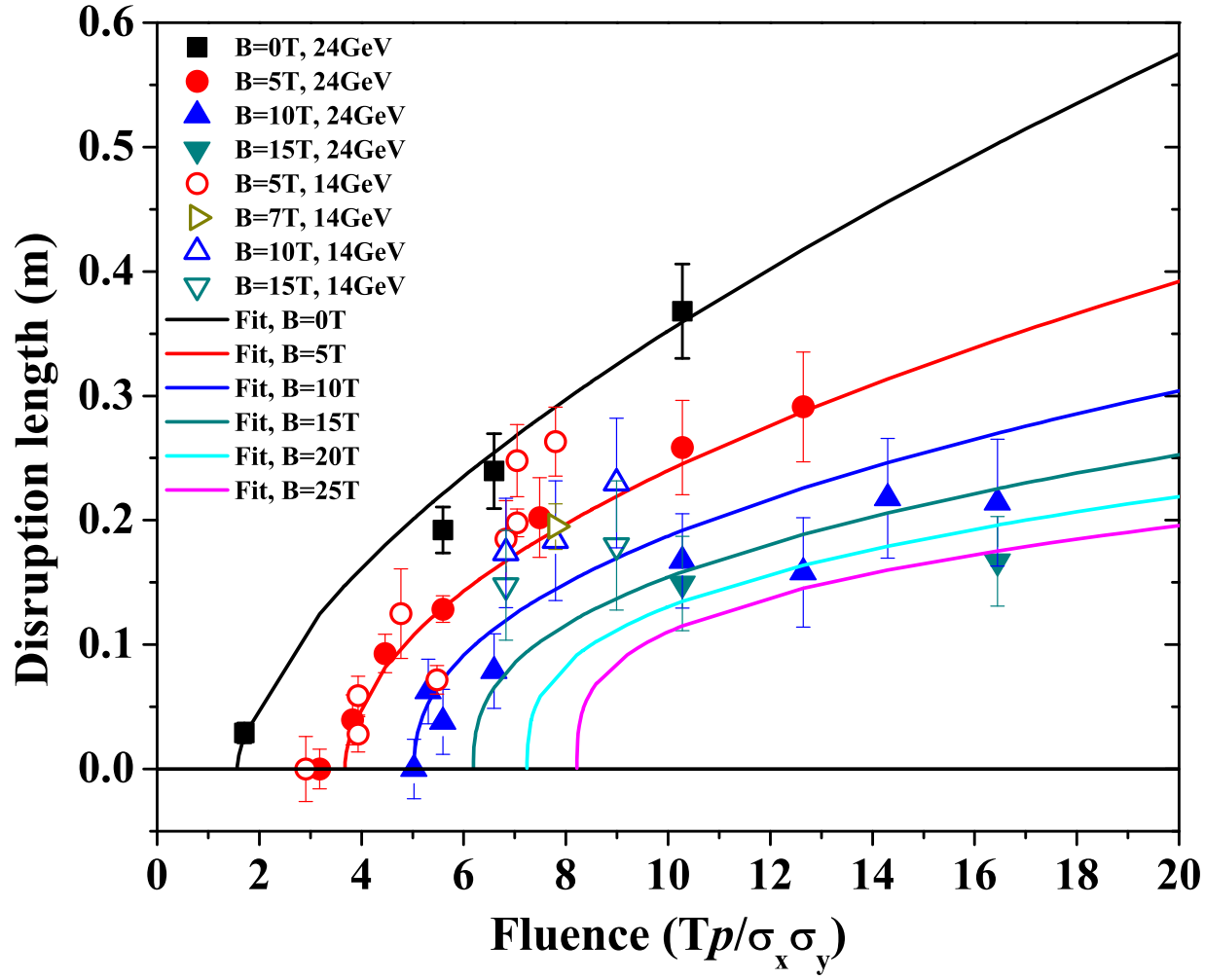


Figure 5.25: Disruption of mercury jet in magnetic fields as a function of fluence and fit of model using Eqn. (5.15).

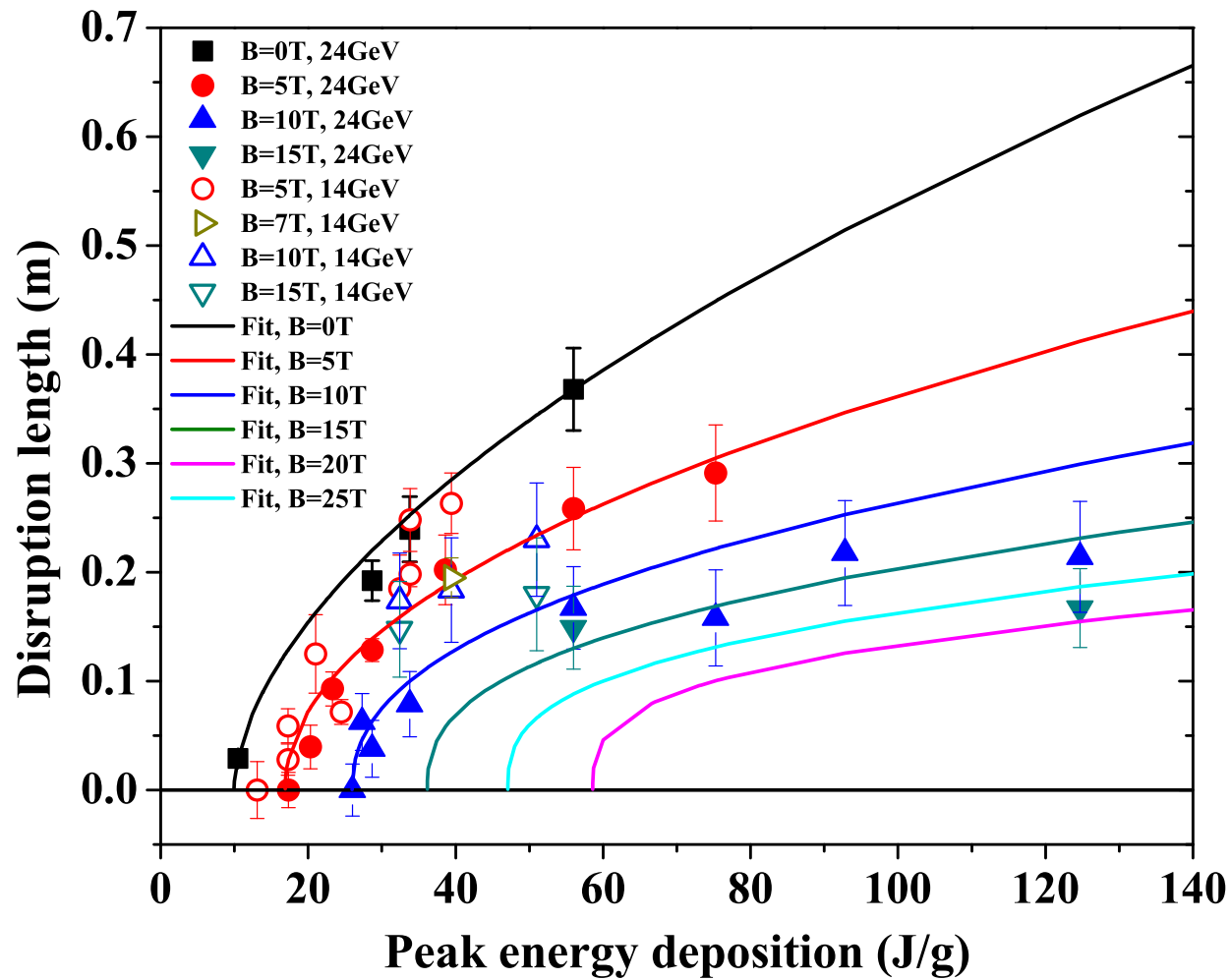


Figure 5.26: Disruption of mercury jet in magnetic fields as a function of peak energy deposition and fit of model using Eqn. (5.15).

## Chapter 6

# Mercury Jet Surface Development in Magnetic Field

3000

3001 In this chapter, the motions of filaments emanating from jet surface caused  
3002 by disruption in magnetic field are investigated. The energy deposition induced  
3003 by the proton beam generates filaments on the Hg jet surface due to thermal  
3004 stresses. The filaments velocity leaving from the jet surface and the effect of  
3005 magnetic field to it are discussed. It explains that the joule damping dissipates  
3006 the kinetic energy on a time scale of joule damping term.

3007

## 6.1 Filament Model on Jet Surface

### 6.1.1 Geometry of viewing mercury filaments

3010 It is investigated (McDonald, 2009) that the observed motion of filament by  
3011 images has geometric relation with the viewing angle by focal length in optics.  
3012 The filaments ejected from mercury jet by the proton beam interaction are  
3013 viewed via shadow photography from a focal length  $f = 9.15$  cm from the  
3014 center of the jet. The jet is supposed to have elliptical cross section. The

schematic geometry of viewing mercury filaments is shown in Fig. 6.1. The measurements describes the projection  $y_m(t)$  onto the  $y$  axis of a ray from the observer to the surface. McDonald (2009) assumes that the filaments leave perpendicularly as shown in Fig. 6.1. The elliptic expression is given as Eqn. (6.1):

$$\frac{x^2}{a^2} + \frac{y^2}{b^2} = 1, \quad (6.1)$$

where the jet is circular with radius  $b$  if  $a = b$ . Suppose a filament leaves the surface with velocity  $v_o$  at time  $t_o$  from point  $(x_o, y_o)$ , at time  $t > t_o$ , the travel distance  $d$  is then  $v_o(t - t_o)$  assuming that the velocity is constant. The position of the filament is  $x_d = x_o + d \sin(\theta)$ ,  $y_d = y_o + d \cos(\theta)$ . Using the trigonometric notation of slope at point  $(x_o, y_o)$ , the position of the filament,  $y_m$ , as projected onto the  $y$  axis is

$$\begin{aligned} y_m &= y_d \frac{f}{f - x_d} \approx y_d \left(1 + \frac{x_d}{f}\right) \\ &= b \cos \theta + v_o(t - t_o) \cos \theta + \frac{[a + v_o(t - t_o)][b + v_o(t - t_o)]}{2f} \sin 2\theta. \end{aligned} \quad (6.2)$$

Thus, the apparent velocity of the filament along  $y$  axis is

$$v_m = \frac{dy_m}{dt} \approx v_o \left[ \cos \theta + \frac{a + b + 2v_o(t - t_o)}{2f} \sin 2\theta \right]. \quad (6.3)$$

The earliest time  $t_{om}$  that a filament can be seen vis projected shadow photography when  $y_m = b$  is given as

3035

3036

$$t_{om} \approx t_o + \frac{b(1 - \frac{v_m}{v_o})}{v_m} \quad (6.4)$$

3037

and

3038

3039

$$v_m \approx \frac{v_o}{1 + v_o \frac{(t_{om} - t_o)}{b}}. \quad (6.5)$$

3040

### 6.1.2 Distribution of filaments on jet surface

3041

3042

3043

3044

3045

3046

3047

$$P(\theta)d\theta = \frac{d\theta}{2\pi}. \quad (6.6)$$

3048

3049

3050

3051

$$P(\theta)d\theta = \frac{d\phi}{2\pi} = \frac{ab}{a^2 \sin^2 \theta + b^2 \cos^2 \theta} \frac{d\theta}{2\pi}. \quad (6.7)$$

3052

3053

3054

Third, in case that the filaments are distributed uniformly in position  $s$  around the circumference  $C$  of the ellipse, the probability of the existence of the filaments is

3055

3056

$$P(\theta)d\theta = \frac{ds}{C} \approx \frac{2\sqrt{a^2 \cos^2 \theta + b^2 \sin^2 \theta}}{3(a+b) - \sqrt{(3a+b)(a+3b)}} \frac{d\theta}{2\pi}. \quad (6.8)$$

3057

### 6.1.3 Estimation of filaments velocity

3058

3059

3060

3061

3062

Sievers and Pognat (2000) reported the response of solid and liquid target to rapid heating by the incident proton beam. The parabolic radial energy deposition density  $E_{beam}$  is considered, dropping to 0 at the outer radius  $a = 1$  cm as follow :

3063

$$E_{beam} = E_o[1 - (r/a)^2]. \quad (6.9)$$

3064

3065

3066

3067

3068

3069

The increase in temperature causes pressure rise. It is assumed that the rise time for the temperature is of the same order of magnitude with the beam energy deposition,  $10^{-9}$  s, thermal expansion is initially prevented by the mass inertial of the material. From the definition of bulk modulus  $K$ , the resulting instantaneous thermal pressure for mercury is

3070

$$\Delta p(r) = K\alpha_v \Delta T(r). \quad (6.10)$$

3071

3072

3073

3074

3075

If the thermal heating occurs very slowly comparable to the material's dynamic frequency, it would correspond to quasi-static thermal expansion. It is believed that the energy stored in the material due to the initial thermal expansion may be converted into kinetic energy bombarding the liquid flow away. Corresponding to the thermal expansion caused by the pressure rise,

strain energy is stored in the liquid flow due to the compression, which is expressed as

$$\frac{E_c}{V} = \frac{K(\alpha_v \Delta T(r))^2}{2}, \quad (6.11)$$

where  $E_c$  represents the converted beam energy. The order of the velocity with which the boundary of the liquid material is given by the thermal expansion at the boundary divided by the time over which the sound travels across the radius of the jet, which is in units of  $c\alpha_v T_o$ . The pressure and the velocity at the boundary are reduced by extending the time of heating, which depends on the compressibility like

$$p \sim \frac{1}{\kappa} \quad , \quad v \sim \frac{1}{\sqrt{\kappa}}, \quad (6.12)$$

where  $\kappa$  is the compressibility of material.

## 6.2 Observation of Filaments Development on Mercury Jet Surface

### 6.2.1 Image calibration

#### 6.2.1.1 *image calibration with proton beam arrival signal*

In order to investigate the time response of filaments, we need to establish the accuracy and calibration of the measurement based on the experimental setup. Figure 3.6 shows the traced signals on an oscilloscope when the beam and the beam triggering are delivered. The scintillating fiber signal gives the



beam arrival time. Therefore, it is possible to set up the trigger timing for the cameras and laser driver inputs, which is  $\sim 2 \mu s$  after the master electronic triggering signal from the proton synchrotron. Therefore, the first image of the SMD camera tells the status of jet for the time before the beam arrives since the exposure time of SMD camera is 150 ns. All of the electronic delays including the cable delays are less than  $1 \mu s$ . The maximum frame rate of SMD camera is up to 1 MHz. The accuracy of camera frame rate is checked by using laser pulses. Laser pulses with certain periods are generated and then monitored at oscilloscope through photodiode. The frame rate of camera is set at the corresponding values of laser pulse period. The frame rate is checked by monitoring the variation of intensity of image captured from camera, which is judged as negligibly uniform.

#### **6.2.1.2 *time delay structure of proton beam to light source triggering***

Figure 6.2 (b) shows the time structures between freezing image after laser enabling and proton beam arrival. Figure 6.2 (a) shows the specifications of 25 W laser, where the response time to reach the peak laser, wavelength of laser, and optical power for various pulse rates are shown (Tsang, 2006). Laser emits  $\sim 250$  ns after receiving the 16 pulse trigger from the pulse generator. The time of flight of light to the primary vessel is  $\sim 60$  ns. Once the light source arrives at the primary vessel, the freezing image of mercury jet flow is instantaneously generated and it is then transmitted through the optical fiber corresponding to the light speed  $\sim 4$  ns/m, where  $\sim 60$  ns is taken for

3119 the used imaging fiber length. From the traced signals in Fig. 3.6, the proton  
3120 beam arrival time is measured. Considering the time of flight from primary  
3121 vessel through scintillating fiber,  $\sim 60$  ns delay is estimated, so that the time  
3122 delay between the 1<sup>st</sup> acquired image and the actual proton beam arrival is  
3123 given as  $T_3 - T_2$  in Fig. 6.2 (b), which is considered for the velocity analysis  
3124 of filaments.

## 3125 **6.2.2 Parameter optimization with uncertainty**

### 3126 **6.2.2.1 *nonlinear curve fit for estimation of model***

3127 Selecting a model of the right form to fit a set of data requires the use of  
3128 empirical evidence in the data, knowledge of the process and some trial-and-error  
3129 experimentation. Much of the need to iterate stems from the difficulty in  
3130 initially selecting a function that describes the data well. Some scientific  
3131 theory describing the mechanics of a physical system provide a functional  
3132 form for the process, which type of function makes an ideal starting point  
3133 for model development. So, a practical approach is to choose the simplest  
3134 possible functions that have properties ascribed to the process. Complex  
3135 models are fine, but they should not be used unnecessarily. Fitting models  
3136 that are more complex than necessary means that random noise in the data  
3137 will be modeled as deterministic structure. This will unnecessarily reduce  
3138 the amount of data available for estimation of the residual standard deviation,  
3139 potentially increasing the uncertainties of the results obtained when the model  
3140 is used. Numerical methods for model validation, such as  $R^2$  statistic, are

useful. Graphical methods have an advantage over numerical methods for model validation because they illustrate a broad range of complex aspects of the relationship between the model and the data. Numerical methods tend to be focused on a particular aspect of the relationship between the model and the data and try to compress that information into a single descriptive number. The residuals from a fitted model are the differences between the responses observed at each combination values of the explanatory variables and the corresponding prediction of the response computed using the regression function.

The nonlinear regression model is

$$\mathbf{Y} = f(\mathbf{X}, \Theta) + \epsilon, \quad (6.13)$$

where  $\mathbf{X} = (x_1, x_2, \dots, x_m)$  are independent variables and  $\Theta = (\Theta_1, \Theta_2, \dots, \Theta_k)$  are parameters and  $\epsilon$  is the random error assuming the mean is equal to 0 with normal distribution, where  $k$  is the degree. A measure of the quality of nonlinear fitting parameters is the chi-square value :

$$\chi^2 = \sum_{i=1}^n w_i (y_i - \hat{y}_i)^2, \quad (6.14)$$

where  $w_i$  is the weighting coefficient,  $y_i$  are the experimental data points, and  $\hat{y}_i$  are the theoretical points. To fit the model, the residual is defined as

$$r_i = y_i - \hat{y}_i. \quad (6.15)$$

3163 It conforms to a normal distribution with the mean equal to 0 and the  
 3164 variance equal to  $\sigma_i^2$ . Then the maximum likelihood estimates of the parameters  
 3165  $\Theta_i$  can be obtained by minimizing the chi-square value , defined as

$$3166 \chi^2 = \sum_{i=1}^n \frac{(y_i - \hat{y}_i)^2}{\sigma_i^2}. \quad (6.16)$$

3168 If the error is treated as weight,  $w_i = \frac{1}{\sigma_i^2}$  can be defined in the chi-square  
 3169 minimizing equation, where  $\sigma_i$  are the measurement errors. The quality of  
 3170 regression can be measured by the coefficient of determination,  $R^2$ , which is  
 3171 defined as

$$3172 R^2 = 1 - \frac{\sum_{i=1}^n w_i (y_i - \hat{y}_i)^2}{\sum_{i=1}^n (y_i - \bar{y})^2}. \quad (6.17)$$

3174 In order to express the relationship between independent variables and  
 3175 dependent variables and a degree of confidence in regression model, the adjusted  
 3176  $R^2$  for validation of goodness of fit measurement is defined as

$$3177 \bar{R}^2 = 1 - \frac{\frac{\sum_{i=1}^n w_i (y_i - \hat{y}_i)^2}{n^* - k}}{\frac{\sum_{i=1}^n (y_i - \bar{y})^2}{n^*}}. \quad (6.18)$$

3179 Note that if intercept is included in the model, the degree of freedom is  
 3180  $n^* = n - 1$ . Otherwise,  $n^* = n$ . The adjusted  $R^2$  will avoid the effect of the  
 3181 degrees of freedom by adding variables in the model, which results in rising of  
 3182  $R^2$ . Therefore, the adjusted  $R^2$  overcomes the rise in  $R^2$  when fitting a small  
 3183 sample size by multiple predictor model.

3184 The covariance value indicates the correlation between two variables, and

the matrices of covariance in regression show the inter-correlations among all parameters. The correlation matrix rescales the covariance values. The covariance matrix of the regression and correlation between parameters are defined as

$$Cov (\Theta_i, \Theta_j) = \sigma^2 (X' X)^{-1} \quad (6.19)$$

and

$$Cor (\Theta_i, \Theta_j) = \frac{Cov (\Theta_i, \Theta_j)}{\sqrt{Cov (\Theta_i, \Theta_i)} \sqrt{Cov (\Theta_j, \Theta_j)}}. \quad (6.20)$$

Parameter errors are equal to the square root of diagonal terms in covariance matrix.

#### 6.2.2.2 *Levenberg-Marquardt minimization*

To estimate the  $\hat{\Theta}$  value with the least square method, we need to solve the normal equations which are set to be zero for the partial derivatives of  $\chi^2$  with respect to each  $\hat{\Theta}_p$  :

$$\frac{\partial \chi^2}{\partial \hat{\Theta}_p} = 0. \quad (6.21)$$

Employing an iterative strategy to estimate the parameter values, it starts with some initial values  $\Theta_o$ . With each iteration,  $\chi^2$  value is computed and then the parameter values are adjusted to reduce the  $\chi^2$ . When  $\chi^2$  values computed in two successive iterations are small enough compared with the tolerance, the fitting is converged. The Levenberg-Marquardt algorithm is employed for an

3207 iterative technique that locates a local minimum of a multivariate function that  
 3208 is expressed as the sum of squares of nonlinear function. Levenberg-Marquardt  
 3209 is considered as a combination of steepest descent and the Gauss-Newton  
 3210 method (Pujol, 2007). When the solution is far from a local minimum, the  
 3211 algorithm behaves like a steepest descent method. When the solution is close  
 3212 to a local minimum, it becomes a Gauss-Newton method and exhibits fast  
 3213 convergence (Pujol, 2007).

3214 Given the residuals  $r_i$  ( $i = 1, \dots, n$ ) of parameters  $\Theta = (\Theta_1, \Theta_2, \dots, \Theta_p)$   
 3215 , with  $n \geq k$ , the Gauss-Newton algorithm finds the minimum of  $\chi^2$  given in  
 3216 Eqn. (6.16). Starting with an initial guess  $\Theta_o$  for the minimum, the method  
 3217 proceeds by the iteration  $\Theta^{s+1} = \Theta^s + \delta\Theta$  with an increment  $\delta\Theta$  satisfying the  
 3218 normal equation given as Eqn. (6.22) using Eqn. (6.21):

3219

$$3220 \quad (\mathbf{J}_r^T \mathbf{J}_r) \delta\Theta = -\mathbf{J}_r^T \mathbf{r}, \quad (6.22)$$

3221 where  $\mathbf{r}$  is the vector of  $r_i$  and  $\mathbf{J}_r$  is the Jacobian of  $\mathbf{r}$  with respect to  $\Theta$ .  
 3222 The residuals  $r_i$  are defined as  $r_i(\Theta) = y_i - f(x_i, \Theta)$ . In order to find the  
 3223 parameters  $\Theta$  that a given model function  $y = f(x, \Theta)$  fits best data points,  
 3224 the increment  $\delta\Theta$  can be expressed in terms of Jacobian of the function as  
 3225 follow:

3226

$$3227 \quad (\mathbf{J}_f^T \mathbf{J}_f) \delta\Theta = \mathbf{J}_f^T \mathbf{r}. \quad (6.23)$$

3228 The Levenberg-Marquardt iteration is a variation on the Newton iteration.  
 3229 The normal equations  $\mathbf{N} \delta\Theta = \mathbf{J}_f^T \mathbf{r}$  are augmented to  $\mathbf{N}' \delta\Theta = \mathbf{J}_f^T \mathbf{r}$  where

3230  $N'_{ij} = (1 + \delta_{ij} \lambda) N_{ij}$  with  $\delta_{ij}$  the Kronecker delta. The  $\lambda$  is initialized to  
3231 a small value, e.g.  $10^{-3}$ . If the value obtained for  $\delta\Theta$  reduce the residuals,  
3232 the increment is accepted and  $\lambda$  is divided by 10 before the next iteration. If  
3233 the residuals increase then  $\lambda$  is multiplied by 10 and the augmented normal  
3234 equations are solved again until an increment is obtained that reduces the  
3235 residuals. For large  $\lambda$ , the iteration approaches a steepest descent (OriginLab,  
3236 2007).

### 3237 6.2.2.3 *chi-square probability*

3238 The chi square statistic for an experiment with  $n$  possible outcomes, performed  
3239  $m$  times, in which  $Y_1, Y_2, \dots, Y_n$  are the number of experiments which resulted  
3240 in each possible outcome, with probabilities of each outcome  $p_1, p_2, \dots, p_n$  is:

$$3241 \chi^2 = \sum_{1 \leq i \leq n} \frac{(Y_i - mp_i)^2}{mp_i} . \quad (6.24)$$

3243 Note that  $y_1, \dots, y_n$  are independently normally distributed with mean  
3244  $\mu$  and variance  $\sigma^2$ , then  $\bar{y}$  will be precisely normally distributed with mean  
3245 mean  $\mu$  and variance  $\sigma^2/n$ . By substitution of  $d S^2/\sigma^2 = t$  into sampling  
3246 distribution, the probability density function  $P$  that a  $\chi^2$  value calculated for  
3247 an experiment with  $d$  degrees of freedom is due to chance is:

$$3248 P_{\chi^2, d} = [2^{d/2} \Gamma(\frac{d}{2})]^{-1} \int_{\chi^2}^{\infty} (t)^{\frac{d}{2}-1} e^{-\frac{t}{2}} dt , \quad (6.25)$$

3250 where  $\Gamma$  is the generalisation of the factorial function to real and complex  
3251 arguments:

3252

3253

$$\Gamma_x = \int_0^\infty (t)^{x-1} e^{-t} dt . \quad (6.26)$$

3254

3255

Tables for the chi-square distribution with  $d$  degrees of freedom are given in percentiles (Evans, 1992). The  $p$  percentile is given as

3256

3257

$$Pr(\chi^2(d) \leq \chi_p^2(d)) = p . \quad (6.27)$$

3258

3259

3260

Not that the probability calculation from  $\chi^2$  is an approximation which is valid for large values of  $n$ , and is only meaningful when calculated from a large number of independent experiments.

3261

## 6.2.3 Filaments distribution and uncertainty of measurement

3262

### 6.2.3.1 *onset of filamentation on jet surface*

3263

3264

3265

3266

3267

3268

3269

3270

3271

Figure 6.3 shows photographs of filament evolution on the Hg jet surface at 25  $\mu$ s frame rate, where the beam is 10 Tp, 24 GeV and the magnetic field is 10 T. Figure 6.4 shows the locations of filaments where the individual velocity is measured as a function of time, shown in Fig. 6.6 and Fig. 6.7 (a), (b). The first collected image among 16 images is brighter than the rest of 15 images. It indicates that the radiation generated by the interaction of Hg with proton beam affects the transmittance and/or reflectance of optical components, resulting in the production of darker images as one sees at the rest of collected 15 images.



### 3272 6.2.3.2 *measurement of traveled distance of filament*

3273 To obtain the vertical filament velocity, the distance traveled by a fixed  
3274 point on the jet surface is tracked over a given time period. The jet volume,  
3275 where the maximal energy is deposited, results in the initial generation of  
3276 the filaments. The higher jet velocity occurs when the filaments is initially  
3277 protruded out of the jet surface and then the jet velocity decreases due to the  
3278 magnetic damping and viscous dissipation. So, the velocity at steady state  
3279 is obtained in order to evaluate the relationship with the beam intensity and  
3280 magnetic field.

3281 The quality of optical images varies from shot to shot since the radiation  
3282 or jet dispersion may make image quality varies. The most difficulty in  
3283 measurement is to discern the edge of filaments as it moves somewhat far away  
3284 from surface because the initial jet filament edge is dense (clearly black) but it  
3285 looks like dissipating, dilute, disappearing (grey or similar with background)  
3286 as it moves further. Because measurement is done in several points, there  
3287 may be some error in measurement after some steady velocity (constant peak  
3288 velocity) at weak filament velocity measurement.

3289 The image size at Viewport 2 is 240 by 240. Using graphic software, pixels  
3290 on image is picked to locate the edge of filament. Therefore, the uncertainty  
3291 while locate the position  $y_m$  is reported to be  $\pm 2$  pixels, which corresponds  
3292 to the difference of  $\sim \pm 17$  m/s filaments velocity. This uncertainty can occur  
3293 randomly uniformly. The peak strong filament which gives constant velocity  
3294 within  $\pm 2$  pixels until the end of 15 frames is assumed to be considered as there

is constant uncertainty,  $\pm 2$  pixels. The weak filament which gives constant velocity within  $\pm 2$  pixels until the filament reaches some frames, for example,  $3 \sim 7$  frames, is also assumed to be considered as there is constant uncertainty,  $\pm 2$  pixels, where the black edge of filament is clearly observed. However, after the some frames, for example,  $3 \sim 7$  frames, because the original edge of filament dilute or dissipates or disappear, the uncertainty in measurement may not be constant. In this case, measurement is stopped at that frames.

## 6.2.4 Linear regression with the first order polynomial

### 6.2.4.1 *curve fit function*

The heaviside step function is defined as the integral of the Dirac delta function as follow:

$$H(t) = \int_{-\infty}^t \delta(\xi) d\xi. \quad (6.28)$$

The ramp function is the antiderivative of the Heaviside step function:

$$R(t) = \int_{-\infty}^t H(\xi) d\xi = tH(t). \quad (6.29)$$

In discrete form, it is now defined as an alternative form for our linear regression model as follow:

$$R(t) = \begin{cases} y_m = s, & t \leq t_o \\ y_m = s + v(t - t_o), & t > t_o \end{cases}, \quad (6.30)$$

where  $y_m$ ,  $s$ ,  $v$ ,  $t_o$  denote the measured position of the filament as projected onto the  $y$  axis in image, the position of jet surface before the filaments

developed, the apparent velocity of the filament along the  $y$  axis, and onset time delay of filaments respectively.

#### 6.2.4.2 *parameter estimation using multiple position of filaments*

Shot 11019 is chosen for illustration. Using Eqn. (6.30) for linear regression model with measured data points  $y_m$  and  $t$ , minimizing  $R^2$  yields  $s$ ,  $v$ , and  $t_o$ . Figure 6.5 (a) shows the illustration of multiple data points where the intercept of  $x$  axis and slope estimate the onset time of filament and apparent velocity projected on  $y$  axis in image, which are  $t_o = 43.6 \pm 4.5 \mu s$  and  $v = 55.5 \pm 0.8 \text{ m/s}$  respectively. The reduced  $R^2$  value and adjusted  $\bar{R}^2$  values are 1.749 and 0.998 respectively. Based on Eqn. (6.30), the fit to data points is as follows:

$$y = C_1(x - B_1) + A_1, \quad (6.31)$$

where  $x$  and  $y$  denote the measured position of the filaments and time respectively. Note the parameterized values of coefficients and error values to fit function are given in Table 6.1.

In case of larger velocity of filaments, maximally measurable data points are limited to  $\sim 2 \sim 3$  points due to the limited field of view in optical diagnostic image. Figure 6.5 (b) shows the illustration of 3 data points. The onset time from regression model yields underestimated value such as negative time delay because the data points are equal or smaller than the number of parameters in fit function. Thus, assumption is that the real onset time for such a large

velocity should be between typical onset time  $50 \mu s$  and  $0 \mu s$ , which yields the onset time of  $25 \pm 25 \mu s$ . Therefore, the slope of fit curve is determined by fixing the assumed onset time accordingly, which yields the filament velocity of  $148 \pm 24.5 \text{ m/s}$ . The error is determined directly by dividing approximated filament velocity of the cases of  $t_o = 0$  and  $t_o = 50 \mu s$  by 2. The shot 10008 is chosen for the illustration of parameter estimation of 3 data points. The fit to data points is as follow:

$$y = C_1 x + A_1 \quad (6.32)$$

for the case of negative onset time (black solid line) in Fig. 6.5 (b), and Eqn. (6.31) is employed for the case of having fixed  $B_1 = 0 \mu s$  and  $B_1 = 50 \mu s$  onset time (blue and red solid line) in in Fig. 6.5 (b). As one expects, this approach for a special case yields large uncertainty.

#### 6.2.4.3 *filaments velocity distribution on jet surface*

Figure 6.6 (a) shows the velocity distribution of filaments over the jet surface shown in Fig. 6.3. Fig. 6.6 (b) shows the approximated onset time distribution of filaments according to the approximated velocity of filaments. As the approximated apparent velocity of filaments projected on y axis in image increases, the approximated onset time of filaments decreases. This shows the evidence of the geometric effects of viewing of filaments. Assuming the filaments are generated perpendicular to the jet surface, as the filaments leaves farther from the jet surface, it takes more time to make an initial

observation in images. Thus, it is possible to consider the low velocity of filaments with large onset time leaves from more close to the center of jet normal to the side view shown in images. Note that the velocity of each filament is approximated with uncertainty by doing linear regression using the fit function in order to give one representative velocity according to each filament. Low velocity of filaments close to 0 showed larger error of approximation of onset time due to the uncertainty of the very small observed traveling distance of filaments.

Each filament used for measurement of velocity in Fig. 6.3 has been numbered in Fig. 6.4 for particular indication of each filament. According to the notation in Fig. 6.4, Fig. 6.7 (a) shows the velocity of filaments on the upper free surface of jet as a function of time and Fig. 6.7 (b) shows the velocity of filaments on the lower free surface of jet as a function of time. Note that the instantaneous velocity as defined in Eqn. (6.33) is used for measurement in Fig. 6.7. The onset time of filament increases as the peak velocity of filament decreases, which indicates the possible evidence of the geometric effect of viewing of filaments.

## **6.3 Velocity of Filaments on Mercury Jet Surface**

### **6.3.1 Magnetic dissipation of energy**

As a conducting liquid moves through a static magnetic field, electric currents are generated. This, in turn, leads to ohmic heating such as Joule dissipation. As the thermal energy of the fluid rises, there is a corresponding

filament in its kinetic energy, and so the fluid decelerates. This results in a suppression of the motion of liquid jets. According to P. A. Davidson's approximation (1999), the Eqn. (2.42) shows the energy decay with respect to time depending on the magnetic damping time constant, where  $\tau = \rho/\sigma B^2$ . The implication is that the filaments decelerates on a time scale of  $\tau$ . Figure 2.3 (a) shows the decay of the normalized energy of flow in magnetic fields with respect to time due to the magnetic damping. Higher magnetic field dissipates energy faster. Figure 2.3 (b) shows the integral calculation of energy with respect to time.

### 6.3.2 Time response of filaments in magnetic field

Since the camera is triggered before beam arrives at the Hg jet and the laser pulse width is 150 ns, the first collected image shows the status of Hg jet before beam comes. Thus, the velocity of filament can always be judged as 0 m/s in the following Fig. 6.8.

Since the joule damping dissipates the energy with an exponential factor, the energy dissipation arises rapidly in the beginning depending on the magnetic field term  $B^2$ . Thus, higher magnetic field will have higher damping effect so that it takes more rising time. The magnitude of steady peak velocity is reduced by increased applied magnetic field strength, which is possible indication of the magnetic damping role induced by the joule damping dissipation.

Figure 6.8 represents the time response of instantaneous filament velocity as a function of magnetic field with 14 GeV, 20 Tp beam and 24 GeV, 10 Tp

beam respectively. The expression for the calculation of instantaneous velocity assuming  $\Delta T_n$  is small enough is

$$v_n = \frac{y_m(T_n) - y_m(T_{n-1})}{\Delta T_n}. \quad (6.33)$$

### 6.3.3 Beam induced filaments velocity in magnetic field

#### 6.3.3.1 *filaments velocity with 14 GeV beam in magnetic field*

Figure 6.9 (a) shows the filament velocity as a function of 14 GeV beam intensity and magnetic field corresponding to the observed onset time of filaments shown in Fig. 6.9 (b). Note that the data points without having onset time data is measured by crude measurement of 2 positions of filament from 500  $\mu$ s frame rate shot images, where the estimation of onset time by fitting is inadequate. The filament velocity increases with the beam intensity. However, the magnetic field suppresses the filament velocity. At low intensity of proton beam, the charged beam may be fluctuating depending on the initial conditions at experiment. Thus, the observed onset time of filaments is large at low intensity of beam and it decreases as the intensity of proton beam increases, see Fig. 6.9 (b). Therefore, there are scattering distributions of filament velocity at lower intensity of beam over the resulting data points. The slope of the data points at higher magnetic fields decreases comparing with that associated with lower magnetic field. All velocities are less than 50 m/s regardless of the magnetic field. The filament velocity at 14 GeV, 30 Tp, 10 T is  $\sim 30$  m/s.

### 6.3.3.2 *filaments velocity with 24 GeV beam in magnetic field*

Figure 6.10 (a) shows the filament velocity as a function of 24 GeV beam intensity and magnetic field corresponding to the observed onset time of filaments shown in Fig. 6.10 (b). Again, at low intensity of proton beam, the charged beam may be fluctuating depending on the initial conditions at experiment. Thus, the observed onset time of filaments is large at low intensity of beam and it decreases as the intensity of proton beam increases, see Fig. 6.10 (b). The filament velocity increases with the beam intensity. The slope of the increase is  $\sim 4 \times$  larger than that for the 14 GeV case, where the ratio of peak energy deposition between 14 GeV and 24 GeV beam energy is  $\sim 2.3$  based on the calculation given in Fig. 5.13 (a). It implies the relationship of peak energy deposition to maximum filament velocity. However, the magnetic field suppresses the filament velocity. At relatively low intensity of beam as in the 14 GeV case, the charged beam is unstably fluctuating depending on the event conditions at experiment. Thus, the observed onset time of filaments is large at low intensity of beam and it decreases as the intensity of proton beam increases, see Fig. 6.10 (b). All velocities are less than 180 m/s regardless of the magnetic field, and the filament velocity for the 24 GeV, 30 Tp, 15 T is  $\sim 60$  m/s.



### 6.3.3.3 *filament velocity measurement in pump-probe condition as a check of experiment*

Figure 6.11 shows the measured filament velocity of multiple events with pump-probe conditions as a check of experiment. The conditions of each group in pump-probe events are given in Table A.4. There are 2 groups at 14 GeV and each group has different number of bunches and time delay between pump and probe. Figure 6.11 (a) shows the histogram of disruption length and Fig. 6.11 (b) shows statistics summary such as average, minimum, maximum, and median value. In group 2, qualitatively meaningful distribution of measurements are shown, which is  $10.2 \pm 3.6$  m/s. The pump condition is meaningful due to the delay of beam delay, though there is no significant difference in sub-category of group 2. However, This check shows low velocity comparing with the results shown in Fig. 6.9 (a). One thing to evaluate is that there is another error that should be considered in filament velocity analysis, so called distribution of filament velocity under repetition with same condition of experiment. This is judged by  $\sim 40$  % of the measured velocity, which is integrated in the following key result shown in Fig. 6.12.

## 6.4 Filament Velocity on Jet Surface By Energy Deposition

The energy deposition depending on colliding number of protons at both 14 GeV and 24 GeV beam energy is calculated by Fig. 5.13. Thus, Fig. 6.9 and Fig. 6.10 could be combined as a function of energy deposition, which shows

the results of experiment in maximum filament velocity together. Figure 6.12 shows the filament velocity in magnetic fields as a function of peak energy deposition and fit is according to Eqn. (6.34). Figure 6.13 shows the filament velocity in magnetic fields as a function of total energy deposition and fit is according to Eqn. (6.34). The same threshold value of peak energy and total energy deposition in various magnetic fields with those in Fig. 5.24 and Figure 5.26 in order to connect mutual interplay between results. In other words, the threshold peak energy deposition for filament velocity uses the same value with that for disruption length in order to keep consistency between the onset of disruption and filament.  $\chi^2$  values between Fig. 6.12 and Fig. 6.13 are not significantly different, although Fig. 5.24 has lower  $\chi^2$  value possibly due to effects of the forcefully adopted threshold values from Fig. 5.24 and Figure 5.26.

As discussed, the filament velocity on jet surface is dominated by the distribution of energy deposition interacting with proton beam. Hence, the peak energy deposition plays a role in determining the maximum filament velocity in viewpoint that the velocity distribution on jet surface can be normalized using the peak energy deposition.

The employed global fit with multi-variables for filament velocity using the measured filament velocity is:

$$z = A_1(x - (B_1 + B_2 y^{B_3}))^{C_1 + C_2 y + C_3 y^2}, \quad (6.34)$$

where  $x$  and  $y$  are peak energy deposition and magnetic field respectively.

3490 Note that the parameterized values of coefficients and errors of the fit functions  
 3491 are provided in Table 6.1. Note the error of each measured filament is adjusted  
 3492 by  $\sim 40\%$  of the measured velocity in order to expect somewhat improved  
 3493 fit result with reduced  $\chi^2$ , as discussed previously in multiple events analysis  
 3494 with pump-probe condition. According to Fig. 6.12, the threshold of filament  
 3495 velocity increases in 1.2 power of magnetic field, and it is  $\sim 10$  J/g of peak  
 3496 energy energy deposition with no magnetic field. The filament velocity increases  
 3497 in linear ( $\sim 1.24$ ) power of peak energy deposition with no magnetic field, but  
 3498 it is reduced in  $\sim 1.24 - 0.015B$  power of peak energy deposition with magnetic  
 3499 field.

3500 For muon collider in the future, higher beam intensity equivalent with  
 3501 80 Tp, 20 T of 24 GeV proton beam energy is required. The peak energy  
 3502 deposition at 80 Tp, 24 GeV is  $\sim 255$  J. The total energy deposition 80 Tp,  
 3503 24 GeV is  $\sim 20.7$  kJ. The maximum filament velocity at 255 J of peak energy  
 3504 at 20 T is expected to be  $\sim 119$  m/s. The maximum filament velocity at  
 3505 20.7 kJ of total energy at 20 T is expected to be  $\sim 129$  m/s.

Table 6.1: Parameterized coefficients, its error, and statistics summary of fit function in figures.

Figure	1	2	3	4	5	6	7	8	9	10
6.5(a)	128	0.93517	43.57	4.44411	-	-	-	-	-0.26374	0.00392
6.5(b)(black)	112.1	-	-	-	-	-	-	-	-0.52	-
6.5(b)(blue)	122	0	0	0	-	-	-	-	-0.5865	0.01587
6.5(b)(red)	122	0	50	0	-	-	-	-	-0.81911	0.10777
6.12	0.76998	0.65104	9.93998	0	0.98744	0	1.21081	0	1.23776	0.398
6.13	0.02454	0.0425	338.243	0	115.38	0	0.82899	0	1.00378	0.29245
Figure	11	12	13	14	15	16	17	18	19	
6.5(a)	-	-	-	-	15	12	1.74908	0.99773	0.0505	
6.5(b)(black)	-	-	-	-	2	0	0	0	0	
6.5(b)(blue)	-	-	-	-	3	2	12.31396	0.99622	0	
6.5(b)(red)	-	-	-	-	3	2	281.74259	0.91351	0	
6.12	-0.01468	0.01776	0	0	25	22	2.19995	0.08635	0.0009	
6.13	-0.00671	0.0079	0	0	25	22	1.85595	0.22959	0.0082	

---

**1** : A1 value, **2** : A1 standard deviation,

**3** : B1 value, **4** : B1 standard deviation, **5** : B2 value, **6** : B2 standard deviation,

**7** : B3 value, **8** : B3 standard deviation , **9** : C1 value, **10** : C1 standard deviation,

**11** : C2 value, **12** : C2 standard deviation, **13** : C3 value, **14** : C3 standard deviation,

**15** : Number of points, **16** : Degrees of freedom, **17** : Reduced  $\chi^2$ , **18** : Adjusted  $\mathbf{R}^2$ , **19** :  $\chi^2$  probability.

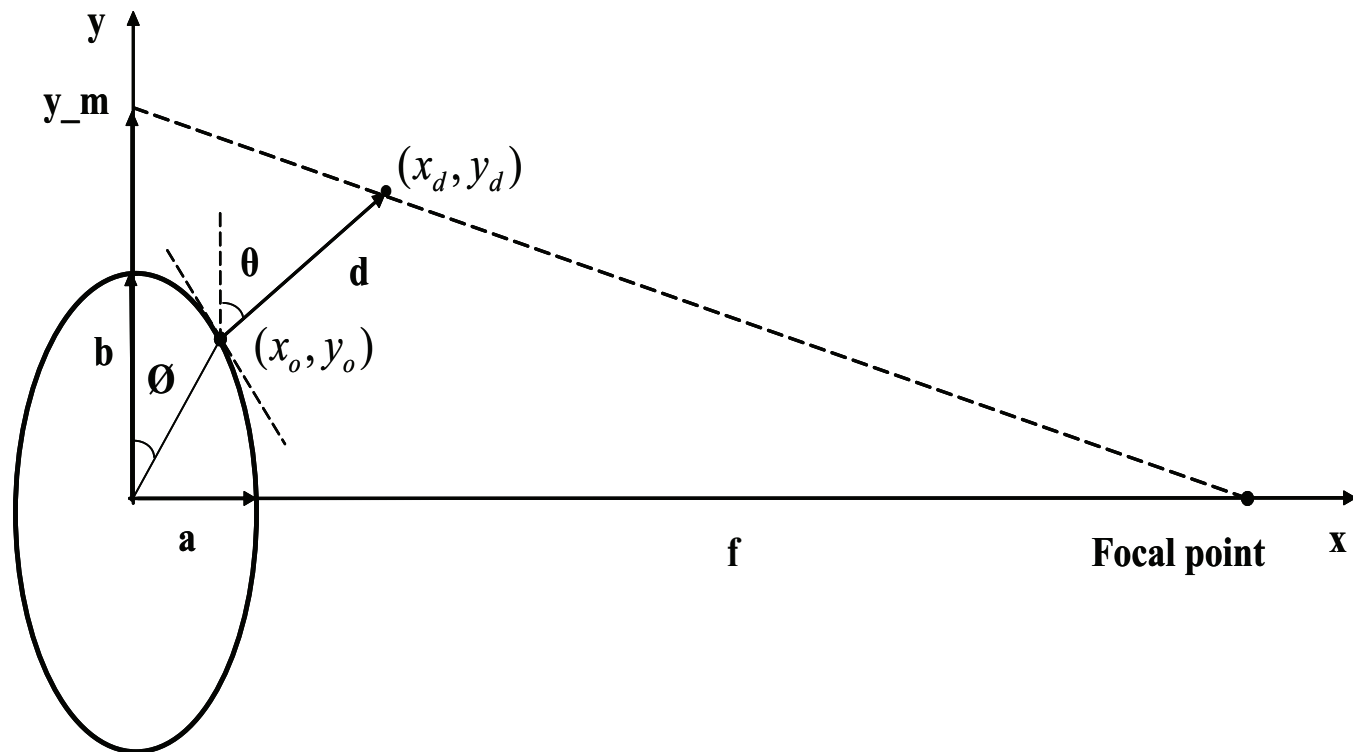


Figure 6.1: Schematic geometry of viewing mercury filaments (McDonald, 2008).

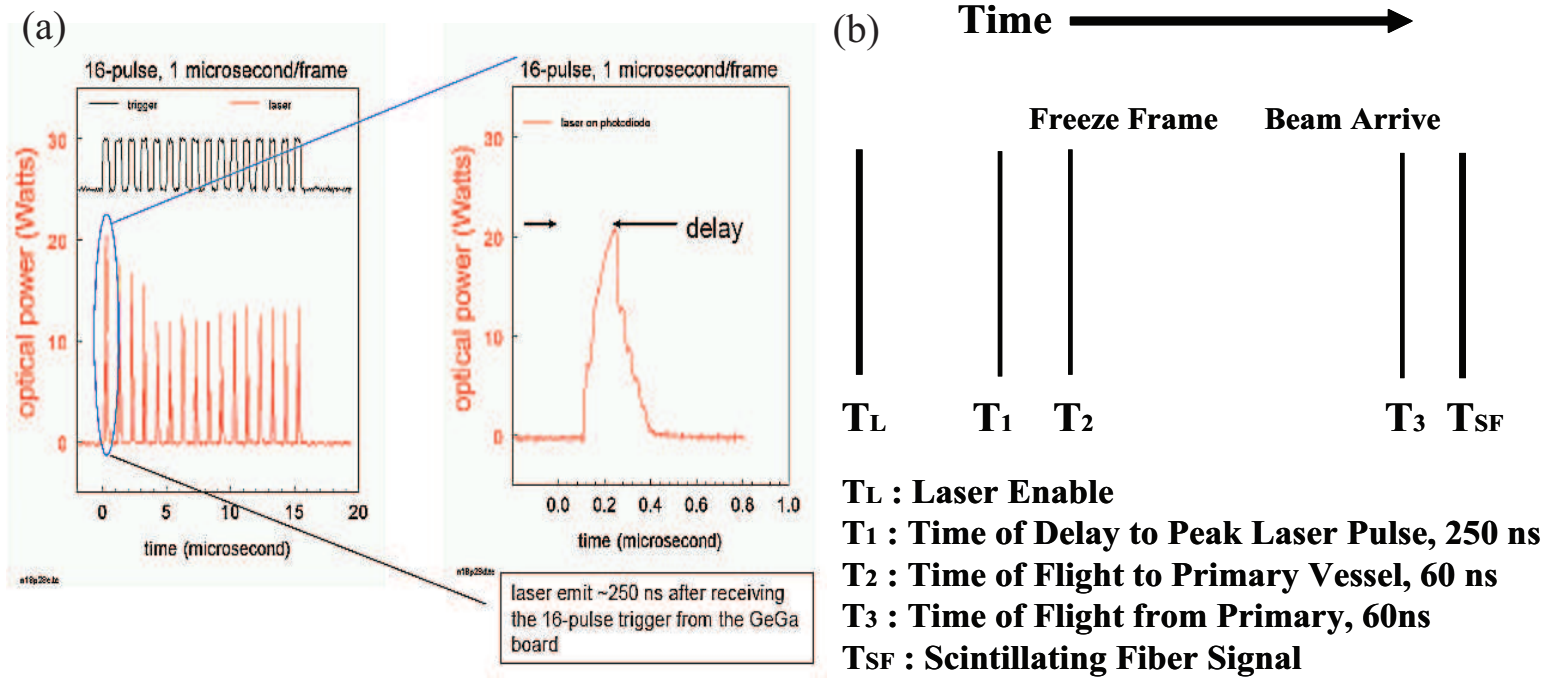


Figure 6.2: Time delay estimation of devices for triggered image calibration. a.) Measurement of characteristic response of 25 laser used for high speed camera at Viewport 2 (Tsang, 2006). b.) Time structures between light source enabling and proton beam arrival.

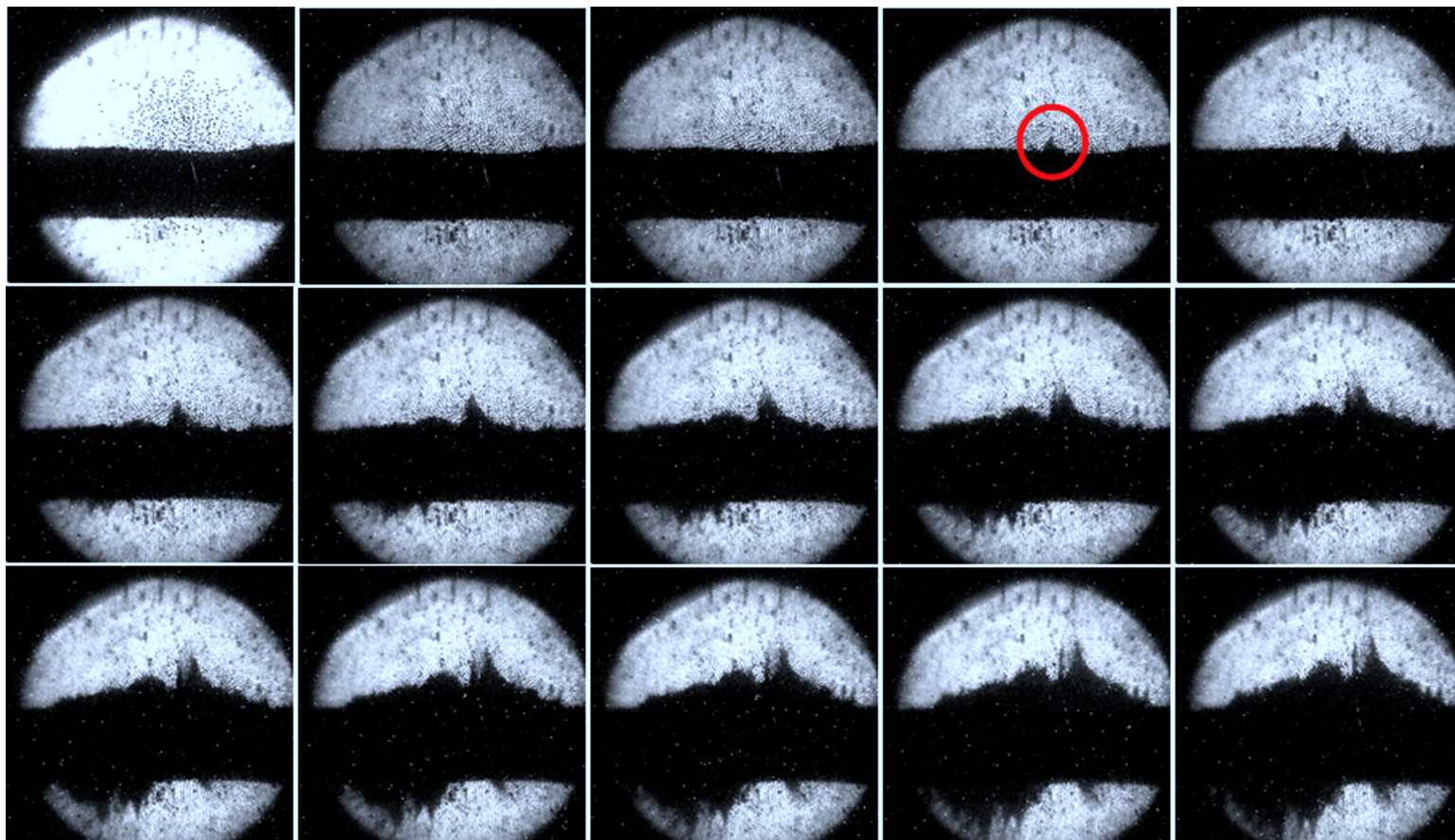


Figure 6.3: Photographs of filament evolution on the Hg jet surface as a function of time at  $25 \mu\text{s}$  frame rate. The beam is 10 Tp, 24 GeV. The magnetic field is 10 T. The red circle on the 4<sup>th</sup> image of the top row points the filament that is used for velocity measurement in Fig. 6.8 (b).



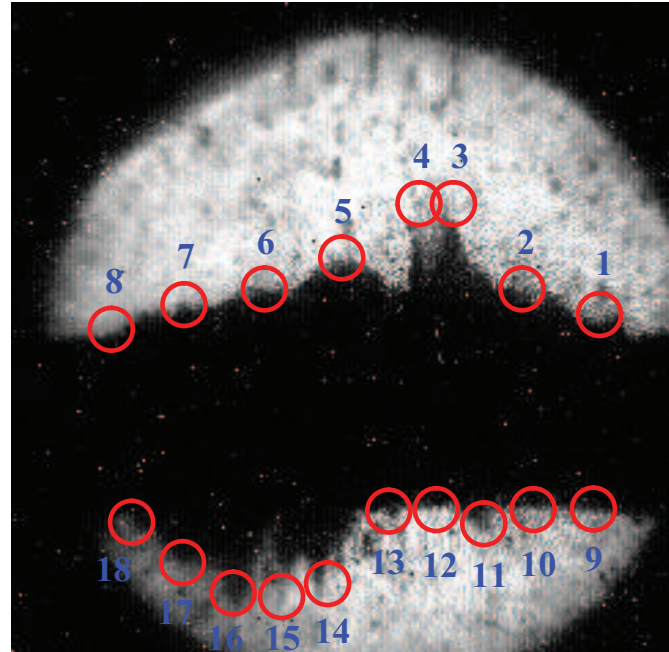


Figure 6.4: Location on the Hg jet surface for velocity measurement of 18 points of filament. The shot condition same with Fig. 6.3. The numbers above red circles points the filament that is used for velocity estimation in Fig. 6.6 and Fig. 6.7.



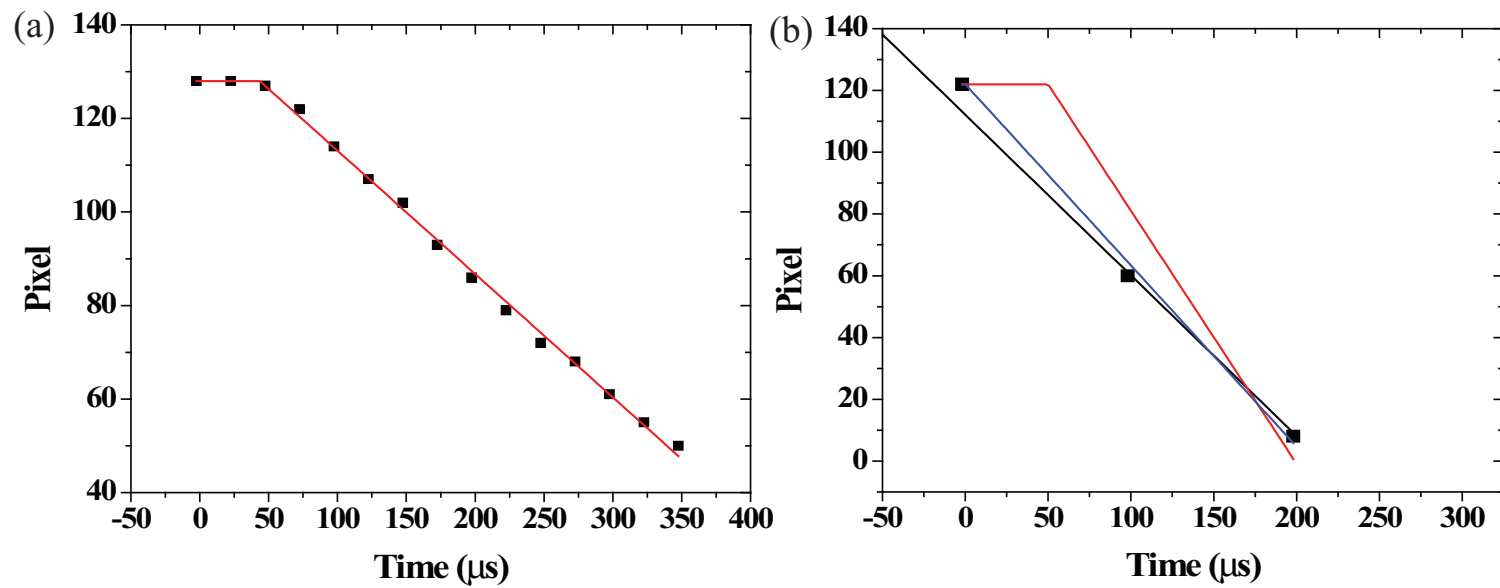


Figure 6.5: Illustration of bilinear fit for parameters estimation. a.) Multiple data points. b.) 3 data points.

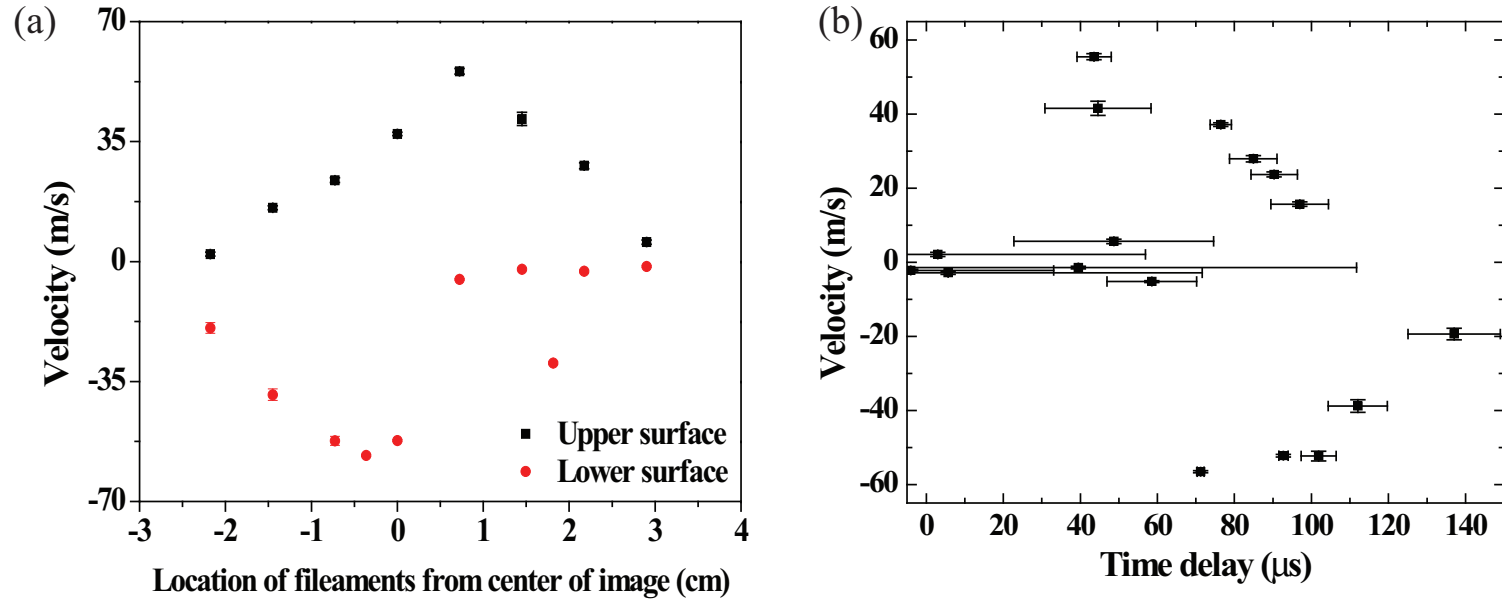


Figure 6.6: Estimation of velocity and onset time of filaments shown in Fig. 6.3. The beam is 10 Tp, 24 GeV. The magnetic field strength is 10 T. a.) Estimation of filament velocity. b.) Estimation of onset time of filaments.

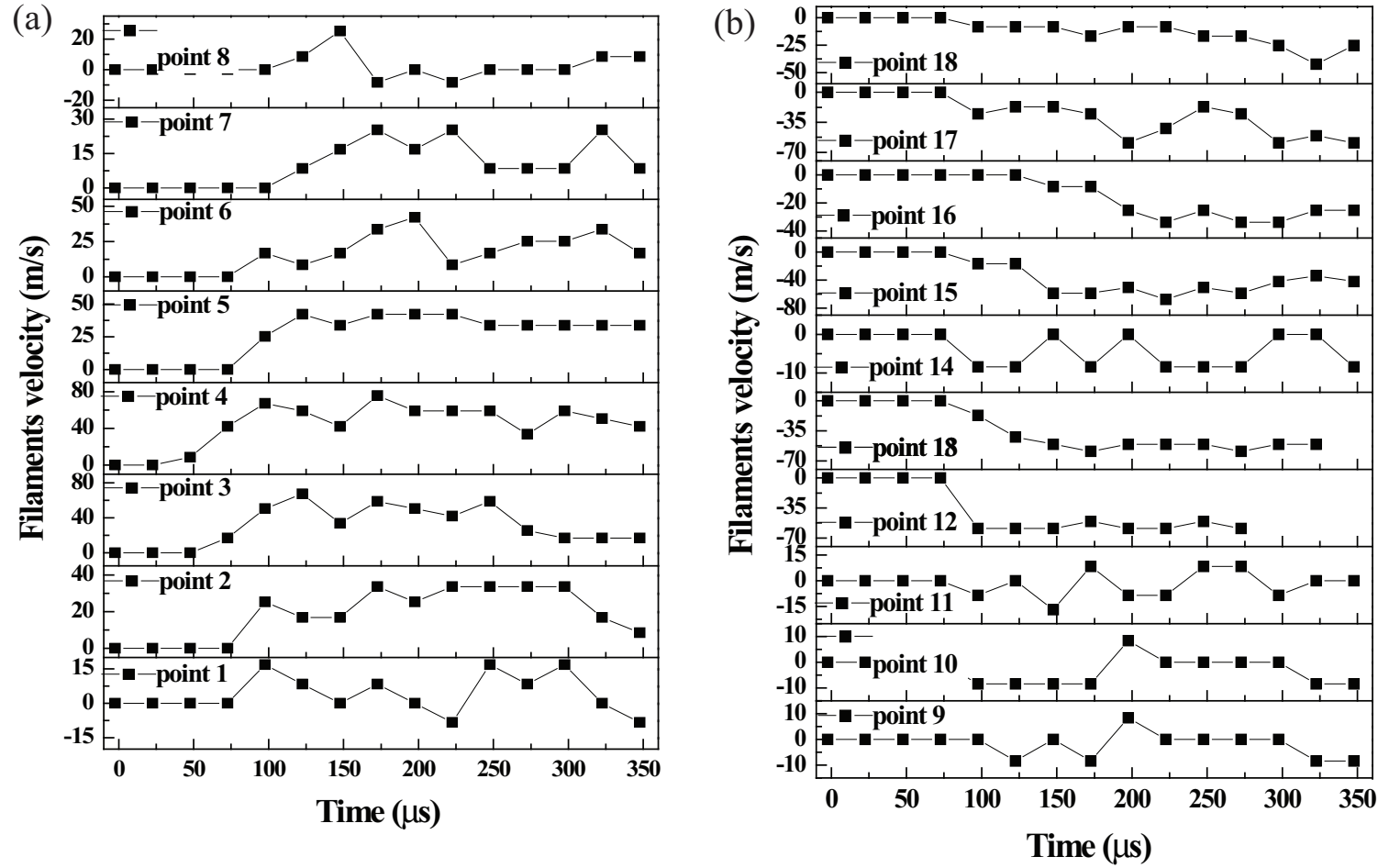


Figure 6.7: Time response of instantaneous filament velocity at jet surface for various filaments shown in Fig. 6.4. The beam is 10 Tp, 24 GeV. The magnetic field is 10 T. a.) Upper surface. b.) Lower surface.

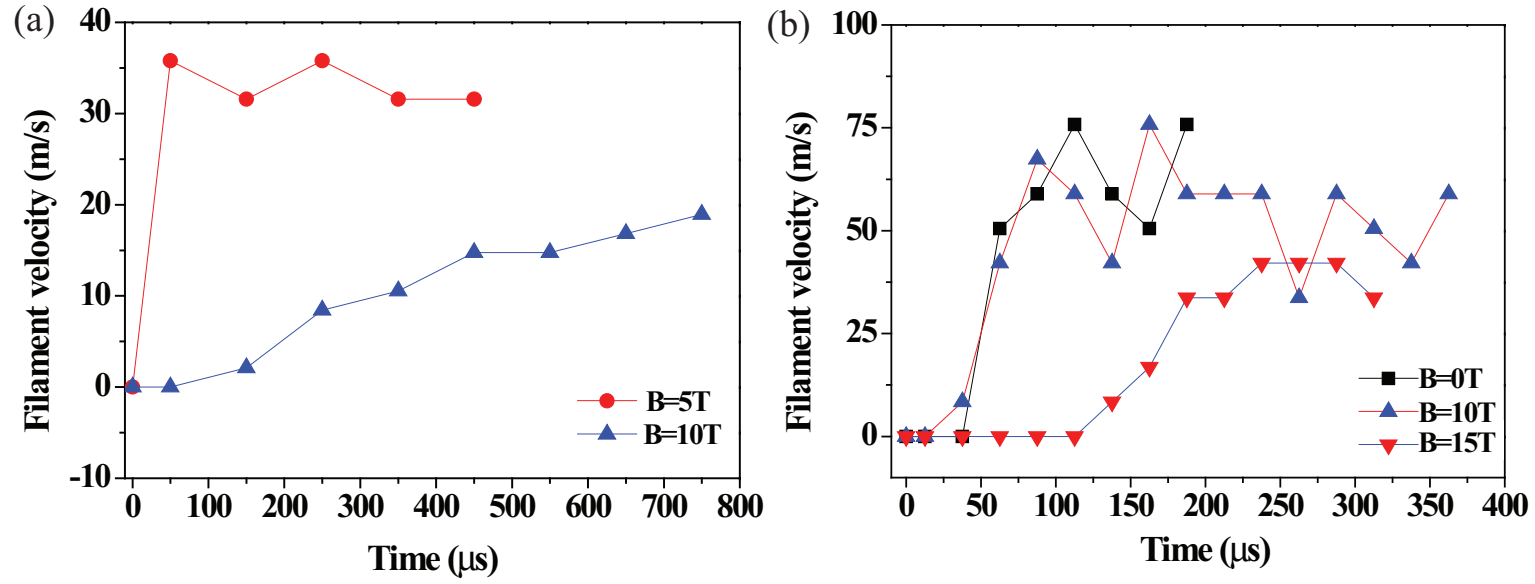


Figure 6.8: Time response of instantaneous filament velocity as a function of magnetic field. Equation (6.33) is used for measuring instantaneous filament velocity. The half of elapsed time between each frame is used to indicate the time at each filament velocity. a.) 14 GeV, 20 Tp beam. b.) 24 GeV, 10 Tp beam.

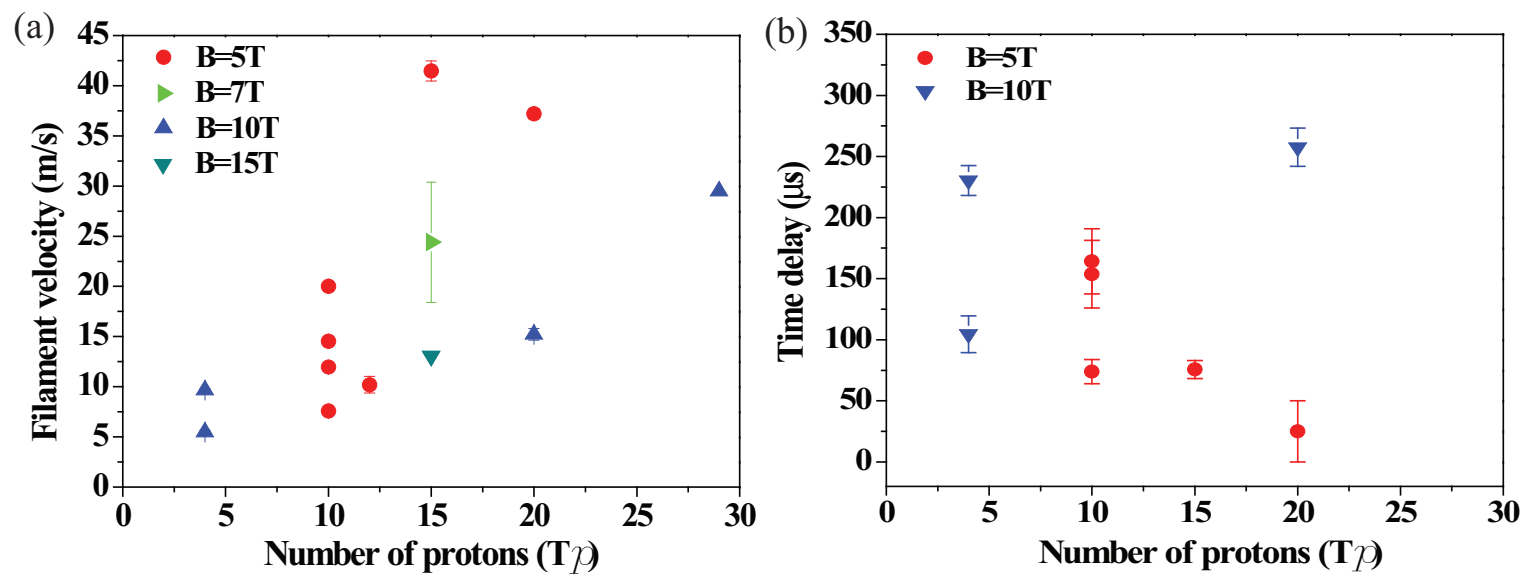


Figure 6.9: Maximum observed filament velocity as a function of  $14$  GeV beam intensity in various magnetic field. a.) Maximum observed filament velocity. b.) Onset time of that filament.

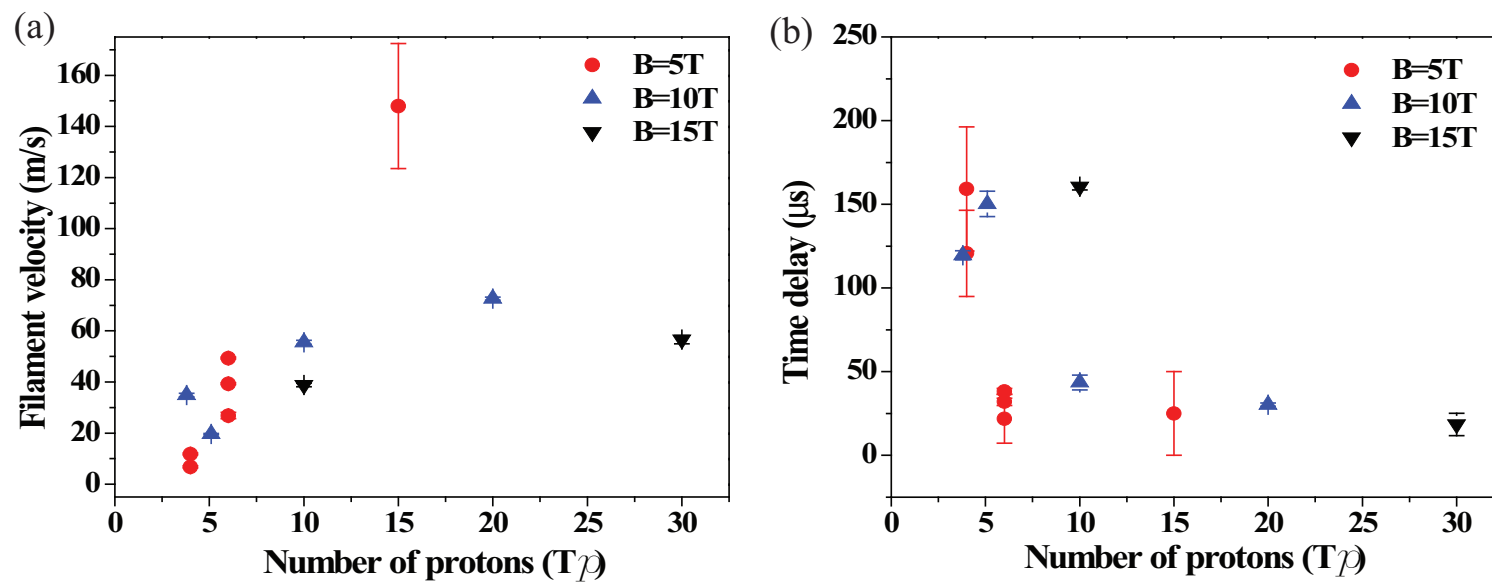


Figure 6.10: Maximum observed filament velocity as a function of 24 GeV beam intensity in various magnetic field. a.) Maximum observed filament velocity. b.) Onset time of that filament.

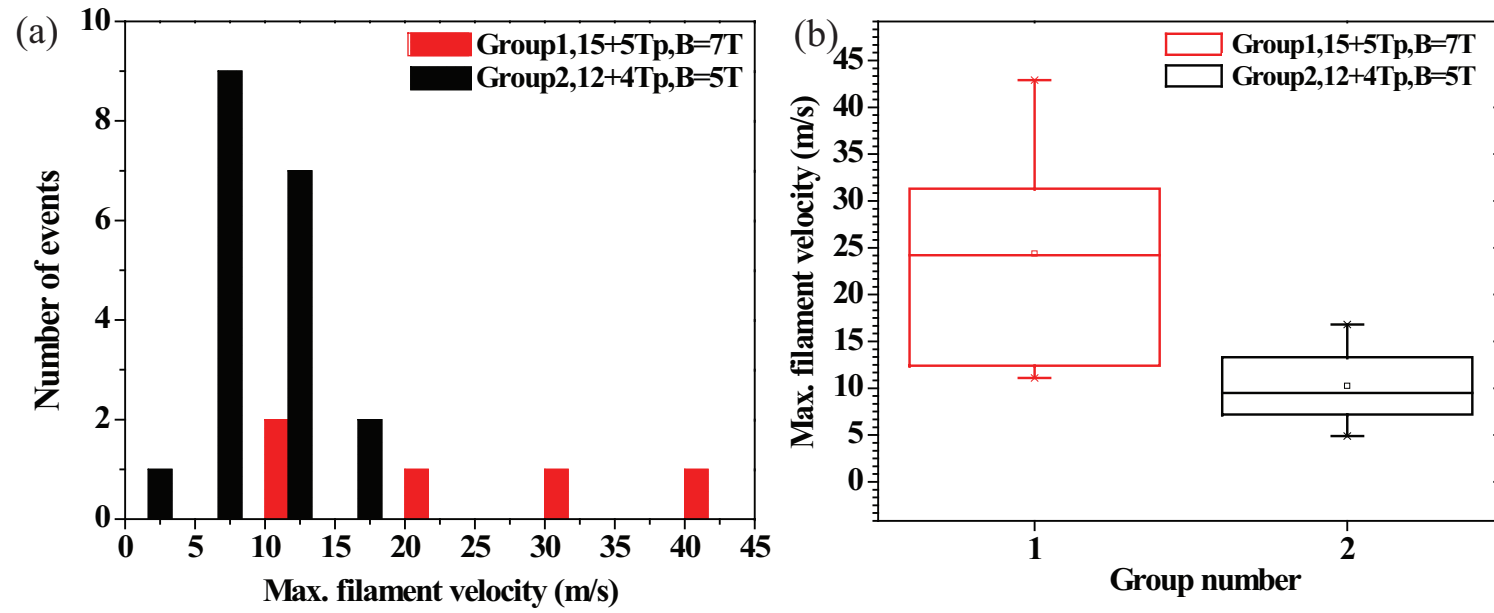


Figure 6.11: Filament velocity measurement in same conditions. Pump-probe conditions with harmonic 8 and 16 bunches are used. The conditions of each group in pump-probe events are given in Table A.4. a.) Histogram of maximum filament velocity in each group. b.) Maximum filament velocity of each group.

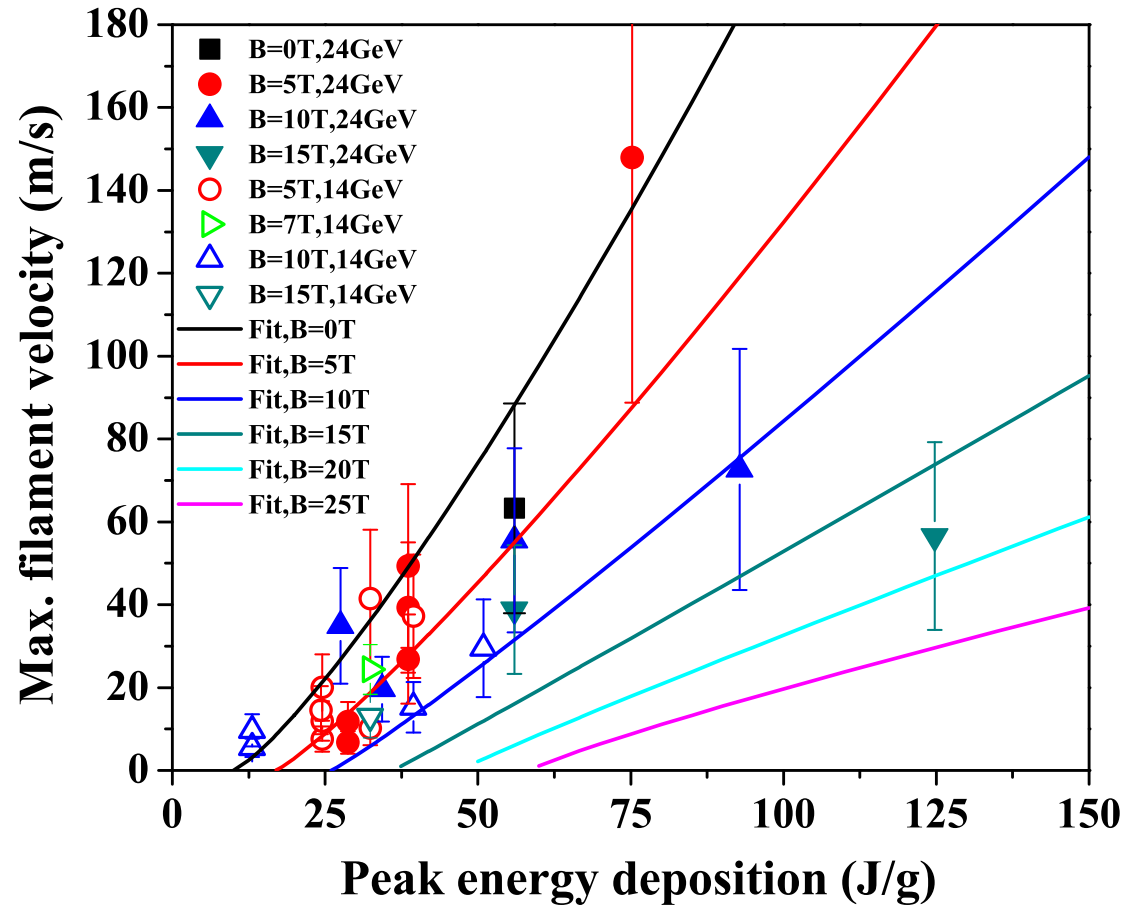


Figure 6.12: Maximum observed filament velocity as a function of peak energy deposition in various magnetic fields and fit is according to Eqn. (6.34).



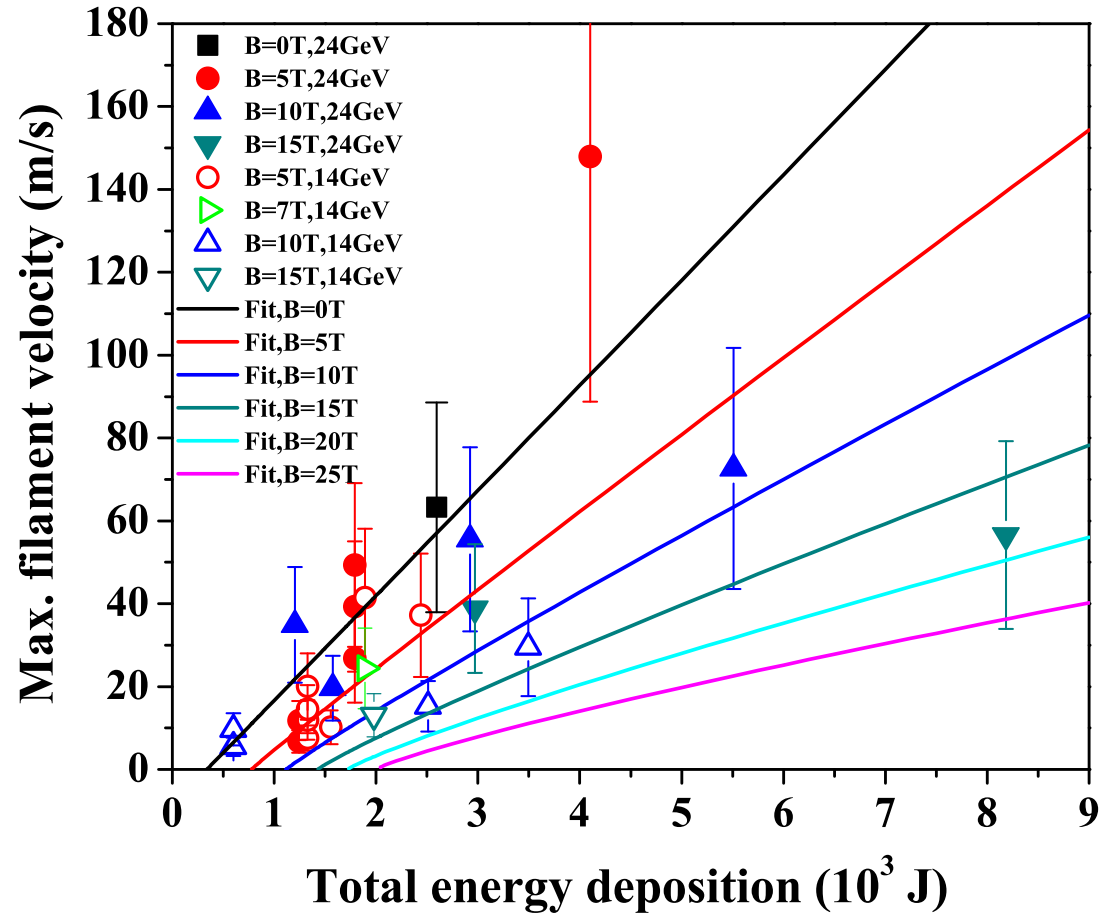


Figure 6.13: Maximum observed filament velocity as a function of total energy deposition in various magnetic fields and fit is according to Eqn. (6.34).

## Chapter 7

## Conclusions

The experiment is a proof-of-principle test for a target system capable of accepting a high-intensity 4 MW proton beam. The system allows for the production of copious pions which subsequently decay into muons. An experiment at the CERN Proton Synchrotron that combines a free mercury jet target with a 15 T solenoid magnet and 14 GeV and 24 GeV proton beam is performed. It validates the liquid type of target concept for production of an intense secondary source of muons. When interacted with a beam pulse of  $30 \times 10^{12}$  protons on the mercury target, this generates a peak energy deposition of  $\sim 125$  J/g, which leads to the disruption of mercury target so that could result in low efficient target for particle production. For this experiment, a 15 T pulsed solenoid is designed. The Hg jet loop system generates a mercury jet from 1 cm diameter nozzle with velocity up to 15 m/s. An optical diagnostic system based on back-illuminated laser shadow photography is employed to investigate the mercury jet flow. Synchronized short laser light pulses are used to illuminate and freeze the motion of the jet. A total of four optical imaging heads for each Viewport are mounted on

the exterior of the primary containment vessel. Four high speed cameras are used to simultaneously collect images on four Viewports. Integrated all-in-one compact optical heads, consisting of ball lens, illumination fiber, objective lens, and imaging fiber bundle, are placed at the radius of curvature of a retro-reflector allowing for the illumination and imaging collection on one side of the mercury primary containment vessel. Due to the short time of frame rate, the time delay from the light source to the image arrival at the camera CCD is adjusted considering the delay from the electronics as well as the fiber-optics. The optimum timing delay is judged by the uniformity of consecutive collected image brightness as well as the triggering signal pulse on the oscilloscope for each component of device, so that timing of the motion of jet is validated. Also, note that the trigger timing is adjusted using the response of the scintillating fiber on the oscilloscope with respect to the beam triggering timing. The motions of mercury jet at Viewport 1, 2, 3 and 4, which enables to understand mercury jet condition at upstream, midstream, and downstream. Image processing provides the mercury jet thickness at various magnetic field strengths. The optical diagnostic observation shows the effects of the magnetic field on the distortion of mercury jet. In addition, it reveals the jet instability which might be caused by the strong induced axial magnetic field, which is possibly the onset of a quadrupole effect. Nevertheless, the experimental results clearly show that the magnetic field stabilizes the mercury jet by smoothing out the edges of the otherwise turbulent mercury flow, as previously reported in the literatures (Shercliff 1956, Gold 1962, Kozyrev 1981,

3548 Bernshtam 1982). The comprehensive optical diagnostic method allows us to  
3549 have a better understanding of the behavior of a conducting jet moving in a  
3550 high magnetic field environment.

3551 In order to achieve an understanding of conducting flow in a magnetic field,  
3552 magnetohydrodynamic equations considering Lorentz force effect based on the  
3553 Navier-Stokes equations as well as Maxwell equations are studied. Also, the  
3554 suppression of vorticity by the perpendicular magnetic field is studied based  
3555 on the role of Stuart number. As a result, the rotational motion of jet on the  
3556 surface becomes more two dimensional motion of flow and thus the jet surface  
3557 is more stabilized, which is observed qualitatively.

3558 For investigation of flow in magnetic field, the mercury jet behavior is  
3559 observed for various magnetic field strengths and then the jet height for deformation  
3560 is measured. The fluctuation on the jet surface decreases as the magnetic field  
3561 increases and the jet height increases slightly with magnetic field assuming  
3562 the major and minor axis of Hg jet is reversed at 10 T. Gravity affects the  
3563 jet trajectory, so that the jet bends down as it goes downstream. But this  
3564 deflection of the jet by gravity is reduced at higher magnetic field. The jet  
3565 axis becomes more straight toward the direction of magnetic field line.

3566 The stabilizing effect of the magnetic field on a turbulent jet is observed.  
3567 It is well known that the turbulent fluctuation is suppressed by magnetic field  
3568 and it is observed that the wave length on the jet surface increases. Thus, the  
3569 jet surface is getting flattened as the magnetic field increases. Therefore, the  
3570 jet is getting more stabilized. However, the jet has a different type of instability

3571 at magnetic fields larger than 10 T. The jet height becomes larger at larger  
3572 magnetic field than 10 T. This seems to be induced by the longitudinal current  
3573 due to the tilted jet axis with respect to the magnet axis. Thus, the induced  
3574 current generates a Lorentz force. As a result, additional anisotropic magnetic  
3575 force is changing the jet height. As the magnetic field increase up to 5 T, the  
3576 jet fluctuation decreases and the jet is more elongating to the flow direction.  
3577 Thus, the jet height decreases from 0 T to 5 T. However, the magnetic pressure  
3578 is influencing at larger than 5 T. Since the optical diagnostics depends on the  
3579 side view of jet flow, it is hard to tell in which direction the jet deflects since  
3580 the jet and the magnetic field line is axially symmetric. However, the jet  
3581 height clearly increases at 15 T, which indicates that the magnetic pressure  
3582 apparently affects the jet height at 15 T.

3583 The longitudinal jet velocity is not varied. Again, the jet elongation to  
3584 the field direction by the magnetic field is indicated from this result. The  
3585 longitudinal magnetic field does not influence the jet flow velocity. The transverse  
3586 magnetic field will change the jet velocity. This is known as the Hartmann  
3587 flow. The longitudinal magnetic field does not influence the longitudinal jet  
3588 flow as indicated in governing MHD equation.

3589 The pipe pressure driven by the syringe piston is measured. It shows  
3590 that the Hg driving pressure is same regardless of the magnetic field. The  
3591 driving pressure at Hg pipe inlet is independent of the magnetic field strength.  
3592 Therefore, the mercury delivery is not influenced by the longitudinal magnetic  
3593 field. However, there may be some pressure loss or jet velocity profile change

3594 due to pipe bend. According to the velocity measurement at upstream, mid-stream,  
3595 and downstream, it is not significantly different and it is same comparing with  
3596 the flow velocity at 0 T. Therefore, the field effect at the pipe bend is expected  
3597 to be somewhat negligible. To support this result, the pipe loss due to the  
3598 geometry and friction is given.

3599 Numerical Monte Carlo simulation is performed for calculation of energy  
3600 deposition into mercury jet, where jet size, trajectory, and beam spot size  
3601 from experimental result are used. The peak energy deposition as well as  
3602 total energy deposition into mercury jet are calculated. Multi-variable fit  
3603 provides the relation of peak energy deposition and total energy deposition  
3604 with number of protons, beam energy, and magnetic field. Also, the averaged  
3605 energy deposition shows the distribution of energy along jet axis as well as the  
3606 relation with number of protons and magnetic field.

3607 The observation of interaction of proton beam up to 30 Tp at both 14 GeV  
3608 and 24 GeV with jet is performed, which provides clue to validate the performance  
3609 of high power target for future accelerator. The disruption as manifested by  
3610 the jet break up is caused by energy deposition of proton beam. The disruption  
3611 begins on the bottom surface of Hg jet where the proton beam enters. The  
3612 disruption ends on the top surface of Hg jet where the proton beam leaves. The  
3613 jet breakup is occurring at midstream of jet flow where the maximum energy  
3614 is deposited. This phenomenon is consistent with the beam trajectory across  
3615 the jet as well as the result of distribution of energy deposition calculation by  
3616 MARS code. However, Hg jet breakup is influenced by the magnetic field. In

order to validate the measured disruption length, elliptic jet shape are modeled in MARS code for calculation of energy deposition. Deposition of peak energy to Hg jet according to the beam intensities and magnetic field strengths are analyzed. Based on the hypothesis of threshold of beam intensity causing the disruption of Hg jet at various magnetic field strength, the disruption length is estimated, which gives good agreement with experimentally measured disruption length. The beam pulse structure is composed of 8 and 16 bunches with a doubled time difference. The effect of pulse structure to disruption length is negligible qualitatively, which means that the instantaneous time of pulse incident to mercury jet does not affect to difference of energy deposition into mercury jet. Using the values from fit to total energy deposition and peak energy deposition, the energy deposition into mercury jet according to number of protons, beam energy, and magnetic field is estimated, so that it is possible to show the disruption length as a function of energy deposition and magnetic field, which also provides an estimation up to 25 T for future possible feasibility. The threshold of disruption increases in  $\sim 0.8$  power of magnetic field, and it is  $\sim 338$  J of energy energy deposition with no magnetic field. Also, the threshold of disruption is  $\sim 10$  J of peak energy deposition with no magnetic field, and it increases in 1.2 power of magnetic field. The disruption length increases in square root power of total energy deposition with no magnetic field, but it is suppressed in  $\sim 1/(2 + 0.04B)$  power of total energy deposition with magnetic field.

The time scale of magnetic damping indicates the rate of decay of global

kinetic energy due to the magnetic field strength. Thus, the energy decreases faster as the magnetic field increases. Therefore, the rising time to the maximum velocity increases as the magnetic field increases. It indicates that the magnetic damping is getting larger by magnetic field in terms of the transient response time. At low intensity of proton beam, the charged beam may be fluctuating depending on the initial conditions at experiment. Thus, the observed onset time of filaments is large at low intensity of beam and it decreases as the intensity of proton beam increases. Therefore, the distribution of filament velocity at lower intensity of beam is more scattered. Also, the geometric effect of viewing the filament is observed. The onset time of filament decreases as filament velocity on uniformly distributed jet surface increases. The maximum filament velocity increases as beam intensity increases due to increased energy deposition but the magnetic field slows the filament velocity. The peak energy deposition plays a role in determining the maximum filament velocity in viewpoint that the velocity distribution on jet surface can be normalized by peak energy deposition.

Using the values from fit to energy deposition, the energy deposition into mercury jet according to number of protons, beam energy, and magnetic field is estimated, so that it is possible to show the filament velocity as a function of energy deposition and magnetic field, which also provides an estimation up to 25 T for future possible feasibility. Note that multiple events with repetition under same condition using pump-probe shot shows well agreement with disruption length results and provides possible error value for



deviation occurred by repeating experiment. To be consistent with the onset of disruption, the threshold of filament velocity is forced to be same value with the onset of threshold energy for disruption length, and it increases in 1.2 power of magnetic field. The filament velocity increases in linear ( $\sim 1.24$ ) power of peak energy deposition with no magnetic field, but it is slowed  $\sim 1.24 - 0.015B$  power of peak energy deposition with magnetic field.

Finally, to conclude, the performance and feasibility of utilizing liquid metal jet as a high power target is investigated. The liquid jet target concept is based on the target being recycled after each pulse. Therefore, the power of the target is evaluated in terms of the replacing capability. The optimal interaction length for the 24 GeV beam energy is in the region of 30 cm which corresponds to approximately 2 interaction length for mercury. For a 20 m/s jet velocity, replacing two interaction lengths will be taken in 14 ms thus allowing for operations with a repetition rate of up to 70 Hz. The disruption length at 15 T is less than 20 cm and the total energy deposition is  $\sim 8000$  J. Therefore,  $100 \sim 133$  kJ of beam energy can be recycled with a 70 Hz repetition rate for 20 m/s jet. This result validates that a target system capable of supporting proton beams with powers of up to 8 MW, which concludes the experiment for investigation of feasibility of mercury jet as a high power target.

## 3682 Bibliography

- 3683 [1] A. Bernadon *et al.*, 1998, “A proposal for an R&D program for targetry  
3684 and capture at a muon collider source,” *BNL E951 Proposal*.<sup>1</sup>
- 3685 [2] M. M. Alsharoa *et al.*, 2003, “Recent progress in neutrino factory and  
3686 muon collider research within the muon collaboration,” *Phys. Rev. ST*  
3687 *Accel. Beams*, **6**, p. 081001.<sup>2</sup>
- 3688 [3] C. M. Ankenbrandt *et al.*, 1999, “Status of muon collider research and  
3689 development and future plans” *Phys. Rev. ST Accel. Beams*, **2**, p. 081001.
- 3690 [4] J. R. J. Bennett *et al.*, 2004, “Studies of a target system for a  
3691 4 MW, 24 GeV proton beam,” proposal to the CERN INTC Committee,  
3692 INTC-P-186, *CERN-INTC-2003-033*, *INTC-I-049*.<sup>3</sup>
- 3693 [5] Robert P. Benedict, 1980, *Fundamentals of pipe flow*, John Wiley & Sons,  
3694 Inc.
- 3695 [6] V. A. Bernshtam, S. V. Kozyrev, A. I. Él’kin, 1982, “Stability of flow  
3696 of films of a conducting viscous liquid in longitudinal magnetic field,”  
3697 *Magnetohydrodynamics*, **18**, p. 132.
- 3698 [7] Herman Branover, 1978, *Magnetohydrodynamic flow in ducts*, John Wiley  
3699 & Sons, Inc.
- 3700 [8] Michael P. Brenner, 2002, “Single bubble sonoluminescence,” *Rev. Mod.*  
3701 *Phys.*, **74**, pp. 425-440.

---

<sup>1</sup><http://www.hep.princeton.edu/~mcdonald/mumu/target/targetprop.pdf>

<sup>2</sup><http://www.cap.bnl.gov/mumu/pubs/prstab-030422/prstab.pdf>

<sup>3</sup>[http://www.hep.princeton.edu/~mcdonald/mumu/target/cern\\_proposal.pdf](http://www.hep.princeton.edu/~mcdonald/mumu/target/cern_proposal.pdf)

- 3702 [9] G. A. Carlson, 1975, "Dynamic tensile strength of mercury," *J. Appl.*  
3703 *Phys.*, **46**, pp. 4069-4070.
- 3704 [10] Donald Chang, Thomas Lundgren, 1961, "Duct flow in  
3705 magnetohydrodynamics," *Z. Angew. Math. Phys.*, **12**, pp. 100-114.
- 3706 [11] I. G. Currie, 1993, *Fundamental Mechanics of Fluids*, Marcel Dekker, Inc.
- 3707 [12] P. A. Davidson, 1999, "Magnetohydrodynamics in materials processing,"  
3708 *Annu. Rev. Fluid Mech.*, **31**, pp. 273-300.
- 3709 [13] G. F. D. Duff, D. Naylor, 1966, *Differential equations of applied*  
3710 *mathematics*, John Wiley & Sons, Inc.
- 3711 [14] I. Efthymiopoulos, A. Fabich, J. Lettry, 2005, "CERN installation,"  
3712 *MERIT Review*.<sup>4</sup>
- 3713 [15] I. Efthymiopoulos, 2008, "The MERIT experiment (nToF11)," *MUTAC*  
3714 *Review*.<sup>5</sup>
- 3715 [16] David H. Evans, 1992, *Probability and its applications for engineers*,  
3716 Marcel Dekker, Inc.
- 3717 [17] A. Fabich, 2002, "High power proton beam shocks and  
3718 magnetohydrodynamics in a mercury jet target for a neutrino factory,"  
3719 *CERN-THESIS-2002-038*.<sup>6</sup>
- 3720 [18] A. G. Fedin, 1973, "Use of optical methods in investigating MHD  
3721 processes," *Magnetohydrodynamics*, **9**, pp. 301-308.
- 3722 [19] T. A. Gabriel, J. R. Haines, T. J. McManamy, P. Spampinato, and  
3723 B. W. Riemer, 2001, "Targets for high intensity particle production,"  
3724 *Proc. Part. Accel. Conf.*, Chicago, pp. 737-741.
- 3725 [20] J. Gallardo *et al.*, 2001, "Calculation for a mercury jet target in a solenoid  
3726 magnet capture system," *Proc. Part. Accel. Conf.*, Chicago, pp. 627-629.

---

<sup>4</sup>[http://www.hep.princeton.edu/~mcdonald/mumu/target/fabich/Fabich\\_121205.pdf](http://www.hep.princeton.edu/~mcdonald/mumu/target/fabich/Fabich_121205.pdf)

<sup>5</sup>[http://www.hep.princeton.edu/~mcdonald/mumu/target/Ilias/ie\\_080408.pdf](http://www.hep.princeton.edu/~mcdonald/mumu/target/Ilias/ie_080408.pdf)

<sup>6</sup><http://www.hep.princeton.edu/~mcdonald/mumu/target/thesis-2002-038.pdf>

- 3727 [21] J. Gallardo *et al.*, 2002, “First order perturbative calculations for  
3728 a conducting liquid jet in a solenoid,” *MUC-NOTE-TARGET-242*,  
3729 *MU-047*. <sup>7</sup>
- 3730 [22] D. Gao, N. B. Morley, 2002, “Equilibrium and initial linear stability  
3731 analysis of liquid metal falling film flows in a varying spanwise magnetic  
3732 field,” *Magnetohydrodynamics*, **38**, No. 4, pp. 359-375.
- 3733 [23] A. K. Geim, M. D. Simon, M. I. Boamfa, M. J. Lighthill, 1999, “Magnetic  
3734 levitation at your finger tips,” *Nature*, **400**, p. 323.
- 3735 [24] M. B. Glanert, M. J. Lighthill, 1955, “The axissymmetric boundary layer  
3736 on a long thin cylinder,” *Proc. Roy. Soc. Ser.*, **A230**, p. 188.
- 3737 [25] Richard R. Gold., 1962, “Magnetohydrodynamic pipe flow: Part 1,” *J.*  
3738 *Fluid Mech.*, **13**, pp.505-512.
- 3739 [26] R. J. Goldstein, 1991, *Optical systems for flow measurement*, McGraw  
3740 Hill, Inc.
- 3741 [27] Andrew Gray and G. B. Mathews, 1966, *A treatise on Bessel functions*  
3742 *and their applications to physics*, Dover, Inc.
- 3743 [28] V. Graves, 2007, “MIT testing results,” *MUTAC Review*. <sup>8</sup>
- 3744 [29] V. Graves, 2007, “Hg system operation review,” *MERIT Review*. <sup>9</sup>
- 3745 [30] J. Hartmann, 1937, “Hg dynamics I,” *Kgl. Danske Videnskab Selskabs*  
3746 *Math. Fys.*, **15**, No. 6.
- 3747 [31] A. Hassanein, I. Konkashbaev, 2001, “Dynamics of liquid metal jets  
3748 penetrating a strong magnetic field in high power colliders,” *Proc. Part.*  
3749 *Accel. Conf.*, Chicago, pp. 624-626.
- 3750 [32] F. Haug, 2009, “Cooling system for the MERIT high power target  
3751 experiment,” *NFMCC Review*. <sup>10</sup>

---

<sup>7</sup><http://www-mucool.fnal.gov/mcnotes/public/pdf/muc0242/muc0242.pdf>

<sup>8</sup><http://www.hep.princeton.edu/~mcdonald/mumu/target/graves/VGraves-070418.pdf>

<sup>9</sup>[http://www.hep.princeton.edu/~mcdonald/mumu/target/graves/Hg\\_System\\_Operation\\_Review.ppt](http://www.hep.princeton.edu/~mcdonald/mumu/target/graves/Hg_System_Operation_Review.ppt)

<sup>10</sup>[http://www.hep.princeton.edu/~mcdonald/mumu/target/Pereira/MERIT\\_PRESENTATION.pdf](http://www.hep.princeton.edu/~mcdonald/mumu/target/Pereira/MERIT_PRESENTATION.pdf)

- 3752 [33] H. Ito, 1960, "Pressure losses in smooth pipe bends," *Trans. ASME.: J.*  
3753 *Basic Eng.*, **82**, p. 131.
- 3754 [34] Uhlenbusch J., Fishcer E., 1961, "Hydromagnetische strömung im  
3755 kreiszylindrischen rohr," *Z. Phys.*, **165**, pp. 190-198.
- 3756 [35] Colin Johnson, 2002, "A self focusing mercury jet target,"  
3757 *CERN-NUFACT-113*.<sup>11</sup>
- 3758 [36] T. Kakuta, T. Shikama, M. Marui, 1999, "Optical fibers and their  
3759 applications for radiation measurement," *Seventh Int. Conf. Nucl. Eng.*,  
3760 Tokyo, Japan, pp. 19.
- 3761 [37] H. G. Kirk *et al.*, 2001, "Target studies with BNL E951 at the AGS,"  
3762 *Proc. Part. Accel. Conf.*, Chicago, pp. 1531-1537.
- 3763 [38] H. G. Kirk *et al.*, 2008, "The MERIT high power target experiments at the  
3764 CERN PS," *Proc. European Part. Accel. Conf.*, Genoa, Italy, *WEPP169*.
- 3765 [39] H. G. Kirk *et al.*, 2008, "A 15 T pulsed solenoid for a high power target  
3766 experiment," *Proc. European Part. Accel. Conf.*, Genoa, Italy, *WEPP170*.
- 3767 [40] B. A. Kolovandin, 1965, "Stability of flow of conducting liquid with free  
3768 surface in the presence of magnetic and electric fields," *Prikl. Mekh.*, **1**,  
3769 No. 11, p. 95.
- 3770 [41] S. V. Kozyrev, A. I. Él'kin, 1981, "Stability of flow of thin films of  
3771 electrically conducting liquid in crossed magnetic and electric fields,"  
3772 *Magnetohydrodynamics*, **17**, No. 4, p. 353.
- 3773 [42] H. C. Lee, 1977, "Boundary layer around a liquid jet," *IBM J. Res.*  
3774 *Develop.*, p. 48.
- 3775 [43] J. Lettry *et al.*, 2003, "Thermal shocks and magnetohydrodynamics in  
3776 high power mercury targets," *J. Phys. G: Nucl. Part. Phys.*, **29**, p. 1621.
- 3777 [44] Junwoo Lim *et al.*, 1998, "Control of streamwise vortices with uniform  
3778 magnetic fluxes," *Phys. Fluids*, **10**, No. 8, p. 1997.

---

<sup>11</sup><http://slap.web.cern.ch/slap/NuFact/NuFact/nf113.pdf>

- 3779 [45] S. P. Lin, D. J. Kang, 1987, “Atomization of a liquid jet,” *Phys. Fluids*,  
3780 **30**, pp. 2000-2006.
- 3781 [46] C. A. Martins, 2005, “Power converter for the TT2 mercury target  
3782 project” *MERIT Review*.<sup>12</sup>
- 3783 [47] K. T. McDonald *et al.*, 2001, “The primary target facility for a neutrino  
3784 factory based on muon beams,” *Proc. Part. Accel. Conf.*, Chicago, p. 1583.
- 3785 [48] K. T. McDonald, 2000, “Cooling of a target by helium gas,” *Princeton*  
3786 */μμ/00-25*.<sup>13</sup>
- 3787 [49] K. T. McDonald, 2000, “Damping of radial pinch effects,” *Princeton*  
3788 */μμ/00-26*.<sup>14</sup>
- 3789 [50] K. T. McDonald, 2000, “Magnetohydrodynamics of a continuous mercury  
3790 jet coaxially entering a solenoid,” *Princeton /μμ/00-29*.<sup>15</sup>
- 3791 [51] K. T. McDonald, 2000, “Magnetohydrodynamics of a pulsed mercury jet  
3792 entering a solenoid at an angle,” *Princeton /μμ/00-30*.<sup>16</sup>
- 3793 [52] K. T. McDonald, 2000, “Optics for E951 target tests in the A3 beamline,”  
3794 *Princeton /μμ/00-28*.<sup>17</sup>
- 3795 [53] K. T. McDonald, 2008, *Private Communication*.
- 3796 [54] P. Michael, 2005, “PSFC west cell power convertors,” *MERIT Review*.<sup>18</sup>
- 3797 [55] N. V. Mokhov, 2001, “Paricle production for a muon storage ring:  
3798 I. Targetry and  $\pi/\mu$  yield,” *Nucl. Inst. Methods Phy. Res.*, **A472**,  
3799 pp. 546-551.

---

<sup>12</sup>[http://www.hep.princeton.edu/~mcdonald/mumu/target/CERN/martins\\_160305.pdf](http://www.hep.princeton.edu/~mcdonald/mumu/target/CERN/martins_160305.pdf)

<sup>13</sup><http://www.hep.princeton.edu/~mcdonald/mumu/target/thermal.pdf>

<sup>14</sup><http://www.hep.princeton.edu/~mcdonald/mumu/target/radialpinch.pdf>

<sup>15</sup><http://www.hep.princeton.edu/~mcdonald/mumu/target/continuousjet.pdf>

<sup>16</sup><http://www.hep.princeton.edu/~mcdonald/mumu/target/pulsedjet.pdf>

<sup>17</sup><http://www.hep.princeton.edu/~mcdonald/mumu/target/a3optics.pdf>

<sup>18</sup>[http://www.hep.princeton.edu/~mcdonald/mumu/target/MIT/West\\_Cell\\_Power\\_Convertors.pdf](http://www.hep.princeton.edu/~mcdonald/mumu/target/MIT/West_Cell_Power_Convertors.pdf)

- 3800 [56] N. V. Mokhov, O. E. Krivosheev, 2000, "MARS code status,"  
3801 *FERMILAB-Conf-00/181*.<sup>19</sup>
- 3802 [57] Neil B. Morley *et al.*, 2000, "Liquid megnetohydrodynamics: recent  
3803 progress and future directions for fusion," *Fusion Eng. and Des.*, **51**,  
3804 pp. 701-713.
- 3805 [58] Neil B. Morley, Sergey Smolentsev, Donghong Gao, 2002, "Modeling  
3806 infinite/axisymmetric liquid metal magnetohydrodynamic free surface  
3807 flows," *Fusion Eng. and Des.*, **63**, pp. 343-351.
- 3808 [59] 2007, *Origin 8 User Guide*, OriginLab Corporation.
- 3809 [60] S. Ozaki, R. Palmer, M. Zisman, J. Gallardo, 2001, "Neutrino factory  
3810 feasibility study 2," *BNL-52623*.<sup>20</sup>
- 3811 [61] N. Otsu, 1979, "A threshold selection method from gray-level  
3812 histograms," *IEEE Trans. Sys. Man. Cyber.*, **9**, pp. 62-66.
- 3813 [62] Shuzo Oshima *et al.*, 1987, "The shape of a liquid metal jet under a  
3814 non-uniform magnetic field," *JSME Int. J.*, **30**, No. 261, pp. 437-448.
- 3815 [63] R. B. Palmer, 1998, "Muon collider design," *BNL-65242*,  
3816 CAP-200-MUON-98C.<sup>21</sup>
- 3817 [64] Mark A. Pinsky, 1991, *Partial differential equations and boundary value  
3818 problems with applications*, McGraw-Hill, Inc.
- 3819 [65] Jose Pujol, 2007, "The solution of nonlinear inverse problems and the  
3820 Levenberg-Marquardt method," *Geophys.*, **72**, pp. W1-W16.
- 3821 [66] R. D. Reitz, F. V. Bracco, 1982, "Mechanism of atomization of a liquid  
3822 jet," *Phys. Fluids*, **25**, pp. 1730-1742.
- 3823 [67] Uflyand Y. S., 1960, "Hartmann problem for a circular tube," *Soviet  
3824 Phys.*, **5**, pp. 1194-1196.

---

<sup>19</sup><http://lss.fnal.gov/archive/2000/conf/Conf-00-181.pdf>

<sup>20</sup><http://www.cap.bnl.gov/mumu/studii/FS2-report.html>

<sup>21</sup><http://www.osti.gov/bridge/servlets/purl/658363-S5MT4Z/webviewable/658363.pdf>

- 3825 [68] Roman Samulyak, 2006, “Target simulations,” *MUTAC Review*.<sup>22</sup>
- 3826 [69] SAE, 1960, “Aero-space thermodynamics manual,” pp. A18-A20.
- 3827 [70] R. Samulyak, 2006, “Target simulations” *MUTAC Review*.<sup>23</sup>
- 3828 [71] R. Samulyak, J. Du, J. Glimm, Z. Xu, 2007, “A numerical algorithm for  
3829 MHD of free surface flows at low magnetic Reynolds numbers,” *J. Comp.*  
3830 *Phys.*, **226**, pp. 1532-1549.
- 3831 [72] J. A. Shercliff, 1953, “Steady motion of conducting fluids in pipes under  
3832 transverse magnetic fields,” *Proc. Camb. Phil. Soc.*, **49**, pp. 136-144.
- 3833 [73] J. A. Shercliff, 1956, “The flow of conducting flows in circular pipes under  
3834 transverse magnetic fields,” *J. Fluid Mech.*, **13**, pp. 644-666.
- 3835 [74] J. A. Shercliff, 1962, “Magnetohydrodynamic pipe flow: Part 2 High  
3836 Hartmann number,” *J. Fluid Mech.*, **13**, pp. 513-518.
- 3837 [75] J. A. Shercliff, 1965, *A textbook of magnetohydrodynamics*, Pergamon  
3838 Press.
- 3839 [76] N. Simos, 2005, “MERIT experiment window study,” *BNL Review*.<sup>24</sup>
- 3840 [77] P. Sievers, P. Pugnati, 2000, “Response of solid and liquid targets to  
3841 high power proton beams for neutrino factories,” *CERN LHC/2000-4*,  
3842 *CERN-NuFACT Note 035*.<sup>25</sup>
- 3843 [78] G. Skoro, 2008, “MERIT beam spot size : saturations and projections,”  
3844 *MERIT Review*.<sup>26</sup>
- 3845 [79] K. Stewartson, 1955, “The asymptotic boundary layer on a circular cylinder  
3846 in axial incompressible flow,” *Q. Appl. Math.*, **13**, p. 113.
- 3847 [80] P. T. Spampinato *et al.*, 2005, “A free jet mercury system for use in a high  
3848 power target experiment,” *Proc. Part. Accel. Conf.*, Knoxville, p. 1637.

---

<sup>22</sup>[http://www.hep.princeton.edu/~mcdonald/mumu/target/samulyak/mutac06\\_samulyak\\_targetsimulations.pdf](http://www.hep.princeton.edu/~mcdonald/mumu/target/samulyak/mutac06_samulyak_targetsimulations.pdf)

<sup>23</sup>[http://www.hep.princeton.edu/~mcdonald/mumu/target/samulyak/mutac06\\_samulyak\\_targetsimulations.pdf](http://www.hep.princeton.edu/~mcdonald/mumu/target/samulyak/mutac06_samulyak_targetsimulations.pdf)

<sup>24</sup>[http://www.hep.princeton.edu/~mcdonald/mumu/target/simos/Simos\\_121205.pdf](http://www.hep.princeton.edu/~mcdonald/mumu/target/simos/Simos_121205.pdf)

<sup>25</sup><http://cdsweb.cern.ch/record/468537/files/lhc-2000-004.pdf>

<sup>26</sup>[http://www.hep.princeton.edu/~mcdonald/mumu/target/Skoro/Saturation\\_profiles.pdf](http://www.hep.princeton.edu/~mcdonald/mumu/target/Skoro/Saturation_profiles.pdf)



- 3849 [81] S. Striganov, 2009, Private Communication.
- 3850 [82] P. Thieberger, H. G. Kirk, R. J. Weggel, K. T. MacDonald, 2003, “Moving  
3851 solid metallic targets for pion production in the muon collider/neutrino  
3852 factory project,” *Proc. Part. Accel. Conf.*, Portland, p. 1634.
- 3853 [83] P. H. Titus, 2007, “Design report: MERIT BNL E951 15 T pulsed magnet  
3854 for mercury target development,” *MERIT Review*.<sup>27</sup>
- 3855 [84] T. Tsang, 2006, Private Communication.
- 3856 [85] N. Tsoupas *et al.*, 2003, “Injection acceleration and extraction of high  
3857 intensity proton beam for the neutrino facility project at BNL,” *Proc.*  
3858 *Part. Accel. Conf.*, Portland, p. 1637.
- 3859 [86] C. D. West, 2000, “Cavitation in a mercury target,” *ORNL/TM2000/263*.  
3860<sup>28</sup>
- 3861 [87] H. Q. Yang, 1992, “Asymmetric instability of a liquid jet,” *Phys. Fluids*,  
3862 **30**, pp. 681-689.
- 3863 [88] K. T. Yen, 1967, “Role of intermittency in free turbulent flows,” *AIAA*,  
3864 **5**, No. 12 pp. 2187-2192.
- 3865 [89] W. M. Yao *et al.*, 2006, “Accelerator physics of colliders,” *J. Phys.*, **33**,  
3866 No. 1, pp. 35-62.

---

<sup>27</sup>[http://www.hep.princeton.edu/~mcdonald/mumu/target/MIT/design/magnet\\_design\\_0307.pdf](http://www.hep.princeton.edu/~mcdonald/mumu/target/MIT/design/magnet_design_0307.pdf)

<sup>28</sup>[http://www.hep.princeton.edu/~mcdonald/mumu/target/hg\\_cavitation.pdf](http://www.hep.princeton.edu/~mcdonald/mumu/target/hg_cavitation.pdf)

# Appendix A

## Tabular Data for Chapter 3, Chapter 4, Chapter 5, and Chapter 6

### A.1 Specifications of Optics

Table A.1: Specifications of optical components in optical diagnostics.

Item	Value
<b>Right angle prism mirror</b>	Gold coated, 25 × 25 × 35.4, Surface flatness $\lambda/10$
<b>Gradient index lens</b>	
Size	d=1.0 mm, L=2.48 mm
Numerical aperture	0.5
Working distance	Infinity
Coating	AR coated at 800 ~ 960 nm
Sapphire ball lens	D=0.5 mm, Al <sub>2</sub> O <sub>3</sub> , Index of refraction=1.77
<b>Retro-reflecting Parabolic mirror</b>	
Diameter	76.2 mm
Thickness	12.7 mm
Focal length	444 mm
Coating	Gold
<b>Microscope objective</b>	

*Continued on next page*

Table A.1: *Continued from previous page*

Item	Value
Magnification	40 $\times$
Numerical aperture	0.65
Working distance	0.6 mm
Clear aperture	5.0 mm
Power	160 mm (tube length) / f
<b>Optical fiber</b>	
Number of picture elements	30000
Jacketing diameter	800 $\mu\text{m}$
Picture elements area diameter	720 $\mu\text{m}$
Coating diameter	960 $\mu\text{m}$
Core material	GeO <sub>2</sub> containing Silica
Coating material	Silicone
Numerical aperture	0.35
Allowable bending radius	40 mm
Core diameter	200 $\mu\text{m}$

3875

A.2 Mercury Properties

Table A.2: Properties of mercury.

Property	Value	Unit
Atomic number	80	-
Atomic mass	200.59	-
Number of neutrons	121	-
Classification	Transition metal	-
Melting point	-38.87	°C
Boiling point	356.58	°C
Density	13.456 at 25 °C	g/cm <sup>3</sup>
Naturally occurring isotopes	Hg-194 Hg-206	-
Group in periodic table	12	-
Period in periodic table	6	-
Electrical conductivity	$1.06 \times 10^6$ at 25 °C	$\Omega^{-1} \text{ m}^{-1}$
Thermal conductivity	8.34	$\text{W m}^{-1} \text{ K}^{-1}$ at 27 °C
Specific heat	0.139	$\text{J g}^{-1} \text{ K}^{-1}$
Heat of vaporization	59.229	kJ/mol
Heat of fusion	2.295	kJ/mol
Electrical resistivity	961 at 25 °C	n $\Omega \cdot \text{m}$
Speed of sound	1451.4 at 20 °C	m/s
Coefficient of thermal expansion	$60 \times 10^{-6}$ at 20 °C	$\text{K}^{-1}$
Bulk modulus	25	GPa
Dynamic viscosity	$1.552 \times 10^{-3}$	$\text{kg m}^{-1} \text{ s}^{-1}$
Kinematic viscosity	$1.145 \times 10^{-7}$	$\text{m}^2 \text{ s}^{-1}$
Dielectric constant	1.00074	-
Surface tension	485.5 (Hg-Air) at 25 °C	mN/m °C
Magnetic susceptibility	$- 2.9 \times 10^{-5}$	-

3878

### A.3 Specifications of Hg Pressure Sensor

Table A.3: Features of pressure transducer (Swagelok PTI-S-AG400-15AW).

3879

Item	Value
Accuracy	0.5 % LPC of span
Hysteresis	0.1 % of span
Response time	1 milliseconds
Process connection	G1/2B EN, Internal diaphragm type
Max. working pressure	400 bar
Min. working pressure	0 bar
Sensor type	Metal thin film
Over pressure rating	800 bar
Temperature rating(media)	-30 to 100 °C

3880 **A.4 Measurement of Events with Pump-Probe**  
3881 **Conditions**  
3882

Table A.4: Measurement of disruption and filament velocity in pump-probe conditions with 8 and 16 harmonic bunches.

Condition		N <sup>1</sup> , DL <sup>2</sup>	A <sup>3</sup> , DL	S <sup>4</sup> , DL	N, V <sup>5</sup>	A, V	S, V
Group 1	12+4 bunches 15+5 Tp 7 T	5	19.5	4.1	5	24.4	13.4
Group 2	6+2 bunches 12+4 Tp 5 T	30	19.8	6.1	19	10.2	3.6
Group 2, Spec. 1	700 $\mu$ s delay	12	19	5	6	12.4	3.7
Group 2, Spec. 2	350 $\mu$ s delay	11	22.2	7.2	7	8.4	1.9
Group 2, Spec. 3	40 $\mu$ s delay	7	17.3	5	6	10.2	4.1
Group 3	8 bunches 16 Tp 5 T	6	24.8	7.1	-	-	-
Group 4	8 bunches 6 Tp 5 T	6	5.9	3.8	-	-	-

---

<sup>1</sup> N represents number of events for measurement.

<sup>2</sup> DL (cm) represents disruption length of jet.

<sup>3</sup> A represents average of measurement.

<sup>4</sup> S represents standard deviation of measurement.

<sup>5</sup> V (m/s) represents filament velocity on jet surface.

3883

A.5 Beam Program List and Disruption Length

3884

Measurements

3885

Table A.5: Measured disruption length and beam shot program. Item 1 is shot number. The first digit represents experiment run day and last 2  $\sim$  3 digits represent shot numbers of the day. For example, in shot 2003, 2 represents experiment day 2 and 3 represents shot number 3 of experiment day 2. Item 2 is number of bunches. Item 3 is number of protons (Tp). Item 4 is magnetic field (T). Item 5 is jet velocity (m/s). Item 6 is  $L_{disruption}$  (m). Item 7 is  $\sigma_{disruption}$  ( $\pm$  m).

1	2	3	4	5	6	7
2002	1	0.25	0	0	-	-
2003	1	0.25	0	0	-	-
2004	1	0.25	0	0	-	-
2005	1	0.25	0	0	-	-
2006	1	0.25	0	0	-	-
2007	1	0.25	0	0	-	-
2008	1	0.25	0	0	-	-
2009	1	0.25	0	0	-	-
2011	1	0.25	0	0	-	-
2012	1	0.25	0	0	-	-
2013	1	0.25	0	0	-	-
2014	1	0.25	0	0	-	-
2015	1	0.25	0	0	-	-
2016	1	0.25	0	0	-	-
2017	1	0.25	0	0	-	-
2018	1	0.25	0	0	-	-
2019	1	0.25	0	0	-	-
2020	1	0.25	0	0	-	-
2021	1	0.25	0	0	-	-
2022	1	0.25	0	0	-	-

Continued on Next Page...

Table A.5 – Continued

1	2	3	4	5	6	7
2023	1	0.25	0	0	-	-
2026	1+1	0.5	0	15	0.085	4.000
3003	1+1	0.5	0	0	-	-
3005	1+1	0.5	0	0	-	-
3006	12+4	4	0	0	-	-
3007	12+4	4	0	0	-	-
3008	12+4	4	0	0	-	-
3011	12+4	4	0	0	-	-
3012	12+4	4	0	0	-	-
3014	1	0.25	0	0	-	-
3015	1	0.25	0	0	-	-
3016	1	0.25	0	15	No image	-
3017	1	0.25	0	15	0	0.000
3018	1	0.25	0	15	0	0.000
3019	1	0.25	0	15	0.013	0.021
3020	1	0.25	0	15	0	0.000
3021	1	0.25	0	15	0.005	0.016
3022	1	0.25	0	15	0.029	0.027
3023	1	0.25	0	15	0	0.000
3024	1	0.25	0	15	No image	-
3025	1	0.25	5	15	0	0.000
4001	1	0.25	0	15	0.018	0.023
4002	1	0.25	5	15	0	0.000
4003	1	0.25	5	15	0	0.000
4004	1	0.25	5	15	0	0.000
4005	1	0.25	5	15	0.054	0.032
4006	1	0.25	5	15	0.019	0.023
4007	1	0.25	5	15	0	0.000
4008	1	0.25	5	15	0	0.000
4009	1	0.25	5	15	No image	-
4010	1	0	5	0	-	-
4011	1	0.3	0	0	-	-
4012	1	0.3	5	0	-	-
4013	1	0.3	0	0	-	-
4014	1	0.3	5	15	0.007	0.017
4015	16	10	5	15	0.031	0.027

Continued on Next Page...



Table A.5 – Continued

1	2	3	4	5	6	7
4016	16	10	5	0	-	-
4017	16	10	0	15	0.038	0.029
4019	16	10	0	15	0.062	0.033
4020	2	0.5	0	0	-	-
4021	2	0.5	0	0	-	-
4023	2	0.5	0	0	-	-
4024	2	0.5	0	0	-	-
4025	2	0.5	0	0	-	-
4026	2	0.5	0	0	-	-
4028	16	10	0	0	-	-
4030	16	10	0	15	0.143	0.043
4031	16	10	5	15	0.08	0.036
5003	4	1	5	15	0	0.000
5004	16	10	5	15	0.111	0.040
5005	16	10	5	15	No image	-
5006	16	10	5	15	No image	-
5007	16	10	5	15	0.024	0.025
5008	16	10	5	15	0.031	0.027
5009	8	5	5	15	0.033	0.028
5010	8	5	5	15	0.022	0.025
5011	8	5	0	15	0.084	0.037
5012	16	10	5	15	No image	-
5014	16	15	0	15	No image	-
5015	16	15	5	15	0.189	0.047
5016	16	15	5	15	0.18	0.046
5017	16	20	5	15	0.303	0.054
5018	16	20	5	15	0.283	0.053
5019	16	20	5	15	0.204	0.048
5020	16	20	10	15	0.184	0.046
6001	16	4	0	15	0	0.000
6002	16	4	0	15	0.027	0.026
6003	16	10	5	15	0.105	0.039
6004	16	10	5	15	0.105	0.039
6005	16	10	5	15	0.035	0.028
6006	16	10	5	15	0.173	0.046
6007	16	10	5	15	0.028	0.026

Continued on Next Page...

Table A.5 – Continued

1	2	3	4	5	6	7
6008	16	10	5	15	0.052	0.032
6009	16	10	5	15	0.079	0.036
6010	16	10	5	15	0.074	0.035
6011	16	10	5	0	-	-
6012	1	0.25	0	0	-	-
6013	1	0.25	0	0	-	-
6014	1	0.25	0	0	-	-
6015	1	0.25	0	0	-	-
6016	1	0.3	0	0	-	-
6017	1	0.3	0	0	-	-
6018	1	0.3	0	0	-	-
6019	1	0.3	0	0	-	-
6020	1	0.3	0	0	-	-
6021	1	0.3	0	0	-	-
6022	1	0.3	0	0	-	-
6023	1	0.3	0	0	-	-
6024	16	4	0	0	-	-
6025	16	4	0	0	0.092	0.038
6026	16	4	0	15	0.101	0.039
6027	16	4	0	15	0.095	0.038
6028	16	4	5	15	0.005	0.016
6029	16	4	5	15	0.038	0.029
6030	16	4	10	15	0.044	0.030
6031	16	4	10	15	0.058	0.033
7001	16	4	0	0	-	-
7002	16	4	5	0	-	-
7003	16	4	10	0	-	-
7004	16	4	0	15	0.019	0.023
7005	16	4	0	15	0.036	0.028
7006	16	4	10	15	0.014	0.021
7008	16	4	0	0	-	-
7009	16	4	0	0	-	-
7010	16	4	0	0	-	-
7011	16	4	0	0	-	-
7012	16	4	0	0	-	-
7013	16	4	0	0	-	-

Continued on Next Page...

Table A.5 – Continued

1	2	3	4	5	6	7
7014	16	4	0	0	-	-
7015	16	4	0	0	-	-
7016	16	4	10	15	0	0.000
7017	16	4	10	0	-	-
7021	16	4	0	0	-	-
7022	16	4	0	0	-	-
7023	16	4	10	15	0.082	0.036
7024	16	4	10	0	-	-
7025	16	4	10	0	-	-
8001	16	4	0	0	-	-
8002	16	4	0	15	0.016	0.022
8003	16	4	0	15	0.024	0.025
8004	16	4	0	0	-	-
8005	16	4	0	15	0.051	0.032
8006	16	4	0	0	-	-
8007	16	4	0	15	0.147	0.043
8008	16	4	0	0	-	-
8009	16	4	0	15	0.132	0.042
8010	16	4	0	15	0.419	0.059
8011	16	4	0	0	-	-
8012	16	4	0	15	0.041	0.030
8013	16	4	0	0	-	-
8014	16	4	0	15	0.107	0.039
8015	16	4	0	0	-	-
8016	16	4	5	15	0	0.000
8017	16	4	5	0	-	-
8018	16	4	5	15	0.027	0.026
8019	16	4	5	0	-	-
8020		0	5	15	0	0.000
8021	16	4	5	15	0	0.000
8022	16	4	5	0	-	-
8029	16	4	7	15	No image	
8030	16	4	7	15	0	0.000
8031	16	4	7	0	-	-
8032	16	4	7	15	0	0.000
8033	16	4	7	0	-	-

Continued on Next Page...

Table A.5 – Continued

1	2	3	4	5	6	7
8034	12+4	15+5	7	15	0.208	0.048
8035	12+4	15+5	7	15	0.152	0.044
8036	12+4	15+5	0	0	-	-
8037	12+4	15+5	7	15	0.16	0.044
8038	0	0	7	0	-	-
8039	-	-	0	0	-	-
8040	-	-	0	0	-	-
8041	12+4	15+5	7	15	0.203	0.048
8042	12+4	15+5	7	0	-	-
8043	12+4	15+5	7	0	-	-
8044	12+4	15+5	7	15	0.253	0.051
8045	12+4	15+5	7	15	0.165	0.045
8046	12+4	15+5	0	0	-	-
8047	12+4	15+5	7	0	-	-
9003	1	0.25	5	15	0	0.000
9004	16	4	5	15	0.064	0.034
9005	16	4	5	15	0.082	0.036
9006	16	4	5	15	0.215	0.049
9008	16	4	5	15	0.08	0.036
9009	12	3	5	15	0.108	0.040
9010	8	2	5	15	0	0.000
9011	-	-	-	-	0.068	0.034
9012	10	2.5	5	15	0.04	0.029
9013	-	-	-	-	0.04	0.029
9014	12	3	5	15	0.078	0.036
9015	16	6	7	15	0.162	0.045
9016	16	4	7	15	0.109	0.040
9017	12	3.32	7	15	0.005	0.016
9018	12	3.64	7	15	0	0.000
9019	12	3.78	7	15	0.04	0.029
9020	12	5.1	10	15	0.079	0.036
10001	16	4	0	0	No image	-
10002	16	4	0	0	No image	-
10003	16	4	0	15	0.188	0.047
10004	16	4	5	15	0.202	0.048
10005	16	4	5	15	0.128	0.042

Continued on Next Page...

Table A.5 – Continued

1	2	3	4	5	6	7
10006	18	4	10	15	0.038	0.029
10007	16	10	5	15	0.258	0.051
10008	16	15	5	15	0.291	0.053
10009	4	6	5	15	0.154	0.044
10010	2+2	6	5	15	0.184	0.046
10011	2+2	6	5	15	0.294	0.053
10012	4	6	5	15	0.228	0.049
10013	4	6	5	15	0.182	0.046
10014	4	6	5	0	-	-
10015	2+2	6	5	15	No image	-
10016	8	6	5	15	0.155	0.044
10017	8	6	5	0	-	-
10018	4+4	6	5	15	0.25	0.051
10019	4+4	6	5	0	-	-
11001	4	1	0	15	0.029	0.027
11002	16	6	5	15	0.202	0.048
11004	4	6	5	15	0.26	0.051
11005	4	6	5	15	0.246	0.051
11006	4	6	5	15	0.239	0.050
11007	4	6	5	15	0.174	0.046
11008	4	6	5	15	0.122	0.041
11010	4	6	5	15	0.194	0.047
11019	16	10	10	15	0.167	0.045
11020	16	3.5	10	15	0	0.000
11021	16	3.8	10	15	0.062	0.033
11022	16	15	10	15	0.158	0.044
11032	16	20	10	15	0.218	0.049
11033	16	30	10	15	0.214	0.049
11034	16	30	15	15	0.164	0.045
12001	4	5	0	15	0.201	0.048
12003	4	5	0	15	0.238	0.050
12004	4	5	0	15	0.273	0.052
12005	4	5	0	15	0.245	0.051
12007	-	-	0	15	0.039	0.029
12006	4	4	0	15	0.149	0.044
12008	4	4	0	15	0.252	0.051

Continued on Next Page...

Table A.5 – Continued

1	2	3	4	5	6	7
12009	4	4	5	0	-	-
12010	4	4	5	15	0.103	0.039
12011	4	4	5	15	0.079	0.036
12012	4	4	5	15	0	0.000
12013	4	4	5	0	-	-
12014	4	4	0	0	-	-
12015	4	4	5	15	0.105	0.039
12016	4	4	5	0	-	-
12029	8	15	15	15	0.046	0.031
12031	8	10	0	15	0.368	0.057
12032	8	10	15	15	0.149	0.044
12033	16	30	15	20	0.17	0.045
13001	2	2.5	0	15	0.042	0.030
13002	4	5	0	15	0.129	0.042
13003	4	5	0	15	0.138	0.043
13004	4	8	0	15	0.156	0.044
13007	6+2	16	5	15	0.157	0.044
13008	6+2	16	5	15	0.202	0.048
13009	6+2	16	5	15	0.196	0.047
13010	6+2	16	5	15	0.157	0.044
13011	6+2	16	5	15	0.17	0.045
13012	6+2	16	5	0	-	-
13013	6+2	16	5	15	0.221	0.049
13014	6+2	16	5	0	-	-
13015	6+2	16	5	15	0.167	0.045
13016	6+2	16	5	0	-	-
14008	6	6	5	15	0.061	0.033
14009	6	6	5	15	0.103	0.039
14010	6	6	5	15	0	0.000
14011	6	10	5	15	0.174	0.046
14012	6	10	5	0	-	-
14013	6	10	5	0	-	-
14014	6	10	5	15	0.151	0.044
14015	6	10	5	15	0.261	0.052
14017	6+2	16	5	15	0.29	0.053
14018	6+2	16	5	15	0.239	0.050

Continued on Next Page...

Table A.5 – Continued

1	2	3	4	5	6	7
14019	6+2	0	5	15	0.127	0.042
14020	6+2	16	5	0	-	-
14021	6+2	16	5	0	-	-
14022	6+2	16	5	15	0.233	0.050
14023	6+2	16	5	0	-	-
14024	6+2	16	5	15	0.119	0.041
14025	6+2	16	5	0	-	-
14026	6+2	16	5	15	0.215	0.049
14027	6+2	16	0	0	-	-
14028	6+2	16	5	15	0.186	0.047
14029	6+2	16	5	15	0.283	0.053
14030	6+2	16	5	0	-	-
14031	6+2	16	5	15	0.138	0.043
14032	6+2	16	5	0	-	-
14033	6+2	16	5	15	0.189	0.047
14034	6+2	16	5	15	0.383	0.058
14035	6+2	16	5	0	-	-
14036	6+2	4	5	15	0.032	0.027
14037	8	4	5	15	0	0.000
15001	8	4	5	15	0.014	0.021
15002	6+2	16	5	15	0.228	0.049
15003	6+2	16	5	15	0.117	0.041
15004	6+2	16	5	15	0.259	0.051
15005	6+2	16	5	0	-	-
15006	6+2	16	5	15	0.245	0.051
15007	6+2	16	5	0	-	-
15008	6+2	16	5	15	0.2	0.048
15009	6+2	16	5	0	-	-
15010	6+2	16	5	15	0.103	0.039
15011	6+2	16	5	15	0.188	0.047
15012	6+2	16	5	15	0.26	0.051
15013	6+2	16	5	0	-	-
15014	6+2	16	5	15	0.195	0.047
15015	6+2	16	5	0	-	-
15016	6+2	16	5	15	0.173	0.046
15017	6+2	16	5	0	-	-

Continued on Next Page...

Table A.5 – Continued

1	2	3	4	5	6	7
15018	6+2	16	5	15	0.157	0.044
15019	6+2	16	5	15	0.132	0.042
15020	8	16	5	15	0.341	0.056
15021	8	16	5	15	0.165	0.045
15022	8	16	5	15	0.236	0.050
15023	8	16	5	15	0.26	0.051
15024	8	16	5	0	-	-
15025	8	16	5	15	0.175	0.046
15026	8	16	5	0	-	-
15027	8	16	5	15	0.313	0.054
15028	8	16	5	15	-	-
15029	8	6	5	15	0.066	0.034
15030	8	6	5	0	-	-
15031	8	6	5	15	0.068	0.034
15032	8	6	5	0	-	-
15033	8	6	5	15	0.026	0.026
15034	8	6	5	0	-	-
15035	8	6	5	15	0.021	0.024
15036	8	6	5	0	-	-
15037	8	6	5	15	0.115	0.040
15038	8	10	5	15	0.08	0.036
15039	8	8	5	15	0.053	0.032
15040	8	8	5	15	0.054	0.032
15041	8	6	5	15	0.008	0.018
15042	8	6	5	15	0.007	0.017
15043	16	6	5	15	0.027	0.026
15044	4	12	5	15	0.043	0.030
15045	4	12	5	15	0.027	0.026
16001	4	2	0	15	0.082	0.036
16002	4	10	4.1	15	0.068	0.034
16003	4	12	4.1	15	0.205	0.048
16004	4	14	6	15	0.222	0.049
16005	8	12	5	15	0.136	0.042
16006	8	12	5	15	0.208	0.048
16007	8	12	5	15	0.189	0.047
16008	4+4	6+6	5	15	0.212	0.048

Continued on Next Page...



Table A.5 – Continued

1	2	3	4	5	6	7
16009	4+4	6+6	5	15	0.071	0.035
16010	4+4	6+6	5	15	0.164	0.045
16011	4+4	6+6	5	15	0.215	0.049
16012	4	14	5	15	0.229	0.050
16013	4	14	10	15	0.188	0.047
16014	4	12	10	15	0.172	0.045
16015	4	12	15	15	0.144	0.043
16016	4	10	5	15	0.131	0.042
17001	16	6	5	15	0.015	0.022
17002	16	8	5	15	0.125	0.041
17003	16	6	5	15	0.037	0.029
17004	16	6.3	5	15	0.048	0.031
17005	16	6	5	15	0.013	0.021
17006	16	6	7	15	0.093	0.038
17007	16	4.2	7	15	0	0.000
17008	16	8	7	15	0.101	0.039
17009	8+8	8	7	15	0.074	0.035
17010	8+8	8	7	15	0.062	0.033
17011	8+8	8	7	15	0.155	0.044
17012	8+8	8	7	15	-	-
17013	8+8	8	7	15	0.047	0.031
17014	8+8	8	7	15	0	0.000
17015	8+8	7.5	7	15	0.016	0.022
17016	8+8	7.4	7	15	0.086	0.037
17017	8+8	8.4	7	15	0.111	0.040
17018	8+8	6	7	15	0.057	0.033
17019	8+0	4	7	15	0.007	0.017
17020	8+0	6	7	15	0.059	0.033
17021	16	15	10	15	0.174	0.046
17022	16	15	15	15	0.148	0.043
17023	16	29	15	15	0.18	0.046
17024	16	29	10	20	0.23	0.050

## Appendix B

### Image Data for Chapter 6

#### B.1 Images for Filament Velocity Measurement at Viewport 2

Table B.1: Properties of shots used for filaments velocity analysis. Item 1 is shot number. Item 2 is camera frame rate ( $\mu\text{s}$ ). Item 3 is beam energy (GeV). Item 4 is number of bunches. Item 5 is number of protons (Tp). Item 6 is magnetic field (T). Item 7 is nominal jet velocity (m/s). Item 8 is lag time between peak laser emission and proton beam arrival ( $\mu\text{s}$ ).

1	2	3	4	5	6	7	8
11004	25	24	4	6	5	15	-4.03
11007	25	24	4	6	5	15	-3.97
11010	25	24	4	6	5	15	-3.99
11019	25	24	16	10	10	15	-2.43
11021	25	24	16	3.8	10	15	-2.43
11032	25	24	16	20	10	15	-2.03
12031	25	24	8	10	0	15	-1.93
12032	25	24	8	10	15	15	-1.83
12033	25	24	16	30	15	20	-1.85

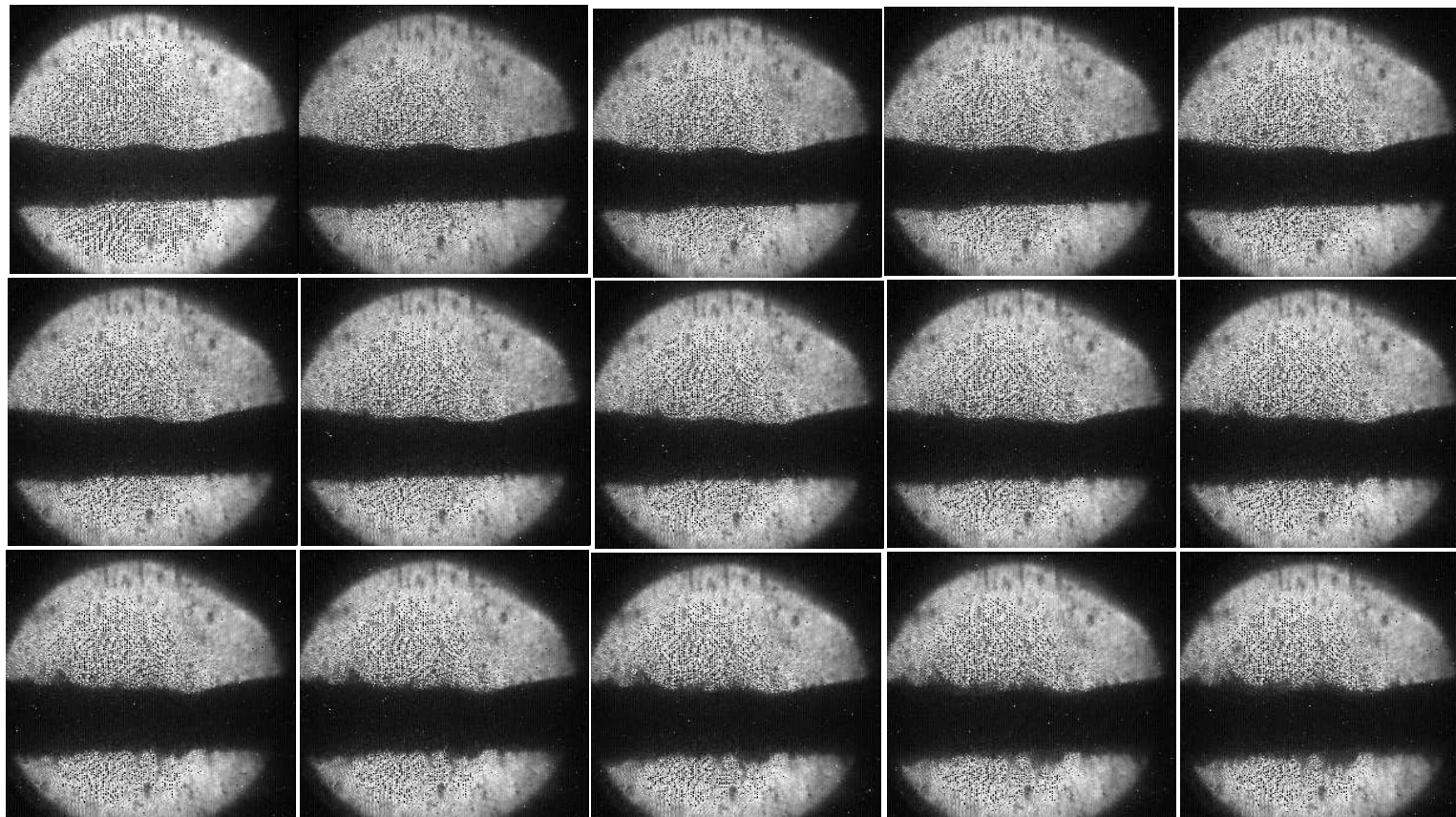


Figure B.1: Shot number is 11004. Photo of sequence of 15 frames of captured image, where the timing for the 1<sup>st</sup> image is given in column 8 in Table B.1.

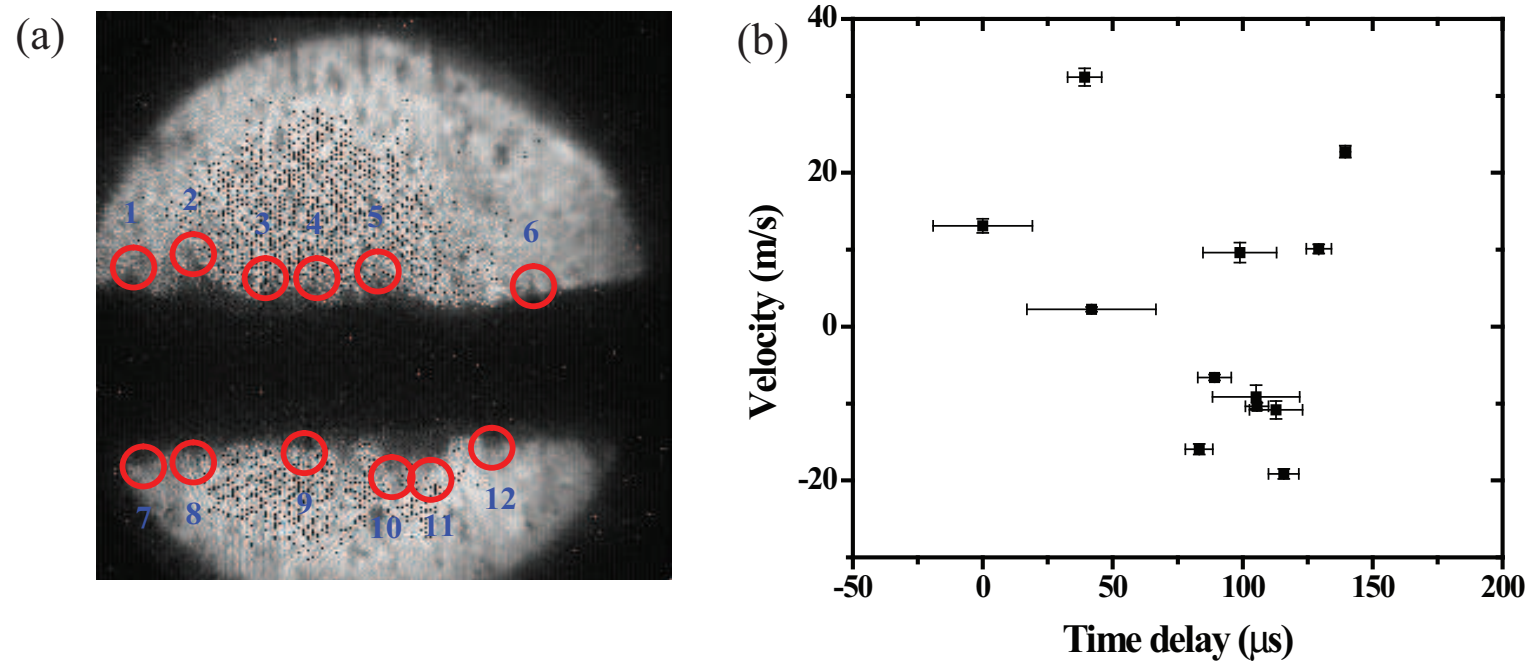


Figure B.2: Location on the Hg jet surface for velocity measurement of filaments. Red circles indicate the location of filaments analysis. Shot number is 11004. a.) Illustration of measured filaments. b.) Measured velocity onset time.



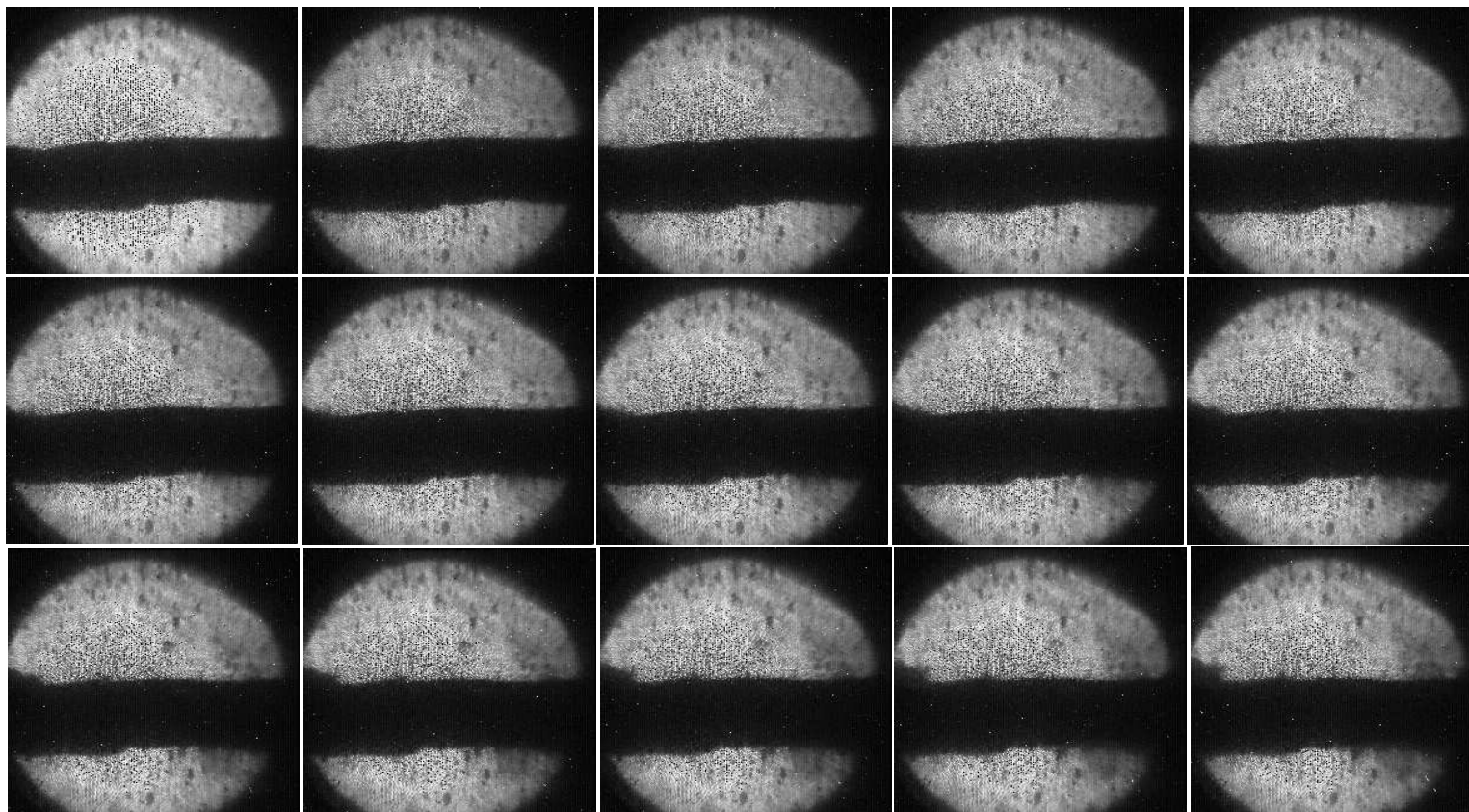


Figure B.3: Shot number is 11007.

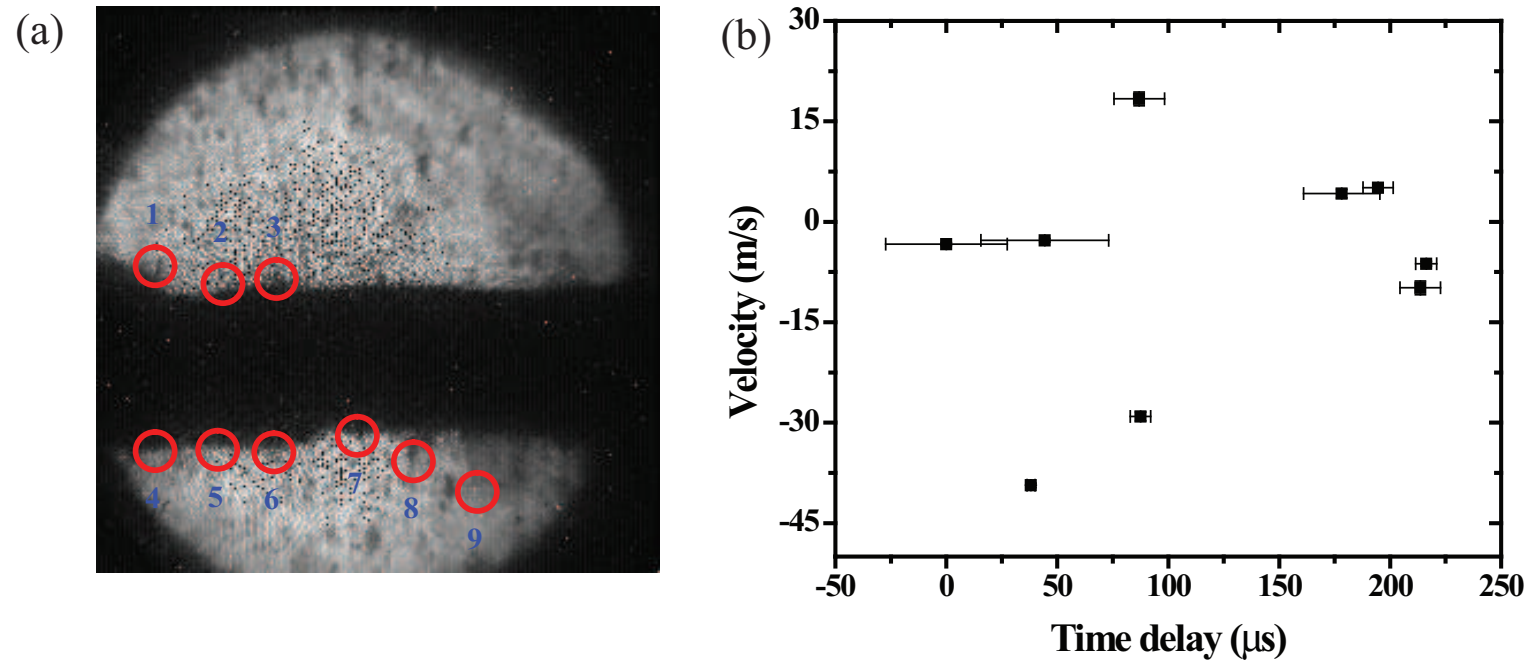


Figure B.4: Shot number is 11007. a.) Illustration of measured filaments. b.) Measured velocity onset time.

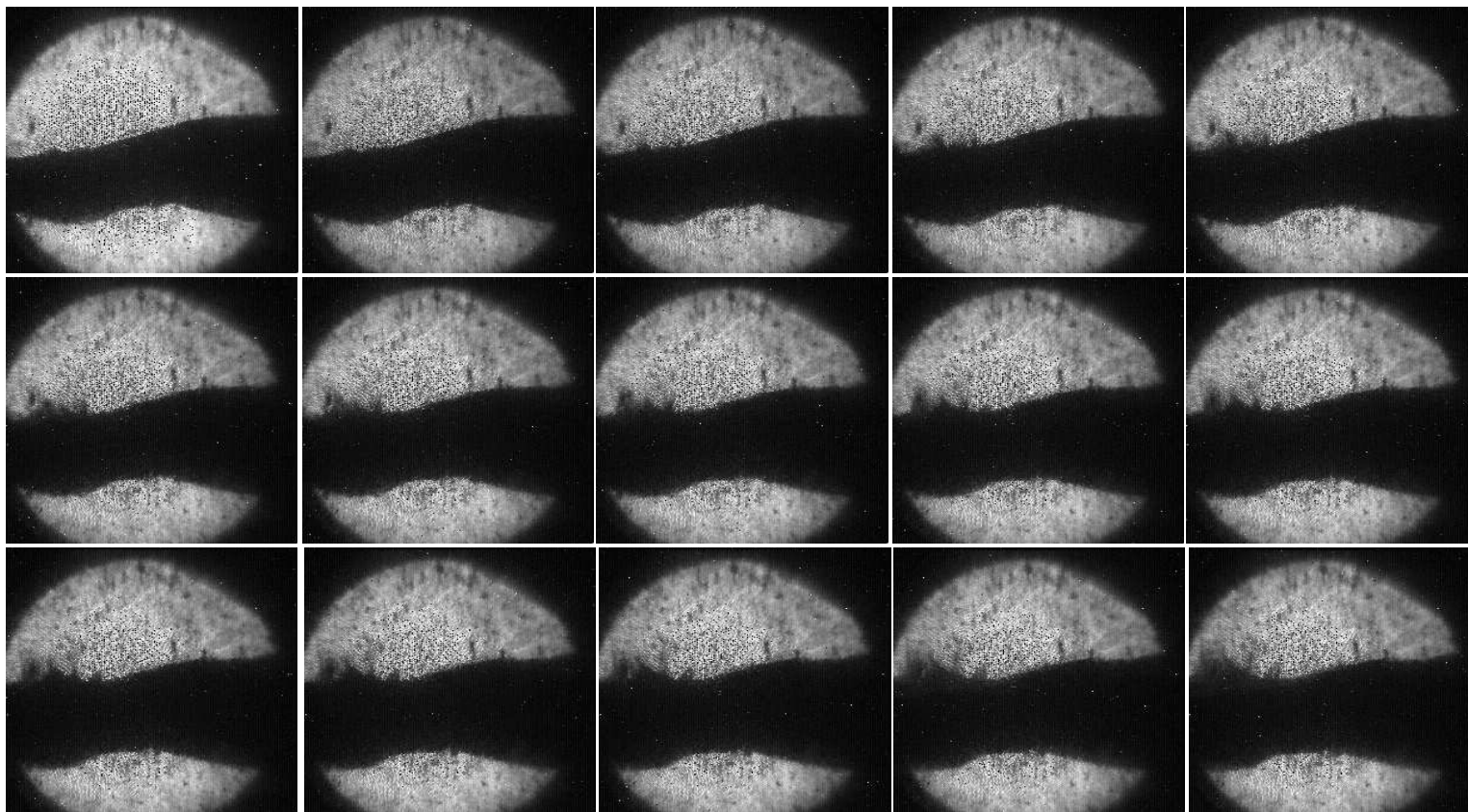


Figure B.5: Shot number is 11010.

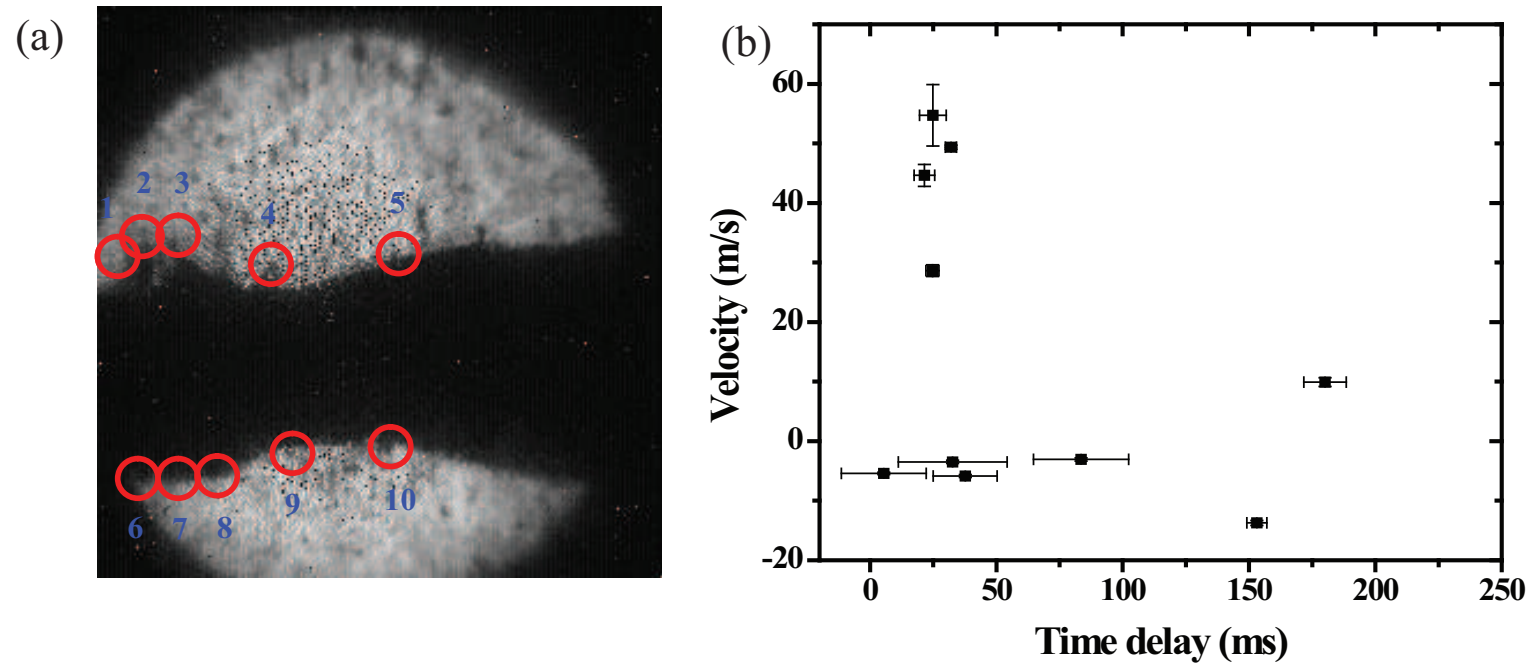


Figure B.6: Shot number is 11010. a.) Illustration of measured filaments. b.) Measured velocity onset time.



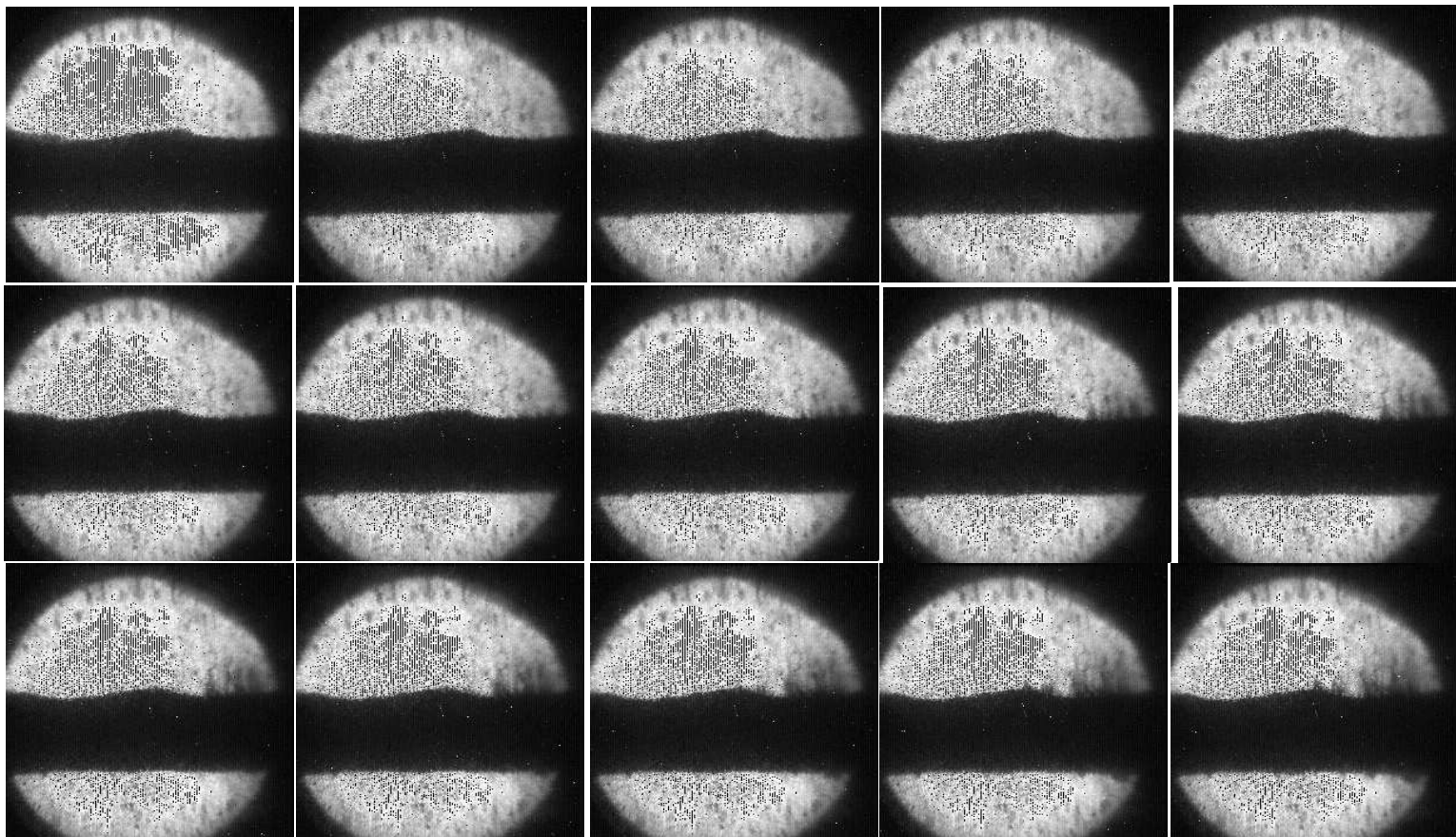


Figure B.7: Shot number is 11021.

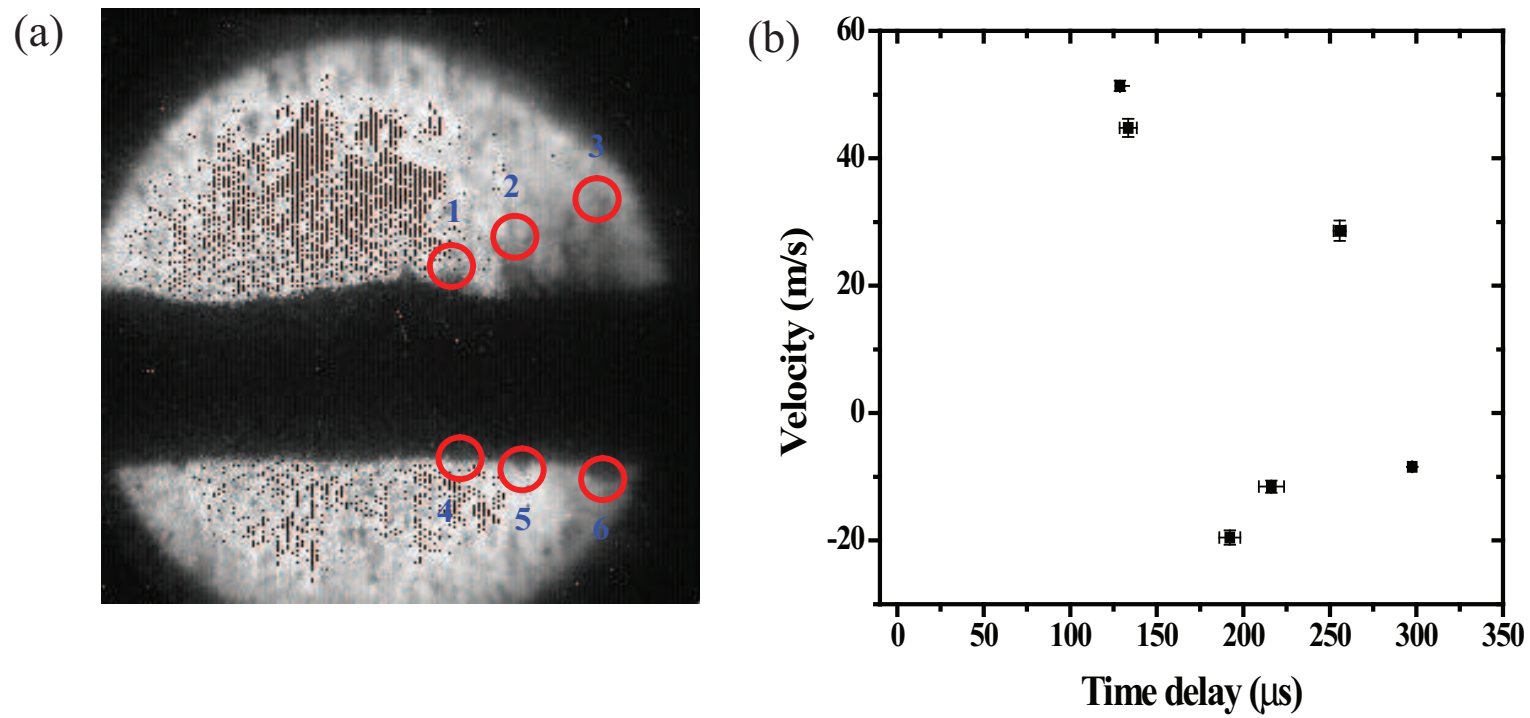


Figure B.8: Shot number is 11021. a.) Illustration of measured filaments. b.) Measured velocity onset time.

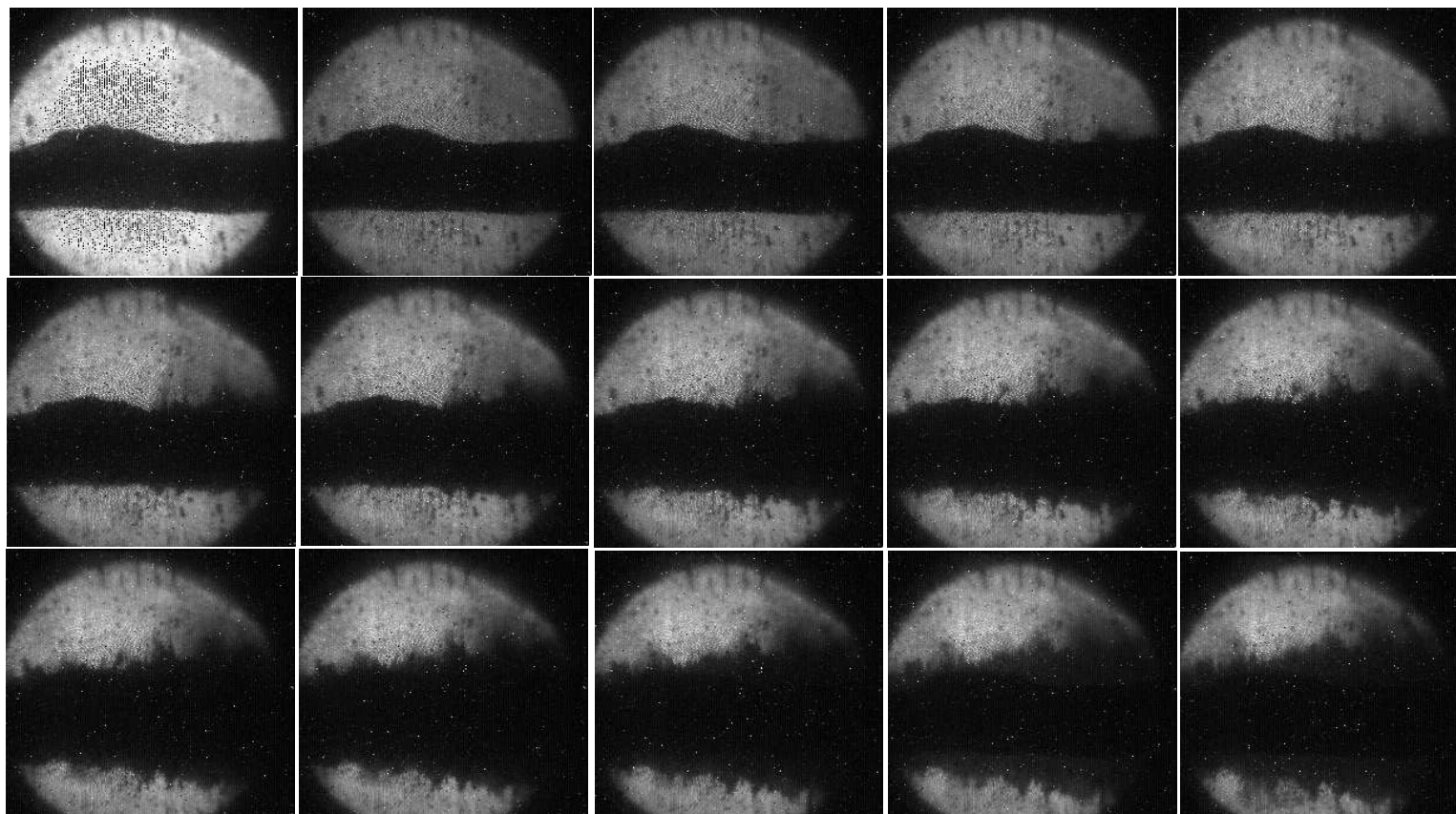


Figure B.9: Shot number is 11032.

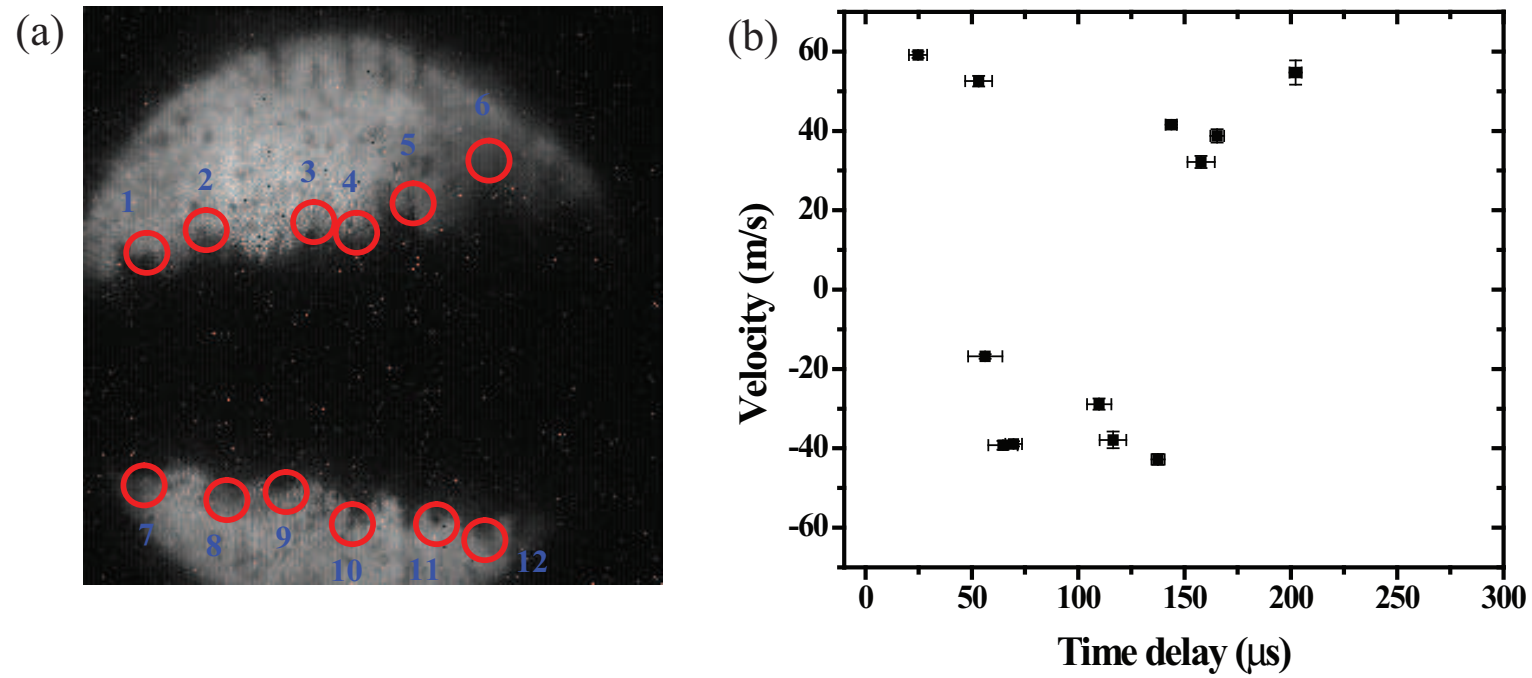


Figure B.10: Shot number is 11032. a.) Illustration of measured filaments. b.) Measured velocity onset time.



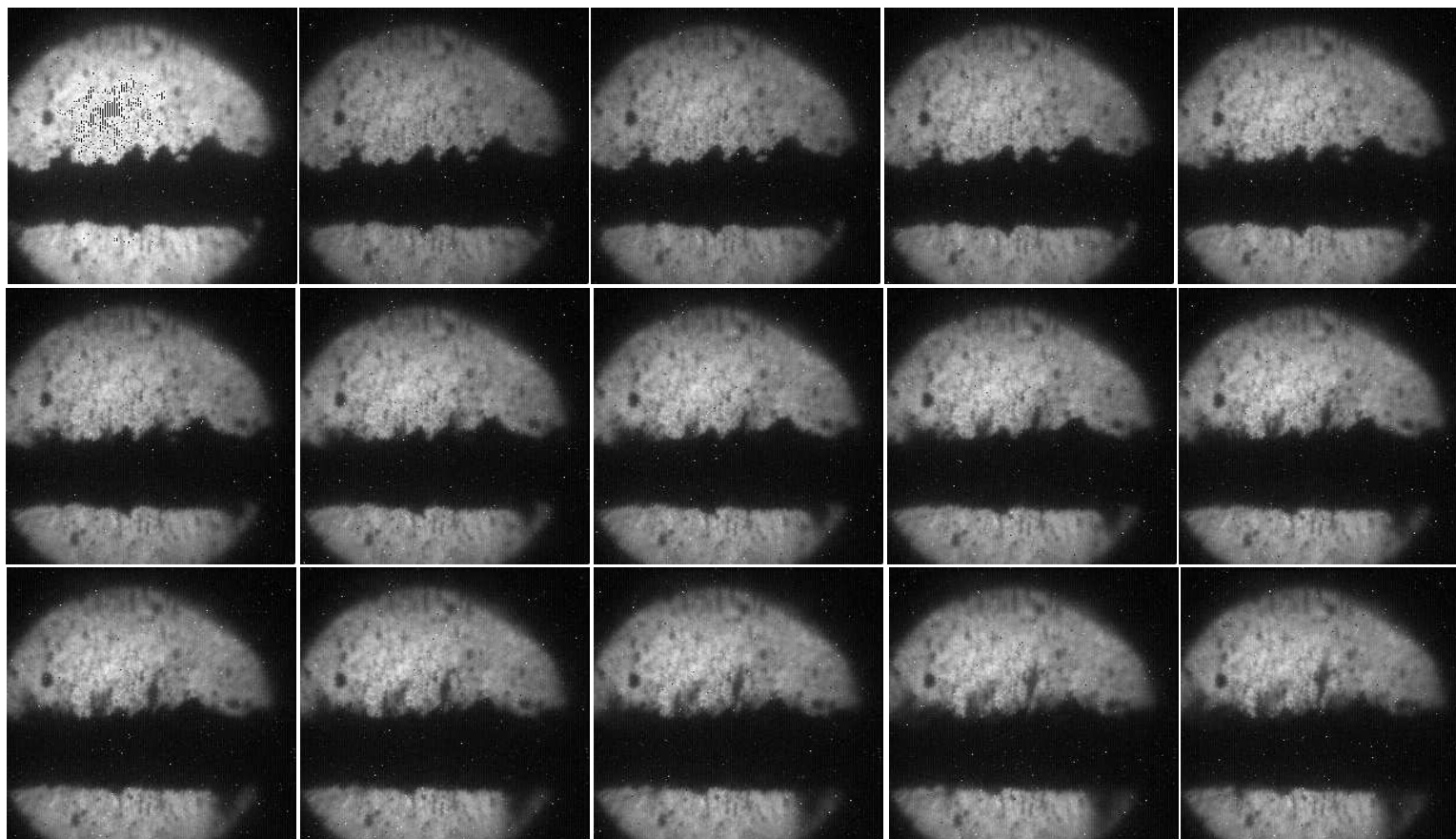


Figure B.11: Shot number is 12031.

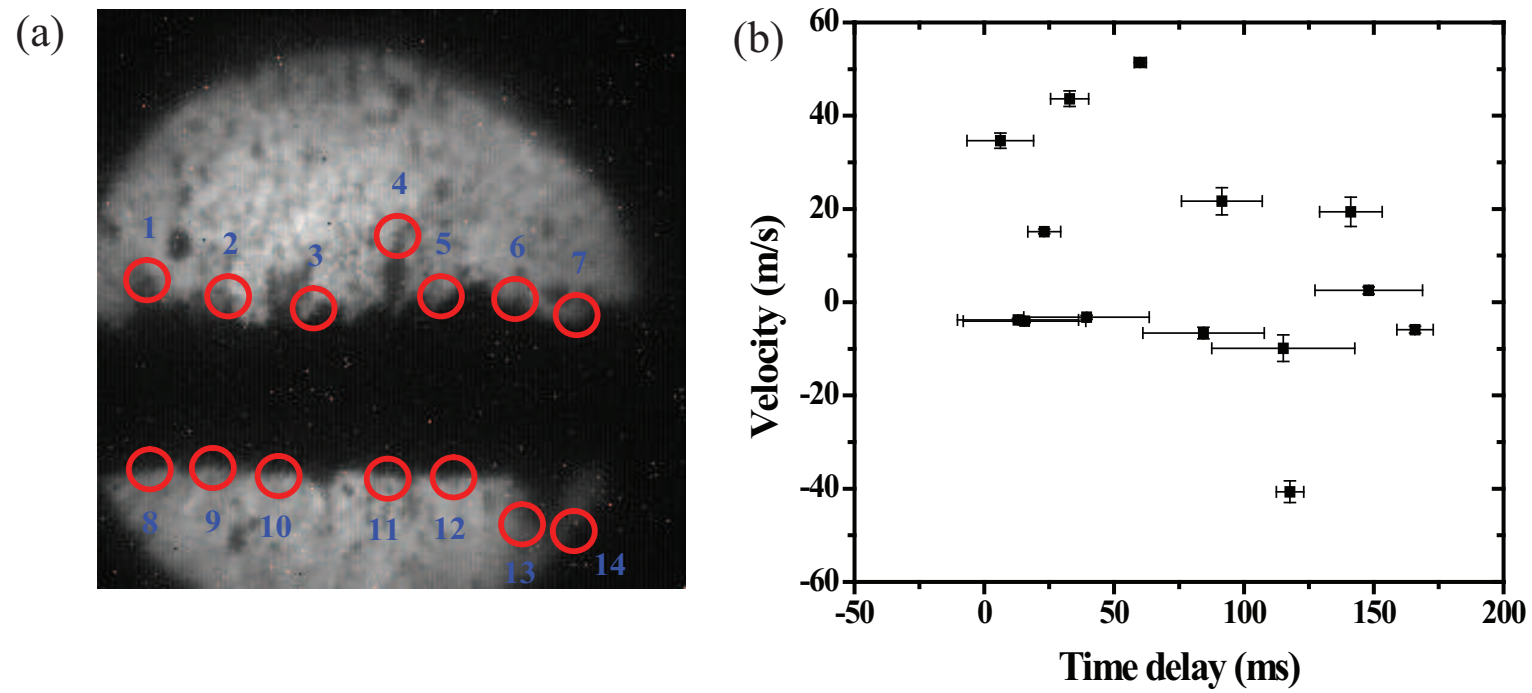


Figure B.12: Shot number is 12031. a.) Illustration of measured filaments. b.) Measured velocity onset time.

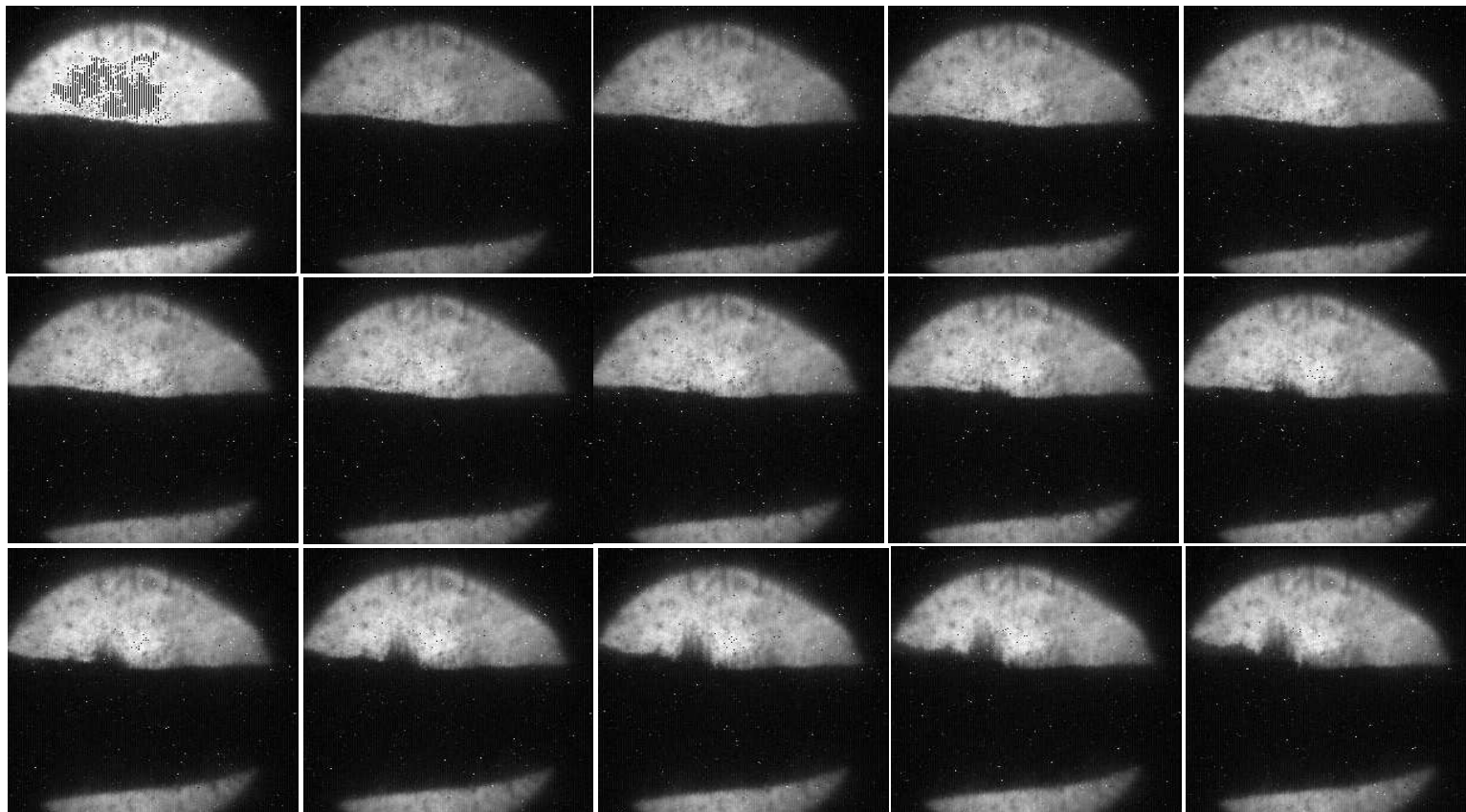


Figure B.13: Shot number is 12032.

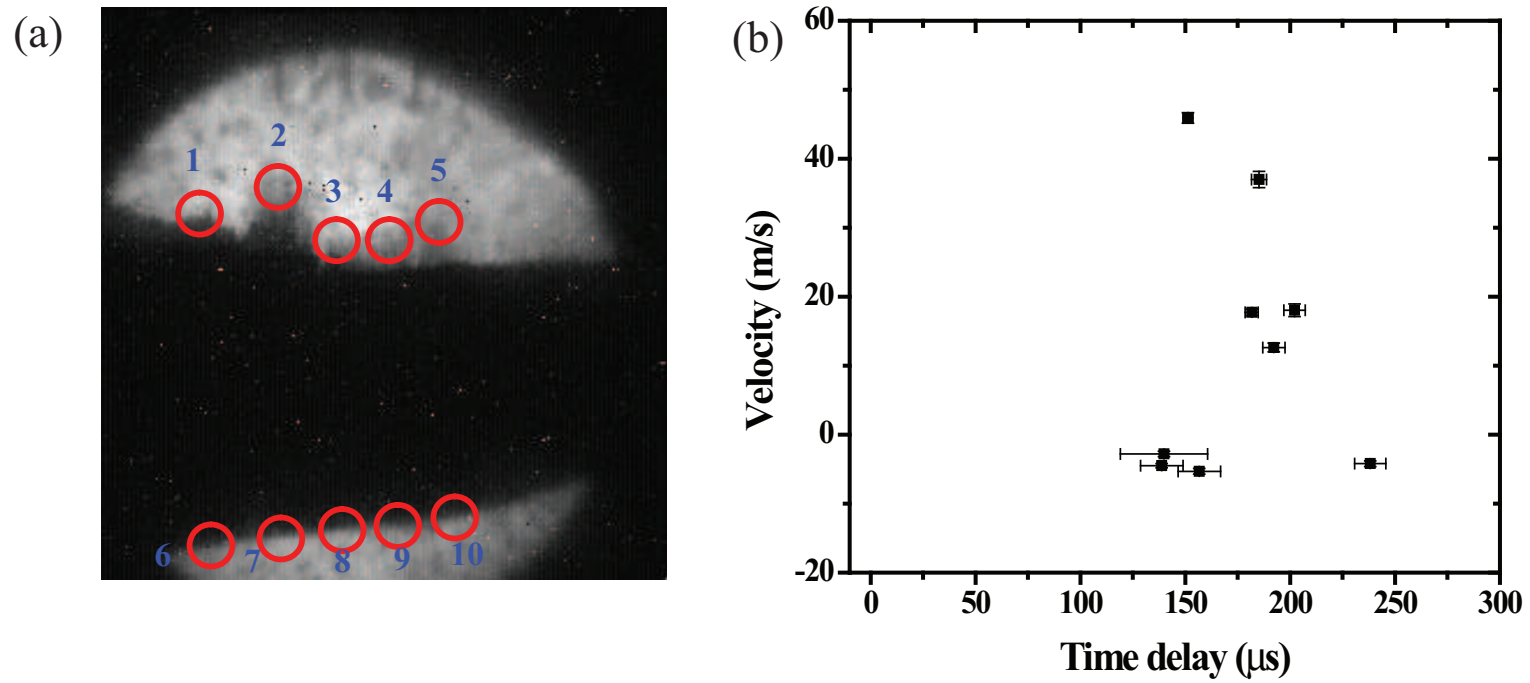


Figure B.14: Shot number is 12032. a.) Illustration of measured filaments. b.) Measured velocity onset time.



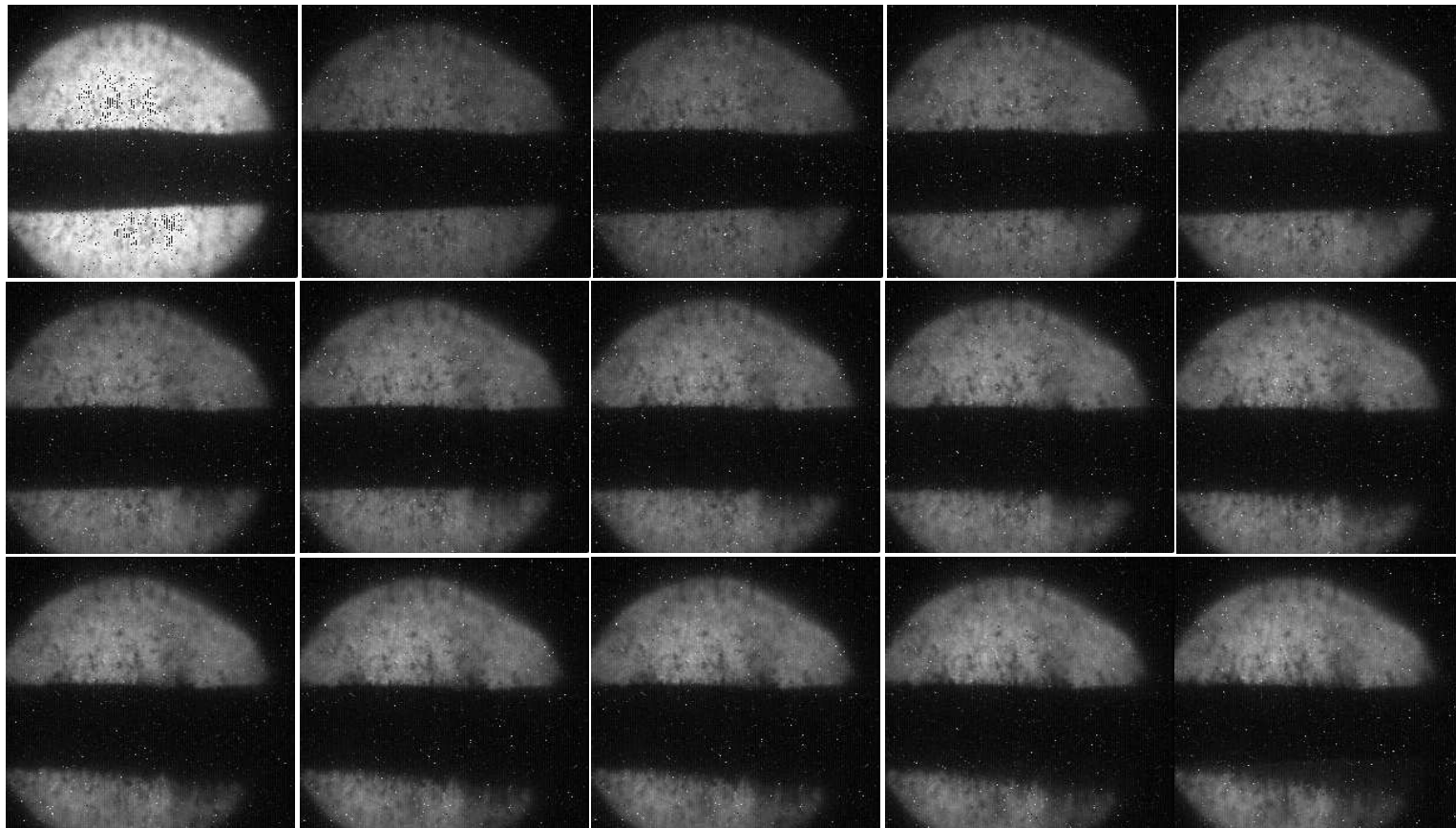


Figure B.15: Shot number is 12033.

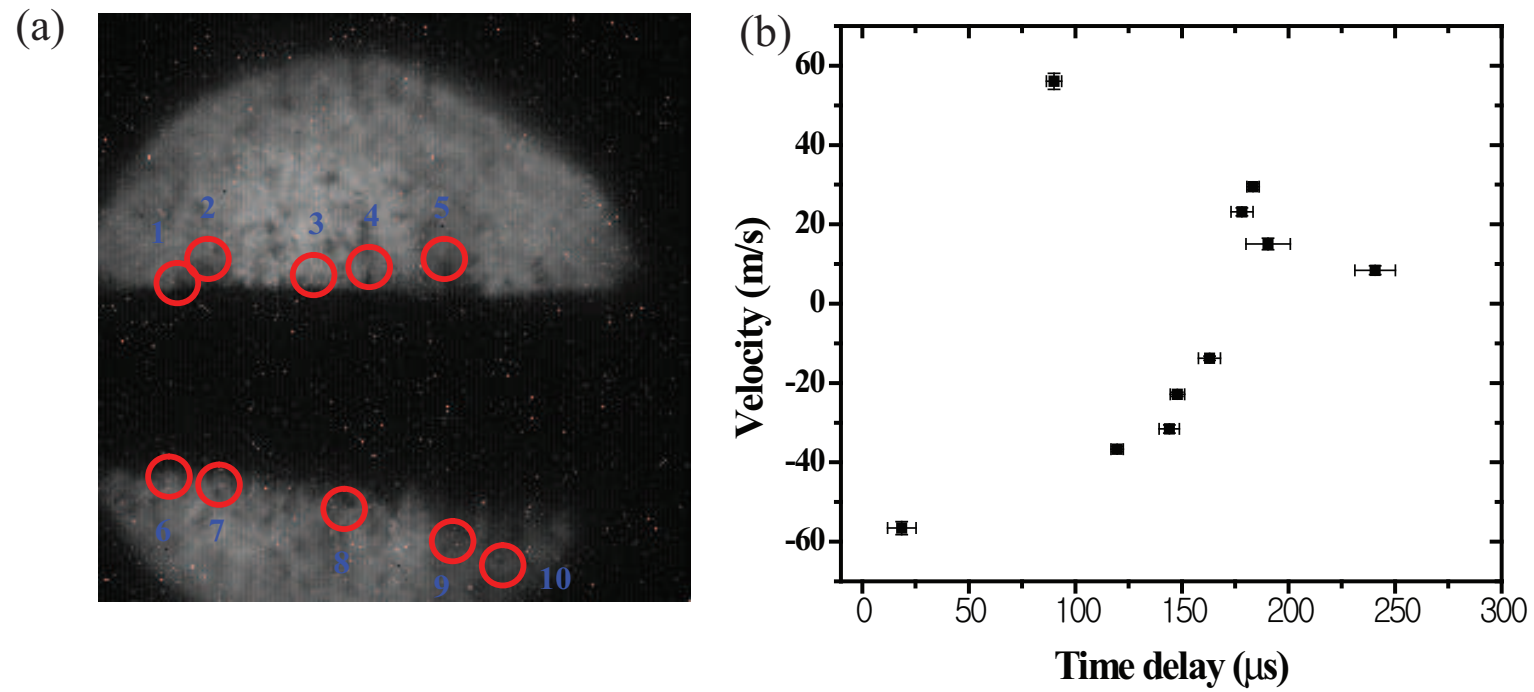


Figure B.16: Shot number is 12033. a.) Illustration of measured filaments. b.) Measured velocity onset time.

## Appendix C

### Mathematical Derivation for Chapter 2

#### C.1 The Governing Equations of MHD Flow in Cylindrical Coordinates

The momentum equations in the  $(r, \theta, z)$  coordinates in Fig. 2.2 can be written as follows:

$$\begin{aligned} & -\rho\left(v_r \frac{\partial v_r}{\partial r} + \frac{v_\theta}{r} \frac{\partial v_r}{\partial \theta} + v_z \frac{\partial v_r}{\partial z}\right) - \frac{\partial p_t}{\partial r} - \rho g \cos \theta + \eta\left(\frac{\partial^2 v_r}{\partial r^2} + \frac{1}{r} \frac{\partial v_r}{\partial r} + \frac{1}{r^2} \frac{\partial^2 v_r}{\partial \theta^2} + \frac{\partial^2 v_r}{\partial z^2}\right) \\ & + \frac{1}{\mu}\left(B_r \frac{\partial B_r}{\partial r} + \frac{B_\theta}{r} \frac{\partial B_r}{\partial \theta} + B_z \frac{\partial B_r}{\partial z}\right) = \rho \frac{\partial v_r}{\partial t}, \end{aligned} \tag{C.1}$$

$$\begin{aligned} & -\rho\left(v_r \frac{\partial v_\theta}{\partial r} + \frac{v_\theta}{r} \frac{\partial v_\theta}{\partial \theta} + v_z \frac{\partial v_\theta}{\partial z}\right) - \frac{1}{r} \frac{\partial p_t}{\partial \theta} + \rho g \sin \theta + \eta\left(\frac{\partial^2 v_\theta}{\partial r^2} + \frac{1}{r} \frac{\partial v_\theta}{\partial r} + \frac{1}{r^2} \frac{\partial^2 v_\theta}{\partial \theta^2} + \frac{\partial^2 v_\theta}{\partial z^2}\right) \\ & + \frac{1}{\mu}\left(B_r \frac{\partial B_\theta}{\partial r} + \frac{B_\theta}{r} \frac{\partial B_\theta}{\partial \theta} + B_z \frac{\partial B_\theta}{\partial z}\right) = \rho \frac{\partial v_\theta}{\partial t}, \end{aligned} \tag{C.2}$$

and

3912

$$- \rho \left( v_r \frac{\partial v_z}{\partial r} + \frac{v_\theta}{r} \frac{\partial v_z}{\partial \theta} + v_z \frac{\partial v_z}{\partial z} \right) - \frac{\partial p_t}{\partial z} + \eta \left( \frac{\partial^2 v_z}{\partial r^2} + \frac{1}{r} \frac{\partial v_z}{\partial r} + \frac{1}{r^2} \frac{\partial^2 v_z}{\partial \theta^2} + \frac{\partial^2 v_z}{\partial z^2} \right) \\ + \frac{1}{\mu} \left( B_r \frac{\partial B_z}{\partial r} + \frac{B_\theta}{r} \frac{\partial B_z}{\partial \theta} + B_z \frac{\partial B_z}{\partial z} \right) = \rho \frac{\partial v_z}{\partial t} ,$$

3913

(C.3)

3914

where  $p_t = p + \frac{\mathbf{B}^2}{2\mu}$ . The magnetic induction equation in the  $(r, \theta, z)$  coordinate directions can be written as follows:

3915

3916

$$\frac{1}{\mu\sigma} \left[ \frac{\partial^2 B_r}{\partial r^2} + \frac{1}{r} \frac{\partial B_r}{\partial r} + \frac{1}{r^2} \frac{\partial^2 B_r}{\partial \theta^2} + \frac{\partial^2 B_r}{\partial z^2} \right] + \frac{1}{r} B_r \left( r \frac{\partial v_r}{\partial r} \right) + \frac{1}{r} B_\theta \frac{\partial v_r}{\partial \theta} + B_z \frac{\partial v_r}{\partial z} \\ - \frac{1}{r} v_r \left( r \frac{\partial B_r}{\partial r} \right) - \frac{1}{r} v_\theta \frac{\partial B_r}{\partial \theta} - v_z \frac{\partial B_r}{\partial z} = \frac{\partial B_r}{\partial t} ,$$

3917

(C.4)

3918

$$\frac{1}{\mu\sigma} \left[ \frac{\partial^2 B_\theta}{\partial r^2} + \frac{1}{r} \frac{\partial B_\theta}{\partial r} + \frac{1}{r^2} \frac{\partial^2 B_\theta}{\partial \theta^2} + \frac{\partial^2 B_\theta}{\partial z^2} \right] + \frac{1}{r} B_r \left( r \frac{\partial v_\theta}{\partial r} \right) + \frac{1}{r} B_\theta \frac{\partial v_\theta}{\partial \theta} + B_z \frac{\partial v_\theta}{\partial z} \\ - \frac{1}{r} v_r \left( r \frac{\partial B_\theta}{\partial r} \right) - \frac{1}{r} v_\theta \frac{\partial B_\theta}{\partial \theta} - v_z \frac{\partial B_\theta}{\partial z} = \frac{\partial B_\theta}{\partial t} ,$$

3919

(C.5)

3920

and

3921

$$\frac{1}{\mu\sigma} \left[ \frac{\partial^2 B_z}{\partial r^2} + \frac{1}{r} \frac{\partial B_z}{\partial r} + \frac{1}{r^2} \frac{\partial^2 B_z}{\partial \theta^2} + \frac{\partial^2 B_z}{\partial z^2} \right] + \frac{1}{r} B_r \left( r \frac{\partial v_z}{\partial r} \right) + \frac{1}{r} B_\theta \frac{\partial v_z}{\partial \theta} + B_z \frac{\partial v_z}{\partial z} \\ - \frac{1}{r} v_r \left( r \frac{\partial B_z}{\partial r} \right) - \frac{1}{r} v_\theta \frac{\partial B_z}{\partial \theta} - v_z \frac{\partial B_z}{\partial z} = \frac{\partial B_z}{\partial t} .$$

3922

(C.6)

3923

The Ampère's law can be written as

3924

$$j_r = \frac{1}{\mu} \left( \frac{1}{r} \frac{\partial B_z}{\partial \theta} - \frac{\partial B_\theta}{\partial z} \right) , \\ j_\theta = \frac{1}{\mu} \left( -\frac{\partial B_z}{\partial r} + \frac{\partial B_r}{\partial z} \right) , \\ j_z = \frac{1}{\mu} \left( \frac{\partial B_\theta}{\partial r} - \frac{1}{r} \frac{\partial B_r}{\partial \theta} \right) .$$

3925

(C.7)

The equation of continuity and the solenoidal condition for the magnetic field are

$$\frac{1}{r} \frac{\partial}{\partial r}(rv_r) + \frac{1}{r} \frac{\partial v_\theta}{\partial \theta} + \frac{\partial v_z}{\partial z} = 0 \quad (\text{C.8})$$

and

$$\frac{1}{r} \frac{\partial}{\partial r}(rB_r) + \frac{1}{r} \frac{\partial B_\theta}{\partial \theta} + \frac{\partial B_z}{\partial z} = 0 . \quad (\text{C.9})$$

## C.2 Derivation of Rayleigh's Instability at An Interface Separating Two Flows in Magnetic Field

### C.2.1 Kinematic boundary condition at interface

We consider the  $(x, y, z)$  coordinate system in Fig. 2.1. A particle of fluid that is at some time on the free surface will always remain on the free surface. Then, since the equation of the free surface is  $y - (\xi + a) = 0$ , it follows that

$$\frac{D}{Dt}(y - (\xi + a)) = 0 . \quad (\text{C.10})$$

Neglecting quadratically small terms, Eqn. (C.10) yields at the interface( $y = \pm a$ ):

$$\frac{\partial \xi}{\partial t} + U_i \frac{\partial \xi}{\partial x} = \frac{\partial \phi_i}{\partial y} . \quad (\text{C.11})$$

In the region  $(-a < y < a)$ , the velocity potential  $\phi_i$  must satisfy  $\frac{\partial^2 \phi_1}{\partial x^2} + \frac{\partial^2 \phi_1}{\partial y^2} = 0$ ,  $|\nabla \phi_1| = \text{finite}$ . In the region  $y > a$ ,  $y < -a$ , the velocity potential must satisfy  $\frac{\partial^2 \phi_2}{\partial x^2} + \frac{\partial^2 \phi_2}{\partial y^2} = 0$ ,  $|\nabla \phi_2| = \text{finite}$ . In view of the shape of the interface, the solutions should be trigonometric in  $x$ , then the  $y$  dependence will be exponential. In view of the finite conditions of velocity potentials, the negative exponential should be rejected for  $\phi_1$  and the positive exponential should be rejected for  $\phi_2$ . Therefore, the general solutions are

3953

$$\phi_1(x, y, t) = A_1 e^{(2\pi/\lambda)y} e^{i(2\pi/\lambda)(x-ct)} ,$$

3954

$$\phi_2(x, y, t) = A_2 e^{-(2\pi/\lambda)y} e^{i(2\pi/\lambda)(x-ct)} . \quad (C.12)$$

3955

Imposing the kinematic conditions on these solutions, the coefficients are determined at  $y = a$  and  $y = -a$  respectively:

3956

3957

$$\phi_1(x, y, t) = -i\epsilon(c - U_1) e^{i(2\pi/\lambda)(x-ct)} ,$$

3958

$$\phi_2(x, y, t) = i\epsilon(c - U_2) e^{i(2\pi/\lambda)(x-ct)} , \quad (C.13)$$

3959

3960

where  $U_1 = U_1(a)$ ,  $U_2 = U_2(a)$  and

$$\phi_1(x, y, t) = i\epsilon(c - U_1) e^{i(2\pi/\lambda)(x-ct)} ,$$

3961

$$\phi_2(x, y, t) = -i\epsilon(c - U_2) e^{i(2\pi/\lambda)(x-ct)} , \quad (C.14)$$

3962

where  $U_1 = U_1(-a)$ ,  $U_2 = U_2(-a)$ .

3963

3964

3965

Since the perturbed surface at  $y = a$  and  $y = -a$  are supposed to be symmetric, half of the jet section for the surface stability is considered in the following work.

3966

## C.2.2 Hydrodynamic stability in magnetic field

3967

3968

3969

3970

3971

3972

Substituting the perturbed expressions into the equations of motion, neglecting second order terms in the perturbed quantities, and making use of the fact that U, P satisfy the flow equations and the current density in Lorentz force term can be represented using Ohm's law, one will have the linearized equations governing the motion of disturbance:

$$\begin{aligned} & \frac{\partial v'_{xi}}{\partial t} + U_i \frac{\partial v'_{xi}}{\partial x} + v'_{xi} \frac{dU_i}{dy} \\ & = -\frac{1}{\rho_i} \frac{\partial p'_i}{\partial x} - \frac{\sigma_i}{\rho_i} B_y^2 v'_{xi} + \frac{\sigma_i}{\rho_i} B_x B_y v'_{yi} \end{aligned} \quad (C.15)$$

3973

3974

and

3975

$$\begin{aligned} & \frac{\partial v'_{yi}}{\partial t} + U_i \frac{\partial v'_{yi}}{\partial x} \\ & = -\frac{1}{\rho_i} \frac{\partial p'_i}{\partial y} - \frac{\sigma_i}{\rho_i} B_x^2 v'_{yi} + \frac{\sigma_i}{\rho_i} B_x B_y v'_{xi} , \end{aligned} \quad (\text{C.16})$$

3976

3977 where  $p'_i = f_i(c, \lambda, y) e^{i(2\pi/\lambda)(x-ct)}$ .

3978 The perturbed velocity  $v'_x, v'_y$  are given as follow:

3979

$$\begin{aligned} v'_x &= \frac{\partial \phi_1}{\partial x} = i \left( \frac{2\pi}{\lambda} \right) A_1 e^{(2\pi/\lambda)y} e^{i(2\pi/\lambda)(x-ct)} \\ v'_y &= \frac{\partial \phi_1}{\partial y} = \left( \frac{2\pi}{\lambda} \right) A_1 e^{(2\pi/\lambda)y} e^{i(2\pi/\lambda)(x-ct)} . \end{aligned} \quad (\text{C.17})$$

3980

3981 Putting Eqn. (C.17) into Eqn. (C.15) and Eqn. (C.16), equate the hydrodynamic  
3982 pressures since it is isotropic, which leads to Rayleigh's stability equation for  
3983 the flow in magnetic field as follow:

3984

$$\sigma_1 B_x B_y + i \sigma_1 B_x^2 = \sigma_1 B_y^2 i - \sigma_1 B_x B_y + \rho_1 \left( \frac{\lambda}{2\pi} \right) \frac{d^2 U_1}{dy^2} , \quad (\text{C.18})$$

3985

3986 where  $U_1 = U_1(y)$ .

3987 In the same manner, the Rayleigh's stability equation for the upper flow  
3988 in magnetic field is derived as follow:

3989

$$\sigma_2 B_x^2 + \sigma_2 B_x B_y i = \sigma_2 B_y^2 - i \sigma_2 B_x B_y - \rho_2 i \left( \frac{\lambda}{2\pi} \right) \frac{d^2 U_2}{dy^2} , \quad (\text{C.19})$$

3990

3991 where  $U_2 = U_2(y)$ .

### 3992 C.2.3 Dynamic boundary condition at interface

3993 The difference of the normal stresses must be balanced by the normal stress  
3994 induced by surface tension at the interface, which is expressed as follow:

3995

$$(P_1 + \frac{\partial P_1}{\partial y} \xi + \frac{\partial^2 P_1}{\partial y^2} \xi + \dots + p'_1) - (P_2 + \frac{\partial P_2}{\partial y} \xi + \frac{\partial^2 P_2}{\partial y^2} \xi + \dots + p'_2) + \Gamma \frac{\partial^2 \xi}{\partial x^2} = 0 , \quad (\text{C.20})$$

3996

3997 where  $\Gamma$  is surface tension.

3998 Considering the gravity force in the free surface waves, Eqn. (C.20) can be  
 3999 rewritten as follow:  
 4000

$$\begin{aligned}
 & (\rho_2 - \rho_1)g \cos \theta + \rho_1(c - U_1)^2\left(\frac{2\pi}{\lambda}\right) + \rho_2(c - U_2)^2\left(\frac{2\pi}{\lambda}\right) \\
 & + \rho_1(c - U_1)\frac{dU_1}{dy} - \rho_2(c - U_2)\frac{dU_2}{dy} + iB_y^2(\sigma_1(c - U_1) + \sigma_2(c - U_2)) \\
 4001 & + B_x B_y(\sigma_2(c - U_2) - \sigma_1(c - U_1)) - \Gamma\left(\frac{2\pi}{\lambda}\right)^2 = 0 , \tag{C.21}
 \end{aligned}$$

4002 where  $U_1 = U_1(a)$ ,  $U_2 = U_2(a)$ .

4003 Consider the case that  $U_2 = 0$ ,  $\frac{dU_2}{dy} = 0$ ,  $\rho_2 = 0$ ,  $\sigma_2 = 0$ . This would  
 4004 correspond to the stationary fluid on the upper and the density and conductivity  
 4005 of the upper fluid are very small compared with these of the lower fluid. The  
 4006 wave velocity is represented as follow:  
 4007

$$\begin{aligned}
 c = [ & -\rho_1\frac{dU_1}{dy} + B_x B_y \sigma_1 - iB_y^2 \sigma_1 + 2\left(\frac{2\pi}{\lambda}\right)\rho_1 U_1 \\
 & \pm \sqrt{\rho_1^2\left(\frac{dU_1}{dy}\right)^2 + 4\left(\frac{2\pi}{\lambda}\right)\cos\theta g \rho_1^2 - 2B_x B_y \rho_1 \sigma_1 \frac{dU_1}{dy} + 2iB_y^2 \rho_1 \sigma_1 \frac{dU_1}{dy}} \\
 & \sqrt{+B_x^2 B_y^2 \sigma_1^2 - 2iB_x B_y^3 \sigma_1^2 - B_y^4 \sigma_1^2 + 4\left(\frac{2\pi}{\lambda}\right)^3 \rho_1 \Gamma} \quad ] \times \frac{1}{2\left(\frac{2\pi}{\lambda}\right)\rho_1} . \tag{C.22}
 \end{aligned}$$

4008